Technische Universität München

TUM School of Engineering and Design

Characterization of Lithium-Ion Batteries in Electric Vehicles over their Lifetime

Leo Frederick Enrico Wildfeuer, M.Sc.

Vollständiger Abdruck der von der TUM School of Engineering and Design der Technischen Universität München zur Erlangung eines

Doktors der Ingenieurwissenschaften (Dr.-Ing.)

genehmigten Dissertation.

Vorsitz:	Prof. Dr.-Ing. Rüdiger Daub
Prüfende der Dissertation:	1. Prof. Dr.-Ing. Markus Lienkamp
	2. Prof. Dr.-Ing. Andreas Jossen

Die Dissertation wurde am 26.02.2025 bei der Technischen Universität München eingereicht und durch die TUM School of Engineering and Design am 21.04.2025 angenommen.

Abstract

Lithium-ion batteries play a pivotal role in reducing greenhouse gas emissions in the mobility sector. However, they are also the Achilles' heel in this transition, as much of the hesitation to adopt battery electric vehicles (BEVs) stems from concerns about the battery. This thesis provides experimental results and analytical methods to optimize the development and operation of lithium-ion batteries in BEVs. It presents five studies across the research dimensions of *modeling*, *aging*, and *system design*, all centered on the *electric behavior* of lithium-ion batteries.

A single lithium-ion cell is the smallest unit that can be optimized in a battery system, and a thorough understanding of its electric behavior lays the groundwork for all subsequent development steps. Study I presents a systematic approach to cell teardown and half-cell measurements for electrically characterizing a commercial lithium-ion cell. The mechanistic OCV model is extended to determine the capacities of both electrodes and the lithium inventory, enabling the calculation of degradation modes for aged cells. Furthermore, kinetic loss processes are assigned to each electrode, ensuring a physically meaningful parameterization of electric models.

The automotive industry relies on simulation models to accelerate time-to-market and facilitate customer-relevant onboard functionalities. This thesis introduces new methods for parameterizing dynamic parameters in equivalent circuit models (ECM) throughout the development and operation of BEVs. Study II enhances resistance parameterization by combining time-domain and frequency-domain measurements via the distribution of relaxation times (DRT). Study III enables online resistance parameterization across a wide frequency range, handling arbitrary load profiles from BEV operation. Both approaches are physically motivated, ensuring greater accuracy and robustness compared to existing methods.

Complex degradation mechanisms diminish battery performance over their lifetime. Study IV examines 196 lithium-ion cells subjected to calendar, cycle, and dynamic aging across a broad range of all main stress factors. Capacity fade, resistance increase, loss of lithium inventory (LLI), and loss of active material (LAM) at both electrodes were monitored to gain a comprehensive view of how aging impacts the electric properties of batteries. The results show that periodic check-ups significantly affect calendar aging rates, revealing that the calendar life of batteries has been underestimated in the past. The open-source dataset, with over 4,000 check-up measurements, offers a valuable resource for developing advanced data-driven aging models to reduce the impact of battery degradation on customers.

The electric behavior of BEVs is influenced not only by individual lithium-ion cells but also by the battery pack as a whole. Understanding system-level effects when scaling electric characteristics from cell to pack level is crucial. Based on a statistical analysis of 600 characterized fresh lithium-ion cells, Study V demonstrates that inherent cell-to-cell parameter variations due to production tolerances are negligible compared to the inhomogeneities caused by temperature gradients in battery packs. This finding suggests that future production quality standards could be relaxed to reduce BEV purchasing costs.

Foreword

This dissertation presents the research I conducted as a PhD candidate at the Institute of Automotive Technology at the Technical University of Munich from April 2018 to March 2022, under the supervision of Prof. Dr.-Ing. Markus Lienkamp. I am deeply grateful for the opportunity, support, and trust I was given. Furthermore, I would like to thank Prof. Dr.-Ing. Andreas Jossen for taking over the co-evaluation of this thesis and Prof. Dr.-Ing. Rüdiger Daub for chairing the final examination.

The dissertation is built on the five main publications written during this period and integrated into the main body of this work [1–5]. I would like to thank all my co-authors for their excellent contributions. Special thanks go to Nikolaos Wassiliadis and Alexander Karger, with whom I share the first authorship on one of these publications, respectively.

Additionally, two other research articles not included in this thesis but considered state of the art were published as (shared) first author at the beginning of my time as a research associate [6, 7]. These publications are built on the findings of my semester and master's theses [8, 9]. I am particularly thankful to Michael Baumann and Stephan Rohr for their supervision of my student theses and their later support, through their battery software company TWAICE Technologies GmbH, of the joint research project *bawaii*, funded by the Bavarian Ministry of Economic Affairs under the grant number IUK-1808-0013 [10].

Experiments conducted at the battery laboratory of the Institute of Automotive Technology form a significant portion of this dissertation. Whenever appropriate, the measurement data were published as open source alongside the corresponding articles [11–14]. It's rewarding to see that these data have been utilized beyond my own research, in particular, allowing me to support Alexander Karger's work even after my active time as researcher [15–19].

Several other research articles, in which I acted as a co-author, were published. I would like to thank everyone for the opportunity to contribute [20–27]. In addition to the publications, I supervised numerous bachelor, semester, and master's theses. Many of these works laid the foundation for this dissertation, and I am thankful for everybody's efforts [28–57].

I would like to thank Alexander Karger, Philip Bilfinger, Remco van der Burg, and Julian Chudoba for proofreading this thesis. Additionally, this thesis was reviewed for language and grammar using the AI tools Grammarly [58] and ChatGPT [59], which were solely utilized for linguistic refinement and not for content creation.

Contents

List of Abbreviations ..... **III**
Formula Symbols ..... **V**
1 Introduction **1**
1.1 Goal and Outline **2**
1.2 Electric Behavior of Lithium-Ion Cells **5**
1.2.1 Capacity 5
1.2.2 Open-Circuit Voltage 6
1.2.3 Resistance 9
1.3 Modeling the Electric Behavior **13**
1.3.1 Equivalent Circuit Models 14
1.3.2 Parameter Identification 15
1.4 Influence of Aging on the Electric Behavior **16**
1.4.1 Aging Domains and Stress Factors 16
1.4.2 Degradation Mechanisms 17
1.4.3 Degradation Modes and Aging Effects 18
1.5 Influence of System Design on the Electric Behavior **20**
1.5.1 Scaling Electric Parameters from Cell to Pack Level 20
1.5.2 Parameter Variations and Inhomogeneities in Battery Packs 21
1.6 Research Questions **23**
2 Contributions **25**
2.1 Electrical Characterization based on Half-Cell Measurements **26**
2.2 Methods for Resistance Parameterization in ECMs **44**
2.2.1 Experimental Determination of Resistance Parameters 44
2.2.2 Online Estimation of Resistance Parameters in Electric Vehicles 70
2.3 Experimental Degradation Study **86**
2.4 Quantification of Inherent Cell-to-Cell Parameter Variations **104**
3 Discussion **119**
3.1 Leveraging Half-Cell Measurements **119**
3.2 Parameterizing Resistance Throughout Development and Operation of BEVs **120**
3.3 Impact of Aging on SOH_C, SOH_R, LLI, LAM_{an}, and LAM_{cat} **122**
3.4 Role of Inherent Cell-to-Cell Variations in Battery Packs of BEVs **123**
4 Conclusion **125**
List of Figures ..... **i**
Bibliography ..... **iii**
Prior Publications ..... **xxi**
Supervised Student Theses ..... **xxv**

List of Abbreviations

BEV	battery electric vehicle
CC	constant current
CCCV	constant current constant voltage
CV	constant voltage
DC	direct current
DOD	depth of discharge
DRT	distribution of relaxation times
DVA	differential voltage analysis
ECM	equivalent circuit model
EIS	electrochemical impedance spectroscopy
GITT	galvanostatic intermittent titration technique
LAM	loss of active material
LFP	lithium iron phosphate
LLI	loss of lithium inventory
NCA	nickel cobalt aluminium oxide
NMC	nickel manganese cobalt oxide
OCP	open-circuit potential
OCV	open-circuit voltage
OEM	original equipment manufacturer
RC	resistor capacitor
SEI	solid electrolyte interphase
SOC	state of charge
SOH	state of health

Formula Symbols

Formula Symbols	Unit	Description
α_{an}	-	anode scaling parameter in the mechanistic OCV model
α_{cat}	-	cathode scaling parameter in the mechanistic OCV model
β_{an}	-	anode alignment parameter in the mechanistic OCV model
β_{cat}	-	cathode alignment parameter in the mechanistic OCV model
C	Ah	capacity
C_{an}	Ah	capacity of the anode
C_{cat}	Ah	capacity of the cathode
C_{li}	Ah	capacity of lithium inventory
C_n	Ah	capacitance of the n-th RC element in an ECM
C_{pack}	Ah	capacity of a battery pack
f	Hz	frequency
I	A	current
$\mathrm{LAM}_{\mathrm{an}}$	%	loss of active material at the anode
$\mathrm{LAM}_{\mathrm{cat}}$	%	loss of active material at the cathode
LLI	%	loss of lithium inventory
p	-	number of parallel connected cells
R	Ω	resistance
R_0	Ω	pure ohmic resistance in an ECM
R_n	Ω	resistance of the n-th RC element in an ECM
$R_{\mathrm{additional}}$	Ω	additional resistance due to wiring, fuses, etc.
R_{contact}	Ω	contact resistance
R_{ct}	Ω	resistance caused by the charge transfer process
R_{DC}	Ω	direct-current resistance
R_{diff}	Ω	resistance caused by diffusion
R_{ohm}	Ω	ohmic resistance

R_{pack}	Ω	resistance of a battery pack
R_{SEI}	Ω	resistance caused by the solid electrolyte interphase
s	-	number of serial connected cells
SOC	%	state of charge of the full-cell
SOC_{an}	%	state of charge of the anode
SOC_{cat}	%	state of charge of the cathode
SOH_{C}	%	state of health based on capacity
SOH_{R}	%	state of health based on resistance
t	s	time
t_0	s	time step at the beginning of a DC pulse
t_n	s	time step during a DC pulse
Δt	s	sampling rate
τ	s	time constant
τ_n	s	time constant of the n-th RC element in an ECM
T	°C	temperature
U	V	voltage
U_0	V	overpotential at R_0 in an ECM
U_{an}	V	anode open-circuit potential
U_{cat}	V	cathode open-circuit potential
U_{ct}	V	overpotential caused by the charge transfer
U_{diff}	V	overpotential caused by diffusion
U_{OCV}	V	open-circuit voltage
$U_{\text{OCV,pack}}$	V	open-circuit voltage of a battery pack
U_{ohm}	V	overpotential caused by the ohmic resistance
$U_{\text{RC}n}$	V	overpotential at the n-th RC element in an ECM
U_{SEI}	V	overpotential caused by the solid electrolyte interphase
U_{terminal}	V	voltage measured between the cell terminals
Z	Ω	impedance
Z_{real}	Ω	real part of the impedance
$Z_{\text{imaginary}}$	Ω	imaginary part of the impedance
$Z_{\text{RC}n}$	Ω	impedance of the n-th RC element in an ECM

1 Introduction

Scientific evidence for the warming of the Earth's climate is undeniable [60], and the transition of our society to reduce greenhouse gas emissions has become one of the major challenges of the 21st century. At the 2015 United Nations Climate Change Conference, an agreement was reached to limit the increase in global average temperature to well below 2 °C above pre-industrial levels, recognizing that this target would significantly reduce the risks and impacts of climate change [61].

To achieve this objective, greenhouse gas emissions must be significantly reduced across all sectors, including energy and transportation [62]. In the energy sector, the primary strategy for reducing CO_2 emissions is transitioning from fossil fuels to renewable energy sources. However, since renewables like solar and wind power are weather-dependent and fluctuate, battery energy storage systems play a critical role in enabling this transition. Simultaneously, renewable energies are a prerequisite for a significant reduction of CO_2 emissions in the transportation sector. The strategy here involves replacing combustion engine vehicles with electric vehicles, particularly battery electric vehicles (BEVs), which benefit from green electricity [62].

According to the EU Climate Law of June 2021 with the objective to reduce greenhouse gas emissions by 55 % until 2030 and 100 % until 2050, new combustion engine vehicles should be completely replaced by 2035 [62]. This trend has already begun, not only in Europe but also in other major markets such as the USA and China, as reported in the Global Electric Vehicle Outlook 2024 by the International Energy Agency (IEA) [63]. Figure 1.1 shows their data on the relative sales of BEVs.

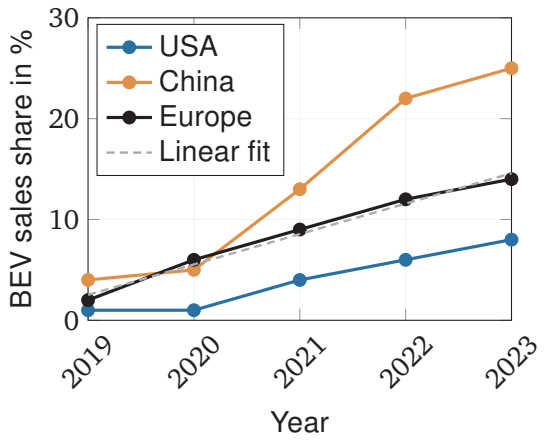

Figure 1.1: BEV sales share in Europe, China, and USA between 2019 and 2023. Data taken from the Global Electric Vehicle Outlook 2024 by the International Energy Agency [63].

The annual registration of BEVs and their corresponding sales share has continuously increased over the past 5 years. However, the growth rate of the sales share is sublinear, far from the exponential growth needed to complete the transition to full electrification by 2035. A linear fit

over Europe's sales share data from the last five years reveals that only about 50 % of total car sales in 2035 will be BEVs if the growth rate doesn't increase in the future. In Germany, the sales share for electric cars (BEVs and plug-in hybrid electric vehicles) even fell from 30 % in 2022 to 25 % in 2023 [63].

This can be explained by the phase-out of several purchase subsidies, as well as by lingering concerns among customers. The German National Academy of Science and Engineering (acatech) publishes the results of a representative survey on mobility in Germany each year—the mobility monitor [64]. Their 2024 survey revealed that the number of people expressing interest in buying a BEV continuously declined in the last 5 years from 24 % in 2020 to 17 % in 2024. A study by McKinsey & Company presents similar results [65]. Both studies also provide insights into the reasons preventing people from purchasing a BEV. Some of the stated concerns refer to limited charging infrastructure or increases in electricity prices. Additionally, many of the stated concerns refer to the electric vehicle as a product itself [64, 65]:

- High purchase price
- Unclear resale value due to rapid technology advancements
- Limited driving range
- Long charging times
- Reduced battery lifetime
- High safety risk

This shows that on the one hand, lithium-ion batteries are a key enabler of the electrification of individual mobility but on the other hand, they are also the Achilles' heel because most of the reluctance of customers in buying BEVs originates in the battery. These purchasing barriers must be addressed to increase the market share of BEVs and achieve the ambitious goal of fully decarbonizing the mobility sector. Hence, current research activities focus on different fields ranging from fundamental science to applied engineering: Material scientists experiment with new material compositions to push toward higher energy densities. Production engineers optimize the cell design and push towards more efficient production processes to reduce cost. In the context of automotive engineering, researchers aim to optimize the development and operation of battery systems for electric vehicles.

1.1 Goal and Outline

This thesis provides experimental results and analytical methods to optimize the development and operation of lithium-ion batteries in BEVs. Five studies are presented to address research questions across different research dimensions, which are illustrated in Figure 1.2. Characterizing the *electric behavior* of lithium-ion cells forms the foundation of this work. From here, the thesis moves along and in between the research dimensions *modeling*, *aging*, and *system design*, all three concerning the electric behavior of lithium-ion batteries. The research dimensions are further motivated below.

Electric behavior: From an original equipment manufacturer (OEM) perspective, the single lithium-ion cell is the smallest entity that can be influenced and optimized. There are hundreds of cell types with different characteristics on the market [66] and typically, OEMs work together with cell manufacturers to adapt cell properties for the application's requirements. Since the purpose

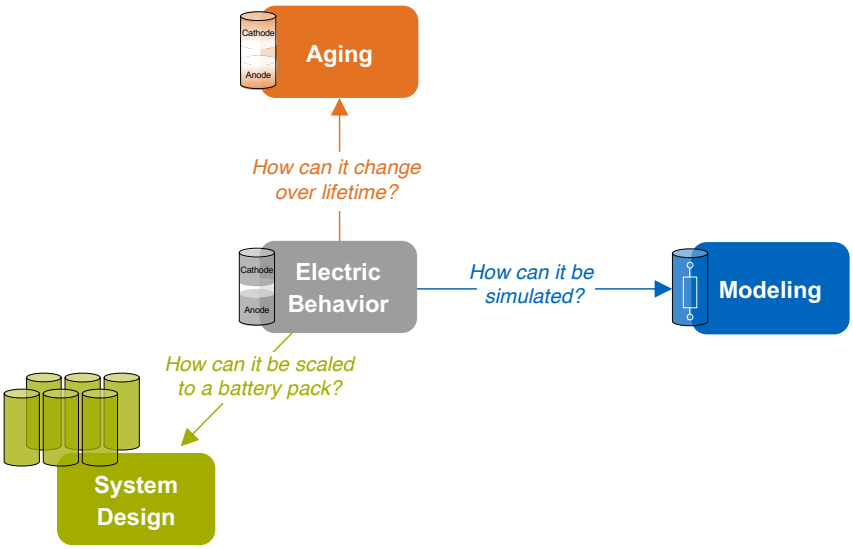

Figure 1.2: Overview of the pursued research dimensions.

of the battery is to provide energy and power, the electric characteristics of a chosen lithium-ion cell influence customer-relevant features such as driving range and charging speed [27, 67, 68]. Thus, understanding the electric behavior of a specific lithium-ion cell is the foundation for all downstream steps in the development process.

Modeling: The automotive industry aims to quickly integrate advancements in battery technology into their products. To achieve faster time-to-market, OEMs accelerate the development cycle of BEVs by utilizing simulation models in different stages of the development process. Simulative analyses can reduce the effort and time for prototyping and physical testing during, e.g., the cell selection process [69] or battery pack design process [21]. Furthermore, electric models are utilized for onboard functionalities such as range estimation or adaptive charging protocols [26, 70, 71], which emphasizes the need for reliable and accurate models.

Aging: Range anxiety is one of the biggest reasons why customers are hesitant to buy BEVs and to make it even worse, battery aging leads to capacity fade which further reduces the driving range over time. To make the capacity fade less noticeable for the customer and circumvent a decrease in driving range to a certain extent, OEMs typically limit the usable capacity initially and revoke the throttling progressively over lifetime [20]. Limiting the operating window can also have a positive impact on the aging rate itself [72]. Overall, this means that the battery pack is oversized, which increases costs. Furthermore, battery degradation leads to power fade which at some point can trigger disabling customer-relevant functionality such as fast charging [26]. In order to prevent this, innovative charging protocols need to be developed [71, 73]. In-depth knowledge of how battery degradation impacts the electric behavior of the battery is required to limit its impact on the customer.

System design: In a BEV, lithium-ion battery packs are composed of multiple lithium-ion cells. Eventually, the electric properties of BEVs are not only determined by the chosen lithium-ion cell but by the battery pack as a whole. Decisions in the system design process, such as dimensioning of the battery pack, definition of the topology, and design of the cooling system will all contribute to the overall production costs [74]. Thus, it is important to understand system-level effects when scaling the characteristics from a single cell to pack level during the development process.

Figure 1.3 gives an overview of the structure of this work. Having outlined the goal of this work above, the remainder of Chapter 1 presents the relevant fundamentals and the state of the art in the research dimensions pursued. Section 1.2 introduces the main electrical parameters of lithium-ion batteries, how they can be experimentally determined, and how they are influenced. These parameters are the capacity, which is relevant for the driving range of a BEV, the open-circuit voltage, which describes the static behavior of a battery, and the resistance, which describes the dynamic behavior and power capabilities of a battery. Section 1.3 describes the simulation of battery electric behavior using equivalent circuit models (ECMs) and outlines methods for identifying key parameters. In the aging dimension (Section 1.4), the complex cause-and-effect relationship of stress factors, degradation mechanisms, and aging effects is reviewed. Methods for characterizing changes in electric behavior caused by aging are presented. Section 1.5 addresses the fundamentals of battery system design, detailing how the electric behavior can be scaled from a single lithium-ion cell to a battery pack for BEV applications. Moreover, this section discusses how inhomogeneities within multiple interconnected lithium-ion

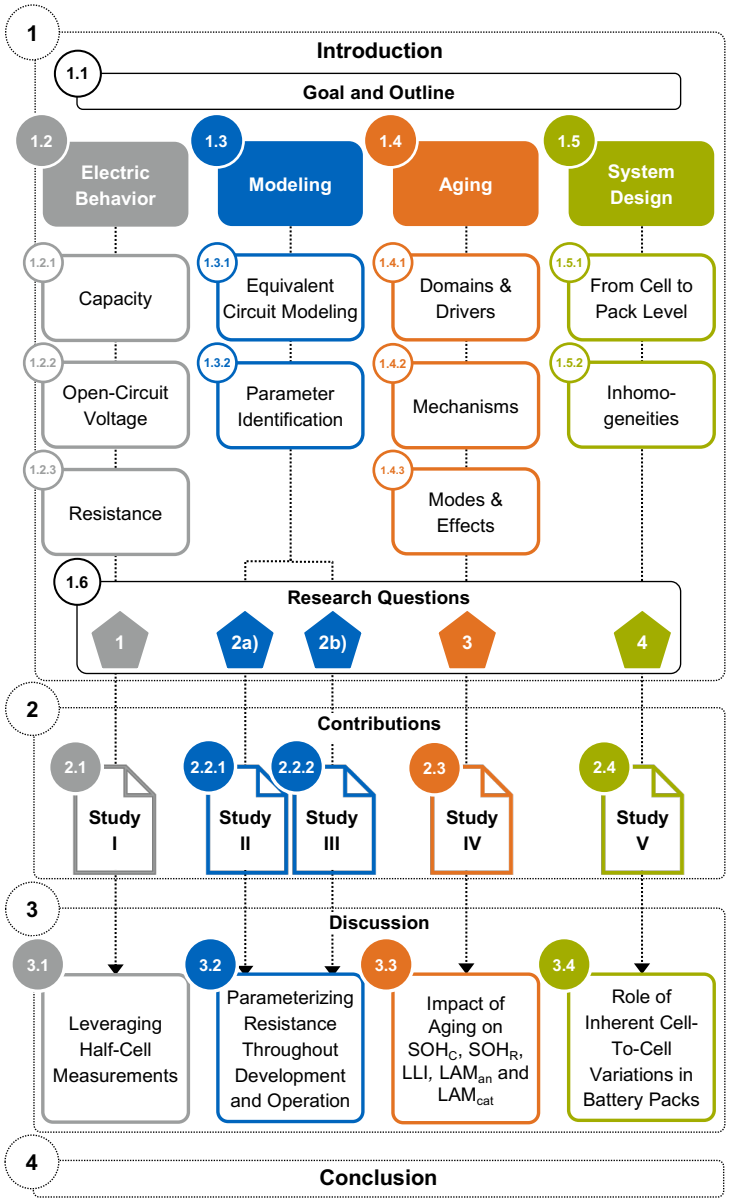

Figure 1.3: Structure of this thesis.

cells affect the overall electric behavior. In Section 1.6, research questions are formulated based on the state of the art within the research dimensions. Chapter 2 presents five publications that address these research questions. Study I leverages insights from the electrodes of a commercial lithium-ion cell to enhance the characterization of key electric parameters (Section 2.1). Studies II and III introduce new methods for the parameterization of resistance in electric models: Study II during the development phase of BEVs, and Study III during the operation of BEVs (Section 2.2). Study IV provides extensive aging data over a broad range of operating conditions and investigates the impact of aging on electric behavior by calculating an extensive set of health parameters (Section 2.3). Study V contributes by assessing the role of cell-to-cell variations caused by production tolerances when scaling the electric behavior from cell level to pack level (Section 2.4). Chapter 3 critically discusses the results within the pursued research dimensions. Chapter 4 concludes the thesis by summarizing how the findings contribute to the objectives of this work and outlining directions for future research.

1.2 Electric Behavior of Lithium-Ion Cells

Lithium-ion cells are composed of two electrodes that enable the intercalation and deintercalation of lithium ions. An electrolyte facilitates the transport of lithium ions between the electrodes. A separator electrically isolates the electrodes so that electrons can flow through the current collectors, positioned at each electrode, and pass through an external electric circuit [75]. In this thesis, the positive electrode is referred to as the cathode and the negative electrode is referred to as the anode. Typical cathode materials are metal oxides such as nickel cobalt aluminium oxide (NCA), nickel manganese cobalt oxide (NMC), or lithium iron phosphate (LFP) [76]. The anode is typically graphite [77]. To achieve higher energy densities, a small amount of silicon, known for its higher theoretical capacity, can be added [78, 79].

1.2.1 Capacity

The capacity C of a lithium-ion cell describes the amount of charge that can be charged and discharged in one cycle and is directly correlated with the driving range of BEVs. The relative remaining capacity that can be discharged at a certain point is defined as the state of charge (SOC). The capacity not only depends on the theoretical gravimetric capacity of used electrode materials but can vary with cell format and size. It ranges from a few Ah for small cylindrical cells to over 100 Ah for large prismatic cells.

Within this thesis, the capacity is defined as the discharge capacity. It can be experimentally determined by fully charging and subsequently fully discharging the cell. The resulting capacity will slightly differ depending on the specific measurement protocol [80]. Typically, the constant current constant voltage (CCCV) method, illustrated in Figure 1.4, is applied. Thereby, the following parameters have to be defined:

- The current during the constant current (CC) phase
- The voltage at which it is switched to the constant voltage (CV) phase
- The cut-off current to eventually stop the CV phase

These parameters must be defined for both the initial charging phase and the subsequent discharging phase. The capacity is calculated by integrating current over time during the discharge

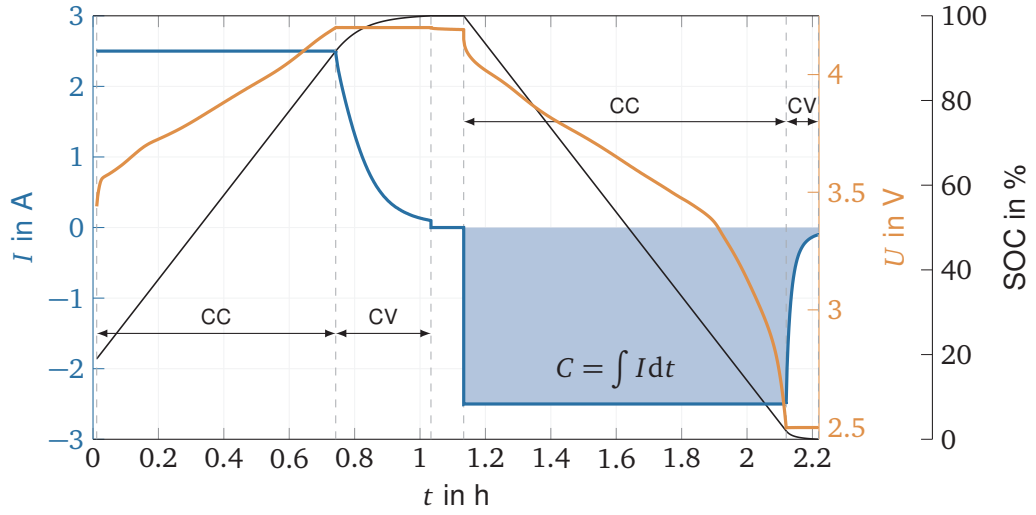

Figure 1.4: CCCV measurement procedure to determine the capacity C of a lithium-ion cell. Measurement performed with a cell of type US18650VTC5A by Sony/Murata.

phase. In general, measured capacity values are higher when either the chosen constant current is small, due to smaller overpotentials, or when the CV phase is long, as more lithium-ions are intercalated and deintercalated. Another option is to apply a small constant current, making the CV phase unnecessary. This method allows for determining the static behavior of a cell, as described in the next section.

1.2.2 Open-Circuit Voltage

Thermodynamic Equilibrium

If a lithium-ion cell is at rest and in equilibrium conditions, the full-cell open-circuit voltage (OCV) U_{OCV} can be measured between the cell terminals. It results from the difference in electrochemical potentials of lithium in the cathode and the anode:

$$U_{\mathrm{OCV}} = U_{\mathrm{cat}} - U_{\mathrm{an}}. \tag{1.1}$$

Here, U_{cat} and U_{an} refer to the cathode and anode open-circuit potentials (OCPs). Different material compositions have different electrochemical potentials against lithium [81], which is why LFP cells have a lower energy density compared to NMC or NCA cells. Despite using the same anode material, the voltage window of the LFP cathode is lower, resulting in a lower nominal voltage of the full cell (3.2–3.3 V for LFP and 3.6–3.7 V for NMC or NCA).

Figure 1.5a) shows U_{OCV}, U_{cat} and U_{an} for a cell with silicon-graphite anode and NCA cathode. It can be seen that both electrode OCPs depend on the degree of lithiation, meaning that U_{cat} and U_{an} change during charging (lithiation of the anode and delithiation of the cathode) and discharging (delithiation of the anode and lithiation of the cathode). The change in electrochemical potential is a result of phase transitions of electrode materials during lithiation and delithiation, which become more apparent by differential voltage analysis (DVA) [82–86]. The differential voltage of U_{OCV}, U_{cat} and U_{an} is shown in Figure 1.5b). Phase transitions are unique for each electrode material composition and their superimposition leads to a nonlinear relationship between OCV and SOC [87]. To a small extent, U_{OCV} is also temperature dependent because of a change in entropy [88–90].

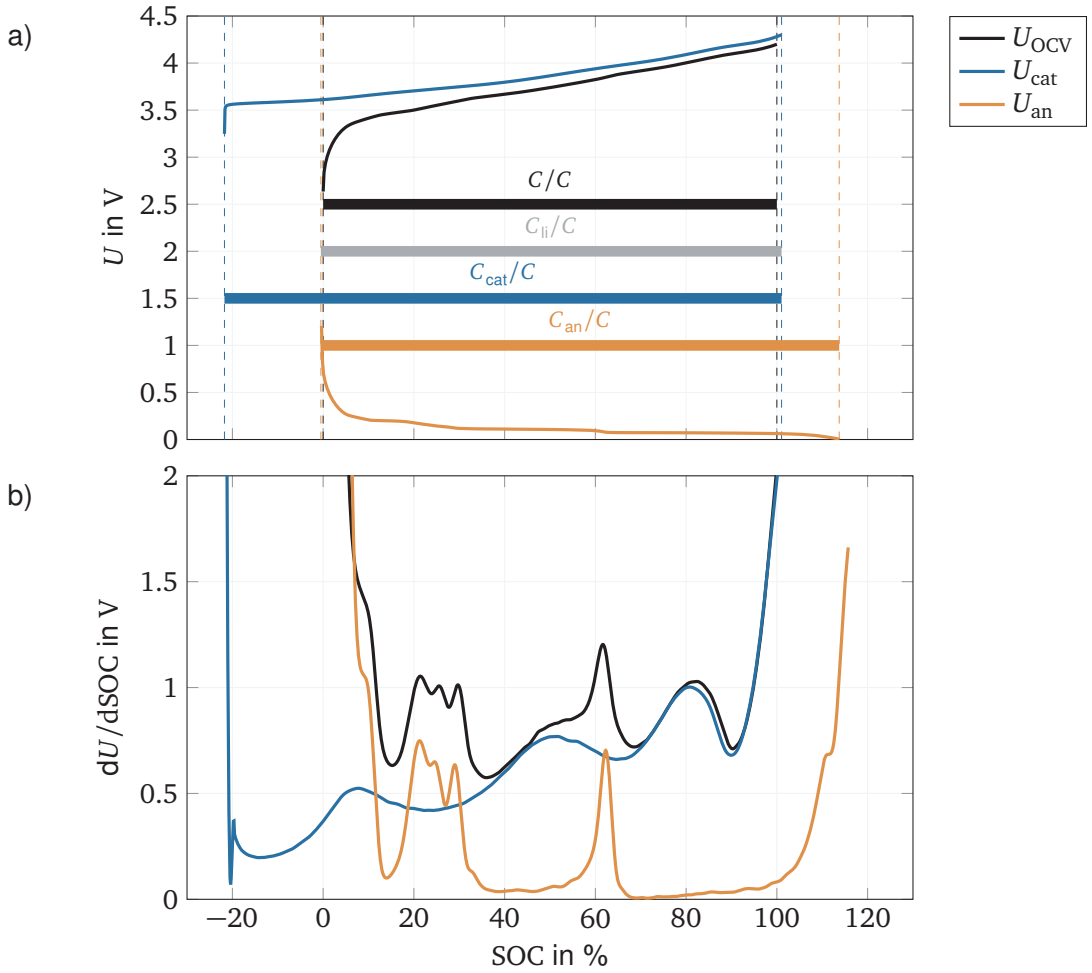

Figure 1.5: a) Full-cell OCV U_{OCV} and half-cell OCPs U_{cat} and U_{an} after half-cell fitting was applied.. b) Corresponding differential voltage curves. Measurements performed with a cell of type US18650VTC5A by Sony/Murata and constructed half cells. The definitions of electrode capacities C_{cat} and C_{an} and capacity of lithium inventory C_{li} are indicated.

Measurement Methods

Two main methods exist to experimentally determine the OCV-SOC relationship. In the first method, the lithium-ion cell is incrementally brought to a certain SOC, and the terminal voltage is measured after a relaxation period. It is known as the incremental OCV measurement [91], relaxation measurement [92] or galvanostatic intermittent titration technique (GITT) [93]. The relaxation time needed to reach a quasi-equilibrium state depends on the SOC, the current applied to reach a certain SOC, and the temperature. It typically lies in the range of several hours [94]. To gather the OCV curve over the full SOC range, the cell is first completely discharged or charged and subsequently charged or discharged stepwise. The number of steps can be varied over the SOC range to cover different areas with higher resolution [95].

The second method is referred to as CC measurement [91, 92]. Here, the battery is completely charged and discharged with a low current (e.g. C/50), which is why it is also called quasi-stationary OCV measurement or pseudo-OCV measurement [94]. This method was applied to measure the curves shown in Figure 1.5. In order to obtain U_{cat} and U_{an}, half-cells are needed. After opening the full-cell under inert gas atmosphere, half-cells can be assembled in either coin-cell or mini-pouch format using the harvested electrodes and a metallic lithium counter electrode [96].

Because of small overpotentials, the CC method and the incremental OCV method with long relaxation times yield slightly different results, even for small constant currents. A general advantage of the CC method is its higher SOC resolution, making it favorable to use when the differential voltage needs to be computed, as nuances in the stage transitions are captured more accurately. Also for half-cell fitting, which is described in the next section, CC measurements are typically used.

Electrode Balancing

In Figure 1.5, all curves are already plotted with respect to the full-cell SOC. The capacitive and stoichiometric balancing of a cell defines how the SOCs of the half cells, $\mathrm{SOC}_{\mathrm{cat}}$ and $\mathrm{SOC}_{\mathrm{an}}$, relate to the full-cell SOC according to

$$U_{\mathrm{OCV}}(\mathrm{SOC}) = U_{\mathrm{cat}}(\mathrm{SOC}_{\mathrm{cat}}) - U_{\mathrm{an}}(\mathrm{SOC}_{\mathrm{an}}), \tag{1.2}$$

where $\mathrm{SOC}_{\mathrm{cat}}$ is transformed by

$$\mathrm{SOC}_{\mathrm{cat}} = \mathrm{SOC} \cdot \alpha_{\mathrm{cat}} + \beta_{\mathrm{cat}}, \tag{1.3}$$

and $\mathrm{SOC}_{\mathrm{an}}$ is transformed by

$$\mathrm{SOC}_{\mathrm{an}} = \mathrm{SOC} \cdot \alpha_{\mathrm{an}} + \beta_{\mathrm{an}}, \tag{1.4}$$

which ultimately yields

$$U_{\mathrm{OCV}}(\mathrm{SOC}) = U_{\mathrm{cat}}(\mathrm{SOC} \cdot \alpha_{\mathrm{cat}} + \beta_{\mathrm{cat}}) - U_{\mathrm{an}}(\mathrm{SOC} \cdot \alpha_{\mathrm{an}} + \beta_{\mathrm{an}}). \tag{1.5}$$

Eq. (1.5) is often referred to as mechanistic OCV model [94, 97–99]. The parameters α_{cat} and α_{an} represent the scaling parameters and β_{cat} and β_{an} represent the alignment parameters for both electrodes, respectively. The capacitive and stoichiometric balancing can be determined by optimizing these four parameters to reconstruct the measured full-cell OCV based on measured half-cell OCPs. This process is referred to as half-cell fitting. The capacities of both individual electrodes C_{cat} and C_{an} are derived from the scaling parameters according to

$$C_{\mathrm{cat}} = \frac{C}{\alpha_{\mathrm{cat}}}, \tag{1.6}$$

and

$$C_{\mathrm{an}} = \frac{C}{\alpha_{\mathrm{an}}}. \tag{1.7}$$

The capacity of the cyclable lithium inventory C_{li} can be calculated as the sum of the amount of lithium that is intercalated in both electrodes from the fitting parameters according to

$$C_{\mathrm{li}} = C \cdot \left(\frac{\beta_{\mathrm{an}}}{\alpha_{\mathrm{an}}} - \frac{\beta_{\mathrm{cat}}}{\alpha_{\mathrm{cat}}} + \frac{1}{\alpha_{\mathrm{cat}}} \right). \tag{1.8}$$

C_{cat}, C_{an} and C_{li} are illustrated in Figure 1.5. The mechanistic OCV model can be leveraged to investigate the influence of aging on the static electric behavior on the electrode level, as described in Section 1.4.

1.2.3 Resistance

Kinetic Loss Processes

When a lithium-ion cell is charged or discharged, various kinetic loss processes lead to overpotentials and a dynamic voltage response to the load [100]. In the following, the main loss processes are assigned to different resistances R, even though most of them are, in reality, associated with time-dependent impedances. This simplification is made to ensure conciseness with respect to the equivalent circuit modeling approach presented in Section 1.3. To illustrate the transition of different overpotentials, the voltage response to a discharge pulse is shown in Figure 1.6.

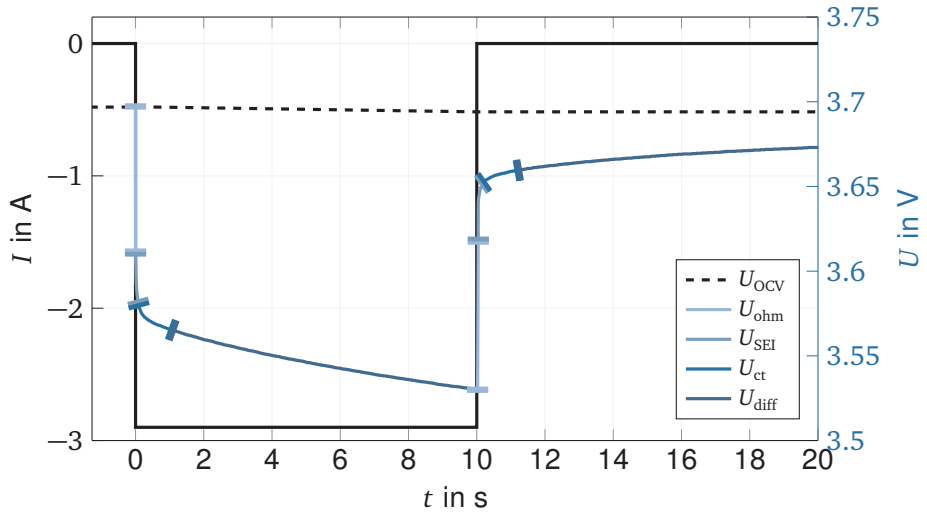

Figure 1.6: Dynamic voltage response of a Panasonic NCR18650PF cell to a 10 s discharge pulse at 50 % SOC and 25 °C. The transition of different kinetic loss processes is qualitatively illustrated. Figure adapted from [7].

Firstly, a significant part of overpotential is caused by the pure ohmic resistance R_{ohm} of current collectors, active material, electrolyte, and separator [100]. The ohmic resistance leads to an instantaneous voltage drop. Secondly, after this instantaneous voltage drop, the resistance caused by the solid electrolyte interphase (SEI) R_{SEI} comes into effect. The SEI is a protecting layer formed on the anode of lithium-ion cells [101]. The time constant of U_{SEI} lies in the range of milliseconds. Thirdly, the charge transfer process contributes to the resistance R_{ct}. This process includes the desolvation of Li^+ in the liquid electrolyte, their migration to the electrode surface, and the subsequent acceptance of an electron by Li^+ to form neutral Li within the electrode [102]. This process includes the double-layer capacitor at both electrodes as a result of the interface space between the charged electrode and the surrounding electrolyte [103]. The time constant of U_{ct} lies in the range of milliseconds to seconds [100]. Lastly, the resistance caused by diffusion through the electrolyte and the porous electrodes, R_{diff}, contributes to the overpotential U_{diff}. The response time lies in the range of seconds up to weeks [100, 104]. The total full-cell resistance is the sum of all individual loss processes according to

$$R = R_{\mathrm{ohm}} + R_{\mathrm{SEI}} + R_{\mathrm{ct}} + R_{\mathrm{diff}}. \tag{1.9}$$

Note that an exact separation of kinetic loss processes is not possible in the time domain, which is why the transition of different overpotentials is only illustrated qualitatively in Figure 1.6 [105]. If the current is interrupted, the described processes occur in the opposite direction but at a different speed. This can be due to OCV hysteresis or load history-dependent OCV variations [106, 107].

In addition to the dynamic overpotentials, the charge throughput during the current pulse leads to a change in SOC and correspondingly to a smaller U_{OCV}. Ultimately, the terminal voltage U_{terminal} is composed of the sum of U_{OCV} and all stimulated overpotentials due to the described kinetic loss processes according to

$$U_{\mathrm{terminal}} = U_{\mathrm{OCV}} + U_{\mathrm{ohm}} + U_{\mathrm{SEI}} + U_{\mathrm{ct}} + U_{\mathrm{diff}}. \tag{1.10}$$

Measurement Methods

There are two main types of measurements to determine resistance: direct current (DC) pulses, which are evaluated in the time domain and referred to as time-domain measurements, and electrochemical impedance spectroscopy (EIS), which is evaluated in the frequency domain and referred to as frequency-domain measurement [108, 109]. Both methods are illustrated in Figure 1.7.

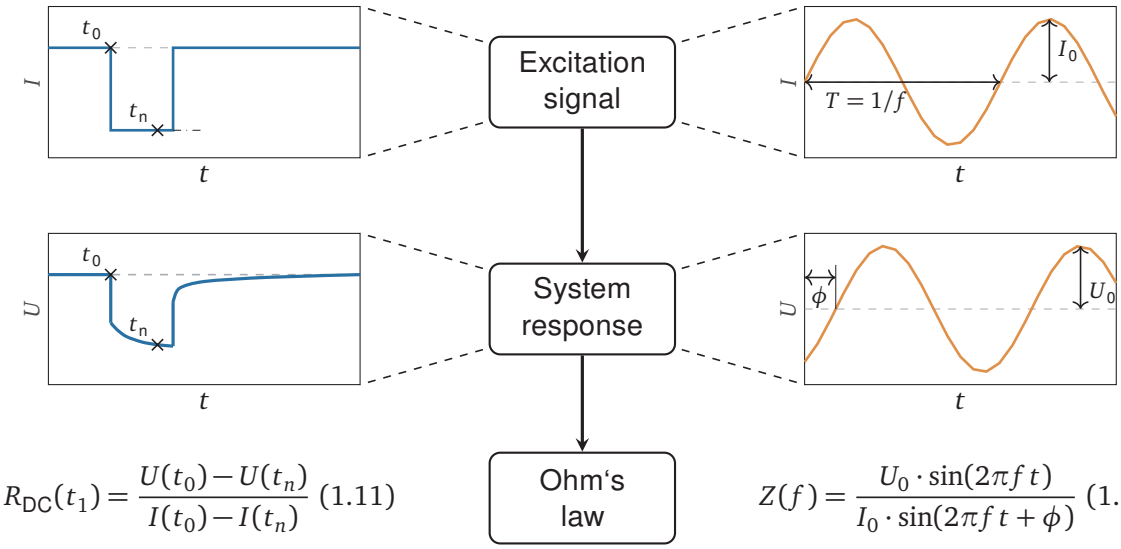

Figure 1.7: Overview of resistance measurement in the time domain (left), and frequency domain (right).

For resistance determination in the time domain, DC pulses are applied to the cell and the voltage response is recorded. Depending on the sampling rate Δt and pulse duration, the cell's DC resistance R_{DC} can be calculated at any time step t_n by applying Ohm's law according to Eq. (1.11) [110]. The described method is suitable when a single resistance value needs to be calculated, such as for parameterizing R_0 in an electric model (Section 1.3), tracking resistance increase over lifetime (Section 1.4), or analyzing resistance variation within a batch of lithium-ion cells (Section 1.5). To achieve reproducible results, the excitation itself must not alter the cell's state, such as SOC and temperature. Additionally, it is important that the cell does not enter a regime of diffusion limitation [105]. Therefore, the discharging or charging procedure by which a certain SOC was reached and the relaxation time before the current pulse can influence the measured resistance [111, 112].

During EIS, a sinusoidal alternating excitation signal is imposed on the cell and the system's response is measured [92, 105, 113]. If the excitation is small enough (e.g. 10 mV), the cell's response is pseudo-linear, wherefore it will have the same frequency but is shifted in phase angle ϕ. Same as in the time domain, the frequency-dependent impedance can be calculated by using Ohm's law (Eq. (1.12)). With the Euler relationship, the resulting expression can be transferred into a complex function and the impedance is ultimately represented as a complex

number [105]. The impedance spectrum can be recorded by performing EIS measurements at multiple frequencies f and the results are typically visualized in a Nyquist diagram (Figure 1.8a)).

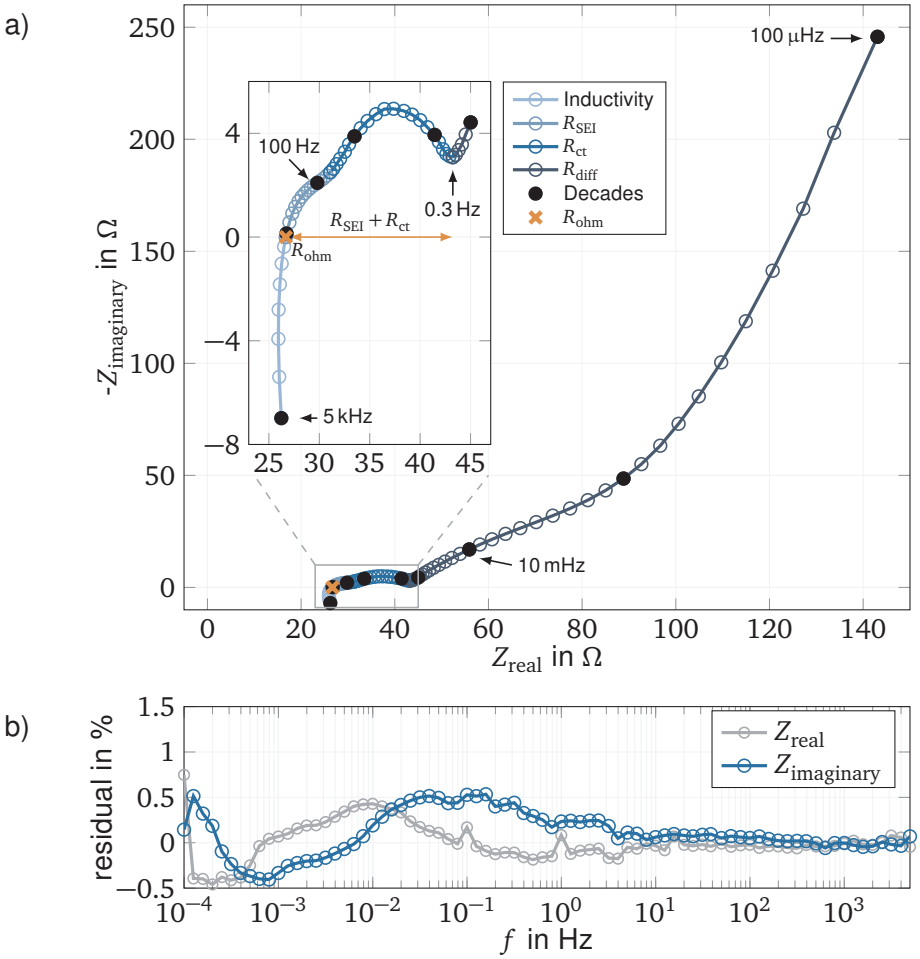

Figure 1.8: a) Impedance spectrum from 5 kHz to 100 µHz of an aged Panasonic NCR18650PF cell at 50 % SOC and 25 °C. Different electrochemical processes are indicated. b) Corresponding residuals according to the *Kramers-Kronig Validity Test Lin-KK for Impedance Spectra* [114]. Figure adapted from [7].

It can be seen that, in contrast to time-domain measurements, the different kinetic loss processes can be distinguished. Hence, characteristic resistance values can be retrieved from the impedance spectrum. This can offer an advantage over time-domain measurements, as it allows the comparison of specific kinetic loss processes, rather than merely evaluating R_{DC} at a fixed pulse duration. Typical candidates include the x-axis intersection, representing R_{ohm}; the minimum after the semi-circle at 0.3 Hz, representing the sum of R_{ohm}, R_{SEI} and R_{ct}; or the difference between these two values, representing R_{SEI} + R_{ct}. In this work, high-frequency resistance refers to the resistance at all frequencies above the minimum after the semi-circle, i.e., the sum of R_{ohm}, R_{SEI} and R_{ct}. Low-frequency resistance refers to the resistance at all frequencies below the semi-circle, i.e., R_{diff}.

To get reproducible results, similar requirements as described for time-domain measurements are also applicable for frequency-domain measurements. The system has to be linear, time-invariant, and causal [115, 116]. These requirements can be checked with the Kramers-Kronig relations, which mathematically relate the real part of an impedance spectrum to its imaginary part and vice versa [114, 115], and the corresponding residuals to the shown impedance spectrum are plotted in Figure 1.8b). It can be interpreted as follows: For high frequencies, residuals are

close to zero and show little noise up to 1 kHz. Between 100 Hz and 10 Hz, residuals start to increase and further oscillate around zero, indicating minor time variance. This is expected for lower frequencies since these measurements take longer. As a result, the frequency range of electrochemical impedance measurements for lithium-ion cells commonly lies between 10 kHz and 10 mHz [117]. This in turn means that R_{diff} cannot be fully retrieved from the impedance spectrum and only parts of the resistance caused by diffusion can be observed.

Influence of Operating Conditions

Kinetic loss processes, i.e., the individual resistance contributors, vary depending on operating conditions. Numerous previous studies have analyzed the dependency of resistance and/or individual loss processes on operating conditions for various lithium-ion cell types, forming the foundation for the following summary [92, 118–121]. Figure 1.9 presents an example from a publication by the author [7], comparing the three main influencing factors—SOC, temperature, and current—on the DC resistance measured after a 2 s discharge pulse. This measurement represents R_{ohm}, R_{SEI}, R_{ct}, and a portion of R_{diff}.

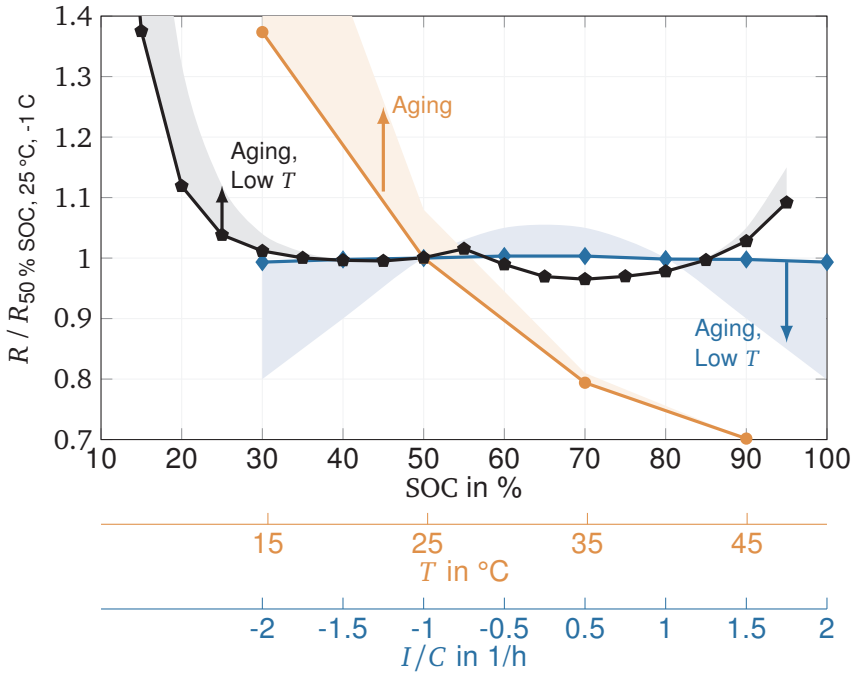

Figure 1.9: Comparison of the influence of operating conditions on $R_{\mathrm{DC,2s}}$. Because of different value ranges, separate abscissas are used and they are matched in color with the corresponding plot. Measurements were performed on Panasonic NCR18650PF cells. One influencing factor was varied at a time, and the measured values were normalized based on $R_{50\,\%\,\mathrm{SOC},\,25\,°\mathrm{C},\,-1\,\mathrm{C}}$. The light-colored areas qualitatively indicate the influence of aging and low temperatures on the magnitude of the shown dependencies based on Waag et al. [118]. Figure adapted from [7].

The resistance increases at high and low SOC, which is typically referred to as the "bathtub" shape. This dependency is mainly driven by R_{ct} and R_{diff}, where the lower SOC range is dominated by R_{ct} and R_{diff} of the cathode and the higher SOC range is dominated by R_{ct} and R_{diff} of the anode [119]. This means, that the magnitude of resistance increase at high and low SOC is not only affected by the chosen materials itself, but also by the electrode balancing. The "bathtub" shape can become more pronounced at lower temperatures [118]. In addition, an increase in resistance is often observed at phase transitions of the electrode materials, which

can be explained by a homogenization effect caused by the local lithium distribution on the electrode [92, 119, 122].

The resistance follows the Arrhenius dependency and decreases with increasing temperature according to

$$\frac{1}{R} = A \cdot e^{\frac{-E_\mathrm{A}}{R_\mathrm{gas} \cdot T}}, \tag{1.13}$$

with the universal gas constant R_gas, the activation energy E_A, and the Arrhenius factor A [123]. The Arrhenius fit can be done separately for individual resistance contributors because they have different activation energies. R_ohm has the smallest temperature dependency because, on the one hand, the ionic conductivity of the electrolyte increases with increasing temperature but, on the other hand, parts of R_ohm (for example the resistance of the metallic conductors) are constant over a wide temperature range. The majority of the temperature dependency of the total cell resistance is driven by R_SEI, R_ct, and R_diff where the exact activation energy is affected by the material composition. Furthermore, the activation energy can vary for different SOC ranges due to the aforementioned effects of anode vs. cathode dominance and phase transitions of the electrode materials.

With increasing absolute current rate (in both, charge and discharge direction), the resistance decreases according to the Butler-Volmer relationship, which describes the relationship between current density and overpotential [111, 124]. Thereby, the current rate affects R_ct and R_diff. At moderate and elevated temperatures, this effect is almost negligible but it becomes more pronounced at lower temperatures because electrodes become less receptive. Moreover, degradation can amplify the influence of current, SOC, and temperature on the resistance [111]. It can be concluded that the resistance depends strongly on temperature, in certain ranges also on SOC, and to a lesser extent on current. These effects have to be considered when modeling the electric behavior of lithium-ion cells.

1.3 Modeling the Electric Behavior

Simulation models are utilized for various purposes in the development process of BEVs. Dedicated electric models simulate a lithium-ion cell's voltage response to a requested current or power profile considering the previously described static and dynamic effects. They are used, e.g., for the dimensioning of battery packs [74] or in SOC estimation algorithms [70]. Dedicated thermal models simulate the temperature response of a cell due to reversible and irreversible heat generation and are used, e.g., to design thermal management systems [125, 126]. Electric and thermal behavior mutually affect each other, which is why both aspects are often combined in a coupled electrical-thermal model [74, 95, 127]. On the one hand, the cell temperature needs to be known to accurately simulate the electric behavior as it influences the electric model parameters. On the other hand, the SOC and overpotentials caused by the resistance must be known to simulate the cell heating [128]. Building on top of electric and thermal models, aging models aim to simulate the influence of the operating conditions on the degradation of lithium-ion cells [129–134]. They are used, e.g., to optimize the allowed operating window over lifetime [135]. This thesis specifically focuses on electric models and their parameterization methods.

1.3.1 Equivalent Circuit Models

Electric models of lithium-ion batteries can be grouped into three categories:

- **Electrochemical models** couple physical and electrochemical differential equations to represent the material interactions within a lithium-ion cell [136]. The most prominent approach is the pseudo-two-dimensional model developed by Doyle, Fuller, and Newman [137].
- **Equivalent circuit models** simulate the cell's terminal voltage with simple electronic components like voltage sources, resistances, and capacitances [138–140].
- **Data-driven models** do not require in-depth battery domain knowledge but rather rely on large amounts of training data [23]. Numerous different model architectures were proposed in literature [141].

Since ECMs offer a good balance between parameterization effort, simulation time, and accuracy for many automotive engineering applications [142–144], they are the focus of this thesis. The approach follows the electric cell model described by Reiter et al. [21], with contribution from the author, and was published as open-source [145]. Figure 1.10 shows the principle structure of the ECM.

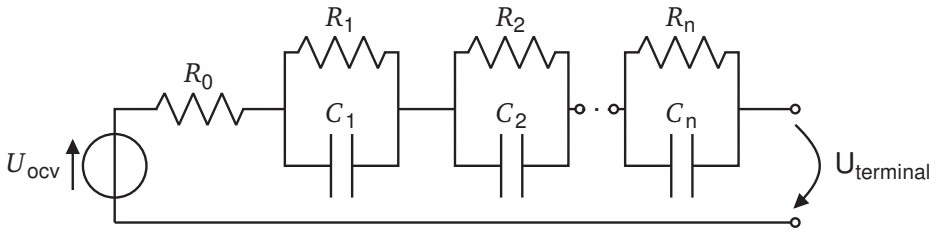

Figure 1.10: Principle structure of an equivalent circuit model with *n* resistor capacitor (RC) elements.

As described in Section 1.2, the terminal voltage is defined by the OCV and the sum of overpotentials according to Eq. (1.10). U_{OCV} is modeled by a voltage source. To describe the dynamic behavior, resistances and RC elements are connected in series. A simple resistance R_0 is used to describe the ohmic resistance R_{ohm}. RC elements provide the possibility to take the different time constants of U_{SEI}, U_{ct} and U_{diff} into account. Depending on the dynamics of the load profile and the requirements on model accuracy, simulation time, and real-time capability, a different number of RC elements can be implemented. In existing studies, application of no RC element [146], one RC element [140, 147–149], two RC elements [150, 151] or higher numbers of RC elements [152, 153] can be found. Next to RC elements, previous studies employed more sophisticated components such as ZARC elements [154, 155] or Warburg elements [152]. These components can provide a more accurate fit to experimental data in the frequency domain, but there are no transfer functions to the time domain, so these elements need to be approximated by RC elements [156]. Ultimately, the terminal voltage is calculated according to

$$U_{\mathrm{terminal}} = U_{\mathrm{OCV}} + U_0 + U_{\mathrm{RC1}} + U_{\mathrm{RC2}} + \ldots + U_{\mathrm{RC}n}. \tag{1.14}$$

As elaborated in Section 1.2, U_{OCV} and the impedance parameters depend on SOC and temperature. The SOC is calculated continuously during simulation runtime by integrating the current profile and dividing it by the cell's capacity. To account for thermal effects, the temperature measured at the cell's surface is used as input to the electric model. The next section discusses how capacity, OCV, and resistances can be parameterized.

1.3.2 Parameter Identification

U_{OCV} can be parameterized using one of the previously described measurement methods and its relationship with the SOC is stored in a look-up table. If the CC method with a low current is used to parameterize U_{OCV}, the capacity can be derived simultaneously for consistency. Alternatively, if the incremental OCV measurement is used for parameterizing U_{OCV}, which can enhance coherence with the resistance parameters, the CCCV method can be employed to determine the capacity.

Both time-domain and frequency-domain measurements can serve to identify the parameters R_0, R_1, C_1,..., R_n, C_n. The procedures described below are referred to as conventional fitting in this thesis, as they are applied directly to measurement data. A comprehensive overview can be found in the dissertation by Baumann [95]. In the time domain, a fitting algorithm can be applied to DC-pulse measurement data to minimize the following cost function:

$$U_{\mathrm{terminal}}(t_n) \stackrel{!}{=} U_{\mathrm{OCV}}(t_n) + U_0(t_n) + U_{\mathrm{RC1}}(t_n) + ... + U_{\mathrm{RC}n}(t_n), \tag{1.15}$$

where

$$U_{\mathrm{OCV}}(t_n) = U_{\mathrm{OCV}}\left(\mathrm{SOC}(t_0) + \frac{\int_{t_0}^{t_n} I(t)\mathrm{d}t}{C}\right), \tag{1.16}$$

and

$$U_0(t_n) = R_0 \cdot I(t_n), \tag{1.17}$$

and

$$U_{\mathrm{RC}n}(t_n) = U_{\mathrm{RC}n}(t_n - \Delta t) \cdot \exp\left(\frac{-\Delta t}{R_n \cdot C_n}\right) + R_n \cdot \left(1 - \exp\left(\frac{-\Delta t}{R_n \cdot C_n}\right)\right) \cdot I. \tag{1.18}$$

R_0 can either be fitted as part of Eq. (1.15) or can be pre-determined. Because simulations are performed with a discrete simulation step size and the occurring frequencies of load profiles in BEVs are significantly lower compared to the pure ohmic resistance, R_0 could be determined at the minimum simulation frequency by using Ohm's law, for example. The physically more accurate assignment of R_0 is achieved when it is pre-determined from the real-axis intersection of a measured impedance spectrum. Frequency-domain measurements can also be used to parameterize RC elements. By applying a fitting algorithm to the measured impedance spectrum Z, the cost function

$$Z(f) \stackrel{!}{=} R_0 + Z_{\mathrm{RC1}}(f) + ... + Z_{\mathrm{RC}n}(f), \tag{1.19}$$

with

$$Z_{\mathrm{RC}n}(f) = \frac{R_n}{1 + j2\pi f \cdot C_n R_n}, \tag{1.20}$$

can be optimized. Again, R_0 can either be fitted in conjunction with the RC elements or determined a-priori. Ultimately, the validity range of the model depends on the operating window for which it was parameterized [140]. The measurement and parameterization procedure described above must, therefore, be repeated for all operating conditions of interest.

1.4 Influence of Aging on the Electric Behavior

Over the lifetime of lithium-ion cells, various electrochemical degradation mechanisms lead to a gradual change in electrical characteristics. This is referred to as battery aging. Datasheets of commercial cells typically give information on the lifetime by stating the remaining capacity after a certain period or number of cycles. This information, however, is not of practical use for developing and monitoring electric vehicles, since the relationship between cause and effect of degradation is more complex, as schematically illustrated in Figure 1.11.

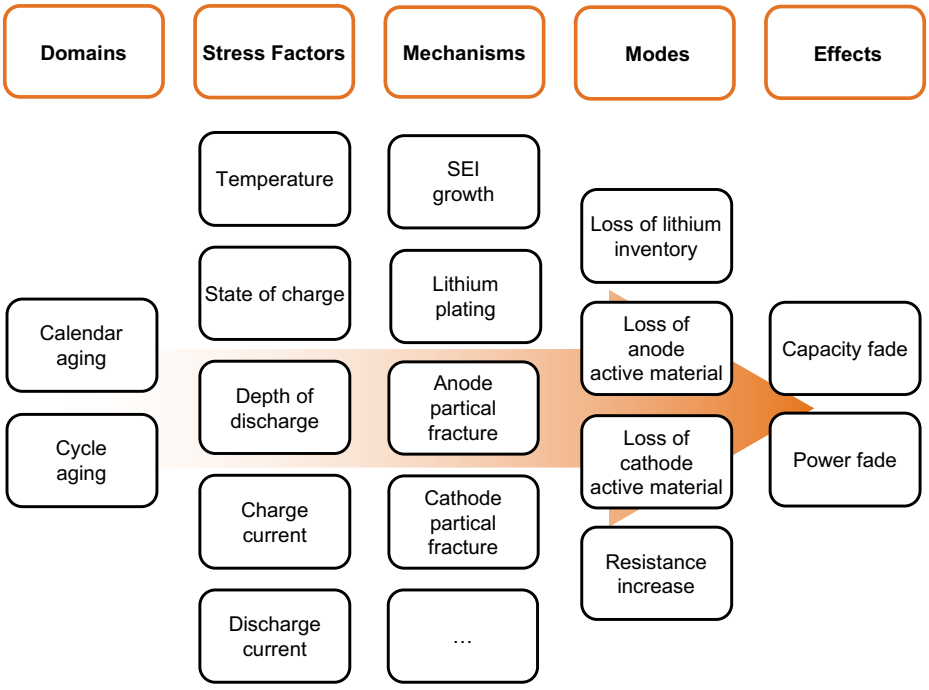

Figure 1.11: Relationship between aging domains, stress factors, degradation mechanisms, degradation modes, and aging effects. More granular versions of this overview can be found in the literature [97, 157].

1.4.1 Aging Domains and Stress Factors

Aging of lithium-ion cells is inevitable and is typically categorized into two domains: calendar aging and cycle aging [158]. Calendar aging occurs continuously during parking, driving, and charging, and is primarily driven by the progression of time [130]. Cycle aging takes place during charging and discharging and is a function of the cumulative charge throughput [131]. In addition to time and charge throughput, the degradation rate is influenced by the conditions under which a cell is stored or cycled, commonly referred to as stress factors.

For calendar aging, the stress factors are SOC and temperature, because higher voltages and higher temperatures are favorable for parasitic side reactions to take place. Temperature and SOC also influence the degradation rate during cycle aging, where the SOC window is often described by two parameters. Throughout this thesis, the mean SOC and the depth of discharge (DOD), defined as the difference between the SOC at the start and the SOC at the end of any charging or discharging phase, are used [159]. Furthermore, the magnitude of charge and discharge current impact the aging rate during cycling because higher current rates lead to increased mechanical stress during cycling. Aging stress factors also partly affect each other. Higher currents, for example, lead to higher temperatures [160]. A detailed review of the influence

and interaction of aging stress factors, and to which extent they were considered in previous aging studies was presented by Gewald et al. [24], with a contribution from the author.

In BEV applications, however, aging domains and stress factors are not constant over time, as operation involves a repetitive yet unpredictable sequence of charging, parking, and driving. This means, that aging domains and stress factors constantly change, which additionally can influence the aging rate [161, 162]. This so-called path dependency of aging was analyzed in more detail by Karger et al. [15], with contribution from the author. It can be concluded that a thorough understanding of the impact and interaction of different aging domains and stress factors is crucial for developing reliable, long-lasting battery systems, as they determine the extent to which certain degradation mechanisms are triggered.

1.4.2 Degradation Mechanisms

Degradation mechanisms refer to the electrochemical and physical processes occurring within the cell and their impact on cell components, such as the electrodes. Numerous degradation mechanisms are documented in the literature; for a comprehensive overview, the reader is referred to relevant review articles [80, 157, 163, 164]. The predominant mechanisms—SEI growth, lithium plating, and particle fracture at both electrodes—are summarized below.

The SEI is a passivation layer that forms on the anode surface during the first cycles when the liquid electrolyte comes into contact with the anode, which operates at voltages below the electrolyte's electrochemical stability [165]. During this process, lithium ions are consumed, and electrolyte decomposes. In theory, once formed, the SEI should prevent further reactions by blocking electron transport. However, even after the initial formation, the thickness of the SEI layer continues to grow, albeit at a decreasing rate, due to the diffusion of solvent molecules through the existing SEI or newly exposed electrode surfaces caused by cracks in the SEI or active material. As the SEI thickness increases over time, it progressively hinders further SEI growth, leading to an approximate square root dependence on time [166]. SEI growth is driven by elevated temperatures and higher SOC (lower anode potential), as well as conditions that promote particle cracking, which exposes new surfaces. As a result, SEI growth occurs during both calendar and cycle aging. Similar to the anode, also the cathode can be operated outside of the range (in this case above) of the electrolyte's thermodynamic stability. Analogous to SEI formation, a layer is formed on the surface of the cathode. This is referred to as positive solid electrolyte interphase or cathode electrolyte interphase and it behaves similarly to the SEI at the anode.

Lithium plating is a parasitic side reaction that can occur during charging of a lithium-ion cell. Normally, lithium ions are transferred from the cathode to the anode and intercalate into anode particles. However, if the potential of the lithiated anode falls below 0 V against pure lithium, lithium deposition on the anode surface becomes thermodynamically favorable [167]. This can occur either when the anode is fully lithiated (thermodynamic plating) or when the overpotentials at the anode are high (kinetic plating). This means that high SOC, high charging currents, and low temperatures all favor the onset of lithium plating. Separation of metallic lithium leads to a loss of cyclable lithium, and parts of the anode's surface may no longer be accessible for lithium-ion intercalation. Lithium plating does not necessarily occur uniformly across the entire electrode surface but can happen locally due to inhomogeneities in the materials and current densities. After lithium is deposited, the inverse reaction can take place and the plated lithium can be recovered during subsequent discharging, a process known as lithium stripping [168]. This means that lithium plating can be an irreversible or reversible degradation mechanism [169].

Ultimately, the consequences of lithium plating can be severe in two ways. Firstly, it can trigger a self-reinforcing process of further plating and SEI growth, which accelerates aging. This phenomenon, often referred to as nonlinear aging, results in a knee-point in the capacity curve [170]. Secondly, it can result in the growth of metallic lithium dendrites, which pose an increased safety risk by causing internal short circuits when they puncture the separator.

Particle fracture refers to the process of electrode particles cracking due to mechanical stress induced by volume changes during lithiation and delithiation. It can occur at both electrodes and, in general, is more pronounced in materials with higher energy density. In particular, silicon in the anode is more prone to particle cracking due to its significantly greater volume change during intercalation compared to graphite. Particle cracking can lead to a reduction of electrical conductivity between active particles and the current collector, increased rate of SEI formation due to newly exposed surfaces, and loss of active material because parts of the active material become isolated from the rest. Extreme temperatures promote particle cracking because graphite becomes more brittle at low temperatures, while thermal stress within the cell increases at elevated temperatures. Moreover, higher current rates lead to higher current density at the electrode surface, resulting in increased mechanical stress during electrochemical operation. SOC and DOD also influence the occurrence of particle cracking because passing material phase transitions during cycling can amplify mechanical stress.

On the one hand, degradation mechanisms provide the most detailed view of aging, and their theoretical understanding forms an essential foundation for comprehending the cause-and-effect relationship of aging. On the other hand, degradation mechanisms are difficult to separate from one another. A mutually exclusive and collectively exhaustive determination is practically impossible. Therefore, a more abstract level of detail—such as degradation modes and aging effects—is necessary to investigate, model, and predict the impact of aging on the electric behavior of BEVs.

1.4.3 Degradation Modes and Aging Effects

Ultimately, degradation mechanisms lead to two aging effects: capacity fade and power fade. These effects directly impact customer-relevant characteristics of BEVs, as they result in reduced driving range and vehicle performance. In the automotive context, the aging state of lithium-ion batteries, known as state of health (SOH), is primarily defined by the remaining capacity, denoted as $\mathrm{SOH_C}$ [171]. It is calculated by comparing the capacity of an aged cell, C_{aged}, to the capacity of a new cell, C_{new}, according to

$$\mathrm{SOH_C} = \frac{C_{\mathrm{aged}}}{C_{\mathrm{new}}}. \tag{1.21}$$

For mobility applications, the end of life is typically reached when $\mathrm{SOH_C}$ drops below 80 % or 70 %. Power fade describes the reduction in the amount of power that can be delivered for a specific time.

Capacity and power fade alone, however, do not fully capture the impact of aging on a cell's electric behavior. To address this, four so-called degradation modes are gaining increasing attention as an intermediate level of abstraction between degradation mechanisms and aging effects [99]. They group the various degradation mechanisms based on their impact on the static and dynamic behavior of the cell's components.

Degradation mechanisms that influence kinetic loss processes are summarized under a single degradation mode: resistance increase. Because resistance increase is directly correlated with power fade, it is sometimes used as a secondary end-of-life criterium in the automotive context. The SOH based on the resistance, denoted as $\mathrm{SOH_R}$ in that case, is defined as

$$\mathrm{SOH_R} = \frac{R_{\mathrm{aged}}}{R_{\mathrm{new}}}. \tag{1.22}$$

Degradation mechanisms that influence the static behavior, i.e., the OCV of a cell, are summarized by three degradation modes: loss of lithium inventory (LLI), loss of active material (LAM) at the anode, denoted as $\mathrm{LAM_{an}}$, and LAM at the cathode, denoted as $\mathrm{LAM_{cat}}$. LLI groups mechanisms that lead to a reduced amount of cyclable lithium. $\mathrm{LAM_{an}}$ and $\mathrm{LAM_{cat}}$ group mechanisms which lead to a reduction of electrode material available for intercalation of lithium-ions. Typically, both electrodes are oversized so that $\mathrm{LAM_{an}}$ and $\mathrm{LAM_{cat}}$ don't limit the overall cell capacity, at least initially and under normal aging conditions. This is why LAM is sometimes referred to as hidden degradation [172]. Still, LAM can give valuable insights into the aging trajectory and can potentially indicate the onset of nonlinear aging.

Since all together—LLI, $\mathrm{LAM_{cat}}$ and $\mathrm{LAM_{an}}$—alter the shape of the OCV curve, they can be determined employing the mechanistic OCV model described in Section 1.2. Performing the half-cell fitting using the OCV curve of an aged cell $U_{\mathrm{OCV,aged}}$ according to

$$\begin{aligned} U_{\mathrm{OCV,aged}}(\mathrm{SOC}) = {} & U_{\mathrm{cat}}(\mathrm{SOC} \cdot \alpha_{\mathrm{cat,aged}} + \beta_{\mathrm{cat,aged}}) - \\ & U_{\mathrm{an}}(\mathrm{SOC} \cdot \alpha_{\mathrm{an,aged}} + \beta_{\mathrm{an,aged}}), \end{aligned} \tag{1.23}$$

returns the shifting and alignment parameters $\alpha_{\mathrm{cat,aged}}$, $\alpha_{\mathrm{an,aged}}$, $\beta_{\mathrm{cat,aged}}$ and $\beta_{\mathrm{an,aged}}$. Note that the same half-cell OCP curves U_{cat} and U_{an}, which were determined from fresh cells, are used. This is done based on the assumption that the half-cell OCP curves themselves don't change over aging, but it's only the stoichiometric and capacitive balancing, i.e., the shifting and alignment parameters, which change [173]. Further, the electrode capacities $C_{\mathrm{cat,aged}}$ and $C_{\mathrm{an,aged}}$ and the capacity of the lithium inventory $C_{\mathrm{li,aged}}$ can be determined according to Eq. (1.6–1.8). Ultimately, the degradation modes LLI, $\mathrm{LAM_{cat}}$ and $\mathrm{LAM_{an}}$ of aged cells are defined as follows:

$$\mathrm{LLI} = 1 - \frac{C_{\mathrm{li,aged}}}{C_{\mathrm{li,new}}}, \tag{1.24}$$

$$\mathrm{LAM_{an}} = 1 - \frac{C_{\mathrm{an,aged}}}{C_{\mathrm{an,new}}}, \tag{1.25}$$

and

$$\mathrm{LAM_{cat}} = 1 - \frac{C_{\mathrm{cat,aged}}}{C_{\mathrm{cat,new}}}. \tag{1.26}$$

In conclusion, the five degradation modes and effects—$\mathrm{SOH_C}$, $\mathrm{SOH_R}$, LLI, $\mathrm{LAM_{an}}$, and $\mathrm{LAM_{cat}}$—provide a comprehensive understanding of how degradation impacts the electrical behavior of lithium-ion cells. Conversely, by measuring the three main electric parameters—capacity, OCV, and resistance—of an aged cell, all five described health parameters can be determined.

1.5 Influence of System Design on the Electric Behavior

To achieve the energy and power requirements of BEVs, individual lithium-ion cells are connected into modules, which are then connected to form battery packs. To increase the total capacity of the battery pack, individual cells are connected in parallel. To increase the voltage level in order to fulfill vehicles' power requirements without excessive current rates, series connections are utilized [174]. The Tesla Model 3 (55 kWh) battery pack, for example, uses 161.5 Ah LFP prismatic cells connected in a 106s1p configuration [175]. The Tesla Model Y (81 kWh) is built out of 828 cylindrical 4680 NMC cells with a capacity of 22 Ah in a 92s9p configuration [67]. The battery pack of the Volkswagen ID.3 is composed of 78 Ah NMC pouch cells connected into nine modules with a 2p12s topology, resulting in a total of 216 cells [27, 68]. A higher number of parallel-connected cells can enhance system reliability in the event of a cell failure but comes at the cost of increased system complexity and greater contacting efforts [176]. Electrical connection between cells is achieved using one of the established joining techniques: laser welding, ultrasonic welding, or resistance spot welding [177]; mechanical joining in the form of screwed connections [178]; or wire bonding, where the thin wire additionally acts as a mechanical fuse [177, 179].

1.5.1 Scaling Electric Parameters from Cell to Pack Level

Assuming that all cells within a battery pack i) are produced with zero tolerances, ii) experience identical loads during operation, and iii) are in the same aging state, the following formulas can be used to scale their main electrical parameters up to pack level. The pack's total capacity is only influenced by the number of parallel connections p and can be calculated by:

$$C_{\text{pack}} = p \cdot C. \tag{1.27}$$

The pack's OCV, in contrast, is only influenced by the number of series connections s and can be calculated by:

$$U_{\text{OCV,pack}} = s \cdot U_{\text{OCV}}. \tag{1.28}$$

Scaling the resistance to pack level, however, is not as straightforward. For pouch cells, in particular, the mechanical compression inside a system, when multiple cells are stacked into a module, is different compared to an individual cell. This alters the dynamic behavior since the applied pressure improves the electrical contact inside the cell and the ohmic resistance decreases with increasing pressure [180]. In contrast, higher compression forces can lead to an increase in R_{ct} due to a reduction in the surface area of the active materials [180]. This means that a-priori knowledge of the expected pressure is essential if resistance measurements of individual cells should reflect the behavior once built into a battery pack. Ultimately, for calculating the pack's resistance, series and parallel connections need to be taken into account and the individual cell resistance can be scaled to the pack level according to

$$R_{\text{pack}} = \frac{s}{p} \cdot (R + 2 \cdot R_{\text{contact}}) + R_{\text{additional}}, \tag{1.29}$$

with the additional resistance $R_{\text{additional}}$ accounting for wiring, fuses, etc. and R_{contact} describing the resulting contact resistance of joining individual cells. Brand et al. [181–183] investigated the contact resistances of several joining techniques with different process parameters. From their overview, it can be concluded that contact resistances roughly vary between 0.1 and 1 $\mu\Omega$.

1.5.2 Parameter Variations and Inhomogeneities in Battery Packs

In practice, multiple sources of inhomogeneities lead to the divergence of individual cell parameters within a battery pack, as illustrated in Figure 1.12. The following review is partly based on a previous publication by Baumann et al. [6], with contribution from the author, where the origins of inhomogeneous operating conditions in battery systems were discussed in detail.

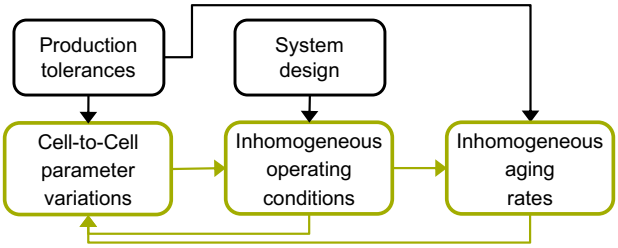

Figure 1.12: Overview of the origins and mutual effects of inhomogeneities within battery packs.

Cell-to-Cell Parameter Variations

Production tolerances can lead to cell-to-cell variations of electric parameters. This can be due to impurities in the cells' raw materials or imperfections in the cell manufacturing process [184–188]. It was shown that commercial electrodes can exhibit inhomogeneities at different length scales. Variations in particle sizes and shapes can lead to inhomogeneities of the microstructure, while imperfections in manufacturing processes can result in differences between samples taken centimeters apart [189]. Over the past ten years, several studies quantified the cell-to-cell variations of electric parameters of fresh lithium-ion cells [6, 27, 190–203]. They all performed characterization procedures on commercially available cells from known manufacturers and the batch size varied between 24 and 1100 individual cells. Figure 1.13 shows the reported relative standard variation of capacity and resistance.

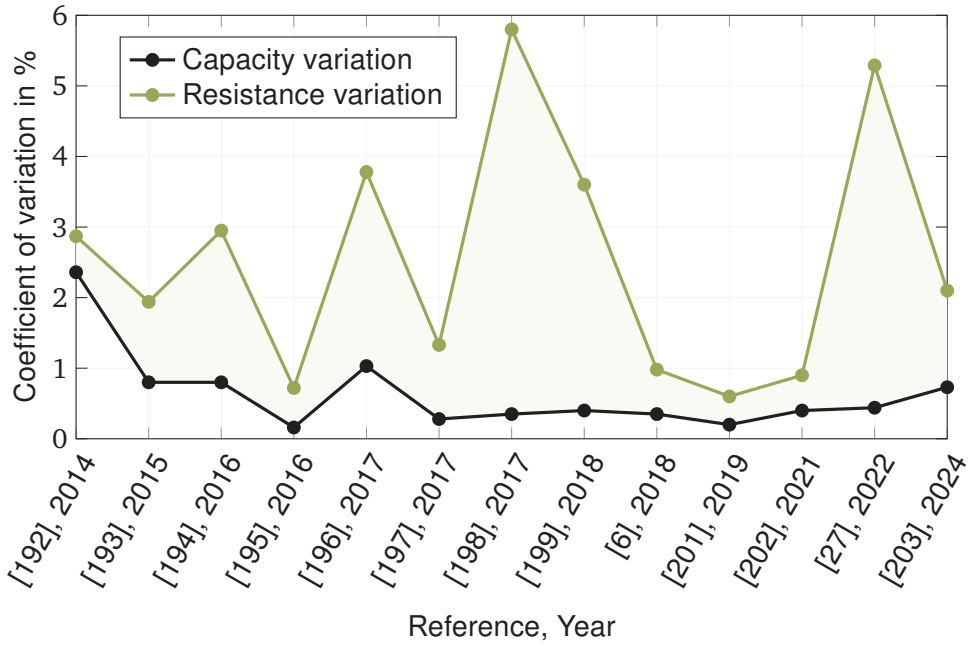

Figure 1.13: Cell-to-cell parameter variations reported in literature. Resistance variations (0.68–5.80 %) are consistently found to be higher than capacity variations (0.16–2.36 %), as indicated by the light-green area.

The capacity variation ranges from 0.16 % to 2.36 %, while the observed resistance variation ranges from 0.68 % to 5.80 %. The differences across studies can be explained by the use of different cell types from different manufacturers, or varying production grades. Additionally, different measurement methods and experimental setups are prone to varying degrees of scattering. This is particularly evident for resistance, which is sometimes determined using DC pulses evaluated at different pulse durations, and other times measured with EIS. Rothgang et al. [192], for example, determined the capacity with a high current rate and no CV phase. Thus, resistance scattering is superimposed to the pure variation of capacity, which explains the high coefficient of variation of above 2 %. In all other cases, as indicated by the light-green area, resistance variations are consistently reported to be higher than capacity variations by a factor of 2.4 to 16.6.

Inhomogeneous Operating Conditions

Inhomogeneous electric parameters can further lead to non-uniform operating conditions, meaning that individual cells within a battery pack experience different loads, triggering a complex chain of cause-and-effect interactions. In serial connections, the driving parameter causing inhomogeneous load is the capacity. Since the current (and thus also charge throughput) is the same, different capacities will lead to different SOCs of cell strings connected in series [74]. Looking at an arbitrary charge and discharge cycle, this means that also the DOD will be different. Since the resistance is dependent on SOC, this can lead to differences in cell temperatures. Typically, SOC drifts are compensated by a balancing mechanism, which helps to prevent extreme divergence of individual cells [204].

When cells are connected in parallel, the cell voltages are all the same but the current flow through each cell might differ. For two parallel connected cells, the current through one cell is calculated by $I_1 = (R_2/R_1) \cdot I_2$, where the individual loss processes with various time constants have to be taken into account [205]. Variations in contact resistances can also lead to a difference between R_1 and R_2 [206–212]. Different resistances lead to uneven current distribution among parallel-connected cells, with a higher internal resistance mismatch resulting in greater current imbalances [213]. The same considerations can be applied to any number of parallel connections [214]. Unequal capacities can also contribute to imbalanced currents. During charging or discharging, cells with a smaller capacity experience a faster change in SOC. As a result, the current through this cell will decrease to maintain equal voltage across all cells [205, 215]. Imbalanced currents further cause temperature inhomogeneities [216–218].

In addition to cell-to-cell parameter variations, the system design—particularly the cooling system—can induce temperature gradients within the system, as current thermal management systems do not control the temperature of each cell [216, 219]. In summary, individual cells within a battery pack experience varying load profiles during operation. Since operating conditions influence electric parameters, the resulting divergence is superimposed on the inherent cell-to-cell variations.

Inhomogeneous Aging Rates

Inhomogeneous operating conditions cause individual cells to age at different rates, meaning that electric parameters change differently over time. This effect is superimposed on the inherent cell-to-cell variations as well. Depending on the magnitude of differences in aging stress factors, degradation mechanisms (e.g. SEI growth) are triggered at different rates. Additionally, new

aging mechanisms may be triggered, such as lithium plating due to higher currents or particle cracking due to higher DOD. Some studies found that parameter variations were smaller for aged cells compared to new cells [220]. On the contrary, other studies reported that parameter variations increased over lifetime [184, 193]. Cell-to-cell aging spreads are not only caused by inhomogeneous operating conditions but also by production tolerances [188, 221].

1.6 Research Questions

In the following, research questions are derived based on the previously described state of the art. Figure 1.14 illustrates them within the research dimensions *electric behavior*, *modeling*, *aging*, and *system design*.

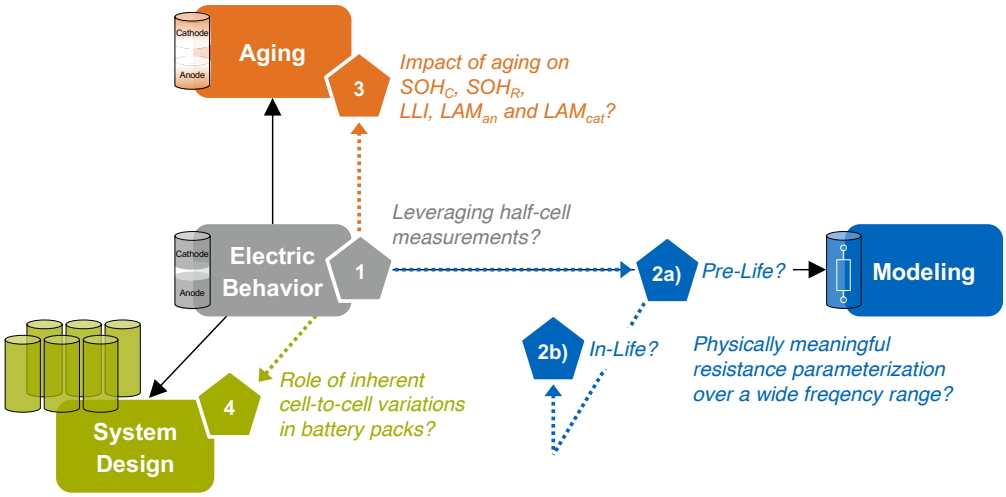

Figure 1.14: Overview of the research questions along the pursued research dimensions.

As described in Section 1.2, experimental methods for characterizing capacity, OCV, and resistance at the full-cell level are well established for downstream applications in all dimensions: parameterizing ECMs in the *modeling* dimension, tracking capacity fade and resistance increase in the *aging* dimension, and scaling the electric behavior of individual cells to the pack level in the *system design* dimension. However, concerning equivalent circuit modeling, resistance parameters determined at the full-cell level oftentimes lack physical meaning, as the kinetic loss processes are rooted at the electrode level. This can limit the validity of these models. Furthermore, in degradation studies, solely tracking capacity fade is only expedient to a certain extent. A deeper understanding of the root causes of aging under different conditions can be achieved when the degradation modes, which describe aging at the cell component level, can also be tracked. The following research question, which forms the foundation for the research dimensions *modeling*, *aging* and *system design*, is motivated:

1 *Can half-cell measurements enhance the parameterization of electric models and facilitate the identification of degradation modes during aging studies?*

Load profiles occurring in BEVs encompass a wide range of dynamics: high frequencies during driving and low frequencies during charging. However, when it comes to parameterizing resistance parameters, the methods described in Section 1.3 have limitations in terms of observing dynamic effects. Frequency-domain measurements are well suited for reliably analyzing

high-frequency processes but lack the ability to observe processes with large time constants. Time-domain measurements, on the other hand, are limited by the sampling rate and measurement accuracy in the high-frequency region and are better suited for gaining insights into low-frequency behavior. Additionally, neither domain guarantees a strong relationship between the fitted parameters and the underlying electrochemical processes as a result of mathematical optimization against experimental data. Furthermore, the sequence of charging, parking, and driving of BEVs is repetitive but unpredictable, which complicates the physically meaningful parameterization and tracking of impedance parameters over a lifetime. The following research question is motivated:

How can high- and low-frequency resistance be parameterized to represent kinetic loss processes in a physically meaningful way:
a) Pre-life (during the development phase) under laboratory conditions?
b) In-life (in electric vehicles) under real-world operating conditions?

In Section 1.4, the complex interaction between the causes and effects of degradation in lithium-ion cells was described. On the one hand, it was concluded that degradation mechanisms, which occur at both the physical and electrochemical scales, are not suitable for investigating the impact of different aging conditions on the electric behavior of lithium-ion cells, as they are practically impossible to determine without a post-mortem analysis. On the other hand, analyzing only capacity fade provides insufficient insights, as it overlooks the effects on both the static and dynamic behavior of the cells. Degradation modes help fill this gap and mark a sweet spot within the different levels of abstraction. Monitoring changes in OCV and the increase in resistance can provide valuable insights into the root causes of aging and potentially signal the onset of nonlinear aging. The following research question arises:

How do different aging domains and stress factors influence SOH_C, SOH_R, LLI, LAM_{an}, and LAM_{cat}? The experimental results should support the development of data-driven aging models.

As described in Section 1.5, there are multiple sources of inhomogeneities in battery packs. At the core of a complex cause-and-effect chain are inherent cell-to-cell parameter differences caused by production tolerances. Previous publications consistently reported resistance variations to be more than twice as high compared to capacity variations, with some cases showing differences of up to 15 times, yet no clear explanation for this behavior has been provided. Since these values are often used as inputs for analyzing downstream effects, such as load imbalances within parallel-connected cells, incorrect assumptions can limit the validity of these investigations. It was also discussed that resistance measurements are sensitive due to the strong dependence of kinetic loss processes on the cell's state and operating conditions. The assumption that the measurement procedure itself induces higher variability in resistance parameters motivates the following research question:

Why are resistance variations greater than capacity variations, and how significant are initial cell-to-cell variations overall?

In Chapter 2, five research articles are presented to address the research questions posed.

2 Contributions

Figure 2.1 places the five publications within the context of the research dimensions. The first research question led to Study I, which is presented in Section 2.1 and forms the foundation for the other research dimensions. To address the research question in the *modeling* dimension, Studies II and III are presented in Section 2.2. The research question in the *aging* dimension motivated Study IV, which is presented in Section 2.3. Finally, the research question in the *system design* dimension resulted in Study V, presented in Section 2.4.

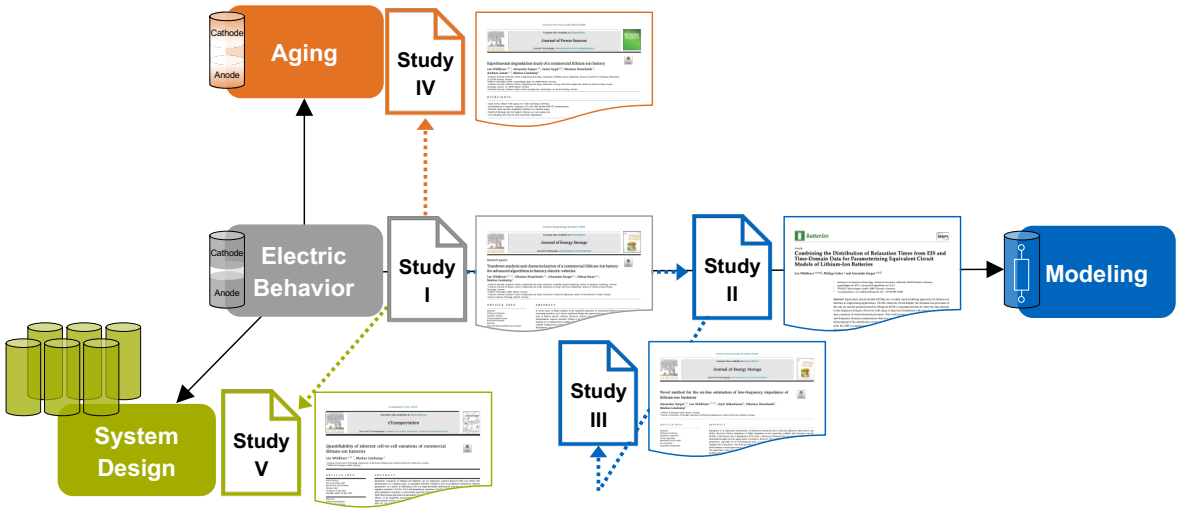

Figure 2.1: Overview of the presented studies along the pursued research dimensions.

All investigations were performed with cells of type US18650VTC5A by Sony/Murata from the same production batch. It has a silicon-graphite anode, with 1.4wt% silicon, and a NCA cathode with the formulation $LiNi_{0.80}Co_{0.15}Al_{0.05}O$ [76, 222]. Figure 2.2 shows a picture and lists the main parameters.

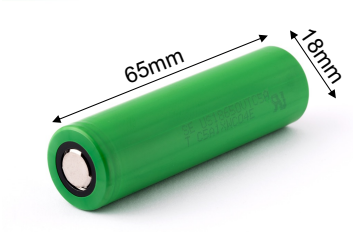

Property	Value
Manufacturer	Sony/Murata
Cell type	US18650VTC5A
Anode material	Silicon-graphite
Cathode material	NCA
Nominal capacity	2.5 Ah
Voltage range	2.5–4.2 V
Maximum charging current	6 A
Maximum discharging current	35 A
Weight	47.1 g

Figure 2.2: Main parameters of the investigated lithium-ion cell of type US18650VTC5A by Sony/Murata.

2.1 Electrical Characterization based on Half-Cell Measurements

Understanding the electric behavior of a lithium-ion cell is essential for optimizing the design and operation of the battery pack in a BEV. Guided by the first research question to lever untapped potential in the parameterization of electric models and to enable the determination of degradation modes over aging, Study I presents the methodology and results of an in-depth experimental characterization of the electric behavior of a commercial lithium-ion cell. Figure 2.3 provides an overview of the performed measurements, the applied analysis techniques, and how the results are utilized in the following sections. The measurement data has been made publicly available as open source [12].

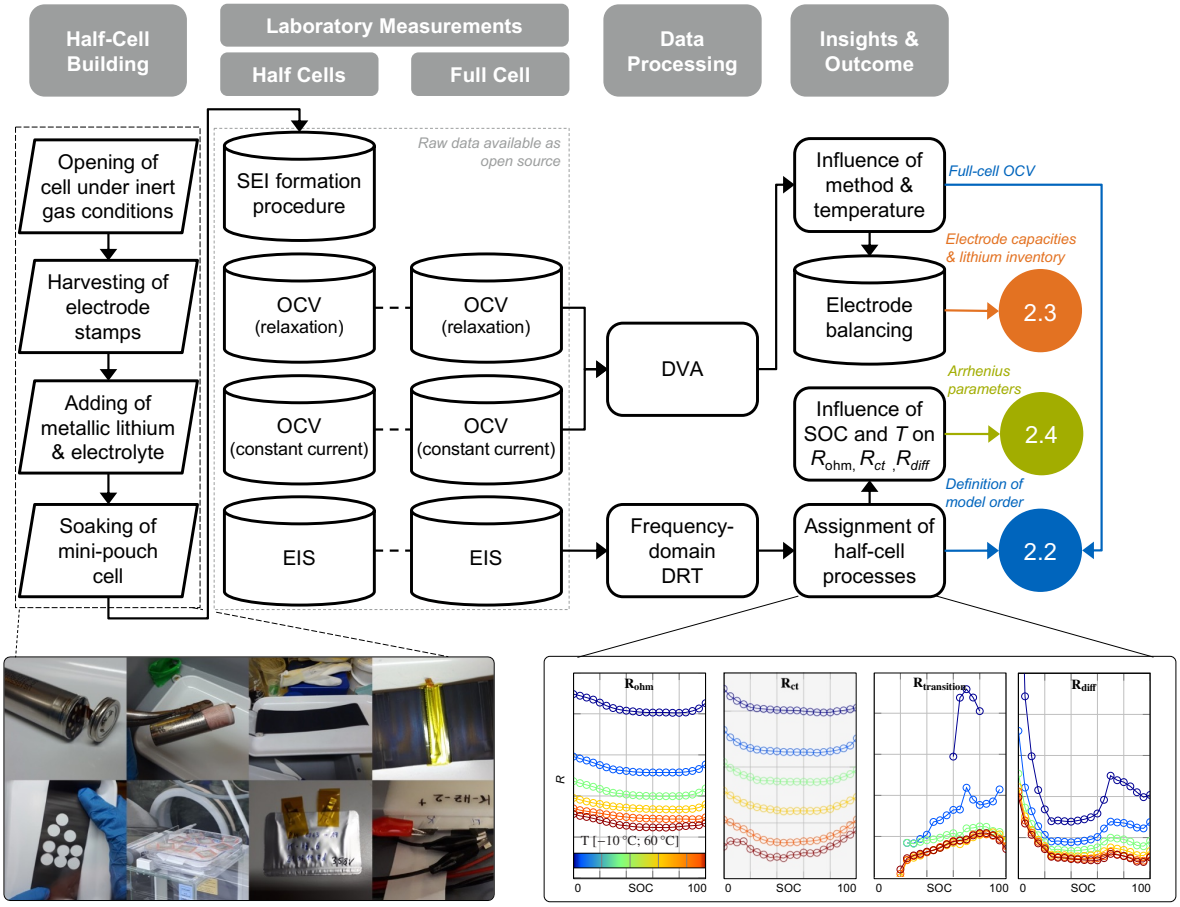

Figure 2.3: Graphical summary of Study I [1].

To characterize the static and dynamic behavior not only of the full cell but also of the individual electrodes, half cells were constructed. For this, a cell was opened under an inert gas atmosphere to extract the individual electrodes, from which circular electrode stamps were punched out. Together with a metallic lithium counter electrode, a Polypropylene separator, an LP30 electrolyte, and current collectors, the electrode stamps were placed in a mini-pouch bag and sealed. After a soaking time of over 24 hours, a dedicated procedure was applied to allow the formation of the SEI.

Full-cell OCV and half-cell OCP curves were determined using the relaxation method and the CC method, with three different current rates, at five ambient temperatures ranging from –10 °C

to 50 °C. DVA was performed on all measurements. Since the experiments were performed in charge direction, the curves measured with the CC method are slightly higher compared to those obtained with the relaxation method for U_{OCV} and U_{cat} and slightly lower for U_{an}. Temperature has the greatest effect on the OCV at low SOC, as a characteristic anode feature disappears at lower temperatures. Section 2.2 further utilizes the OCV curves to parameterize the static behavior of ECMs.

A current rate of C/10 captured all characteristic material phase transitions, proving suitable for half-cell fitting and integration into the aging check-up procedure (Section 2.3). Besides the measurement method, additional factors significantly impacted the half-cell fitting results. In this case, consistent results with well-matching material phase transitions between measured and simulated full-cell OCV were achieved by: i) fitting OCV curves instead of DVA curves, ii) introducing an offset parameter to account for polarization differences, and iii) excluding specific SOC ranges during the fitting procedure. Physical meaningful scaling and alignment parameters are essential for calculating degradation modes in aged cells. Eventually, the capacities of electrodes and lithium inventory were determined as follows: $C_{\mathrm{li}} = 1.003 \cdot C$, $C_{\mathrm{cat}} = 1.228 \cdot C$, and $C_{\mathrm{an}} = 1.141 \cdot C$.

The resistance was characterized using EIS at six temperatures ranging from –10 °C to 60 °C and at 5 % increments across the entire SOC range. In order to assign the dynamic effects of the full cell to either electrode, individual loss processes were isolated by evaluating the distribution of relaxation times (DRT). Section 2.2.1 presents this technique in more detail. Several sub-processes with different time constants caused by either electrode were revealed in the charge transfer region. While R_{ct} is dominated by the anode at high SOC, the low SOC range is dominated by the cathode, which is also responsible for the overall bathtub shape of R_{ct}. Based on these results, R_{ohm}, R_{ct}, R_{diff}, and their respective time constants were determined over the whole available SOC and temperature range. Fitting the Arrhenius equation and determining activation energies revealed that operating conditions have a significantly greater impact on R_{ct} and R_{diff} compared to R_{ohm}. The article demonstrated that assigning full-cell processes to individual electrodes enables a physically motivated definition of the equivalent circuit model order.

Contribution

Leo Wildfeuer and Nikolaos Wassiliadis contributed equally as first authors.

Leo Wildfeuer: Conceptualization, Methodology, Formal analysis, Investigation, Visualization, Data curation, Software, Validation, Writing – original draft, Writing – review & editing. Nikolaos Wassiliadis: Conceptualization, Methodology, Formal analysis, Investigation, Visualization, Data curation, Software, Validation, Writing – original draft, Writing – review & editing. Alexander Karger: Software, Writing – review & editing. Fabian Bauer: Resources, Writing – review & editing. Markus Lienkamp: Resources, Supervision, Writing – review & editing.

Teardown analysis and characterization of a commercial lithium-ion battery for advanced algorithms in battery electric vehicles

Leo Wildfeuer*, Nikolaos Wassiliadis*, Alexander Karger, Fabian Bauer, Markus Lienkamp
*Both contributed equally as first authors.

Journal of Energy Storage, Volume 48, p. 103909, 2022
Digital Object Identifier: 10.1016/j.est.2021.103909
Permanent Weblink: https://doi.org/10.1016/j.est.2021.103909

Journal of Energy Storage 48 (2022) 103909

Contents lists available at ScienceDirect

Journal of Energy Storage

journal homepage: www.elsevier.com/locate/est

Research papers

Teardown analysis and characterization of a commercial lithium-ion battery for advanced algorithms in battery electric vehicles

Leo Wildfeuer [a,c,*,1], Nikolaos Wassiliadis [a,1], Alexander Karger [b,c], Fabian Bauer [d,e], Markus Lienkamp [a]

[a] Technical University of Munich, School of Engineering and Design, Department of Mobility Systems Engineering, Institute of Automotive Technology, Germany
[b] Technical University of Munich, School of Engineering and Design, Department of Energy and Process Engineering, Institute for Electrical Energy Storage Technology, Germany
[c] TWAICE Technologies GmbH, Munich, Germany
[d] Technical University of Munich, School of Engineering and Design, Department of Materials Engineering, Institute of Non-destructive Testing, Germany
[e] Siemens Corporate Technology, Munich, Germany

ARTICLE INFO

Keywords:
Lithium-ion batteries
Teardown analysis
Si-doped graphite anode
Ni-rich NCA cathode
Half cells
Electrochemical impedance spectroscopy

ABSTRACT

In recent years, in-depth analysis of the manifold properties of commercial lithium-ion batteries has gained increasing attention, as it fosters optimized design and operational strategies of battery-powered applications such as battery electric vehicles. However, various properties are not easily accessible and experimental determination requires intensive efforts in the battery lab. In this study, we have performed a tear-down analysis of a commercially available lithium-ion cell with a silicon-doped graphite anode and a Ni-rich NCA cathode. Enhanced by computed tomography (CT) scans, we reveal the cell's internal geometrical properties. Furthermore, mini pouch half cells of the anode and cathode have been built to examine their electrochemical properties in context with full cell measurements. In particular, we examined the open circuit voltage with different measurement methods and for different temperatures and performed reconstruction of the full cell via fitting of electrode potentials. We give detailed insights into the kinetics of the cell by analyzing the distribution of relaxation times (DRT) calculated from electrochemical impedance spectroscopy (EIS). Individual loss processes are assigned to either electrode and their polarization resistances and time constants are quantified over a large SOC and temperature range. A comprehensive open-source dataset of the investigated cell is provided to propel international research activities in the development of advanced models and algorithms for lithium-ion batteries.

1. Introduction

The success of lithium-ion batteries (LIBs) in battery-powered applications has lead to intensive efforts towards maximizing their efficiency as an energy source. In the case of battery electric vehicles (BEVs), it constitutes the most expensive component [1], which is why optimized design and operation of battery systems is of high importance. To this end, capacity retention and battery aging is a crucial phenomenon that has been tackled by many researchers in the past [2–5]. Aging results from complex physical and chemical degradation mechanisms at the cell components [5]. From an engineering perspective, it is necessary to understand the influence of these different degradation mechanisms and scale this knowledge to effects on the application level such as loss of available energy and power, as illustrated in Fig. 1.

In order to lever untapped potential of the battery system's performance and to prolong its lifetime advanced models, algorithms and operational strategies have to be designed, which require tear-down analysis of LIBs to gather in-depth knowledge about the electrochemical system.

1.1. Previous publications

In the past, many authors assessed the electrochemical properties of anode [6–13] or cathode [11,12,14–18] materials. Besides the analysis of individual cell component properties, it is important to understand their behavior in a full cell assembly to project the results to real-world applications. An extract of publications, which perform cell tear-down

* Corresponding author at: Technical University of Munich, School of Engineering and Design, Department of Mobility Systems Engineering, Institute of Automotive Technology, Germany.
E-mail addresses: leo.wildfeuer@tum.de (L. Wildfeuer), nikolaos.wassiliadis@tum.de (N. Wassiliadis).
[1] L.W. & N.W. contributed equally as first authors.

https://doi.org/10.1016/j.est.2021.103909
Received 26 April 2021; Received in revised form 3 December 2021; Accepted 22 December 2021
Available online 21 January 2022

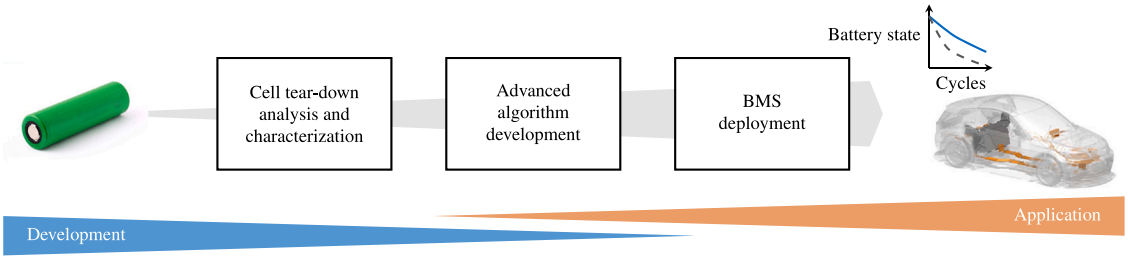

Fig. 1. Pipeline for the development of advanced algorithms for the deployment in Battery Management Systems (BMSs) of battery electric vehicles. This study focuses on the in-depth analysis and characterization of a lithium-ion cell.

and in-depth component analysis on the electrode level and provide comprehensive investigations of corresponding full cell properties, is given in the following.

Safari and Delacourt [10] analyzed the electrochemical properties of an LFP-based LIB and compared the electrode properties to the full cell, thus providing a fundamental dataset for an electrochemical battery model. However, their measurements were performed before 2011, compromising the comparability to today's battery cell generations. Sabet et al. [19,20] analyzed the predominant processes in the impedance spectra of commercial NMC- and NCA-based LIBs, respectively. Schmalstieg et al. [21] provided an electrochemical analysis of the electrode properties of a high-power LIB which they used to parameterize a physico-chemical model of the full cell. Kovachev et al. [22] performed an in-depth material and design analysis of NMC pouch cells, using a battery cell from an unknown manufacturer. Also, first generation Nissan Leaf LMO pouch cells were analyzed from a material recycling perspective [23]. Unfortunately, the investigation was restricted to material analysis only. Lain et al. [24] investigated many commercially available cylindrical LIBs with varying chemistries according to their geometrical and active material properties and compared different design strategies of manufacturers. An electrochemical performance analysis was not in the scope of the work. Recently, Liebig et al. [25] and Chen et al. [26] investigated a prismatic and cylindrical NMC cell, respectively, at the material, electrode and full cell level. They performed scanning electron microscope (SEM) images of the electrodes, geometrical measurements, and further characterization of the electrochemical performance (e.g., EIS). The parameters were used to parameterize an electro-chemical model with thermal dynamics.

It can be concluded that in present literature, only a few studies performed an in-depth investigation of commercially-available battery cells from the electrode to the full cell level, hampering downstream usage of the results for modeling, algorithm design and validation. Further systematic investigations providing insights into the properties of commercially available battery cells from the electrode to the full cell level at various ambient temperatures are needed to avoid time- and resource-intensive rework.

1.2. Contributions

We performed an in-depth analysis of a commercial 18650 LIB (Sony US18650VTC5 A) involving various state-of-the-art characterization methods. The main contributions can be summarized as follows:

1. **Tear-down analysis, half cell building, and investigation of the geometrical properties**
   The design and geometrical properties of the electrodes and of the full cell are investigated via destructive and non-destructive methods.
2. **Analysis of half cell and full cell open-circuit voltages**
   The open-circuit voltages of electrode half cells are analyzed with different measurement methods over a broad temperature range and the results are scaled to full cell level via electrode balancing and alignment.
3. **Analysis of half cell and full cell dynamics**
   The cell's behavior under dynamic conditions is analyzed via electrochemical impedance spectroscopy. The observed loss processes are assigned to either half cell via analysis of the DRT.
4. **Open-source access to the experimental data**
   All measurement data and analysis results are provided open-source alongside the article.

The results of this study can be used to develop and parameterize advanced battery analytics functionality such as physics-enhanced equivalent circuit models (ECMs) for on-line estimation of the impedance throughout the lifetime [27], P2D or reduced-order models to be used in model-based fast charging strategies [28], or determination of degradation modes through the tracking of electrode balancing over lifetime [5].

1.3. Layout

The remainder of this paper is structured as follows: Section 2 introduces the employed methods and boundary conditions for the battery dissection and building of the half cells. In Section 3, the geometrical properties of the investigated cell are stated and discussed. The static behavior of the cell, i.e., OCV of the half cells and fitting to the full cell's OCV, is presented and discussed in Section 4. The assessment of the dynamic cell behavior is presented in Section 5. In Section 6, we summarize the main insights of the article.

2. Cell tear down and building of half cells

In this section, the disassembly of a commercial 18650 cell (Sony US18650VTC5 A with a Si-doped graphite anode, NCA cathode, and 2.5 Ah nominal capacity [24]) and the building of anode and cathode half cells against metallic lithium is described.

2.1. Dissection of the cell

In the first step, a pristine cell was taken from a new manufacturing batch and was constant current constant voltage (CCCV) discharged to 2.5 V to minimize the energy contained within the cell and thus minimize the severity in the case of an unintended short-circuit. Then, the cell top was removed with a pipe cutter tool under inert gas atmosphere, while ensuring that the tool did not get in contact with the electrode materials. After opening, the outer anode cell internal copper tab could be seen, as shown in Fig. 2(a). The visible pierced layer of plastic material may help to avoid any vibration- or shock-induced internal short circuit between the negative electrode layers and the top positive battery tab. The battery cell steel can was then thoroughly unwound from the cell internal materials to expose the active material layers, as visible in Fig. 2(b) and (c), respectively. Once the jelly roll was extracted from the cell can, the electrode layers could be analyzed. Unwrapping the jelly roll revealed the electrode tab positions, as shown in Fig. 2(d).

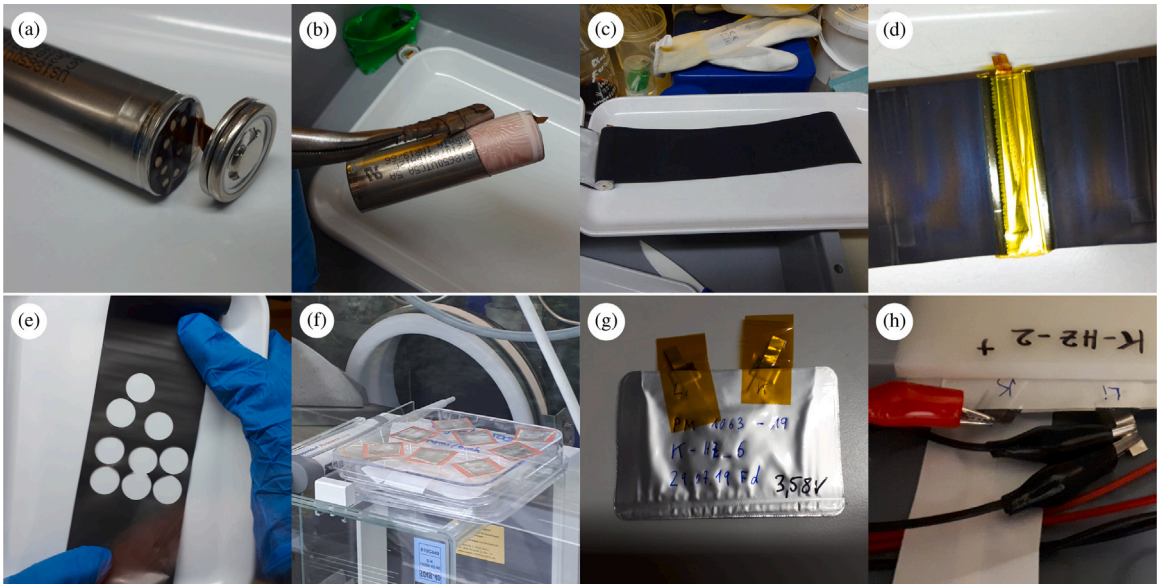

Fig. 2. Preparation of half cells under inert gas atmosphere. The cell disassembly under inert gas atmosphere can be seen in figures (a)–(d), the half cell preparation process with sample stamping of each electrode can be seen in figures (e)–(h).

2.2. Half cell assembly

To test different operating scenarios with pristine half cells and to provide spares in case of defects resulting from the manual process [29,30], we built five plus three half cells per electrode. In the first step, coins of 16 mm diameter were punched out of the now exposed electrode layer, as visible in Fig. 2(e). Since both electrodes are doubled-coated with active material, one side of the electrode was cleaned by mechanically removing the coating from the carrier material with the aid of NMP solvent at 20 °C ambient temperature. In a subsequent step, all electrode stamps were covered with a Celgard Polypropylene mono-layer separator and countered with a layer of metallic lithium, as seen in Fig. 2(f). The final half cell was then equipped with current collectors and placed in a mini pouch bag. To enable charge transfer between the electrodes, each pouch cell was filled with 500 µL of LP30 electrolyte (1M $LiPF_6$ in EC:DMC (1:1, v/v)). In the final step, the mini pouch bag was sealed with a Multivac vacuum machine. After sealing, the half cells were stored for over 24 h to guarantee that the electrolyte completely soaked into the pores of the cell components.

2.3. Formation of half cells

To allow the formation of a solid electrolyte interphase (SEI) at the electrode–electrolyte interface, a formation procedure was undertaken with all half cells by cycling in charge and discharge direction. The formation cycles are plotted in Fig. 3 for both half cells. Stable voltage traces and a coulombic efficiency over 99% was reached after three cycles for all half cells.

During formation, the minimum and maximum voltage limits for the anode were set to 10 mV and 1.5 V, respectively, as voltage gradients steeply ramp up beyond those limits and critical voltages are avoided. The cathode limits were likewise set to 2.5 V and 4.25 V. C/10 was chosen as the charge and discharge current. The resulting current was calculated using the down-scaled areal capacity (Fig. 5) of the electrode section according to:

$$I_{HC} = (16\,\text{mm}/2)^2 \cdot \pi \cdot 0.024\,\text{mAh/mm}^2 \cdot 0.1\,\text{h}^{-1} = 0.481\,\text{mA}. \quad (1)$$

For mini pouch bags, areal pressure has to be considered to make sure that volume changes do not lead to inhomogeneous contact or even internal disconnects. A target pressure of 0.1 MPa was set by placing the half cells with an active area of $(16\,\text{mm}/2)^2 \cdot \pi = 201\,\text{mm}^2$ between two square polymer contact plates and stressing the plates with a weight of 2 kg.

3. Geometrical parameters

In addition to the cell disassembly described in the previous section, we applied computed tomography (CT) to support the geometrical measures with data from the pristine cell. The non-invasive images (Fig. 4) reveal the internal structure of the full cell. The jelly roll has 27 electrode double layers with a total thickness of approximately 100 µm. Note that a more precise digital measurement was not possible due to the limited scan resolution of approximately 50 µm voxel size. The active volume, i.e., the volume which is occupied by the electrode layers including the pore volume, approximates to 87 % of the total cell volume.

The geometric properties and tab placement on the individual electrodes are illustrated in Fig. 5. On the anode, two current collector tabs are placed on uncoated copper foil at both ends. As previous studies pointed out [24], this design offers the potential to minimize resistance and heat generated in the cell core, since heat can be easily transferred from the cell core to the cell can over the center collector. Out of a total anode length of 947 mm, one side of the outer surface shows a larger area with uncoated copper foil (50 mm), which is left out during coating as it wraps the remaining cathode inside the winding and has no countering active material. At the inner surface, the coated area is larger and has a total length of 925 mm.

The cathode has one similar-sized current collector of aluminum, which is placed close to the center of the electrode. The slight offset towards the cell core may be a design feature to further increase the heat flow out of the cell core [24], which appears to be of higher priority than minimum resistance due to equidistant current paths through the cell. Both sides of the cathode are coated equally with NCA.

Both electrodes are wrapped up with a hollow center pin of 2.6 mm in diameter. Beyond production reasons, center pins allow for fast heat transfer out of the cell core during operation [31]. The slight over-sizing of the anode compared to the cathode is known as anode overhang, a design measure to ensure that the cathode is always countered with anode active material [32]. As a consequence, Li-ions can be accepted during charging even if electrodes are slightly misaligned during cell production. Hereby, the risk of local lithium plating at the electrode

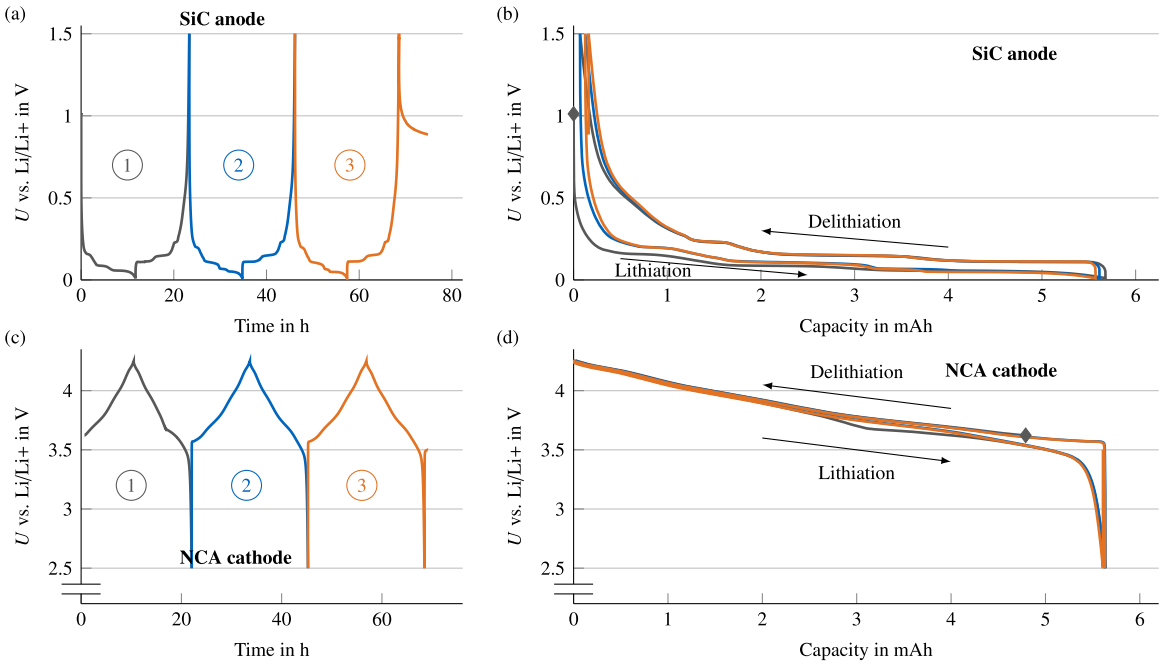

Fig. 3. Formation of the half cells until a stable voltage trace is reached. Voltage over time in (a)/(c) and voltage over capacity in (b)/(d) for anode and cathode half cells, respectively. Colored curves represent the three consecutive charge/discharge cycles, with gray markers indicating the formation starting point.

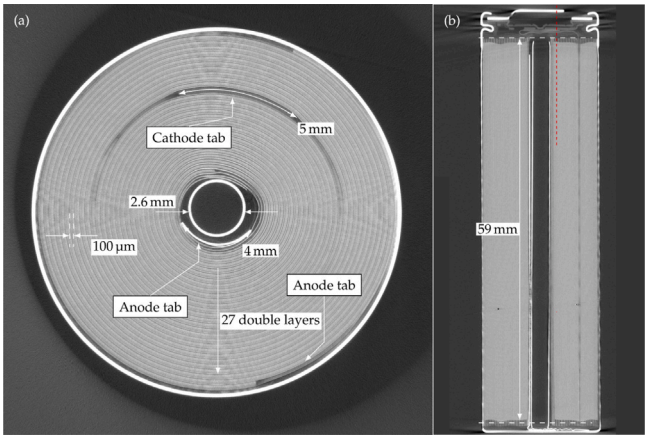

Fig. 4. CT scans of the investigated cell with digital measurements taken in myVGL (Volume Graphics GmbH, Germany). (a) provides a lateral and (b) the axial view into the cell through the cell center and reveals properties of the jelly roll.

edges is avoided. Contradictorily, many studies pointed out that the overhang leads to diffusion of lithium-ions into the overhang edges, which may aggravate inhomogeneous current densities during cycling, further provoking local lithium plating at the edges [29]. According to Lewerenz et al. [33], the ratio of the overhang can be calculated to approximately 7% of the total active area.

4. Open-circuit behavior

In this section, the voltage of the full cell and the constructed half cells at thermodynamic equilibrium are analyzed. For this, different OCV measurement methods are discussed in the first step. In the second step, the temperature dependency of the OCV is investigated between −10 °C and 50 °C. In the last step, both half cell OCVs are used to reconstruct the full cell OCV and reveal the electrode balancing. All measurements were performed with a BaSyTec CTS Lab.

4.1. Influence of measurement methods

There are two common methods for measuring the OCV of a cell, the galvanostatic intermittent titration technique (GITT) and the measurement of a pOCV with a low current rate [34]. To analyze the impact of these methods on the results for the tested cell type, pOCV measurements were performed with a C-rate of C/10, C/50 and C/100 at a reference temperature of 20 °C and GITT measurements with a relaxation time of 2 h at 40 state-of-charge (SOC) steps. The top row of Fig. 6 shows the results for the different methods for the full cell and the two half cells, respectively. Small voltage deviations between the different methods are present, which are caused by different overpotentials during the measurement. The voltage during the pOCV measurements is higher with the increasing current and is generally higher than the voltage measured during GITT.

Additionally, differential voltage analysis (DVA) of each measurement was performed and the results are shown in the bottom row of Fig. 6. The positions of the characteristic peaks in the DVA resulting from stage transitions in the anode [35,36] and cathode [37] (marked in Fig. 6(d)—(f)) are in good accordance for all measurement methods with small deviations propagating from the discussed OCV differences. Despite the limited amount of sampling points of the GITT measurement, the derived DVA curve also matches the stage transitions well. However, information losses occur in regions with higher voltage dynamics, e.g., anode stage IV. As a result, we conclude that for the investigated cell type, a pOCV measured with C/10 is sufficient to identify electrode characteristics and stage transitions at specific SOCs at the cost of higher overpotentials compared to GITT. In doing so, lab testing times, especially when tracking the pOCV during aging studies, can be reduced.

4.2. Temperature dependency

We performed pOCV measurements over a broad temperature range (−10 °C, 5 °C, 20 °C, 35 °C and 50 °C) to investigate the temperature dependence of the full cell's and half cell's OCV [38]. To minimize the influence of increased overpotentials at low temperatures, we chose a current of C/50. For this analysis, five different cells were used.

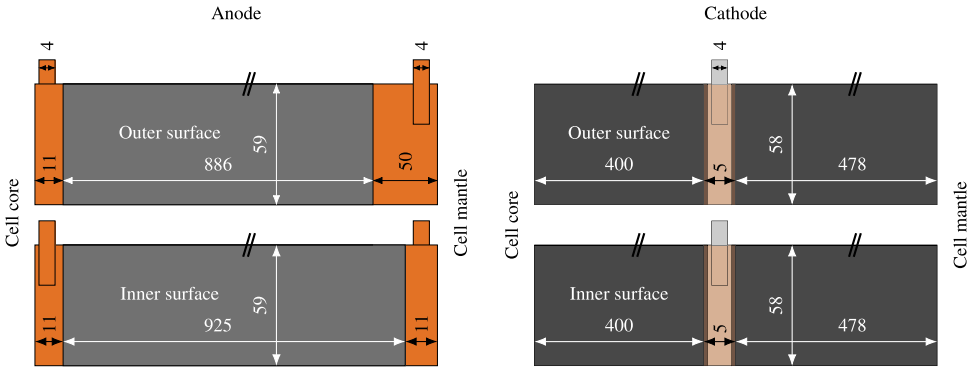

Fig. 5. Cell electrode design: The anode (left) is coated with Si-doped graphite, except for the contacting area of the two current collectors and the anode overlap at the outer surface close to the cell housing. The NCA cathode (right) is designed with a single current collector at the center. The NCA coating covers the remaining electrode wrap. All measures are in mm.

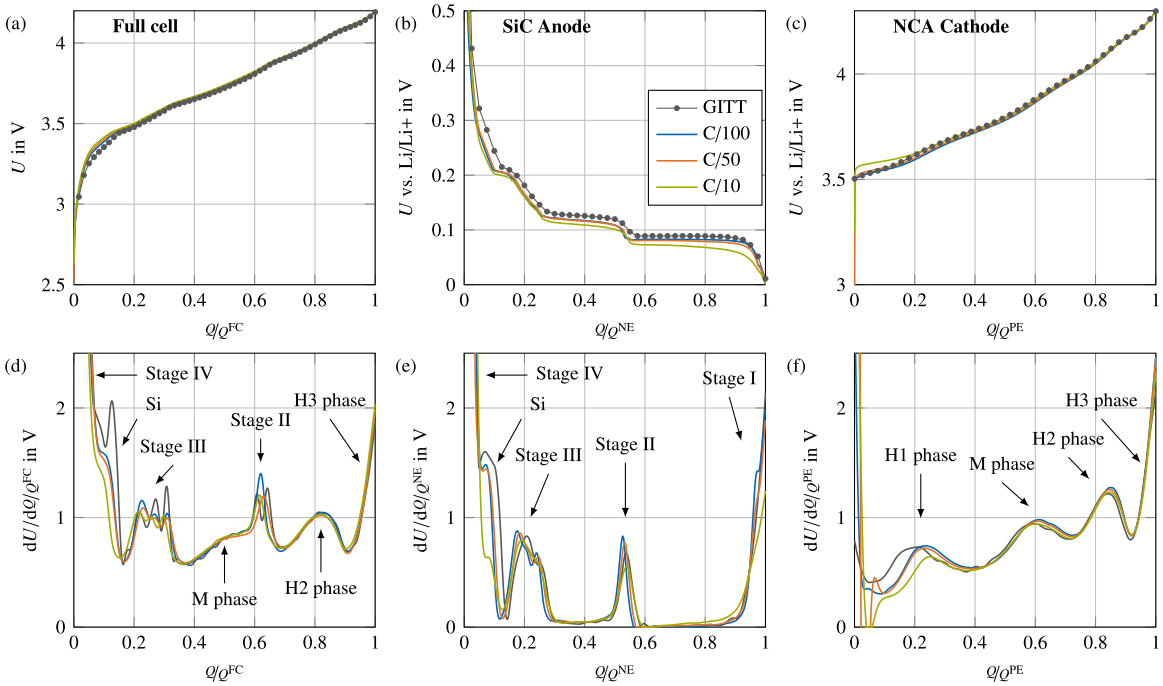

Fig. 6. Influence of different OCV measurement methods on the pseudo-OCV (top row) and corresponding DVA (bottom row) for the full cell (left column), anode (center column), and cathode (right column) over normalized capacity Q/Q^{FC}, Q/Q^{NE}, and Q/Q^{PE}, respectively. The actual measured capacities Q^{FC}, Q^{NE}, and Q^{PE} were used for normalization. OCV curves were measured in charge direction of the full cell at 20 °C. Additionally, lithiation stages and phases of the active material labeled.

Whereas intrinsic parameter variations due to production tolerances of the individual samples are expected to be negligible for the commercial full cell [39–41], these intrinsic variations might increase during manual half cell assembly and subsequent formation. However, Schmid et al. [42] showed that similar orders of magnitude of parameter variations are achievable for manually built half cells, which is why we chose to conduct the measurements with different samples, as subsequent testing of one sample would also influence the measurement results due to degradation of the half cells [30]. Experimental results are presented in Fig. 7. Again, the differential voltage is also plotted to investigate a shift of the characteristic peaks with varying temperature.

At low SOC, the OCV curves fan out and the voltage increases with decreasing temperature. In the DVA of the full cell and the anode, the stage transitions at approx. 10 % SOC (which is assumed to be caused by silicon in the anode [36]) disappears. However, no clear answer can be given as to whether this behavior results from an altered behavior of silicon at low temperatures or from increased overpotentials. This temperature effect is still visible at the stage III transition of graphite. Additionally, directly after the stage III transition, between 30 % SOC and 40 % SOC, an extra peak starts to develop for temperatures higher than 20 °C, which can be attributed to the anode. Apart from these observations, the voltage curves behave consistently over the entire temperature range.

4.3. Electrode balancing

Up to now, all voltage and differential voltage curves have been plotted over their normalized capacity Q/Q^{Cell}. However, to reconstruct the full cell voltage and understand the electrode balancing, the voltage curves of anode and cathode need to be scaled and aligned. In the following, this process is referred to as half cell fitting and the results are shown in Fig. 8. Based on the previous findings of the influence of measurement methods, we chose the C/10 curves for half cell fitting.

Half cell fitting can directly be done by using the OCV curves [5]. However, using derivatives such as incremental capacity analysis (ICA) curves [43] or DVA curves [44] might be beneficial to properly match the characteristic transition phases of the individual electrodes. In theory, all methods should yield the same results. In practice, however,

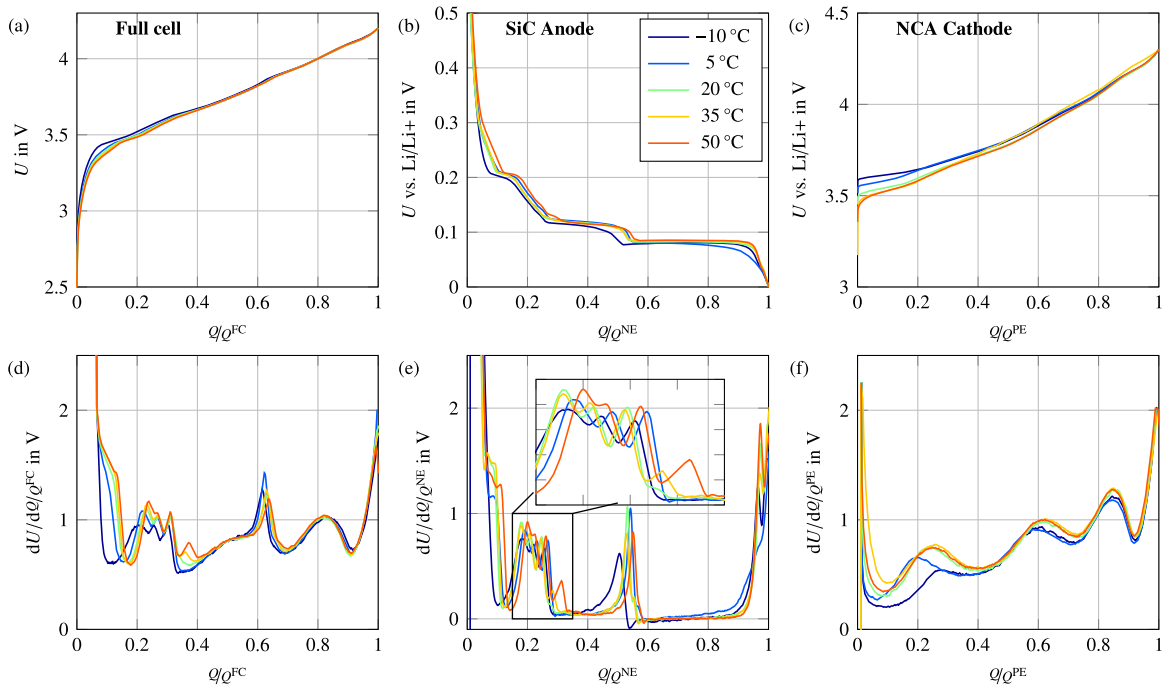

Fig. 7. Temperature dependency of the pseudo-OCV (top row) and corresponding DVA (bottom row) for the full cell (left column), anode (center column), and cathode (right column) over normalized capacity Q/Q^{FC}, Q/Q^{NE}, and Q/Q^{PE}, respectively. The actual measured capacities Q^{FC}, Q^{NE}, and Q^{PE} were used for normalization. pOCVs curves were recorded in charge direction with a current of C/50.

slight differences in the algorithm and the processed data will lead to deviating results. Therefore, half cell fitting was performed in the OCV domain as well as in the DVA domain.

The first step of the half cell fitting is to nondimensionalize the capacities of all potential curves to between 0 and 1. This is necessary because the half cells consist of only a fraction of the full cell's active material. Nondimensionalizing is allowed because the measured half-cell potentials are a material property and independent of the amount of active material.

In the next step, a fitting range is defined to exclude certain SOC ranges, which has been reported to increase the quality of the fit [5]. At low SOC, the voltage curve of the anode is especially steep. Thus the DV increases towards large values, causing a fitting procedure to minimize the error mainly in this range. Furthermore, due to the fast change in anode potential without much charge throughput, this range is highly sensitive to the measurement procedure, which could further distort the results. Thus, by excluding the outer SOC-ranges from the fitting, special attention can be paid to accurately fit the stage transitions of graphite. The difference between the upper bound x_{ub} and lower bound x_{lb} is defined as the fitting range ϑ_{fit}:

$$\vartheta_{\mathrm{fit}} = x_{\mathrm{ub}} - x_{\mathrm{lb}}. \tag{2}$$

In the OCV-domain, the electrode balancing is performed by minimizing the cost function $f_{\mathrm{cost,OCV}}$:

$$f_{\mathrm{cost,OCV}} = \int_{x_{\mathrm{lb}}}^{x_{\mathrm{ub}}} \left({U_{\mathrm{OC}}}^{\mathrm{FC}}(x_{\mathrm{FC}}) - {U_{\mathrm{sim}}}^{\mathrm{FC}}(x_{\mathrm{FC}}) \right) \rightarrow \min. \tag{3}$$

Here, the fitting is performed by computing a simulated full-cell OCV ${U_{\mathrm{sim}}}^{\mathrm{FC}}(x_{\mathrm{FC}})$ via

$$\begin{aligned} {U_{\mathrm{sim}}}^{\mathrm{FC}}(x_{\mathrm{FC}}) = {U_{\mathrm{OC}}}^{\mathrm{PE}}\left(\alpha^{\mathrm{PE}} x_{\mathrm{FC}} - \nu^{\mathrm{PE}}\right) \\ - {U_{\mathrm{OC}}}^{\mathrm{NE}}\left(\alpha^{\mathrm{NE}} x_{\mathrm{FC}} - \nu^{\mathrm{NE}}\right) - \delta_{\mathrm{volt}}. \end{aligned} \tag{4}$$

The fitting parameters $\alpha^{\mathrm{PE/NE}}$ and $\nu^{\mathrm{PE/NE}}$ determine the horizontal scaling and shifting of the cathode and anode voltage curves, respectively, and are dimensionless. The fitting parameters δ_{volt} carries the unit [V] and is introduced to equalize the difference in internal resistance within the experimental half cells compared to the full cell.

Without the introduction of δ_{volt}, which lies between 14 mV and 20 mV in the case of C/10 measurements, the optimization algorithm would be forced to compensate the existing difference in internal resistance by shifting the electrode's potential curves in the x-direction. This could lead to a mismatch of characteristic stage and phase transitions of the measured and simulated full cell curve. A positive value of δ_{volt} means that the resistances of one or both half cells is higher compared to the full cell, even though it is normalized to the active surface area. This is the case and it is visible in the impedance spectra shown in the next section.

In the DVA-domain, the cost function has to be formulated as:

$$f_{\mathrm{cost,DVA}} = \int_{x_{\mathrm{lb}}}^{x_{\mathrm{ub}}} \left(\frac{d{U_{\mathrm{OC}}}^{\mathrm{FC}}}{dx_{\mathrm{FC}}}(x_{\mathrm{FC}}) - \frac{d{U_{\mathrm{sim}}}^{\mathrm{FC}}}{dx_{\mathrm{FC}}}(x_{\mathrm{FC}}) \right) \rightarrow min, \tag{5}$$

with

$$\begin{aligned} \frac{d{U_{\mathrm{sim}}}^{\mathrm{FC}}}{dx_{\mathrm{FC}}}(x_{\mathrm{FC}}) = \frac{\alpha^{\mathrm{PE}}}{\nu_{\mathrm{fit}}} \left(\frac{d{U_{\mathrm{OC}}}^{\mathrm{PE}}}{dx_{\mathrm{FC}}}(\alpha^{\mathrm{PE}} x_{\mathrm{FC}} - \nu^{\mathrm{PE}}) \right) \\ - \frac{\alpha^{\mathrm{NE}}}{\nu_{\mathrm{fit}}} \left(\frac{d{U_{\mathrm{OC}}}^{\mathrm{NE}}}{dx_{\mathrm{FC}}}(\alpha^{\mathrm{NE}} x_{\mathrm{FC}} - \nu^{\mathrm{NE}}) \right). \end{aligned} \tag{6}$$

The effect of a different resistance on the differential potential curves is much lower, as shown in the previous section. Therefore, the optimization algorithm does not need a vertical adjustment parameter such as δ_{volt} to match the stage and phase transitions well.

There are three main factors influencing the fitting results: (i) the measurement procedure (ii) the fitting domain (OCV-domain or DVA-domain), and (iii) the fitting range. To investigate these influencing factors, we performed the fitting for each combination of $x_{\mathrm{lb}} \in [0{:}0.005{:}0.15]$ and $x_{\mathrm{ub}} \in [0.9{:}0.005{:}1]$ in the OCV domain and the DVA domain for both, C/10 and C/50, pOCV measurements. For each configuration, the RMSE was calculated in the OCV domain (with the unit mV) and the DVA domain (with the unit mV/Ah) over the full SOC range (0–1), denoted as ϵ_{full}, and over the reduced SOC range (0.15–0.9), denoted as $\epsilon_{\mathrm{range}}$. The error measures and fitting parameters are

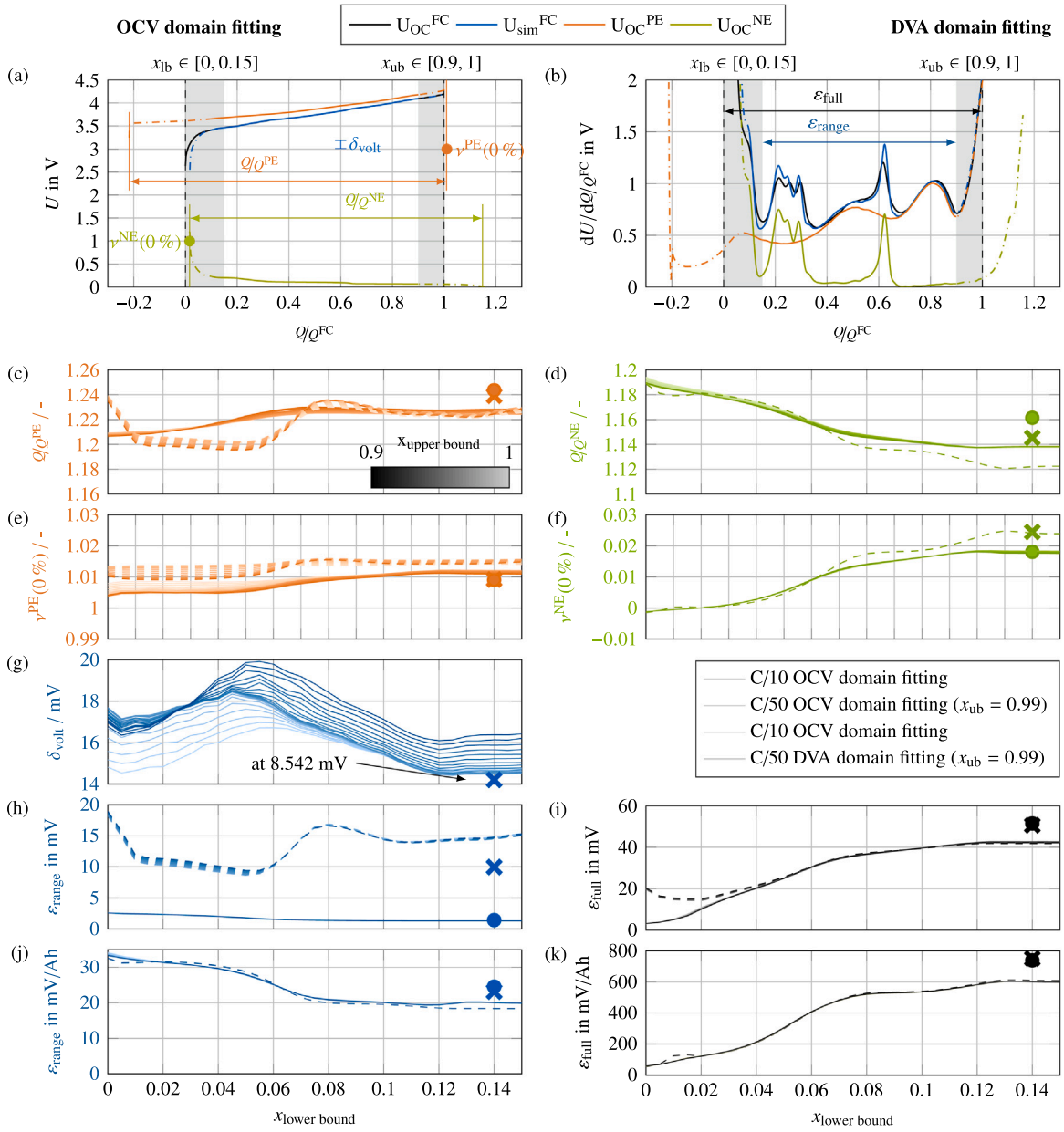

Fig. 8. Full cell OCV and DVA reconstruction from individual electrode potentials. 1st row: Results for fitting in the OCV domain (a) and fitting in the DVA domain (b) pOCV curves with C/10 at 20 °C for x_{lb} = 0.1 and x_{ub} = 0.9. The fitting parameters $\alpha^{PE/NE}$ and $\nu^{PE/NE}$ are additionally illustrated: $Q/Q^{PE/NE}$ are the normalized electrode capacities resulting from $\vartheta_{fit}/\alpha^{PE/NE}$. The shifting parameters $\nu^{PE/NE}(0\%)$ are illustrated at the state, where the respective electrode is fully delithiated. For the anode it is calculated as $\nu^{NE}(0\%) = (\vartheta_{fit}/\alpha^{PE/NE} \cdot (0 - \nu^{PE/NE})) + x_{lb}$. For the cathode it is calculated as $\nu^{PE}(0\%) = (\vartheta_{fit}/\alpha^{PE} \cdot (1 - \nu^{PE})) + x_{lb}$. 2nd–6th row: Fitting parameters and fitting errors dependent on the fitting domain (solid vs. dashed lines), the lower fitting bound x_{lb} (along the x-axis) and the upper fitting bound x_{ub} (different color shading). 2nd–3rd row: Fitting parameters of the cathode (c) and (e), and the anode (d) and (f). 4th row: The parameter δ_{volt} (g) only exists for fitting in the OCV domain. 5th row: RMSE in the OCV domain for the reduced SOC range of 0.15–0.9 (h) and the full SOC range from 0–1 (i). 6th row: RMSE in the DVA domain for the reduced SOC range of 0.15–0.9 (j) and the full SOC range from 0–1 (k). Both. ε is calculated as the root mean square error (RMSE).

presented in Fig. 8. Since the dependency on the lower and upper fitting bound is similar for the C/50 pOCV measurements, only the results for x_{lb} = 0.14 and x_{ub} = 0.99 are shown for better visibility.

In general, the trend is similar for fitting in the OCV domain compared to fitting in the DVA domain and the absolute values only differ slightly. The OCV errors ε_{range} and ε_{full}, which are much higher for the fitting in the DVA domain, reveal the missing parameter δ_{volt} and confirm the need for this additional vertical adjustment parameter in order to find physically reasonable scaling and shifting parameters $\alpha^{PE/NE}$ and $\nu^{PE/NE}$ in the OCV domain. The parameter δ_{volt} is equally dependent on the lower and upper fitting bound and no clear trend is identified. This suggests that the resistance's difference is not uniform across the whole SOC range. For the other fitting parameters and the error measures, the influence of the lower fitting bound x_{lb} is much higher compared the upper bound x_{ub}. The following observations lead to the assumption that this is due to fact that the harvested anode half cell shows different behavior compared to the pristine full cell, especially in the low SOC area.

The RMSE of the reduced range ε_{range} decreases with increasing x_{lb}, whereas the RMSE of the full range ε_{full} increases with increasing x_{lb}. This is because for low values of x_{lb}, the fitting procedure has to find a trade-off between the different characteristic anode features, leading to a better match of the low SOC area at the cost of an increased distance between the anode's stage II and stage III. For higher values of x_{lb} the anode's stages in the mid-SOC area are fitted more accurately at the cost of an increased error in the low SOC area. This is also reflected in

the scaling and shifting parameters, which are highly affected by the lower fitting bound x_{lb}. Q/Q^{NE} decreases with increasing x_{lb}, confirming the trade-off between matching the different anode stages. Especially noticeable is the positive value of $v^{NE}(0\%)$ for x_{lb} above 2 % SOC, which means that the simulated full cell is not defined for very low SOC (up to 2.5 % SOC, depending on the fitting method). For values of x_{lb} towards the first local minimum of the full cell's and anode's differential voltage (at approx. 15 % SOC), the fitting parameters and error measures converge.

Since it is assumed that lithiation of the silicon mainly takes place in the low SOC area [45], our observations are in good accordance with a recent study from Schmitt et al. [45], who investigated the change in silicon–graphite potential curves during aging and observed mainly a decrease in the relative capacity contribution of the silicon. This suggests that the high impact of the lower fitting bound and the imperfect reconstruction of the full cell from the half cell's potential curve for low values of x_{lb} is mainly due to the different behavior of silicon inside the anode. For the present measurement data, we propose to use the first local minimum at approx. 15 % SOC of the differential voltage curve as a lower fitting boundary. This way, the location of the graphite's stage II and stage III are matched perfectly and the cathode's fitting parameters are not disturbed in order to compensate the mismatch of the silicon characteristics. Since the influence of the upper fitting bound on the fitting parameters and error measures is negligible for high values of x_{lb} and the H3 phase is an important feature of the cathode, x_{ub} =99 % SOC is chosen.

5. Kinetic and transport properties

After analyzing the cell's thermodynamic behavior, it is important to understand the loss processes during the dynamic operation in order to get a complete picture of the cell's performance. Since the kinetics of LIBs are highly temperature dependent, we performed EIS on the full cell and half cells at ambient temperatures between −10 °C to 60 °C. Based on the experimental results, we calculate the DRT, which enables us to assign the loss processes of the full cell to either electrode. To quantify these loss processes, we determine the time constant and polarization resistance from the DRT.

5.1. EIS measurements, DRT calculation and parameter identification

EIS was performed using a Gamry Instruments Interface 5000, whereby the hybrid EIS mode with an AC voltage of 10 mV rms, a frequency range of 5 kHz to 10 mHz for the full cells and 5 MHz to 10 mHz for the half cells and ten points per decade was used. We increased the frequency range of half cell measurements due to the occurrence of additional processes at higher frequencies. EIS was performed for every 5 % SOC with a relaxation period of 3 h after discharging to the respective SOC. Full cell impedance spectra were recorded at −10 °C, 5 °C, 20 °C, 35 °C, 50 °C and 60 °C. Half cell impedance spectra were only recorded at 20 °C, 35 °C and 50 °C.

To isolate the individual loss processes, the DRT of an impedance spectrum can be evaluated. It makes the distribution of the total polarization resistance in the continuous space of relaxation times visible and thus provides a higher frequency resolution of the dynamic processes [46–50]. Deconvolution of the DRT is based on the assumption that the impedance of an electrochemical system can be expressed by an infinite number of RC elements [46,51]. For this study, the DRT of the recorded impedance spectra were calculated with an implementation of the algorithm presented by Wan et al. [52]. Since the DRT reveals the time constant of individual relaxation processes of an electrochemical system, assignment of full cell processes to individual electrodes becomes feasible. More details on the methodology can be found in the research articles by Sabet et al. [19,20], who performed similar analysis for NCA and NMC cells.

Furthermore, in addition to the time constants τ of individual relaxation processes, which can directly be extracted from the DRT at the respective local maxima of γ, we also determined their polarization resistance R by integration of γ between the adjacent minima of detected processes. The acquired process parameters are presented over a large operating range in the following section.

5.2. Assignment of full cell processes to half cells

In Fig. 9, impedance spectra and their corresponding DRT are plotted for the full cell and both half cells, respectively. The half cell's SOC of EIS measurements is expressed with reference to the full cell SOC according to the half cell fitting. Starting from a fully delithiated half cell, where the SOC is defined as 0, the half cell was charged in 5% SOC steps according to the precedent pOCV measurement.

Visually analyzing the full cell's impedance spectra, one distinct semi-circle and the diffusive branch can clearly be identified. In contrast to this, three processes are revealed from the DRT, which are denoted as F1, F2, and F3. The first process F1 has a time constant of 1.3 ms that does not change with the SOC and its magnitude only increases slightly towards a high and low SOC. The addition of F1 and F2 form the charge transfer resistance R_{ct} of the full cell. Thereby, F2 is highly dependent on the SOC. It is only visible from 0% SOC to 20% SOC and from 90% SOC to 100% SOC with a time constant of around 10 ms. Its resistance increases strongly towards the outer SOCs. The third process F3 at about 100 ms is least pronounced with a resistance of approximately 1 $\Omega\,cm^2$. It occurs at the transition between charge transfer and diffusion and is denoted as $R_{transition}$.

By analyzing the half cell's impedance spectra and DRT, processes of the full cell can be assigned to either the cathode or the anode. The first observed processes A0 and C0 occur at frequencies which were not captured during full cell measurements and can be attributed to the lithium counter electrode of the half cells [20].

The resistance of A1 and C1 show an exact opposite trend with the SOC while A1 is more pronounced overall. Since for F1 only a small SOC dependency of the resistance was observed, it can be assumed that F1 is the superposition of A1 and C1 with the opposed SOC dependency being counterbalanced in a full cell assembly. The dominance of the anode gets more pronounced at a high SOC and decreases towards a low SOC, where the resistance at the cathode side increases. Similar conclusions have been drawn in [19]. The strong increase of the full cells R_{ct} at a high and low SOC due to F2 seems to be resulting from the cathode's process C2. The changing resistance with the SOC of C2 coincides well with F2. Only the varying time constant of C2 does not fit into the picture.

Similar processes at the transition frequency of F3 can also be observed for the two half cells. C3 on the one hand is distinguishable in the cathode's impedance spectra and shows very similar behavior as F3. A3 on the other hand shows different behavior, especially at a high SOC, where the resistance of the process increases strongly. A sudden leap can be seen in the impedance spectra of the anode at the middle of the diffusion branch, which causes the DRT algorithm to identify two separate processes within the diffusion branch of the anode. This might be caused by impurity of the anode or measurement noise of the EIS measurement. Results at 35 °C (Fig. A.11) and 50 °C (Fig. A.12) are more reasonable for the anode and no transition process is detected at the cathode. Overall, no clear conclusion can be drawn as to whether F3 should be assigned to the anode, cathode, or both and the assignment might vary for different temperatures.

5.3. Quantification of loss process parameters over SOC and temperature

After identifying meaningful processes of the full cell and discussing the assignment of them to either the anode or the cathode, the determined parameters R and τ of the full cell are now quantitatively analyzed. Results are plotted in Fig. 10, which can be read as follows:

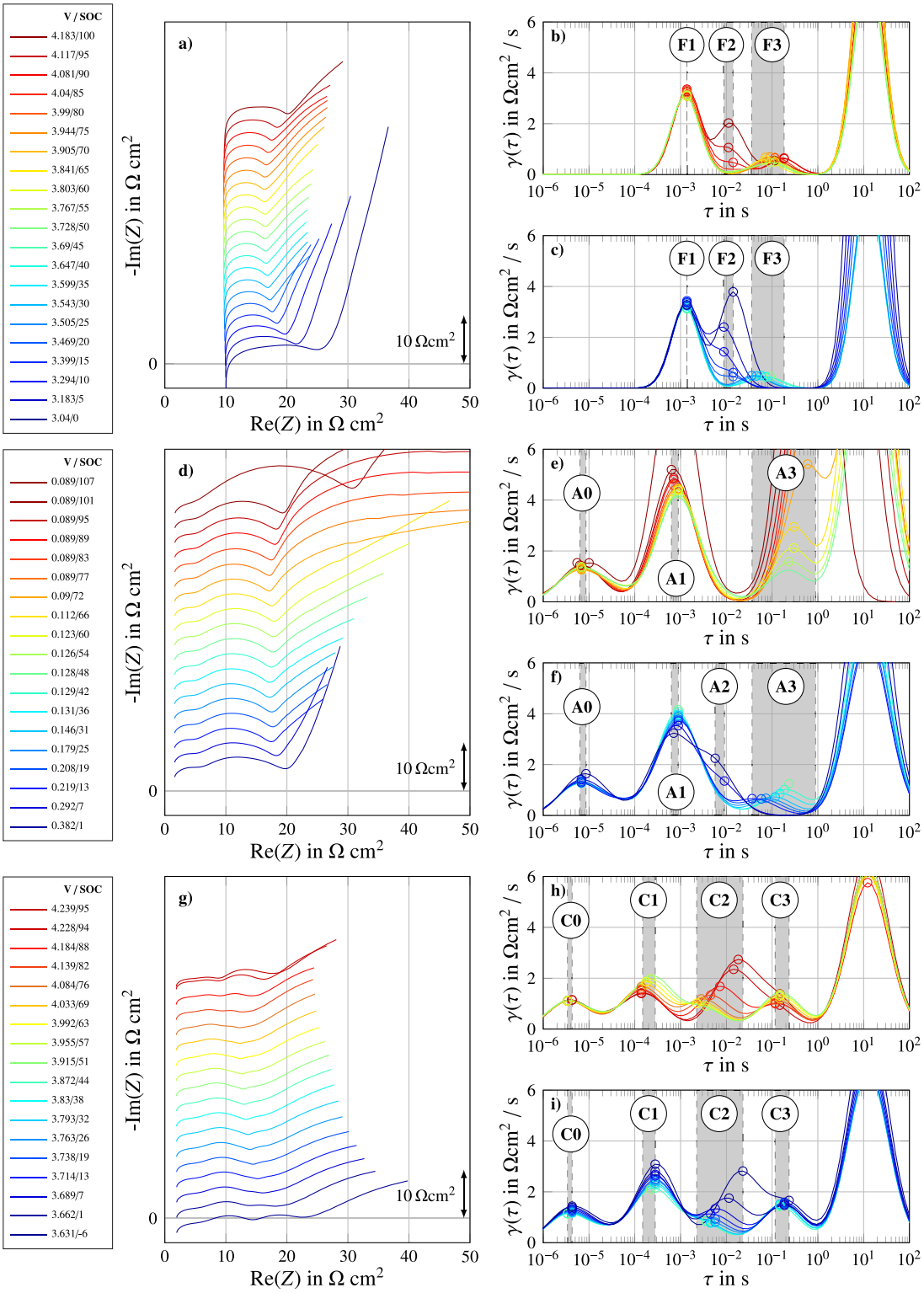

Fig. 9. Impedance spectra from EIS measurements (left column) and corresponding DRT (right column) for different SOCs at 20 °C for the full cell (top), anode (center), and cathode (bottom). DRT plots are subdivided into a high SOC area (100%–50% SOC) and low SOC area (49%–0% SOC). Impedances are normalized by the active electrode surface. SOCs of the half cells are calculated relative to the full cell according to the half cell fitting. For better visibility, impedance spectra in (a), (d), and (g) are shifted in y-direction according to the respective full cell SOC using $-\mathrm{Im}(Z) = -\mathrm{Im}(Z)+\mathrm{SOC}/2$ and the scale is indicated by the 10 Ω cm² arrow.

Resistance values of the four main identified processes are plotted in the first and second row, respectively: (1) The ohmic resistance R_{ohm}, calculated as the intersection point with the x-axis in the Nyquist plot (2) The charge transfer resistance R_{ct}, determined as the sum of all contributing sub-processes (3) $R_{\mathrm{transition}}$, which was identified around the transition frequency between charge transfer and diffusion (4) R_{diff}

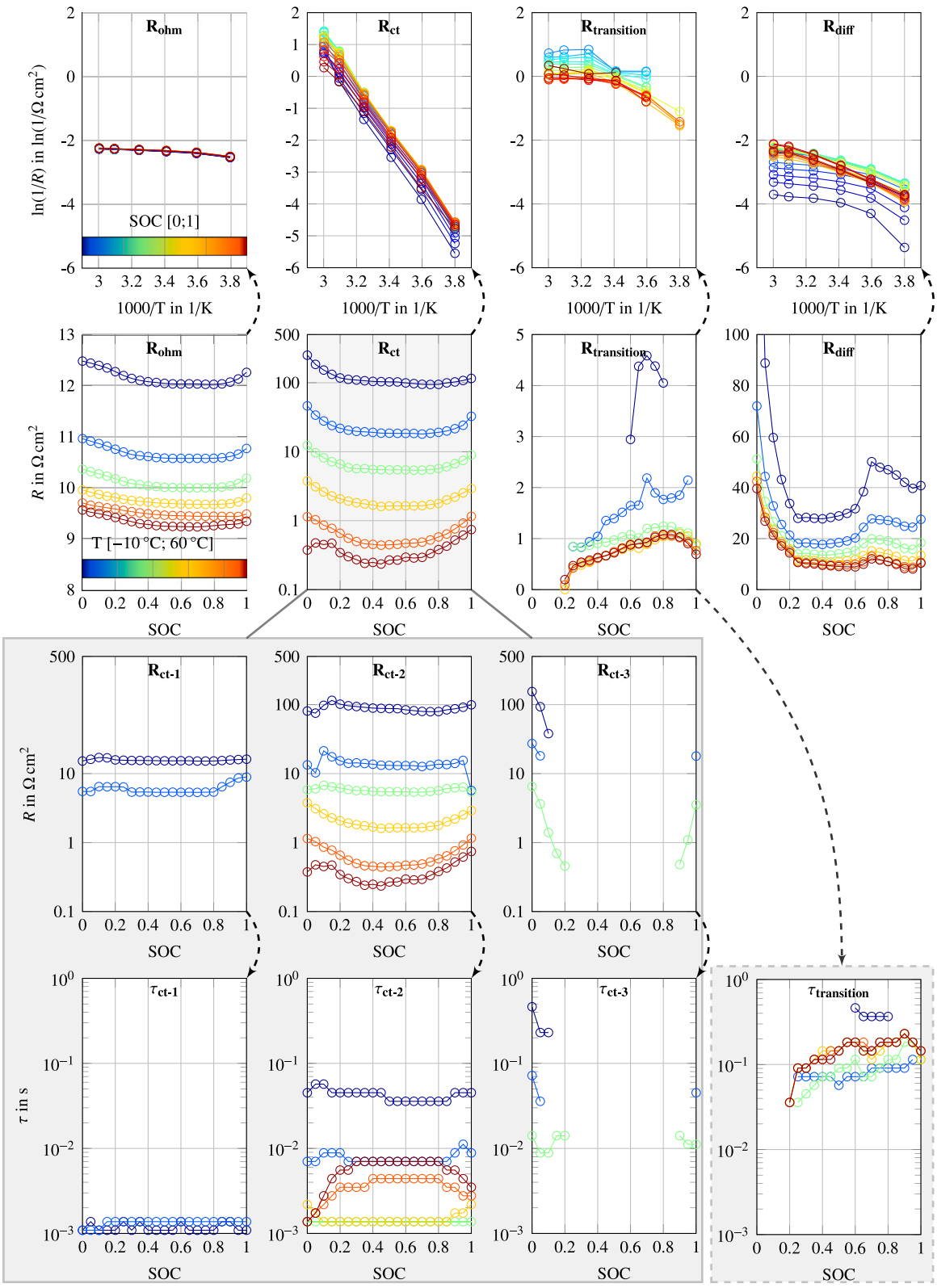

Fig. 10. Quantification of the time constant (determined at the respective local maxima of the DRT) and polarization resistance (determined by integration of the DRT between the adjacent minima) of identified loss process. Resistances are normalized by the active electrode surface. 1st row: Logarithm of the resistance over the inverse temperature according to (7) for different SOC. 2nd row: Resistance over SOC for different temperatures. 3rd row: Resistance over SOC for sub-processes of R_{ct}. 4th row: Time constants over SOC for sub-processes of R_{ct}.

representing the share of the solid state diffusion which was captured until the lowest frequency of 10 mHz.

In the first row, the logarithm of the resistance is plotted over the inverse temperature for every SOC to check for the Arrhenius

dependency according to

$$\frac{1}{R_{ct}} = A \cdot e^{\frac{-E_A}{R \cdot T}}, \quad (7)$$

with the universal gas constant R, the activation energy E_A, and the amplitude A. A linear behavior over the whole temperature range is expected for R_{ct} and R_{diff} [53]. In practice, however, confirmation of the Arrhenius dependency of solid-state diffusion is hardly possible due to the limited frequency range of EIS measurements, which is also the case for our measurements. Nevertheless, for R_{ct}, we observe a good quality of the linear fit ($R^2 > 0.996$) with resulting activation energies between $54\,kJ\,mol^{-1}$ and $65\,kJ\,mol^{-1}$.

In the second row, the resistance values are plotted over the SOC for the six different temperatures. For R_{ohm} and R_{ct}, the typical "bathtub" shape [54] is consistently observed. Thereby, R_{ct} is plotted logarithmically since it shows a strong temperature dependency with a resistance spread over several decades, reaching from below $1\,\Omega\,cm^2$ at 60 °C to above $100\,\Omega\,cm^2$ at −10 °C. The transition process shows a uniform trend with similar magnitude above 20 °C. For low temperatures, the resistance increases and is only visible in a narrow SOC interval. R_{diff} increases strongly towards a low SOC and shows characteristic behavior in the mid-SOC area, which coincides well with the stage 2 transition of graphite and can be explained by the homogenization effect [55–57].

In the third row, R_{ct} is further subdivided based on the DRT analysis. At 20 °C, two separate processes, which form the overall charge transfer resistance, have been identified. For lower temperatures (−10 °C and 5 °C) a third process is revealed by the DRT, which is assumed to be a result of the SEI. In the fourth row, the corresponding time constants τ are plotted over SOC for the three sub-processes of R_{ct} as well as for $R_{transition}$. Whereas the time constants of the charge transfer resistances vary highly with temperature, they are in the same order of magnitude for the transition process. Per definition, there is no time constant for R_{ohm} and τ_{diff} is constant due to the limited frequency range.

In this section, we complemented the study by giving detailed insights into the kinetics of the investigated cell. Thus, physically motivated design of algorithms on the application level is enabled. Based on these results, optimization algorithms, such as on-line estimation of the impedance throughout the lifetime [27], can be initialized and the number of considered loss processes, e.g., in an ECM, can be reasonably chosen.

6. Conclusions

Tear-down analysis of LIBs are essential for gathering in-depth knowledge about the systems' behavior and for enabling advanced algorithms to ensure optimal design and operation of LIBs on the application level. In this study, we presented detailed insights into the geometrical and electrochemical properties of a commercial NCA LIB with a Si-doped graphite anode.

In the first step, the cell was opened under inert gas atmosphere to yield direct measurement of the cell component's length, width, and thickness. Additionally, the battery was imaged by CT to get further insights into the geometrical structure of the jelly roll. The anode overhang was determined to approximately 7% of the total active area. Anode and cathode half cells were built for further experimental investigation of the electrode characteristics, with special focus on their interaction in a full cell assembly and for further utilization in advanced algorithms.

We compared different OCV determination techniques and found that despite small deviations due to different overpotentials, the OCV can be characterized with the GITT as well as pOCV measurements with small current rates ($> C/10$). In certain SOC ranges we observed a temperature dependency of the OCV. However, from our experimental results it is not clear whether this actually is due to temperature-dependent material properties or slower kinetics and increased overpotentials. We used the anode and cathode half cell voltage curves to reconstruct the full cell and to determine the correct balancing and alignment parameters with meaningful assignment of the electrode's characteristic material dependent stages and phases. For fitting in the OCV domain, an additional parameter accounting for different polarization in the full cell and the half cells had to be introduced. Using different configurations of the algorithms leads to slightly different results, which is why it is important to choose consistent measurements data, e.g., throughout the whole parameterization process of electrochemical models.

By analyzing the impedance spectra of the full cell and half cells, we gained detailed insights into the loss processes and their origins. The charge transfer resistance R_{ct} of the full cell at a low SOC seems to be dominated by the cathode, while it is dominated by the anode at a high SOC. R_{ct} is mainly responsible for the strong temperature dependency of the kinetic behavior and a good fit to the Arrhenius equation was confirmed (the activation energy lies between $54\,kJ\,mol^{-1}$ and $65\,kJ\,mol^{-1}$ for different SOCs). Between the charge transfer and the solid state diffusion, a transition process was observed which might, still inconclusively, be assigned to the anode. These results can further be used in physically motivated model development, e.g., by choosing a reasonable number of RC elements for an ECM. For the high frequent kinetic behavior, a minimum of two RC elements should be chosen for R_{ct}, which also could be subdivided into three RC elements, and $R_{transition}$. For the low frequent behavior, i.e., the solid state and electrolyte diffusion, further investigations, such as pulse relaxation measurements, should be performed.

Data availability

Raw measurement datasets related to this article can be found via [58], provided by mediaTUM.

CRediT authorship contribution statement

Leo Wildfeuer: Conceptualization, Methodology, Formal analysis, Investigation, Visualization, Data curation, Software, Validation, Writing – original draft, Writing – review & editing. **Nikolaos Wassiliadis:** Conceptualization, Methodology, Formal analysis, Investigation, Visualization, Data curation, Software, Validation, Writing – original draft, Writing – review & editing. **Alexander Karger:** Software, Writing – review & editing. **Fabian Bauer:** Resources, Writing – review & editing. **Markus Lienkamp:** Resources, Supervision, Writing – review & editing.

Declaration of competing interest

The authors declare that they have no known competing financial interests or personal relationships that could have appeared to influence the work reported in this paper.

Acknowledgments

This work is funded by the Bavarian Ministry of Economic Affairs, Regional Development and Energy under the project bawaii — battery analytics with artificial intelligence (IUK-1808-0013). The authors want to thank Fraunhofer ISC and especially Elena Fleder for supporting with the design and setup of the half cells. Furthermore, we want to acknowledge Matthias Wanzel and Philipp Gieler for their support.

Appendix. Impedance spectra and drt at 35 °C and 50 °C

See Figs. A.11 and A.12.

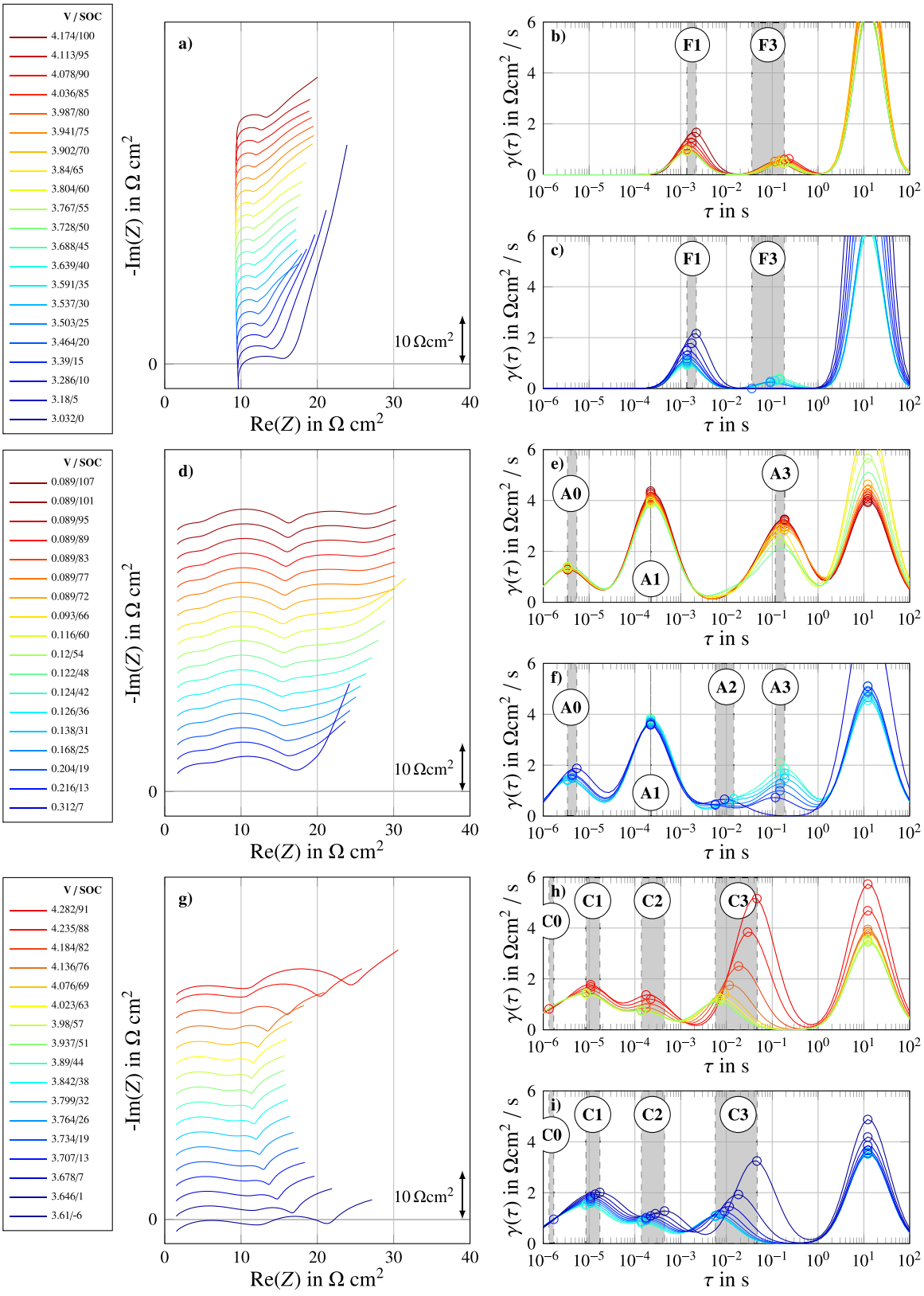

Fig. A.11. Impedance spectra from EIS measurements and corresponding DRT for different SOC at 35 °C. See Fig. 9 for detailed caption.

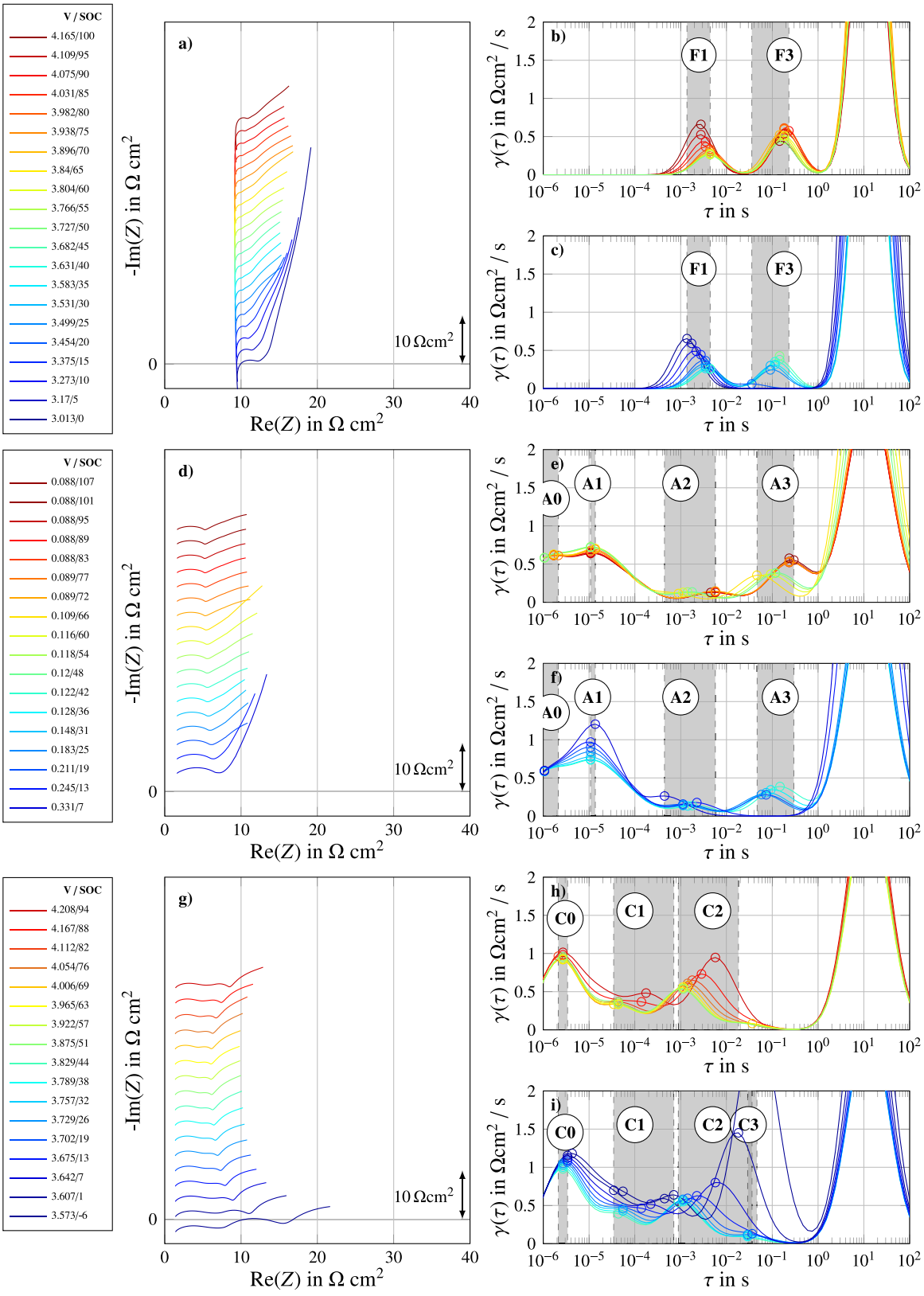

Fig. A.12. Impedance spectra from EIS measurements and corresponding DRT for different SOC at 50 °C. See Fig. 9 for detailed caption.

References

[1] A. König, L. Nicoletti, D. Schröder, S. Wolff, A. Waclaw, M. Lienkamp, An overview of parameter and cost for battery electric vehicles, World Electr. Veh. J. 12 (1) (2021) http://dx.doi.org/10.3390/wevj12010021.

[2] J. Vetter, P. Novák, M.R. Wagner, C. Veit, K.-C. Möller, J.O. Besenhard, M. Winter, M. Wohlfahrt-Mehrens, C. Vogler, A. Hammouche, Ageing mechanisms in lithium-ion batteries, J. Power Sources 147 (1–2) (2005) 269–281, http://dx.doi.org/10.1016/j.jpowsour.2005.01.006.

[3] M. Dubarry, B.Y. Liaw, M.-S. Chen, S.-S. Chyan, K.-C. Han, W.-T. Sie, S.-H. Wu, Identifying battery aging mechanisms in large format Li ion cells, J. Power Sources 196 (7) (2011) 3420–3425, http://dx.doi.org/10.1016/j.jpowsour.2010.07.029.

[4] A. Barré, B. Deguilhem, S. Grolleau, M. Gérard, F. Suard, D. Riu, A review on lithium-ion battery ageing mechanisms and estimations for automotive applications, J. Power Sources 241 (2013) 680–689, http://dx.doi.org/10.1016/j.jpowsour.2013.05.040.

[5] C.R. Birkl, M.R. Roberts, E. McTurk, P.G. Bruce, D.A. Howey, Degradation diagnostics for lithium ion cells, J. Power Sources 341 (2017) 373–386, http://dx.doi.org/10.1016/j.jpowsour.2016.12.011.

[6] M. Morita, N. Nishimura, Y. Matsuda, Charge/discharge cycling behavior of pitch-based carbon fiber in organic electrolyte solutions, Electrochim. Acta 38 (13) (1993) 1721–1726, http://dx.doi.org/10.1016/0013-4686(93)85068-A.

[7] A. Márquez, P.B. Balbuena, Molecular dynamics study of graphite/electrolyte interfaces, J. Electrochem. Soc. 148 (6) (2001) A624, http://dx.doi.org/10.1149/1.1372216.

[8] H. Yang, H.J. Bang, J. Prakash, Evaluation of Electrochemical Interface Area and lithium diffusion coefficient for a composite graphite anode, J. Electrochem. Soc. 151 (8) (2004) A1247, http://dx.doi.org/10.1149/1.1763139.

[9] H.-j. Guo, X.-h. Li, X.-m. Zhang, H.-q. Wang, Z.-x. Wang, W.-j. Peng, Diffusion coefficient of lithium in artificial graphite, mesocarbon microbeads, and disordered carbon, New Carbon Mater. 22 (1) (2007) 7–10, http://dx.doi.org/10.1016/S1872-5805(07)60006-7.

[10] M. Safari, C. Delacourt, Modeling of a commercial graphite/LiFePO4 cell, J. Electrochem. Soc. 158 (5) (2011) A562, http://dx.doi.org/10.1149/1.3567007.

[11] M. Ecker, T.K.D. Tran, P. Dechent, S. Käbitz, A. Warnecke, D.U. Sauer, Parameterization of a physico-chemical model of a lithium-ion battery, J. Electrochem. Soc. 162 (9) (2015) A1836–A1848, http://dx.doi.org/10.1149/2.0551509jes.

[12] J. Landesfeind, J. Hattendorff, A. Ehrl, W.A. Wall, H.A. Gasteiger, Tortuosity determination of battery electrodes and separators by impedance spectroscopy, J. Electrochem. Soc. 163 (7) (2016) A1373–A1387, http://dx.doi.org/10.1149/2.1141607jes.

[13] K. Pan, F. Zou, M. Canova, Y. Zhu, J.-H. Kim, Systematic electrochemical characterizations of Si and SiO anodes for high-capacity Li-Ion batteries, J. Power Sources 413 (2019) 20–28, http://dx.doi.org/10.1016/j.jpowsour.2018.12.010.

[14] D.P. Abraham, S. Kawauchi, D.W. Dees, Modeling the impedance versus voltage characteristics of LiNi0.8Co0.15Al0.05O2, Electrochim. Acta 53 (5) (2008) 2121–2129, http://dx.doi.org/10.1016/j.electacta.2007.09.018.

[15] P. Albertus, J. Christensen, J. Newman, Experiments on and modeling of positive electrodes with multiple active materials for lithium-ion batteries, J. Electrochem. Soc. 156 (7) (2009) A606, http://dx.doi.org/10.1149/1.3129656.

[16] R. Amin, D.B. Ravnsbæ k, Y.-M. Chiang, Characterization of electronic and ionic transport in Li 1-x Ni 0.8 Co 0.15 Al 0.05 o 2 (NCA), J. Electrochem. Soc. 162 (7) (2015) A1163–A1169, http://dx.doi.org/10.1149/2.0171507jes.

[17] M.A. Cabañero, N. Boaretto, M. Röder, J. Müller, J. Kallo, A. Latz, Direct determination of diffusion coefficients in commercial li-ion batteries, J. Electrochem. Soc. 165 (5) (2018) A847–A855, http://dx.doi.org/10.1149/2.0301805jes.

[18] S. Xia, F. Li, F. Chen, H. Guo, Preparation of FePO4 by liquid-phase method and modification on the surface of LiNi0.80Co0.15Al0.05O2 cathode material, J. Alloys Compd. 731 (2018) 428–436, http://dx.doi.org/10.1016/j.jallcom.2017.10.047.

[19] P. Shafiei Sabet, G. Stahl, D.U. Sauer, Non-invasive investigation of predominant processes in the impedance spectra of high energy lithium-ion batteries with Nickel-Cobalt-Aluminum cathodes, J. Power Sources (2018) http://dx.doi.org/10.1016/j.jpowsour.2018.10.024.

[20] P.S. Sabet, D.U. Sauer, Separation of predominant processes in electrochemical impedance spectra of lithium-ion batteries with nickelemanganeseecobalt cathodes, J. Power Sources 425 (2019) 121–129, http://dx.doi.org/10.1016/j.jpowsour.2019.03.068.

[21] J. Schmalstieg, C. Rahe, M. Ecker, D.U. Sauer, Full cell parameterization of a high-power lithium-ion battery for a physico-chemical model: Part I. Physical and electrochemical parameters, J. Electrochem. Soc. 165 (16) (2018) A3799–A3810, http://dx.doi.org/10.1149/2.0321816jes.

[22] Kovachev, Schröttner, Gstrein, Aiello, Hanzu, Wilkening, Foitzik, Wellm, Sinz, Ellersdorfer, Analytical dissection of an automotive li-ion pouch cell, Batteries 5 (4) (2019) 67, http://dx.doi.org/10.3390/batteries5040067.

[23] J. Marshall, D. Gastol, R. Sommerville, B. Middleton, V. Goodship, E. Kendrick, Disassembly of li ion cells—Characterization and safety considerations of a recycling scheme, Metals 10 (6) (2020) 773, http://dx.doi.org/10.3390/met10060773.

[24] Lain, Brandon, Kendrick, Design strategies for high power vs. High energy lithium ion cells, Batteries 5 (4) (2019) 64, http://dx.doi.org/10.3390/batteries5040064.

[25] Liebig, Gupta, Kirstein, Schuldt, Agert, Parameterization and validation of an electrochemical thermal model of a lithium-ion battery, Batteries 5 (3) (2019) 62, http://dx.doi.org/10.3390/batteries5030062.

[26] C.-H. Chen, F. Brosa Planella, K. O'Regan, D. Gastol, W.D. Widanage, E. Kendrick, Development of experimental techniques for parameterization of multi-scale lithium-ion battery models, J. Electrochem. Soc. 167 (8) (2020) 080534, http://dx.doi.org/10.1149/1945-7111/ab9050.

[27] A. Karger, L. Wildfeuer, A. Maheshwari, N. Wassiliadis, M. Lienkamp, Novel method for the on-line estimation of low-frequency impedance of lithium-ion batteries, J. Energy Storage 32 (August) (2020) 101818, http://dx.doi.org/10.1016/j.est.2020.101818.

[28] N. Wassiliadis, J. Schneider, A. Frank, L. Wildfeuer, X. Lin, A. Jossen, M. Lienkamp, Review of fast charging strategies for lithium-ion battery systems and their applicability for battery electric vehicles, J. Energy Storage 44 (2021) 103306, http://dx.doi.org/10.1016/j.est.2021.103306.

[29] J. Sieg, J. Bandlow, T. Mitsch, D. Dragicevic, T. Materna, B. Spier, H. Witzenhausen, M. Ecker, D.U. Sauer, Fast charging of an electric vehicle lithium-ion battery at the limit of the lithium deposition process, J. Power Sources 427 (2019) 260–270, http://dx.doi.org/10.1016/j.jpowsour.2019.04.047.

[30] A.U. Schmid, A. Ridder, M. Hahn, K. Schofer, K.P. Birke, Aging of extracted and reassembled li-ion electrode material in terms of coin cell-capabilities and limitations, Batteries 6 (2) (2020) 33, http://dx.doi.org/10.3390/batteries6020033.

[31] X.-Y. Yao, M.G. Pecht, Tab design and failures in cylindrical li-ion batteries, IEEE Access 7 (2019) 24082–24095, http://dx.doi.org/10.1109/ACCESS.2019.2899793.

[32] B. Gyenes, D.A. Stevens, V.L. Chevrier, J.R. Dahn, Understanding anomalous behavior in Coulombic efficiency measurements on li-ion batteries, J. Electrochem. Soc. 162 (3) (2015) A278–A283, http://dx.doi.org/10.1149/2.0191503jes.

[33] M. Lewerenz, G. Fuchs, L. Becker, D.U. Sauer, Irreversible calendar aging and quantification of the reversible capacity loss caused by anode overhang, J. Energy Storage 18 (2018) 149–159, http://dx.doi.org/10.1016/j.est.2018.04.029.

[34] A. Barai, K. Uddin, M. Dubarry, L. Somerville, A. McGordon, P. Jennings, I. Bloom, A comparison of methodologies for the non-invasive characterisation of commercial Li-ion cells, Prog. Energy Combust. Sci. 72 (2019) 1–31, http://dx.doi.org/10.1016/j.pecs.2019.01.001.

[35] T. Ohzuku, Y. Iwakoshi, K. Sawai, Formation of lithium-graphite intercalation compounds in nonaqueous electrolytes and their application as a negative electrode for a lithium ion (shuttlecock) cell, J. Electrochem. Soc. 140 (9) (1993) 2490–2498, http://dx.doi.org/10.1149/1.2220849.

[36] I. Zilberman, S. Ludwig, A. Jossen, Cell-to-cell variation of calendar aging and reversible self-discharge in 18650 nickel-rich, silicon–graphite lithium-ion cells, J. Energy Storage 26 (August) (2019) 100900, http://dx.doi.org/10.1016/j.est.2019.100900.

[37] K.J. Park, J.Y. Hwang, H.H. Ryu, F. Maglia, S.J. Kim, P. Lamp, C.S. Yoon, Y.K. Sun, Degradation mechanism of Ni-enriched NCA cathode for lithium batteries: Are microcracks really critical? ACS Energy Lett. 4 (6) (2019) 1394–1400, http://dx.doi.org/10.1021/acsenergylett.9b00733.

[38] A. Farmann, D.U. Sauer, A study on the dependency of the open-circuit voltage on temperature and actual aging state of lithium-ion batteries, 2017, http://dx.doi.org/10.1016/j.jpowsour.2017.01.098.

[39] M. Baumann, L. Wildfeuer, S. Rohr, M. Lienkamp, Parameter variations within Li-Ion battery packs – Theoretical investigations and experimental quantification, J. Energy Storage 18 (2018) http://dx.doi.org/10.1016/j.est.2018.04.031.

[40] K. Rumpf, M. Naumann, A. Jossen, Experimental investigation of parametric cell-to-cell variation and correlation based on 1100 commercial lithium-ion cells, J. Energy Storage 14 (2017) 224–243, http://dx.doi.org/10.1016/j.est.2017.09.010.

[41] L. Wildfeuer, M. Lienkamp, Quantifiability of inherent cell-to-cell variations of commercial lithium-ion batteries, ETransportation 9 (2021) 100129, http://dx.doi.org/10.1016/j.etran.2021.100129.

[42] A.U. Schmid, M. Kurka, K.P. Birke, Reproducibility of Li-ion cell reassembling processes and their influence on coin cell aging, J. Energy Storage 24 (2019) 100732, http://dx.doi.org/10.1016/j.est.2019.04.006.

[43] M. Dubarry, V. Svoboda, R. Hwu, B.Y. Liaw, Incremental capacity analysis and close-to-equilibrium OCV measurements to quantify capacity fade in commercial rechargeable lithium batteries, Electrochem. Solid-State Lett. 9 (10) (2006) http://dx.doi.org/10.1149/1.2221767.

[44] S. Schindler, M.A. Danzer, A novel mechanistic modeling framework for analysis of electrode balancing and degradation modes in commercial lithium-ion cells, J. Power Sources 343 (2017) 226–236, http://dx.doi.org/10.1016/j.jpowsour.2017.01.026.

[45] J. Schmitt, M. Schindler, A. Jossen, Change in the half-cell open-circuit potential curves of silicon–graphite and nickel-rich lithium nickel manganese cobalt oxide during cycle aging, J. Power Sources 506 (June) (2021) 230240, http://dx.doi.org/10.1016/j.jpowsour.2021.230240.

[46] J.P. Schmidt, P. Berg, M. Schönleber, A. Weber, E. Ivers-Tiffée, The distribution of relaxation times as basis for generalized time-domain models for Li-ion batteries, J. Power Sources 221 (2013) 70–77, http://dx.doi.org/10.1016/j.jpowsour.2012.07.100.

[47] J. Illig, M. Ender, T. Chrobak, J.P. Schmidt, D. Klotz, E. Ivers-Tiffée, Separation of charge transfer and contact resistance in LiFePO4-cathodes by impedance modeling, J. Electrochem. Soc. 159 (7) (2012) A952–A960.

[48] S. Gantenbein, M. Weiss, E. Ivers-Tiffée, Impedance based time-domain modeling of lithium-ion batteries: Part I, J. Power Sources 379 (2018) 317–327, http://dx.doi.org/10.1016/j.jpowsour.2018.01.043.

[49] E. Goldammer, J. Kowal, Determination of the distribution of relaxation times by means of pulse evaluation for offline and online diagnosis of lithium-ion batteries, Batteries 7 (2021) 36, http://dx.doi.org/10.3390/batteries7020036.

[50] L. Wildfeuer, P. Gieler, A. Karger, Combining the distribution of relaxation times from EIS and time-domain data for parameterizing equivalent circuit models of lithium-ion batteries, Batteries (2021) 1–23.

[51] D. Klotz, Characterization and modeling of electrochemical energy conversion systems by impedance techniques, (Ph.D. thesis), 2012.

[52] T.H. Wan, M. Saccoccio, C. Chen, F. Ciucci, Influence of the discretization methods on the distribution of relaxation times deconvolution: Implementing radial basis functions with DRTtools, Electrochim. Acta 184 (2015) 483–499, http://dx.doi.org/10.1016/j.electacta.2015.09.097.

[53] A. Mertens, I.C. Vinke, H. Tempel, H. Kungl, L.G.J. de Haart, R.-A. Eichel, J. Granwehr, Quantitative analysis of time-domain supported electrochemical impedance spectroscopy data of li-ion batteries: Reliable activation energy determination at low frequencies, J. Electrochem. Soc. 163 (7) (2016) H521–H527, http://dx.doi.org/10.1149/2.0511607jes.

[54] S. Gantenbein, M. Weiss, E. Ivers-Tiffée, Impedance based time-domain modeling of lithium-ion batteries: Part I, J. Power Sources 379 (January) (2018) 317–327, http://dx.doi.org/10.1016/j.jpowsour.2018.01.043.

[55] L. Wildfeuer, N. Wassiliadis, C. Reiter, M. Baumann, M. Lienkamp, Experimental characterization of li-ion battery resistance at the cell, module and pack level, in: 2019 Fourteenth International Conference on Ecological Vehicles and Renewable Energies (EVER), IEEE, 2019, pp. 1–12.

[56] J.P. Schmidt, Verfahren zur charakterisierung und modellierung von lithium-ionen zellen, (Ph.D. thesis), KIT Scientific Publishing, 2013.

[57] F.E. Hust, Physico-chemically motivated parameterization and modelling of real-time capable lithium-ion battery models : a case study on the Tesla Model S battery, (Ph.D. thesis), in: Aachener Beiträge des ISEA, 120, ISEA, 2018, pp. 1 Online–Ressource (vii, 203 Seiten) : Illustrationen, Diagramme, http://dx.doi.org/10.18154/RWTH-2019-00249.

[58] L. Wildfeuer, N. Wassiliadis, A. Karger, F. Bauer, M. Lienkamp, Teardown analysis and characterization of a commercial lithium-ion battery for advanced algorithms in battery electric vehicles, Technical University of Munich, URL https://mediatum.ub.tum.de/1639153, http://dx.doi.org/10.14459/2022mp1639153.

2.2 Methods for Resistance Parameterization in ECMs

2.2.1 Experimental Determination of Resistance Parameters

To accelerate the development cycle of BEVs, electric models are utilized in many stages of the development process and ECMs are the right approach for a variety of tasks. Study I demonstrated that assigning full-cell processes to individual electrodes enables the definition of a model order that reflects kinetic loss processes. Building on this, Study II introduces a new method to identify physically meaningful resistance parameters over a wide frequency range, addressing research question 2a). Figure 2.4 gives an overview of the performed measurements, the proposed algorithm, and brings this section into context with the previous and following section.

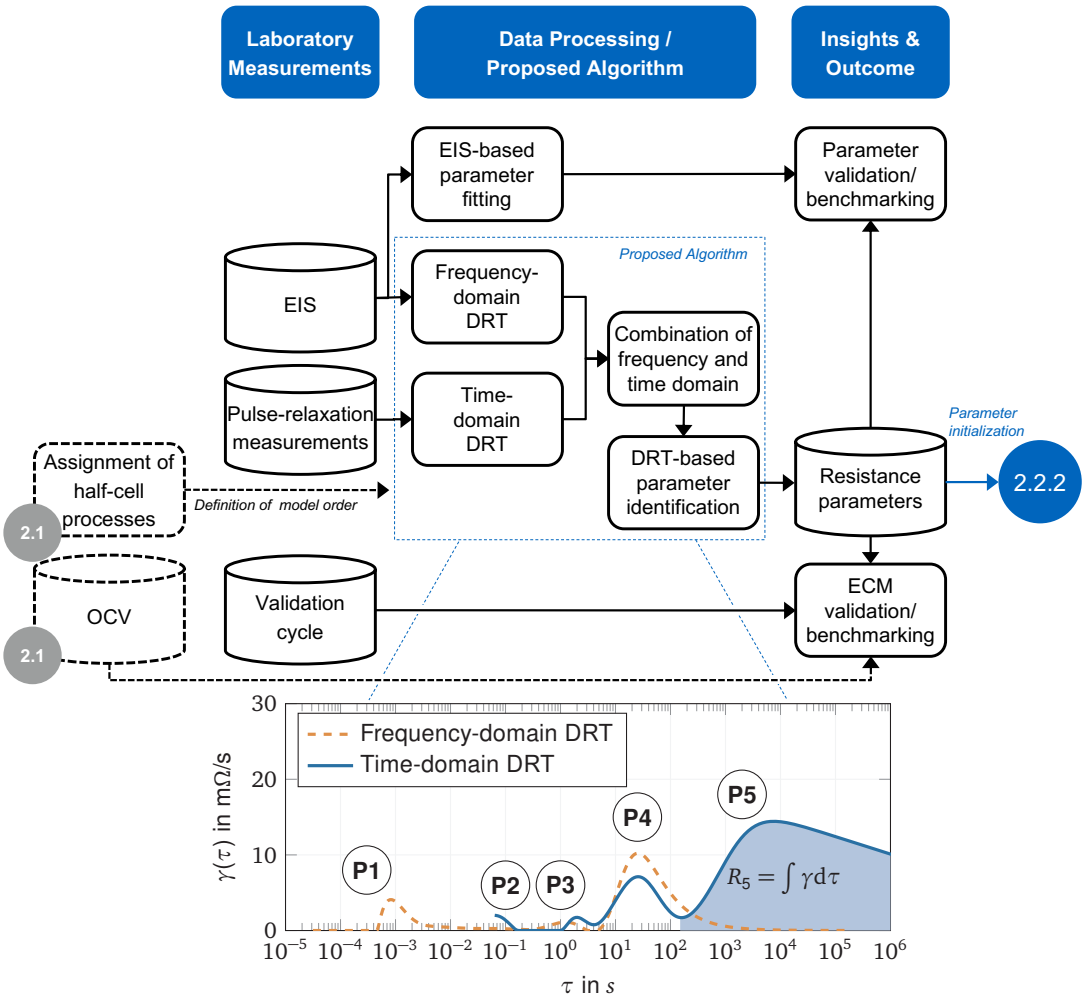

Figure 2.4: Graphical summary of Study II [2].

The publication describes theory and model equations to calculate the DRT from frequency-domain and time-domain measurements in detail. The goal of the DRT is to visualize the distribution of total resistance across the continuous space of relaxation times. Hence, it can give useful insights into kinetic loss processes since it contains the full information of the cell's resistance in the observed frequency range. Existing studies, however, mainly used the DRT to gain a-priori knowledge for a conventional fitting algorithm either in the frequency or time domain.

A purely analytical method is proposed to determine the parameters of RC elements directly from the DRT. This approach promotes physically meaningful RC parameters and removes the need for iterative and time-consuming tuning of starting values and boundary conditions. The time constants τ_n of RC elements are determined at the DRT's local maxima and the resistances R_n are determined by integrating between adjacent minima. In an engineering context, the number of RC elements is often determined by factors such as available computing resources, rather than the actual number of kinetic loss processes present. The proposed method takes this into account by systematically combining RC elements while maintaining physical interpretability. The parameters obtained with this method were validated against impedance spectra and parameters obtained from a conventional fitting on impedance spectra.

EIS alone does not provide sufficient insights into low-frequency behavior. Therefore, pulse-relaxation measurements were additionally conducted across the full SOC range. The goal of pulse-relaxation measurements is to capture the low-frequency behavior during a long relaxation phase (60 h in this case) after exciting the cell with a current pulse (10 s in this case). To avoid distortion of this sensible measurement, relaxation before the procedure is crucial which is why the cells were at rest for three weeks after being brought to their respective SOC. Pulse-relaxation measurements were used to complement the DRT derived from EIS, whereby three different fusing methods were presented and compared:

- **Separate DRT:** EIS and pulse-relaxation measurements are processed independently and resulting RC parameters are allocated to prescribed RC elements.
- **Interconnected DRT:** The parameters obtained from frequency-domain DRT are used to subtract the high-frequent overpotentials from the pulse-relaxation measurements. Time-domain DRT calculation on the remaining voltage response yields the missing low-frequency RC parameters.
- **Combined DRT:** Frequency-domain DRT and time-domain DRT are calculated simultaneously by a merged system of equations.

The proposed methods were validated against a defined validation cycle consisting of CCCV charging and discharging, resting periods, dynamic pulses, and a real driving profile. All three methods to combine EIS and pulse-relaxation measurements reached a comparable RMSE of 42-45 mV, which is ≈40 % lower compared to conventional fitting of impedance spectra (73 mV).

Contribution

Leo Wildfeuer is the first author of the article.

Leo Wildfeuer: Conceptualization, Methodology, Software, Validation, Formal analysis, Investigation, Writing—original draft, Writing—review & editing, Visualization, Supervision, Project administration, Funding acquisition. Philipp Gieler: Methodology, Software, Validation, Formal analysis, Investigation, Writing—original draft, Visualization. Alexander Karger: Software, Validation, Writing—original draft, Writing—review & editing.

Combining the Distribution of Relaxation Times from EIS and Time-Domain Data for Parameterizing Equivalent Circuit Models of Lithium-Ion Batteries

Leo Wildfeuer, Philipp Gieler, Alexander Karger

Batteries, Volume 7 (3), no. 52, 2021
Digital Object Identifier: 10.3390/batteries7030052
Permanent Weblink: https://doi.org/10.3390/batteries7030052

batteries

MDPI

Article

Combining the Distribution of Relaxation Times from EIS and Time-Domain Data for Parameterizing Equivalent Circuit Models of Lithium-Ion Batteries

Leo Wildfeuer [1,2,*], Philipp Gieler [1] and Alexander Karger [1,2]

[1] Institute of Automotive Technology, Technical University of Munich, 80333 Munich, Germany; p.gieler@gmx.de (P.G.); alexander.karger@tum.de (A.K.)
[2] TWAICE Technologies GmbH, 80807 Munich, Germany
* Correspondence: leo.wildfeuer@tum.de; Tel.: +49-89-289-10339

Abstract: Equivalent circuit models (ECMs) are a widely used modeling approach for lithium-ion batteries in engineering applications. The RC elements, which display the dynamic loss processes of the cell, are usually parameterized by fitting the ECM to experimental data in either the time-domain or the frequency-domain. However, both types of data have limitations with regard to the observable time constants of electrochemical processes. This work proposes a method to combine time-domain and frequency-domain measurement data for parameterization of RC elements by exploiting the full potential of the distribution of relaxation times (DRT). Instead of using only partial information from the DRT to supplement a conventional fitting algorithm, we determine the parameters of an arbitrary number of RC elements directly from the DRT. The difficulties of automated deconvolution of the DRT, including regularization and the choice of an optimal regularization factor, is tackled by using the L-curve criterion for optimized calculation of the DRT via Tikhonov regularization. Three different approaches to merge time- and frequency-domain data are presented, including a novel approach where the DRT is simultaneously calculated from electrochemical impedance spectoscropy (EIS) and pulse relaxation measurements. The parameterized model for a commercial 18650 NCA cell was validated during a validation cycle consisting of constant current and real-world automotive cycling and yields a relative improvement of over 40 % compared to a conventional EIS-fitting algorithm.

Keywords: lithium-ion batteries; equivalent circuit model; electrochemical impedance spectroscopy; distribution of relaxation times; Tikhonov regularization

Citation: Wildfeuer, L.; Gieler, P.; Karger, A. Combining the Distribution of Relaxation Times from EIS and Time-Domain Data for Parameterizing Equivalent Circuit Models of Lithium-Ion Batteries. *Batteries* **2021**, *7*, 52. https://doi.org/10.3390/batteries7030052

Academic Editor: Carlos Ziebert

Received: 11 June 2021
Accepted: 19 July 2021
Published: 2 August 2021

1. Introduction

1.1. Motivation

In recent years, lithium-ion batteries (LIBs) have become ubiquitous in many applications. Their advantages in terms of power and energy density over other storage mediums make them the most promising candidate for electric mobility and stationary energy storage. To optimize the operation of lithium-ion batteries, the estimation of battery states such as the state of charge (SOC), state of health (SOH), and state of available power (SOAP) is required.

To estimate the different states of lithium-ion batteries, battery management systems (BMSs) typically employ battery models, which are parameterized in order to best reproduce the electrochemical behavior of the battery. The battery states are then either estimated directly from model parameters, such as from the impedance parameters for the SOAP, or by comparing the measured voltage and model voltage to estimate the SOC and SOH with subsequent algorithms, such as a Kalman filter [1].

To keep the computational effort low to ensure real-time capability and to ensure convergence of estimation algorithms, the complexity of such models and algorithms has

to be limited. A widespread type of model used for this purpose is the equivalent circuit model (ECM), the complexity of which can easily be adjusted by the number of its circuit elements and the parameterization of which does not require destructive analysis of the cell's geometry and material properties. The idea behind ECMs is to model the lithium-ion battery (LIB) with standard circuit elements such as an ideal voltage source modeling the open-circuit behavior, and resistors and capacitors, modeling the kinetics of the LIB. The key challenge lies in parameterization of these circuit elements to ensure high accuracy of BMS algorithms. Thereby, the characterization of the kinetics especially, expressed by the lithium-ion batteries impedance, is of great importance, since a limited set of parameters must cover a broad range of different dynamics in the load profile.

Furthermore, lithium-ion batteries degrade over their lifetime, which, besides capacity fade, also leads to an increase of the impedance [2]. However, the aging trajectory of an individual LIB is highly dependent on the operating conditions such as temperature, voltage window, and current [3,4]. This demands on-line algorithms, which are able to continuously track the battery impedance parameters to keep the ECM up to date [5]. The accuracy of such on-line optimization algorithms often depends on suitable initial values [6]. Hence, accurate estimation of impedance parameters under laboratory conditions, before deployment of the LIB, is needed.

1.2. State of the Art

Many different approaches for estimating the parameters of the circuit elements in ECMs can be found in the literature [7–9]. There are two types of measurements which are usually employed for impedance characterization of LIB: electrochemical impedance spectroscopy (EIS) in the frequency-domain and measurements in the time-domain, e.g., current pulses. The most crucial difference between both methods is the frequency range of electrochemical processes that can be reliably investigated with them. EIS, on the one hand, is very reliable in the high-frequency region up to a few MHz [10]. However, due to the long charging and discharging phases in the sinusoidal excitation at low frequencies, significant SOC-changes occur, which at some point violate the prerequisite of a linear, time-invariant and causal system [11]. This limits EIS to frequencies above approximately 1 mHz [12]. Time-domain measurements (TDMs), on the other hand, are better suited to investigate the low-frequency behavior, while being limited by the sampling rate and measurement accuracy in the high-frequency region [6].

The impedance spectrum of lithium-ion batteries is usually presented in a Nyquist plot, where, to some extent, the loss processes of the measured system can be made visible. However, the time constants of the different electrochemical processes are often close to each other and cannot be fully separated in the Nyquist plot [13,14]. To isolate the individual processes, the distribution of relaxation times (DRT) of an impedance spectrum can be evaluated, since it provides a higher frequency resolution of the dynamic processes. It shows the distribution of the total polarization resistance in the continuous space of relaxation times. The DRT can be used to identify and separate dynamic processes and to investigate how those processes are affected by operating conditions like temperature or battery states such as SOC and SOH [7,13,15–18].

A combination use of EIS and TDM is advisable if the electrochemical behavior of a cell is to be investigated in a wide frequency range. For this, the useful insights into the cell's loss processes provided by the DRT can be used during the parameterization process. Previous efforts, combining both measurement methods with varying extent, are summarized in the following.

Illig et al. [13] used EIS measurements for their ECM parameterization. They first modeled the low-frequency behavior, as well as the purely capacitive behavior, with a capacitance and a Warburg-element, the overvoltage of which they then subtracted from the measurement data. From the remaining impedance spectrum they calculateed the DRT and used it to identify the occurring processes and to determine the starting values of

the following fitting algorithm. The model was completed by fitting a series of three RC elements, an ohmic resistance and an inductance to the preprocessed impedance spectrum.

Gantenbein et al. [7] have introduced a physically motivated ECM consisting of an ohmic resistance, two RC elements, one Warburg element, an inductance, and a capacitance in series. These circuit elements model the ohmic and contact loss, interface loss of the anode, interface loss of the cathode and diffusion loss and capacitive behavior, which they have identified by investigating the DRT of the full cell and its indivual electrodes. The high and medium frequency parts of the model were parameterized by conventional EIS-fitting of the resistance and the RC elements. Diffusion and capacitive behavior were then included in the model by a time-domain fitting of the remaining model parameters.

Withenhausen directly determined certain RC parameters from the DRT [12]. He covered some RC elements by frequency-domain measurements; therefore he used an iterative algorithm, in which several single process peaks were fitted to the DRT. The remaining elements were parameterized by a time-domain fit to the measured voltage relaxation after bringing the cell to a defined SOC.

Schmidt et al. [14] identified ECM parameters purely from the DRT. They used EIS measurements and Fourier-transformed time-domain measurements, which were merged into one impedance spectrum. From this spectrum the DRT was calculated. Together with an added ohmic resistance, the discrete DRT then served directly as an ECM, which led to the relaxation times of its RC elements being evenly spaced on a logarithmic scale like the data points of the DRT. They evaluated the impact of the chosen model order on their parameterization procedure by comparing model configurations with 100, 20, 10, and 4 RC elements. Due to the a priori fixed time constants without physical meaning they needed a comparatively high number of RC elements to obtain an adequate model accuracy.

It can be concluded that in the previous literature, the DRT is often only used to gain a priori knowledge on the investigated cell to enhance conventional fitting algorithms, e.g., by a non-linear least squares algorithm, in either the frequency-domain or time-domain. Such fitting algorithms have the disadvantage that they are highly dependent on boundary conditions and initial starting values, which leads to a time-consuming and iterative parameterization process. The DRT, however, contains the full information of the cell's impedance, which is why we propose an approach to determine RC parameters directly from the DRT.

1.3. Contributions

This work aims to exploit the potential of the DRT during an automated identification of RC parameters of an ECM. The main contributions of our proposed method can be summarized as follows:

- Evaluation of frequency- and time-domain measurements:
  To capture the full dynamic behavior of a cell, both EIS and TDM measurements have been considered in the ECM parameterization process and their DRT computed. Respective measurements in the frequency-domain as well as in the time-domain were performed (Section 2).
- Optimized calculation of the DRT via Tikhonov regularization:
  Since an accurate DRT is essential for the proposed parameterization process, the L-curve criterion was employed to optimize the calculation of the DRT via Tikhonov regularization. Moreover, the impact of different regularization terms on the calculated DRT was investigated (Section 3).
- Process for direct parameterization of RC elements from the DRT:
  Instead of using only partial information from the DRT to supplement a conventional fitting algorithm, the full potential of the DRT was exploited by a parameterization process which determines RC parameters directly from the DRT (Section 4).
- Analysis of various data merging approaches:
  Different methods of combining EIS and TDM data in the parameterization process are presented in this work. One of those methods includes a new way of calculating

the DRT using TDM and EIS simultaneously, uniting the steps of DRT calculation and merging frequency- and time-domain data (Section 5).

A conclusion is given in Section 6.

2. Experimental

In this work, all experiments were performed with a commercial 18,650 cell of type US18650VTC5A by Sony/Murata with a nominal capacity of $C_N = 2.5\,\mathrm{A\,h}$. The anode active material consists of graphite with a small share of silicon, while the cathode active material is nickel cobalt aluminium oxide (NCA) [19]. All measurements were performed at 20 °C inside a Memmert IPP 110 climate chamber.

2.1. EIS

To capture the high-frequency behavior of the cell, EIS measurements were performed in a frequency range from 5 kHz to 10 mHz with 10 points per decade. Starting at a fully charged state, impedance spectra were recorded in 10% SOC steps with a relaxation period of 3 h after discharging to the respective SOC. EIS measurements were carried out using a Gamry Interface 5000 test device applying a hybrid EIS mode. This modified form of galvanostatic EIS continuously adjusts the current such that the desired potential of 10 mV is maintained. In this way, a linear operation range is ensured.

2.2. Time-Domain Measurements (TDMs)

To determine the low-frequency behavior of the cell we performed TDMs. In particular, we applied pulse-relaxation measurements with a discharge pulse current of $I_p = -1\,\mathrm{C}$, a pulse duration of $T_p = 10\,\mathrm{s}$, and a relaxation period of $T_{relax} = 60\,\mathrm{h}$. To match the EIS, pulse-relaxation measurements were also performed at 11 SOC steps between 100% SOC and 0% SOC. Results are shown in Figure 1.

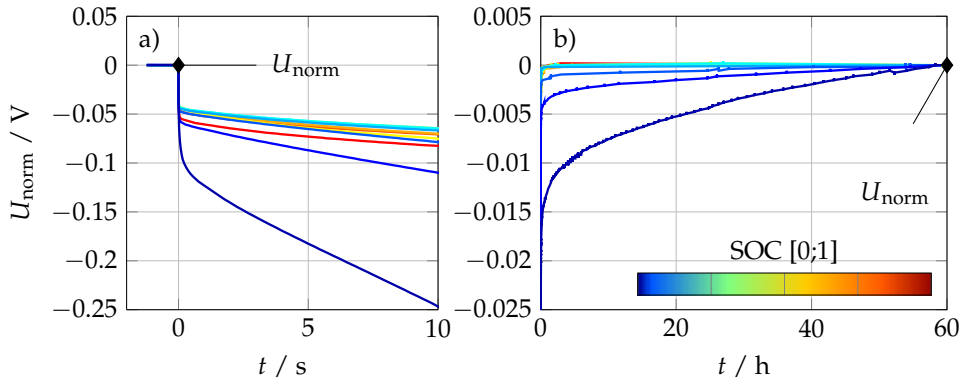

Figure 1. Results of time-domain measurements for all SOC steps between 100% SOC and 0% SOC. (**a**) −1 C discharge pulse for 10 s. The voltage is normalized on the starting voltage for every SOC. (**b**) Relaxation period of $T_{relax} = 60\,\mathrm{h}$. The voltage is normalized on the last data point of the relaxation period for every SOC. Note that the voltage was not totally relaxed after 60 h for low SOCs.

After bringing a cell to its respective SOC, it is crucial to ensure a fully relaxed state before applying the current pulse. Otherwise, the voltage measurement of the relaxation phase is superimposed by a second relaxation, resulting from the previous SOC change. If this second relaxation results from a previous discharge, it can lead to an overestimated duration of the relaxation process. If this second relaxation results from a previous charge, it can lead to an underestimated duration of the relaxation process or even voltage relaxation in the opposite direction.

Previous researchers observed this behavior and assumed it to be originating from a self-discharge process [20,21]. To isolate the pulse-relaxation behavior, they proposed a preprocessing procedure to remove the self-discharge voltage from the relaxation voltage.

We observed that, for the investigated cell, at some SOC relaxation processes were still visible even after two weeks after bringing the cell to its respective SOC. After 3 weeks, however, a constant voltage (within the voltage resolution of the measurement equipment) for longer than T_{relax} was observed at every tested SOC and pulse measurements could be performed.

In order to reduce the measurement time, a separate pristine cell from the same production batch was used for the pulse-relaxation measurements for each tested SOC step. For all time-domain measurements, the cell test system by the BaSyTec GmbH was used, which records the cell voltage with a resolution of 0.3 mV and an accuracy of 1 mV. The first half hour of the measurement was sampled with the maximum sample rate of 0.02 s. In the further course of the measurement, we reduced the sampling rate to limit the amount of data. The raw measurement data were then logarithmically subsampled to further reduce the number of data points and hence lower computational effort and time, as proposed by Schmidt [20].

2.3. Open-Circuit Voltage

Besides the dynamic behavior of the cell over a broad frequency range, the cell's static behavior at thermodynamic equilibrium needs to be characterized to supplement the ECM. This is typically done by the measurement of a pseudo open-circuit voltage (pOCV) with a low current rate or with a galvanostatic intermittent titration technique (GITT), where the open-circuit voltage is measured after bringing the cell to a respective SOC. In Figure 2, the pOCV curve with C/50 is compared to the measured voltage after 3 weeks of relaxation before the pulse-relaxation measurement was performed. Additionally, the differential voltage was analyzed.

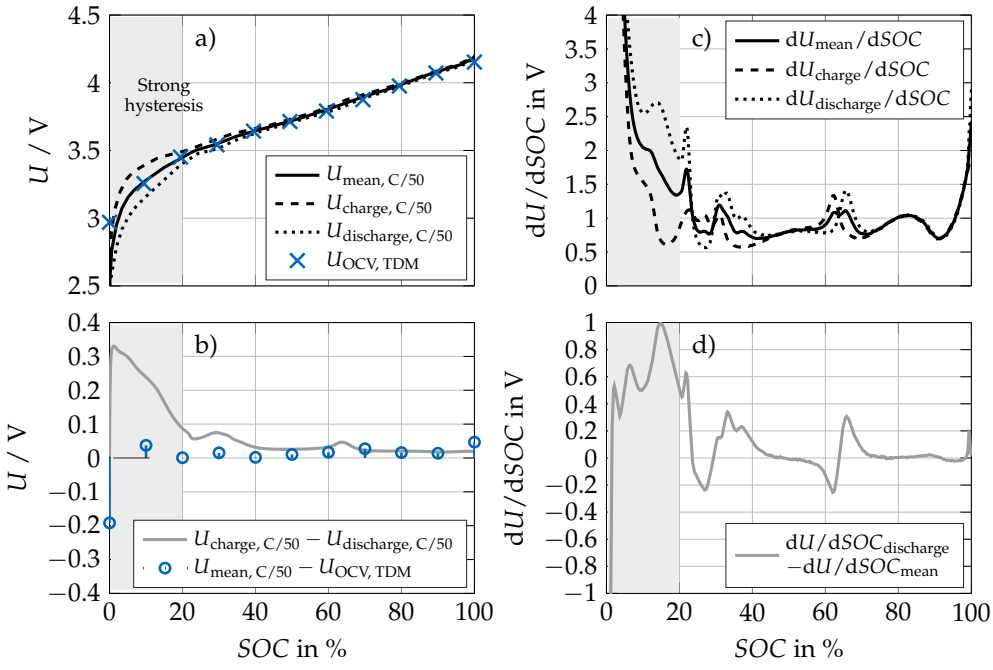

Figure 2. (**a**) Measured pseudo-OCV curve during discharging and subsequent charging with C/50 at 20 °C and the corresponding mean curve. Additionally, the relaxed voltage $U_{\mathrm{OCV,\,TDM}}$, which was measured right before the discharge pulse I_{P} after three weeks of relaxation, are plotted. (**b**) Difference between the charge and discharge pseudo-OCV and difference between mean pseudo-OCV and $U_{\mathrm{OCV,\,TDM}}$ (**c**) Differential voltage of the pseudo-OCV curves. (**d**) Difference between the differential voltage of the discharge and the mean pseudo-OCV curve.

It can be seen that the values for $U_{\mathrm{OCV,\,TDM}}$ match well with $U_{\mathrm{mean,\,C/50}}$ for some SOCs. For other SOCs, especially for which the differential voltage analysis (DVA) reveals a greater slope in the voltage curve and also the difference between $dU/dQ_{\mathrm{discharge}}$ and dU/dQ_{mean} increases, $U_{\mathrm{OCV,\,TDM}}$ shows smaller values compared to $U_{\mathrm{mean,\,C/50}}$ (except for 0% SOC, which is mainly due to the measurement procedure of the pOCV). In our study, we validated both OCV determination methods and ultimately chose $U_{\mathrm{OCV,\,TDM}}$, since it is consistent with the pulse-relaxation measurements for the dynamic behavior.

As discussed in [6], the strong divergence between charging and discharging curves in the low SOC area, which is assumed to be caused by the (de-)lithiation competition of graphite and silicon [22], will have a major impact on the validation results, if an averaged pOCV curve or the values for $U_{\mathrm{OCV,\,TDM}}$ are chosen to parameterize the OCV of the ECM. This has to be kept in mind when analyzing the validation results of different configurations of the proposed DRT-fitting (Section 5) and attributing high residuals to either the cell's thermodynamic or kinetic behavior.

3. Calculation of the DRT

3.1. DRT Calculated from EIS (EIS-DRT)

The DRT is based on the assumption that the impedance of a capacitive electrochemical system can be represented by an infinite number of RC elements with continuous relaxation times [14,23,24]. Based on this assumption, the impedance spectrum of a capacitive electrochemical system can be represented by

$$Z_{\mathrm{DRT}}(f) = \int_{-\infty}^{\infty} \frac{\gamma(\ln\tau)}{1 + j2\pi f\tau}\,\mathrm{d}\ln\tau. \tag{1}$$

$\gamma(\ln\tau)$ can be understood as the distribution of the total polarization resistance along the logarithmic scale of continuous relaxation times τ. Therefore, its integral over the entire space of relaxation times is

$$\int_{-\infty}^{\infty} \gamma(\ln\tau)\,\mathrm{d}\ln\tau = R_{\mathrm{Pol}}, \tag{2}$$

To obtain the DRT from EIS, the difference between $Z_{\mathrm{DRT}}(f)$ and the experimental data $Z_{\mathrm{exp}}(f)$ must be minimized by optimization of $\gamma(\ln\tau)$. Using matrix notation and a discretized DRT, the optimization goal can be expressed as

$$\min_{R_0,\boldsymbol{R}} \left\| \begin{bmatrix} \sqrt{w'}\boldsymbol{A}'_{\mathrm{EIS}} & \sqrt{w'}\mathbf{1} \\ \sqrt{w''}\boldsymbol{A}''_{\mathrm{EIS}} & \mathbf{0} \end{bmatrix} \begin{bmatrix} \boldsymbol{R} \\ R_0 \end{bmatrix} - \begin{bmatrix} \sqrt{w'}\boldsymbol{Z}'_{\mathrm{exp}} \\ \sqrt{w''}\boldsymbol{Z}''_{\mathrm{exp}} \end{bmatrix} \right\|_2^2 \tag{3}$$

or short

$$\min_{\boldsymbol{x}} \| \boldsymbol{B}_{\mathrm{EIS}} \quad \boldsymbol{x} - \quad \boldsymbol{Z}_{\mathrm{exp}} \|_2^2. \tag{4}$$

$\boldsymbol{R}$ is a column vector of the resistances $R_n = \gamma_n \Delta\tau_{\log}$. Since a negative resistance is physically impossible, the additional constraint $x_n \geq 0\ \forall n$ has to be considered in the problem.

The real part $\boldsymbol{Z}'$ and the imaginary part $\boldsymbol{Z}''$ of the impedance can be taken into account with different weights w' and w'' [25]. Due to the Kramers–Kronig relation [26] either one of the two would be adequate for DRT calculation [12,24,27]. However, using both can help to compensate measurement noise. Within this work, both w' and w'' are set to 0.5 for an equal weighting. The derivation of Equation (3) as well as the matrices $\boldsymbol{A}'_{\mathrm{EIS}}$ and $\boldsymbol{A}''_{\mathrm{EIS}}$ can be found in Appendix A. The DRT calculated from EIS is referred to as EIS-DRT further on in this paper.

3.2. DRT Calculated from Time-Domain Measurements (TDM-DRT)

Schmidt [20,21] proposes an approach which uses TDM to calculate the DRT. The measurements he uses are conducted in the form of current pulses. To a pulse of magnitude I_p applied at t_0 for a duration of T_p, a single RC element yields a voltage response of

$$u_n(t) = R_n I_\mathrm{p}[\sigma(t-t_0)(1-\exp{(-\frac{t-t_0}{\tau_n})}) - \sigma(t-(t_0+T_\mathrm{p}))(1-\exp{(-\frac{t-(t_0+T_\mathrm{p})}{\tau_n})})], \tag{5}$$

with $\sigma(x)$ being the Heaviside step function. Applying an infinite number of RC elements, i.e., the DRT, yields

$$u_\mathrm{DRT}(t) = \int_{-\infty}^{\infty} \gamma(\ln\tau) I_\mathrm{p}[\sigma(t-t_0)(1-\exp{(-\frac{t-t_0}{\tau})}) - \sigma(t-(t_0+T_\mathrm{p}))(1-\exp{(-\frac{t-(t_0+T_\mathrm{p})}{\tau})})]\,\mathrm{d}\ln\tau. \tag{6}$$

Analogous to the EIS-DRT, the difference between $u_\mathrm{DRT}(t)$ and the experimental data $u_\mathrm{exp}(t)$ must be minimized by optimization of $\gamma(\ln\tau)$. Evaluating the relaxation phase of the pulse measurement, the matrix equation

$$\min_{U_\mathrm{OCV},\boldsymbol{R}} \left\| \begin{bmatrix} \boldsymbol{A}_\mathrm{TDM} & \mathbf{1} \end{bmatrix} \begin{bmatrix} \boldsymbol{R} \\ U_\mathrm{OCV} \end{bmatrix} - \boldsymbol{u}_\mathrm{exp} \right\|_2^2 \tag{7}$$

or short

$$\min_{\boldsymbol{x}} \| \boldsymbol{B}_\mathrm{TDM} \quad \boldsymbol{x} - \boldsymbol{u}_\mathrm{exp} \|_2^2, \tag{8}$$

can be formed. Again the equation must be minimized while obeying the non-negative constraint $x_n \geq 0\ \forall n$. As in Equation (3), $\boldsymbol{R}$ is a column vector of the resistances $R_n = \gamma_n \Delta\tau_\mathrm{log}$. The derivation of Equation (7) and the matrix $\boldsymbol{A}_\mathrm{TDM}$ can be found in Appendix B. The DRT calculated from time-domain data is henceforth referred to as TDM-DRT.

3.3. Tikhonov Regularization

Since the experimental data $\boldsymbol{Z}_\mathrm{exp}$ and $\boldsymbol{u}_\mathrm{exp}$ are subject to measurement noise and the number of unknowns does not necessarily fit the number of equations, there is no unique solution to the system of linear equations $\boldsymbol{Bx} = \boldsymbol{D}_\mathrm{exp}$, which makes Equation (3) and Equation (7) ill-posed problems [20,25]. Hence, a mathematical tool for stabilizing the problem and generating a unique solution is required. For this purpose we employ Tikhonov regularization [28]. By adding a regularization term, an additional condition is introduced to the minimization problem, which stabilizes the solution:

$$\min_{\boldsymbol{x}} \left(\|\boldsymbol{Bx} - \boldsymbol{D}_\mathrm{exp}\|_2^2 + \lambda \|\boldsymbol{Lx}\|_2^2 \right). \tag{9}$$

The regularization factor λ determines how strong the influence of the regularization term is on the solution. The value of λ has to be chosen carefully to achieve accurate results. The matrix $\boldsymbol{L}$ of the regularization term is arbitrary in theory. However, choosing $\boldsymbol{L}$ in a meaningful way allows to penalize specific features of the solution:

- The standard form of the Tikhonov regularization is the regularization with a squared norm of the solution itself. Hence, it penalizes high magnitudes of the solution and therefore favors solutions with smaller peaks. $\boldsymbol{L}$ has to be set to be the identity matrix $\boldsymbol{I}$ such that $\boldsymbol{Lx} = \boldsymbol{x}$ [29].

- The regularization with the squared norm of the solution's first derivative penalizes high gradients in the solution and therefore favors solutions with moderate slopes. For this, $\boldsymbol{L}$ has to be chosen such that $\boldsymbol{Lx} = \frac{dx}{d\ln\tau}$, as shown in Appendix C [27,29].
- The regularization with the squared norm of the solution's second derivative penalizes high curvatures in the solution and therefore favors flat and smooth solutions. For this, $\boldsymbol{L}$ has to be chosen such that $\boldsymbol{Lx} = \frac{d^2x}{d(\ln\tau)^2}$, as shown in Appendix C [20,21,25,29].

The suitability of different regularization terms depends on the shape of the actual DRT, which, however, is not known in most cases. As shown in Figure 3, the choice of the regularization term has a major impact on the solution. Still, the revealed processes are consistent for EIS-DRT (four identified processes P1–P4) and TDM-DRT (four identified processes P2–P5).

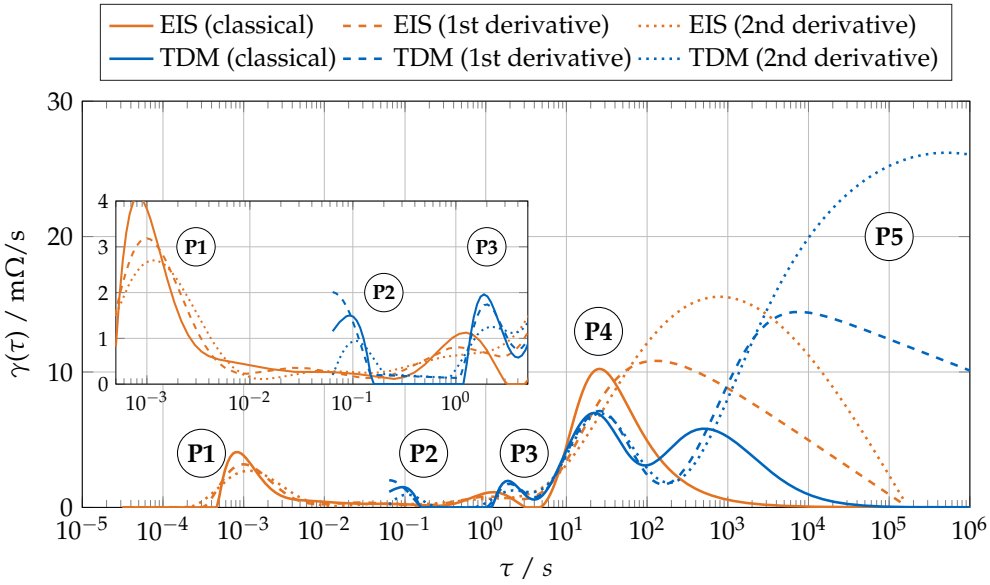

Figure 3. DRT calculated from EIS and TDM at 50% SOC for different regularization terms, respectively. The EIS-DRT reveals the four processes P1–P4 and the TDM-DRT reveals the four processes P2–P5.

The regularization with the solution's second derivative yields wide peaks, especially in the low-frequency range. The penalty on high values in the standard form Tikhonov regularization leads to noticeably smaller peaks of the diffusion process. We assume that the low resistance resulting from this is compensated by shifting the peak to lower relaxation times. This compensation is possible because of the limited excitation time of the current pulse, during which the cell is not completely polarized.

The EIS-DRT only covers the higher frequency range. In the EIS-DRT, the magnitude of all peaks is at a similar level, except P4, which lies beyond the minimal measured frequency. Hence, the standard form Thikhonov regularization provides an equal regularization of the solution. When using only EIS-DRT, the ECMs parameterized with applying standard form Tikhonov regularization yields the lowest voltage error in the validation cycle.

In contrast, ECMs parameterized only by TDM-DRT yields the lowest voltage error when applying regularization with the solution's second derivative. It is assumed that the constraint of a low curvature better characterizes the actual DRT at low relaxation times. This is not consistent with the findings of Hahn et al. [29], who recommend standard form Thikonov regularization for most cases. However, their contrary results can be attributed to the synthetic data used for their investigations. They tested the different regularization terms by reconstructing the DRT of one RC element in series with one ZARC element. Since the accurate DRT of a single ideal RC element forms a Dirac delta function, favoring smooth and wide peaks strongly opposes the correct solution and

therefore a regularization with the solution's second derivative leads to unsatisfactory solutions. In our case, the standard form Tikhonov regularization faces another problem: Due to the high difference of the DRT's magnitude between low relaxation times and high relaxation times, penalizing high function values results in an uneven regularization. The high relaxation time range, where the diffusion behavior forms a large peak in the DRT, is affected significantly stronger by this kind of regularization than the low relaxation time range. This applies especially at low SOC, where the difference in magnitude is the highest.

3.4. L-Curve Method for Optimized Determination of the Regularization Factor λ

The regularization factor λ has a crucial impact on the solution $\boldsymbol{x}_\lambda$ of the fitting problem. If λ is chosen too high, the regularization term dominates the fitting residual in Equation (9) and the solution does not fit the data. This results in a flattening and over-smoothing of relevant peaks. If λ is chosen too low, measurement uncertainties are included in the solution, which leads to the formation of oscillation without any physical meaning (over-fitting). Thus, finding the optimal regularization factor λ_{opt} is a critical task and a balance between the quality of the fit and the smoothness of the solution must be found.

Different criteria for the optimization of the regularization factor, specifically developed for the DRT calculation, can be found in the literature. These criteria are, e.g., re-im-cross-validation [25,27,29] or re-im-discrepancy [27,29]. Since these methods are based on the idea of optimally matching real and imaginary part of the impedance, they do not apply to the TDM-DRT. Therefore, a more general approach to determine the best regularization factor, the so-called L-curve method, which was proposed by Hansen et al. [30,31], is used in this work.

The L-curve method provides a criterion which is universally applicable for Tikhonov regularization and which does not require a priori knowledge of the measurement noise [29,32]. The L-curve visualizes the compromise between the residual norm $\|\boldsymbol{B}\boldsymbol{x}_\lambda - \boldsymbol{D}_{\text{exp}}\|_2$ and the norm of the regularized solution $\|\boldsymbol{L}\boldsymbol{x}_\lambda\|_2$ by plotting the tupels of both values for different regularization factors, which results in a continuous curve for $\lambda \in [0, \infty]$. On a logarithmic scale, this curve typically resembles an L-shape, which is the reason for the name of this method. The optimal compromise between a low residual and an adequate regularization can be identified as the corner-point of the L-shape. Starting from this point, increasing λ results in a rapid rise of the residual norm and therefore a worsening of the fitting quality. Decreasing λ, in contrast, strongly affects the regularization of the solution without considerably improving the fitting quality any further [30,31].

3.5. Defining the Vector of Relaxation Times

To calculate the DRT, the vector of relaxation times $\boldsymbol{\tau}$ must be chosen a priori. The number and range of relaxation times τ_n heavily influence the calculated DRT [29]. The appropriate limits for the relaxation times can be derived from the measured frequency range. While the frequency limits of EIS are defined in the measurement routine, they must be determined from the sampling rate and the measurement time for TDM. On the one hand, the maximum frequency in a TDM is limited by the Nyquist–Shannon sampling theorem, which states that frequencies higher than half the sampling frequency f_{sample} cannot be detected in the measurement data [20,33]. Since the data are logarithmically sampled and the Nyquist–Shannon theorem refers to evenly sampled data, the theoretical minimum relaxation time for the TDM-DRT is raised by a factor of ten, which yields

$$\tau_{\text{min}} = \frac{10}{2\pi \frac{1}{2} f_{\text{sample}}}. \tag{10}$$

On the other hand, the minimum frequency that can be measured from a current pulse and subsequent relaxation is limited by the recorded duration of the relaxation phase T_{relax}.

By definition, the DRT can only portray impedance spectra converging to the real axis at the boundaries of the chosen interval of relaxation times. Because of this, Hahn et al. [29]

propose extending the predefined vector of relaxation times $\boldsymbol{\tau}_n$ beyond the measured frequencies for high relaxation times. This allows the fitted impedance spectrum Z_{DRT} to adequately approximate the diffusion branch of the measured impedance spectrum. With this motivation, we extend the relaxation times of the TDM-DRT beyond $\frac{T_{\mathrm{relax}}}{2\pi}$ to allow for a more accurate fit if the voltage has not relaxed entirely towards the open circuit potential after T_{relax}. Based on these assumptions, the limits of the relaxation times vector in the DRT calculation listed in Table 1 are chosen.

The discrete values of $\boldsymbol{\tau}$ are equally spaced on a log scale with 30 points per decade, following the recommendation of Hahn et al. [29]. Furthermore, the squared residual norm of the EIS-DRT in Equation (3) is multiplied by $\frac{1}{Q}$ to make the minimization problem independent of the number of measurement points Q. Analogously, the squared residual norm of the TDM-DRT in Equation (7) is multiplied by $\frac{1}{M}$.

Table 1. Limits of predefined relaxation times.

EIS-Data		**TDM-Data**	
$\boldsymbol{\tau}_{\mathbf{min}}$	$\boldsymbol{\tau}_{\mathbf{max}}$	$\boldsymbol{\tau}_{\mathbf{min}}$	$\boldsymbol{\tau}_{\mathbf{max}}$
$\frac{1}{2\pi f_{\mathrm{max}}}$	$\frac{10^4}{2\pi f_{\mathrm{min}}}$	$\frac{10}{\pi f_{\mathrm{sample}}}$	$T_{\mathrm{relax}} \cdot 10^5$

4. ECM Parameterization

4.1. Employed ECM

ECMs with an integer number of RC elements connected in series are one of the most widely used electrical models for lithium-ion batteries, because of their small number of parameters. They are an ideal choice for parameterization from the DRT, since the DRT is described by an infinite number of RC elements connected in series. Hence, parameterization of RC parameters from the DRT can be interpreted as a model order reduction of the DRT.

As derived in Section 3.3, five processes are revealed from the DRT. However, when the DRT-fitting is performed on a merged EIS and TDM (Section 5), we employ an ECM comprising four RC elements connected in series to model the charge-transfer resistance (P1 + P2), the transition process (P3), and the diffusion processes (P4 and P5). P1 and P2 both display different subprocesses of the charge-transfer resistance, which become visible to a greater or lesser extent at different temperatures and SOCs. The implementation of only one RC element for these high-frequency processes P1 and P2 is chosen because the models are validated with time-domain measurements with a sampling rate of 100 ms and thus they do not contribute individually to the validation results. Consequently, when performing the proposed DRT-fitting on EIS measurements only, three RC elements (P1 + P2, P3, P4) are used. In addition to the RC elements, there is one additional resistance in series, which models all ohmic resistances occuring within the cell. The open-circuit voltage (OCV) is modeled by an ideal voltage source and the OCV-SOC look-up is gathered from $U_{\mathrm{OCV,\,TDM}}$, measured right before the pulse-relaxation measurement after three weeks of relaxation (Section 2.3).

4.2. DRT-Fitting: Direct RC Parameterization from the DRT

We propose to estimate the RC parameters for an ECM directly from the DRT, making any additional fitting algorithms in the time or frequency-domain superfluous. This approach circumvents the manual specification of starting values and/or boundary conditions for these fitting algorithms and promotes physically meaningful parameter sets. Although our approach is not a fitting algorithm per se, and the RC parameters are determined analytically from the DRT, we call it DRT-fitting in analogy to conventional EIS-fitting (fitting RC parameters to impedance spectra) or pulse-fitting (fitting RC parameters to the time-domain current/voltage data). Since dynamic processes of the investigated system become visible as peaks in the DRT, the relaxation times τ_n of n RC elements can be chosen

at the local maxima of γ. As stated in Equation (2), γ is normalized to the total polarization resistance R_{pol}. Therefore, the polarization resistance R_n of a single relaxation process can be approximated by integrating between the adjacent minima of γ, labeled τ_a and τ_b. Consequently, the parameters R_n and C_n of an RC element can be calculated as

$$R_n = \int_{-\tau_a}^{\tau_b} \gamma(\ln \tau)\, \mathrm{d} \ln \tau, \tag{11}$$

$$C_n = \frac{\tau_n}{R_n}. \tag{12}$$

In engineering applications, the number of RC elements must often be defined a priori, notwithstanding the number of occurring processes in the DRT. This can corrupt the interpretability of RC parameters, when RC elements are not unambiguously correlated to the same electrochemical processes at all SOCs. On this account, Figure 4 proposes a flow chart of a decision logic for parameterizing RC elements directly from the DRT and takes into account the predefined number of RC elements. This process is henceforth denoted as DRT-fitting and is explained in the following.

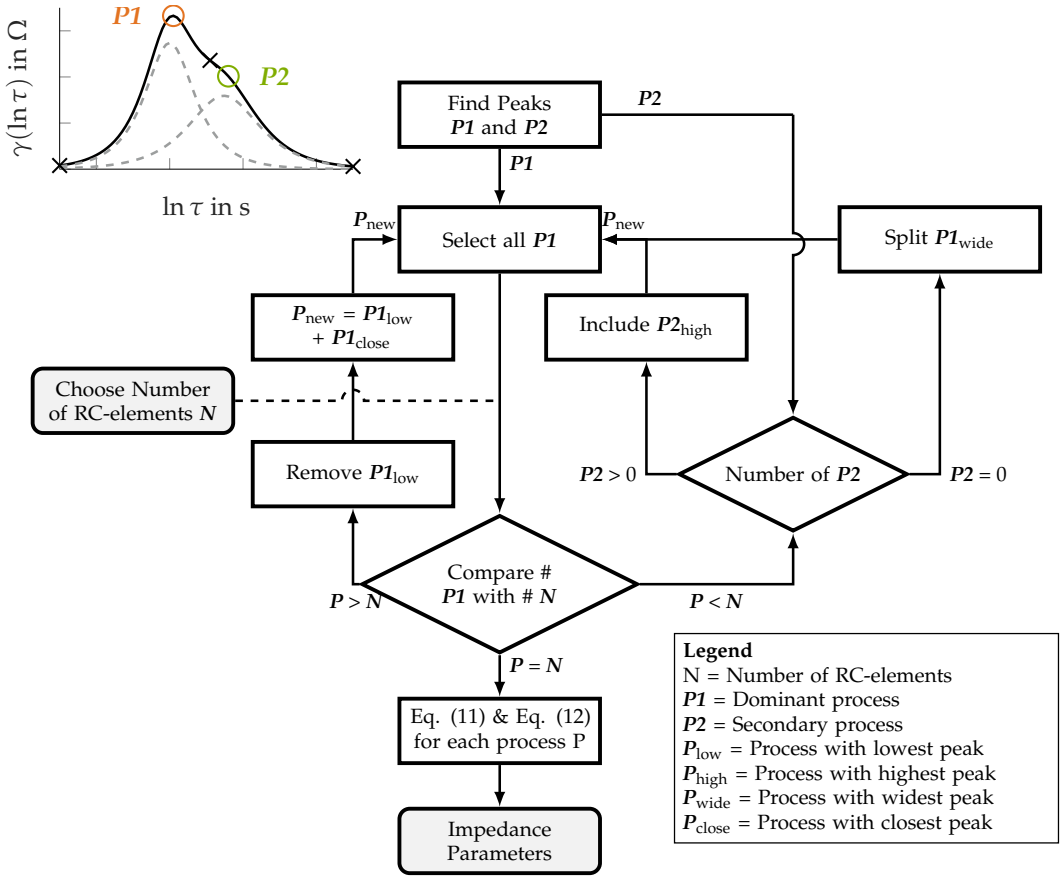

Figure 4. Flow chart of the proposed DRT-fitting for automated parameterization of RC elements from the DRT.

Initially, all local maxima in the DRT are identified and labeled $P1$, while all inflection points are labeled $P2$. To identify the inflection points, the second derivative of γ is consulted and τ_n is determined at the location of its maxima. The idea is that both geometric points indicate an underlying electrochemical process. We propose to associate one RC element to each primary process $P1$. If the predefined number of RC elements N matches the number of primary process $P1$, RC elements can be parameterized according to Equations (11) and (12) and the parameterization process has finished. If the DRT reveals more primary processes $P1$ than the predefined number of RC elements, the polarization

resistance of the lowest peak is added to the process with the closest relaxation time. If the predefined number of RC elements exceeds the number of peaks in the DRT, the secondary processes $P2$ are associated to an additional RC element in descending order of the polarization resistance. In order to divide the polarization resistance between a secondary and a primary process, the integration limit is set to the point were the slope of γ is lowest.

For our tested cell, the number of processes and their corresponding time constants was different at different SOCs. Hence, we ran the algorithm for the DRT of each tested SOC, in order to assure the consistent allocation of the same processes to the same RC elements over the entire SOC range.

4.3. Comparison to Conventional EIS-Fitting

To validate the proposed parameterization procedure (DRT-fitting), it is compared to a reference EIS-fitting algorithm. Conventional EIS-fitting was performed using a MULTISTART algorithm [34] with 100 starting points to fit three RC elements to the measured impedance spectra in the frequency-domain. To ensure comparability of the results, we also only used EIS measurements to calculate the DRT and perform the DRT-fitting. Figure 5 shows the resulting parameters for R and τ and the corresponding impedance spectra compared to the measured ones.

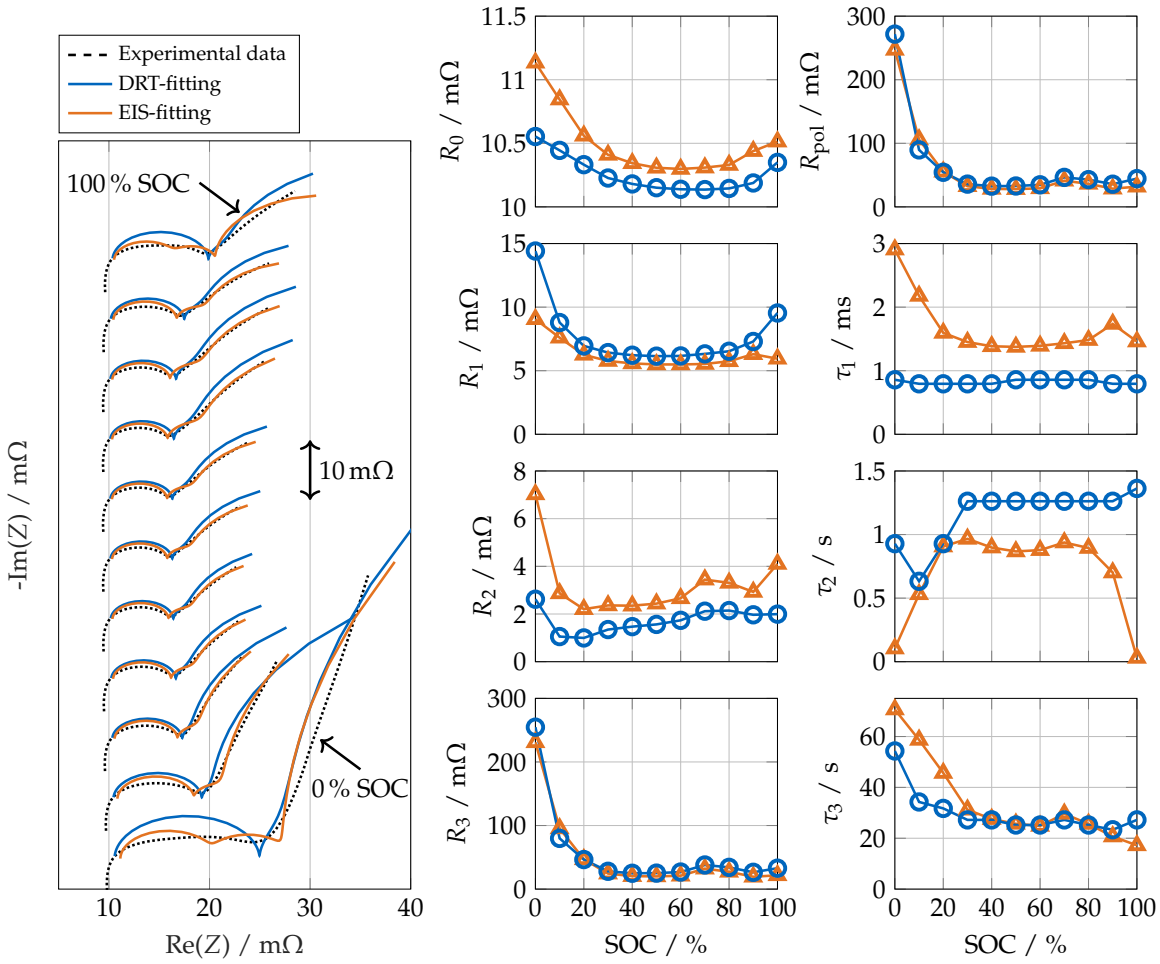

Figure 5. Left: Impedance spectra from EIS measurements and impedance spectra estimated by the proposed DRT-fitting and benchmark EIS-fitting for different SOC at 20 °C. Impedance spectra are shifted in the y-direction according to the SOC for the sake of better visibility. **Right:** Resulting ECM parameters over SOC for DRT-fitting and EIS-fitting.

The Nyquist plots indicate that both ECMs approximate the measured impedance spectra with similar accuracy. Between 10% SOC and 90% SOC both EIS-fitting and DRT-fitting identify one process at the first semi-circle displaying the charge-transfer resistance, one process at the transition frequency and one process at the diffusion branch. While this is expected for the DRT-fitting, it is noticeable that the EIS-fitting algorithm allocates the three RC elements in the same manner. Besides minor offsets and shifts between individual RC elements, parameters of both methods coincide well with each other. At 0% SOC and 100% SOC the assignment of RC elements remains consistent for the DRT-fitting. This leads to the typical bathtub shape of the charge-transfer resistance [7]. The EIS-fitting algorithm, however, allocates the second RC elements to the second emerging charge-transfer process (P2). This leads to inconsistent RC parameters at the edges of the SOC area.

It needs to be noted that the boundaries of the EIS-fitting were set free, which could be changed in a way to force the algorithm to assign individual RC elements to certain frequency ranges. While both approaches lead to similar parameters in most cases, the advantage of the DRT-fitting is that it automatically determines physically reasonable and consistent parameters without a priori knowledge and the need for a manual, iterative, and time-consuming fixing of starting values and boundary conditions.

Since both approaches identify similar RC parameters, they also lead to a comparable accuracy in the validation cycle (Table 2), whereby the error of the DRT-fitting is slightly higher (in the range of few mV) for all validation regimes. It can be concluded that when using EIS data alone, the proposed DRT-fitting does not gain any improvements in accuracy compared to the conventional EIS-fitting algorithm. However, it allows for a convenient combination of EIS and TDM.

5. Combination of EIS and TDM

5.1. Merging Approaches

As reviewed in Section 1.2, there are already some approaches to combine both measurement domains. However, most of these use the the DRT only to gain a priori knowledge and subsequently perform conventional fitting.

In this work, we present and compare three different merging approaches, which occur at various stages during the parameterization process using either a subset of RC parameters (Separate DRT-fitting), intermediate results (Interconnected DRT-fitting) or raw measurement data (Combined DRT-fitting). All three employ the proposed DRT-fitting for direct RC parameterization from the DRT and without the need for any conventional fitting algorithm. The three approaches are illustrated in Figure 6, and are explained in the following:

1. **Separate DRT-fitting (blue):**
   In our first approach, EIS and TDM are used individually to parameterize different RC elements, the allocation of which is defined a priori. With this assumption, EIS and TDM are processed independent from each other. The ohmic resistance and the first RC elements (two in our case) are parameterized purely based on the EIS-DRT, whereas the remaining RC elements (two in our case) are determined from TDM-DRT only. Therefore, relaxation times higher than $\hat{\tau}$, with $\hat{\tau}$ being the highest relaxation time with a local minimum in the EIS-DRT, are ignored in the EIS-DRT. Likewise, the TDM-DRT is only evaluated at $\tau > \hat{\tau}$. Depending on the sampling frequency, it is difficult to capture high-frequent loss processes during TDM, where meaningless oscillations can occur at low relaxation times close to $\hat{\tau}$ of the TDM-DRT. This motivates an interconnected approach.
2. **Interconnected DRT-fitting (orange):**
   The goal of our second approach is to use information of EIS measurements in a more intertwined calculation of the TDM-DRT to avoid the described problems of meaningless oscillations at low relaxation times. Since the DRT equals a series of an infinite number of RC elements, the voltage relaxation which is caused by the high-frequency processes of the cell can be calculated from the EIS-DRT:

$$u_{\mathrm{EIS}}(t > (t_0 + T_\mathrm{p})) = \int_{-\infty}^{\infty} \gamma_{\mathrm{EIS}}(\ln\tau)\ I_\mathrm{p}\ [\exp\left(\frac{t_0 + T_\mathrm{p} - t}{\tau}\right) - \exp\left(-\frac{t_0 - t}{\tau}\right)]\ \mathrm{d}\ln\tau. \quad (13)$$

This virtual voltage response is subtracted from the measured voltage of TDM. Since the EIS-DRT is only used to subtract the high-frequency behavior of the cell, the diffusive branch is removed from the impedance spectrum before evaluating Equation (13). Afterwards, the remaining voltage response is used to calculate the TDM-DRT according to Equation (7). Adding EIS-DRT and TDM-DRT finally yields a DRT of the complete system, which is used for the parameterization of all three RC elements. A disadvantage of this rather complex approach is that errors within calculation of the EIS-DRT propagate into the next step and will influence the voltage signal and thus also the TDM-DRT.

3. **Combined DRT-fitting (green):**
Based on the disadvantages of the first two approaches, we developed a combined DRT-fitting, where the calculation of EIS-DRT and TDM-DRT is performed simultaneously in one single step. This makes decision of a border time constant $\hat{\tau}$ superfluous and avoids complex interconnected fitting. Defining one system of equations in order to find $\gamma(\ln\tau)$, such that it best fits both measurements, directly results in a DRT that displays the complete dynamic behavior of the measured cell from high to low frequencies. This can be implemented by merging Equations (3) and (7) to

$$\min_{U_{\mathrm{OCV}}, R_0, \boldsymbol{R}} \left\| \sqrt{\boldsymbol{w}} \begin{bmatrix} \boldsymbol{A}'_\mathrm{Z} & \boldsymbol{0} & \boldsymbol{1} \\ \boldsymbol{A}''_\mathrm{Z} & \boldsymbol{0} & \boldsymbol{0} \\ \boldsymbol{A}_\mathrm{u} & \boldsymbol{1} & \boldsymbol{0} \end{bmatrix} \begin{bmatrix} \boldsymbol{R} \\ U_{\mathrm{OCV}} \\ R_0 \end{bmatrix} - \sqrt{\boldsymbol{w}} \begin{bmatrix} \boldsymbol{Z}'_{\mathrm{exp}} \\ \boldsymbol{Z}''_{\mathrm{exp}} \\ \boldsymbol{u}_{\mathrm{exp}} \end{bmatrix} \right\|_2^2 \quad (14)$$

$$\min_{\boldsymbol{x}} \| \boldsymbol{B}_{\mathrm{comb}} \quad \boldsymbol{x} \quad - \quad \boldsymbol{D}_{\mathrm{exp}} \|_2^2 \quad (15)$$

This equals a summation of the residuals of EIS-DRT and TDM-DRT. The diagonal Matrix $\boldsymbol{w}$ applies a weighting between EIS and TDM data to achieve an equal influence of both measurements, the derivation of which can be found in Appendix D. Minimizing Equation (15) yields the DRT of the whole system as well as R_0 and U_{OCV} and can thus be used to parameterize all ECM parameters at once.

The presented approaches are validated against a validation cycle in the time-domain in the following.

5.2. Validation Results

We validated our method by comparing the measured voltage with the simulated voltage during a validation cycle with a defined current profile (Figure 7a). The validation cycle started with a CCCV discharge (A) and charge (C) at 1 C with 4 h relaxation (B) after the discharge and 3 h relaxation (D) after the charge phase. This was followed by a dynamic stress test (DST) (E), in which the cell was discharged by a sequence of short charge and discharge pulses between −2 C and 1 C. Finally, after charging the cell back to 100% SOC, a real driving cycle, recorded with a Volkswagen eGolf (F), was repeated until the lower cut-off voltage was reached.

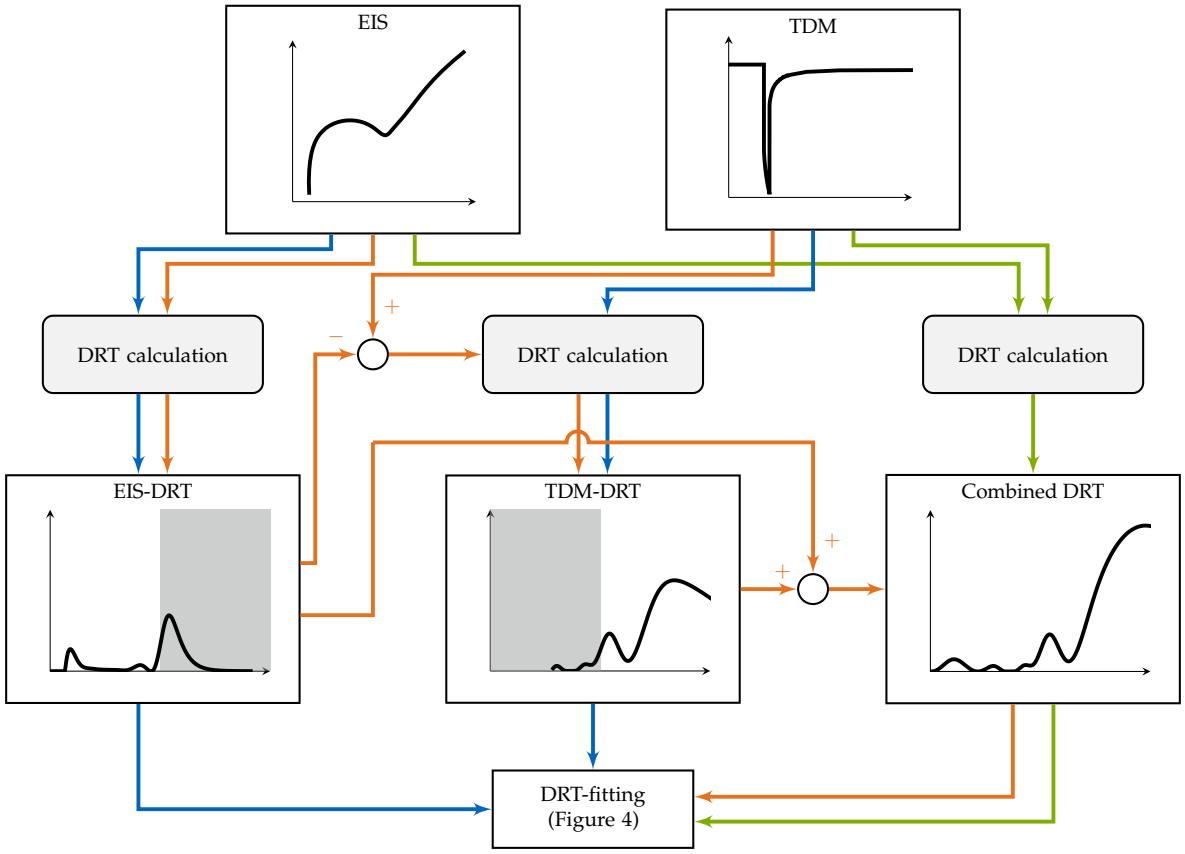

Figure 6. Flow chart of different approaches for combining EIS and TDM before the DRT-fitting is performed to parameterize the RC elements of an ECM. Blue: Separate DRT-fitting. Orange: Interconnected DRT-fitting. Green: Combined DRT-fitting.

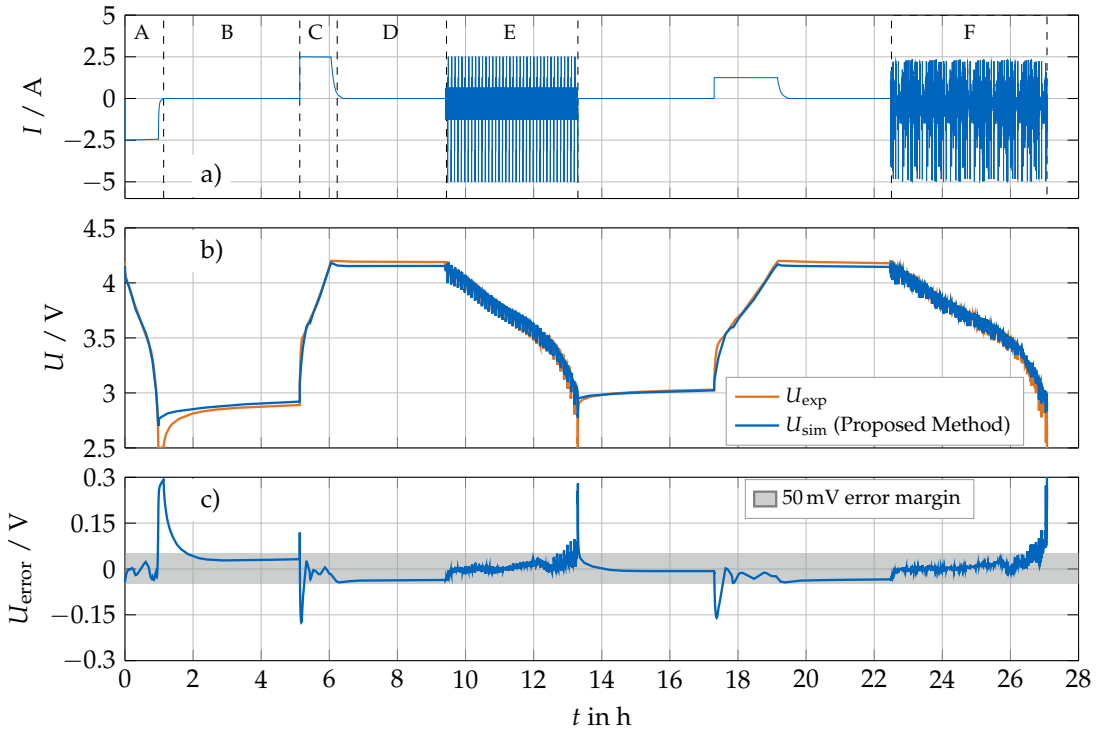

Figure 7. Simulation results of the combined DRT-fitting during the validation cycle. (**a**) Current profile. (**b**) Measured and simulated voltage. (**c**) Model error $U_{error} = U_{sim} - U_{exp}$.

In Table 2, the root mean square error (RMSE) of the different configurations of the proposed DRT-fitting as well as the conventional EIS-fitting is listed for the whole validation cycle and for the different segments A–F separately. Exemplary, Figure 7b) shows the measured and simulated voltage of the combined DRT-fitting, where the DRT is calculated from EIS and TDM simultaneously during the validation cycle. In Figure 7c), the corresponding residual voltage $U_{\text{error}} = U_{\text{sim}} - U_{\text{exp}}$ is plotted.

Table 2. Comparison of the RMSE in mV during the validation cycle of different RC parameter sets.

	EIS-Fitting	*DRT-Fitting*	*DRT-Fitting*		
Measurement	**EIS**	**EIS**	**EIS and TDM**		
Merging Approach	**n.a.**	**n.a.**	*Separate*	*Interconnected*	*Combined*
Regularization Term	**n.a.**	**x**	$\mathbf{x}/\frac{d^2x}{d\ln(\tau)^2}$	$\mathbf{x}/\frac{d^2x}{d\ln(\tau)^2}$	$\frac{d^2x}{d\ln(\tau)^2}$
Whole Validation Cycle	72.56	73.14	45.18	41.52	43.38
A: 1 C Discharge	42.88	46.76	28.78	26.41	26.71
B: Relaxation at 0% SOC	148.12	148.17	38.86	52.44	56.87
C: 1 C Charge	49.61	56.85	95.08	60.87	59.63
D: Relaxation at 100% SOC	37.35	37.35	36.33	36.47	36.74
E: DST	24.14	25.63	22.65	20.59	22.16
F: Driving Profile	31.56	32.05	23.69	25.12	27.39

It can be seen that adding TDMs to the parameterization process by using our proposed merging approaches significantly improved the results compared to the conventional EIS-fitting. The lowest overall RMSE (41.52 mV) was reached by the interconnected DRT-fitting with a relative improvement of 42% compared to the conventional EIS-fitting. Thereby, the differences of the three merging approaches were comparably low (in the range of a few mVs for most regimes). The only big difference occurred at 0% SOC and at the beginning of the charging phase, when using the separate DRT-fitting. In this configuration, apparently, different loss processes were assigned to the RC elements in this region. The RMSE was lower compared to the interconnected and combined DRT-fitting during the relaxation phase and higher at the beginning of the charging phase. The magnitude of the voltage error at 0% SOC and 100% SOC was influenced by the OCV-SOC relationship in this region anyway, as revealed by the strong hysteresis until approx. 20% SOC (Section 2.3).

The voltage error in Figure 7c lay within the 50 mV error margin for most of the time. Only at low SOC, at the end of discharging and at the beginning of charging, the error increased strongly. As discussed before, the high error in the low SOC range could mainly be attributed to the strong hysteresis, which was not modeled in our ECM. Therefore, in the future, more detailed investigations on the modeling of hysteresis are needed to further improve the simulation results, especially for modern LIB with silicon added to anode active material. It needs to be noted that we completely discharged the cell with a CCCV profile applying a low cut-off current of C/50. For most applications, however, such as battery electric vehicles, this low SOC area is of minor importance, since the SOC range is limited for various reasons such as safety or degradation [35].

6. Conclusions

In this study, we presented and validated a novel parameterization process for RC elements of ECMs. The main advantages of this approach can be summarized as follows: (1) merging of frequency- and time-domain measurement data to cover a broad frequency range, (2) automated DRT calculation using Tikhonov regularization and the L-curve criterion, and (3) RC parameterization directly from the DRT (DRT-fitting). Furthermore, we can conclude the following from our investigations.

To cover a broad frequency range of the cell's dynamic behavior we utilize both measurements in the frequency-domain (EIS) and measurements in the time-domain

(pulse-relaxation measurements). The TDMs, which in general are necessary to capture the low-frequency loss processes of the LIB, have shown that a long relaxation period of more than two weeks was necessary prior to the pulse-relaxation measurement itself. This was to eliminate all effects of bringing the cell to its respective SOC. Only when a fully relaxed state has been reached prior to the pulse-relaxation measurement does the procedure solely capture the cell's kinetics and is not biased by any former excitation of the cell.

We investigated different regularization terms in the Tikhonov regularization to stabilize the DRT problem. Besides standard regularization with the solution norm itself, regularization with the norm of the solution's first and second derivative were applied in the calculation of the DRT. The results have shown that in contrast to the EIS-DRT, where the standard regularization showed the best results, using the solution's second derivative leads to an improved deconvolution of the TDM-DRT. During all DRT calculations, the L-curve criterion has successfully been used to find the optimum regularization factor.

We showed that it is possible to determine RC parameters directly from the DRT without the use of any conventional optimization algorithm. The parameters resulting from the DRT-fitting are, with minor differences, comparable to a benchmark EIS-fitting. However, our approach avoids time-consuming work of setting boundary conditions and initial guesses for the fitting algorithm to achieve reasonable and consistent parameters over broad operating conditions.

Additionally, direct DRT-fitting allows for convenient merging of frequency and time-domain data. Therefore, we ultimately compared three methods of combining EIS and TDM data to be used in the proposed DRT-fitting. During a comprehensive validation cycle, all three methods achieved comparable results in most regions. However, they show a strong improvement compared to the conventional EIS-fitting—the RMSE was reduced by over 40%. Modeling of the cell at a low SOC proved to be most difficult for all methods, therefore detailed investigations of the hysteresis behavior are suggested for future work.

Furthermore, it should be kept in mind that the DRT calculation and the ECM parameterization in general is subject to several other influencing factors, which were not further investigated in this work. These include, for example, the range and number of relaxation times in the DRT, the definition of the minimization problem itself (like including an inductance or fixing the U_{OCV} or the R_0 value in the cost function), or applying a different measurement routine. For the TDMs especially, the impact of different measurement protocols should be further investigated. In the introduced ECM parameterization process, the allocation of the total polarization process to the RC elements as well as the number of RC elements have an important influence. Last but not least, validation of models is always dependent on the validation cycle, as shown by the separate evaluation of the different cycle regimes. In this work, we performed parameterization and validation only at 20 °C. In the future, this must be extended to account for the mutual dependency between dynamic loss process and heat generation inside the cell.

Author Contributions: First author, L.W.; conceptualization, L.W.; methodology, L.W. and P.G.; software, L.W., P.G. and A.K.; validation, L.W., P.G. and A.K.; formal analysis, L.W. and P.G.; investigation, L.W. and P.G.; writing—original draft preparation, L.W., P.G. and A.K.; writing—review and editing, L.W. and A.K.; visualization, L.W. and P.G.; supervision, L.W.; project administration, L.W.; funding acquisition, L.W. All authors have read and agreed to the published version of the manuscript.

Funding: The authors want to thank the Bavarian Ministry of Economic Affairs, Regional Development and Energy for funding the project bawaii—battery analytics with artificial intelligence (IUK-1808-0013).

Conflicts of Interest: The authors declare no conflict of interest.

Abbreviations

BMS	battery management system
DRT	distribution of relaxation times
DST	dynamic stress test
DVA	differential voltage analysis
ECM	equivalent circuit model
EIS	electrochemical impedance spectoscropy
GITT	galvanostatic intermittent titration technique
LIB	lithium-ion battery
NCA	nickel cobalt aluminium oxide
OCV	open-circuit voltage
pOCV	pseudo open-circuit voltage
RMSE	root mean square error
SOAP	state of available power
SOC	state of charge
SOH	state of health
TDM	time-domain measurement

Appendix A. EIS-DRT

As an infinite number of RC elements with continuous relaxation times, the DRT yields an impedance spectrum of

$$Z_{\mathrm{DRT}}(f) = \int_0^\infty \frac{g(\tau)}{1 + j2\pi f\tau}\,\mathrm{d}\tau, \tag{A1}$$

where f stands for the frequencies at which the spectrum Z_{DRT} is evaluated and $g(\tau)$ is the distribution function of resistances at the continuous relaxation times τ. $g(\tau)$ is normalized to the total polarization resistance R_{pol}:

$$\int_0^\infty g(\tau)\,\mathrm{d}\tau = R_{\mathrm{Pol}}. \tag{A2}$$

Substituting $\gamma(\ln\tau) = \tau g(\tau)$ in Equations (A1) and (A2) simplifies the use of a logarithmic frequency scale and yields Equations (1) and (2) given in Section 3.1:

$$Z_{\mathrm{DRT}}(f) = \int_{-\infty}^\infty \frac{\gamma(\ln\tau)}{1 + j2\pi f\tau}\,\mathrm{d}\ln\tau \tag{A3}$$

$$\int_{-\infty}^\infty \gamma(\ln\tau)\,\mathrm{d}\ln\tau = R_{\mathrm{Pol}}. \tag{A4}$$

DRT calculations based on the equations above can be found in various publications in one form or another [12–14,16,17,25,27,29,32,36–40]. When dealing with discrete data, the integrals in Equations (1) and (2) can be expressed as sums

$$Z_{\mathrm{DRT}}(f_q) = \sum_{n=1}^{N} \frac{\gamma_n}{1 + j2\pi f_q\tau_n}\Delta\tau_{\log} = \sum_{n=1}^{N} \frac{R_n}{1 + j2\pi f_q\tau_n} \tag{A5}$$

and

$$\sum_{n=1}^{N} \gamma_n\,\Delta\tau_{\log} = \sum_{n=1}^{N} R_n = R_{\mathrm{Pol}}, \tag{A6}$$

which is equal to a series of N RC elements. The values γ_n of the discrete distribution function equal the function values of $\gamma(\ln\tau)$ at the N discrete relaxation times τ_n, which have the equal logarithmic difference $\Delta\tau_{log}$. The impedance is approximated at Q discrete logarithmic equidistant frequencies f_q.

To obtain the minimization problem in Equation (3), real and imaginary part of the impedance are separated and the sum of their squared residuals is used as an error measure to evaluate the approximation of $\gamma(\ln \tau)$:

$$\min_{R_0,R_n} \Big(\sum_{q=1}^{Q} \Big[w'(R_0 + Z'_{\mathrm{DRT}}(f_q) - Z'_{\mathrm{exp}}(f_q))^2 + w''(Z''_{\mathrm{DRT}}(f_q) - Z''_{\mathrm{exp}}(f_q))^2 \Big] \Big). \tag{A7}$$

The resistance R_0 has to be added to the real part of the DRT's impedance, to satisfy the purely ohmic resistance of the measured impedance spectrum. As mentioned in Section 3.1, w' and w'' are used to allow an adjusted weighting of the real and imaginary part. By displaying the discrete values of Z in a vector, Equation (A7) can be transformed into matrix form:

$$\min_{R_0,R_n} \Big(w' \| ((R_0 \mathbf{1} + \boldsymbol{Z}'_{\mathrm{DRT}}) - \boldsymbol{Z}'_{\mathrm{exp}}) \|_2^2 + w'' \| (\boldsymbol{Z}''_{\mathrm{DRT}} - \boldsymbol{Z}''_{\mathrm{exp}}) \|_2^2 \Big). \tag{A8}$$

Stacking the two parts of Equation (A8), yields the minimization problem given in Equation (3) in Section 3.1:

$$\min_{R_0,\boldsymbol{R}} \left\| \begin{bmatrix} \sqrt{w'}\boldsymbol{A}'_{\mathrm{EIS}} & \sqrt{w'}\mathbf{1} \\ \sqrt{w''}\boldsymbol{A}''_{\mathrm{EIS}} & \mathbf{0} \end{bmatrix} \begin{bmatrix} \boldsymbol{R} \\ R_0 \end{bmatrix} - \begin{bmatrix} \sqrt{w'}\boldsymbol{Z}'_{\mathrm{exp}} \\ \sqrt{w''}\boldsymbol{Z}''_{\mathrm{exp}} \end{bmatrix} \right\|_2^2. \tag{A9}$$

Satisfying Equation (A5), the entries of the $Q \times N$ matrices $\boldsymbol{A}'_{\mathrm{EIS}}$ and $\boldsymbol{A}''_{\mathrm{EIS}}$ have to be set to

$$A'_{\mathrm{EIS},q,n} = \frac{1}{1 + (2\pi f_q \tau_n)^2} \tag{A10}$$

and

$$A''_{\mathrm{EIS},q,n} = \frac{-2\pi f_q \tau_n}{1 + (2\pi f_q \tau_n)^2}, \tag{A11}$$

such that

$$\boldsymbol{Z}_{\mathrm{DRT}} = \boldsymbol{A}'_{\mathrm{EIS}}\boldsymbol{R} + j\boldsymbol{A}''_{\mathrm{EIS}}\boldsymbol{R}, \tag{A12}$$

where $\boldsymbol{Z}$ is a vector containing the discrete impedance values $Z(f_q)$ and R is a vector containing the discrete resistance values $R_n = \gamma_n \Delta\tau_{\log}$.

Appendix B. TDM-DRT

Schmidt starts the deduction of the system of equations from the voltage response of a single RC element to a current pulse of magnitude I_{p} applied at t_0 for a duration of T_{p}, which is given in Equation (5) in Section 3.2 as

$$\begin{aligned} u_n(t) = R_n I_{\mathrm{p}} [& \sigma(t - t_0)(1 - \exp(-\frac{t - t_0}{\tau_n})) \\ & - \sigma(t - (t_0 + T_{\mathrm{p}}))(1 - \exp(-\frac{t - (t_0 + T_{\mathrm{p}})}{\tau_n}))], \end{aligned} \tag{A13}$$

where $\sigma(x)$ is the Heaviside step function. In the relaxation phase, where $(t < t_0 + T_{\mathrm{p}})$, this simplifies to

$$u_n(t) = R_n I_{\mathrm{p}} [-\exp(\frac{t_0 - t}{\tau_n}) + \exp(\frac{t_0 + T_{\mathrm{p}} - t}{\tau_n})]. \tag{A14}$$

A summation of N RC-elements with logarithmic evenly spaced relaxation times τ_n directly yields the equation for discrete DRT data:

$$u_{\mathrm{DRT}}(t_m) = \sum_{n=1}^{N} R_n I_\mathrm{p}[\exp(\frac{t_0 + T_\mathrm{p} - t_m}{\tau_n}) - \exp(\frac{t_0 - t_m}{\tau_n})] \tag{A15}$$

$$= \sum_{n=1}^{N} \gamma_n \Delta\tau_{\log} I_\mathrm{p}[\exp(\frac{t_0 + T_\mathrm{p} - t_m}{\tau_n}) - \exp(\frac{t_0 - t_m}{\tau_n})] \tag{A16}$$

at M discrete sampling points in the time domain t_m. As before, $\gamma_n \Delta\tau_{\log} = R_n$. The equation for a continuous DRT $\gamma(\ln\tau)$ is obtained when $\Delta\tau_{\log}$ approaches 0 and N approaches ∞:

$$u_{\mathrm{DRT}}(t) = \int_{-\infty}^{\infty} \gamma(\ln\tau) I_\mathrm{p}[\exp(\frac{t_0 + T_\mathrm{p} - t}{\tau}) - \exp(\frac{t_0 - t}{\tau})]\,\mathrm{d}\ln\tau. \tag{A17}$$

The squared residual is used to find γ, such that u_{DRT} best fits the measurement data u_{exp}:

$$\min_{U_{\mathrm{OCV}}, R_n} \Big(\sum_{m=1}^{M} \Big[((U_{\mathrm{OCV}} + u_{\mathrm{DRT}}(t_m)) - u_{\mathrm{exp}}(t_m))^2 \Big] \Big). \tag{A18}$$

Here, the constant value U_{OCV} has to be added to the the DRT's voltage response to satisfy the offset of the measured cell voltage caused by the open circuit potential. Analogously to the EIS approach, Equation (A18) can be transformed into matrix form by displaying the discrete values of u in a vector:

$$\min_{U_{\mathrm{OCV}}, R_n} \|(U_{\mathrm{OCV}}\mathbf{1} + \boldsymbol{u}_{\mathrm{DRT}}) - \boldsymbol{u}_{\mathrm{exp}}\|_2^2. \tag{A19}$$

This is equal to Equation (7) in Section 3.2:

$$\min_{U_{\mathrm{OCV}}, R_n} \left\| \begin{bmatrix} \boldsymbol{A}_{\mathrm{TDM}} & \mathbf{1} \end{bmatrix} \begin{bmatrix} \boldsymbol{R} \\ U_{\mathrm{OCV}} \end{bmatrix} - \boldsymbol{u}_{\mathrm{exp}} \right\|_2^2.$$

Following Equation (A16), the entries of the $M \times N$ matrix $\boldsymbol{A}_{\mathrm{TDM}}$ have to be set to

$$A_{\mathrm{TDM},m,n} = I_\mathrm{p}[\exp(\frac{t_0 + T_\mathrm{p} - t_m}{\tau_n}) - \exp(\frac{t_0 - t_m}{\tau_n})], \tag{A20}$$

such that

$$\boldsymbol{u}_{\mathrm{DRT}} = \boldsymbol{A}_{\mathrm{TDM}}\boldsymbol{R}, \tag{A21}$$

where $\boldsymbol{u}$ is a vector containing the discrete voltage values $u(t_m)$ and R is a vector containing discrete resistances, analogous to Equation (A12).

Appendix C. Regularization Terms

For a regularization with the norm of the solution's first or second derivative, the regularization matrix $\boldsymbol{L}$ is determined via numerical differentiation. Forward differentiation of $\boldsymbol{x}$ yields the Newton's difference quotient:

$$\frac{d}{d(\ln\boldsymbol{\tau})} x(\ln\tau) \approx \frac{x(\ln\tau + \Delta\tau_{\log}) - x(\ln\tau)}{\Delta\tau_{\log}}. \tag{A22}$$

Hence the regularization term is set to be the first derivative of $\boldsymbol{x}$, by choosing $\boldsymbol{L}$ to be

$$\boldsymbol{L} = \frac{2}{\Delta\tau_{\log}} \begin{bmatrix} -1 & 1 & 0 & \cdots & 0 \\ 0 & -1 & 1 & \ddots & \vdots \\ 0 & 0 & -1 & \ddots & 0 \\ \vdots & \ddots & \ddots & \ddots & 1 \\ 0 & \cdots & 0 & 0 & -1 \end{bmatrix}. \tag{A23}$$

The second derivative is obtained using backward differentiation of Equations (A22) and (A23). This leads to

$$\frac{d^2}{d(\ln \boldsymbol{\tau})^2} x(\ln \tau) \approx \frac{x(\ln \tau + \Delta\tau_{\log}) - 2x(\ln \tau) + x(\ln \tau - \Delta\tau_{\log})}{\Delta\tau_{\log}^2} \tag{A24}$$

and

$$\boldsymbol{L} = \frac{2}{\Delta\tau_{\log}^2} \begin{bmatrix} -1 & 0.5 & 0 & \cdots & 0 \\ 0.5 & -1 & 0.5 & \ddots & \vdots \\ 0 & 0.5 & -1 & \ddots & 0 \\ \vdots & \ddots & \ddots & \ddots & 0.5 \\ 0 & \cdots & 0 & 0.5 & -1 \end{bmatrix}. \tag{A25}$$

Since the last entries of the vector $\boldsymbol{x}$, U_{OCV}, and/or R_0 are actually not part of the discrete DRT $\gamma(\ln \tau_n)$, the corresponding lines and columns in $\boldsymbol{L}$ are set to $\mathbf{0}$.

Appendix D. Weighting of EIS and TDM Data

To achieve an equal influence of EIS and TDM data on the solution of Equation (15) an adequate weighting of the data has to be found.

For an EIS with Q sampling points and a TDM with M sampling points, the matrix Equation (15) consists of $2Q + M$ lines. An unequal number of measurement points of TDM and EIS is evened out by dividing all lines of the equation system corresponding to EIS data by Q and all lines corresponding to TDM data, by M. However, EIS and TDM data are also presented with different physical units and are subject to different noise levels. This has to be additionally compensated by a fit weighting factor. To determine this factor, the squared residual norms of EIS-DRT and TDM-DRT of the conducted measurements are compared. Averaged over all SOCs, a ratio of

$$\frac{\frac{1}{2Q}\|\boldsymbol{B}_{\mathrm{EIS}}\boldsymbol{x}_{\mathrm{EIS}} - \boldsymbol{Z}_{\mathrm{exp}}\|_2^2}{\frac{1}{M}\|\boldsymbol{B}_{\mathrm{TDM}}\boldsymbol{x}_{\mathrm{TDM}} - \boldsymbol{u}_{\mathrm{exp}}\|_2^2} \approx 150\,\frac{\Omega}{\mathrm{V}} \tag{A26}$$

has been observed. Hence the weighting in the combined DRT calculation is chosen to be

$$\boldsymbol{w} = \boldsymbol{diag}\left[\tfrac{1}{2Q}\tfrac{1}{\Omega}, \quad \ldots, \quad \tfrac{1}{2Q}\tfrac{1}{\Omega}, \quad \tfrac{150}{M}\tfrac{1}{\mathrm{V}}, \quad \ldots, \quad \tfrac{150}{M}\tfrac{1}{\mathrm{V}}\right]. \tag{A27}$$

References

1. Wassiliadis, N.; Adermann, J.; Frericks, A.; Pak, M.; Reiter, C.; Lohmann, B.; Lienkamp, M. Revisiting the dual extended Kalman filter for battery state-of-charge and state-of-health estimation: A use-case life cycle analysis. *J. Energy Storage* **2018**, *19*, 73–87. [CrossRef]
2. Birkl, C.R.; Roberts, M.R.; McTurk, E.; Bruce, P.G.; Howey, D.A. Degradation diagnostics for lithium ion cells. *J. Power Sources* **2017**, *341*, 373–386. [CrossRef]
3. Schmitt, J.; Maheshwari, A.; Heck, M.; Lux, S.; Vetter, M. Impedance change and capacity fade of lithium nickel manganese cobalt oxide-based batteries during calendar aging. *J. Power Sources* **2017**, *353*, 183–194. [CrossRef]
4. Zhou, X.; Huang, J.; Pan, Z.; Ouyang, M. Impedance characterization of lithium-ion batteries aging under high-temperature cycling: Importance of electrolyte-phase diffusion. *J. Power Sources* **2019**, *426*, 216–222. [CrossRef]

5. Bruch, M.; Millet, L.; Kowal, J.; Vetter, M. Novel method for the parameterization of a reliable equivalent circuit model for the precise simulation of a battery cell's electric behavior. *J. Power Sources* **2021**, *490*. [CrossRef]
6. Karger, A.; Wildfeuer, L.; Maheshwari, A.; Wassiliadis, N.; Lienkamp, M. Novel method for the on-line estimation of low-frequency impedance of lithium-ion batteries. *J. Energy Storage* **2020**, *32*, 101818. [CrossRef]
7. Gantenbein, S.; Weiss, M.; Ivers-Tiffée, E. Impedance based time-domain modeling of lithium-ion batteries: Part I. *J. Power Sources* **2018**, *379*, 317–327. [CrossRef]
8. Ciucci, F. Modeling electrochemical impedance spectroscopy. *Curr. Opin. Electrochem.* **2019**, *13*, 132–139.. [CrossRef]
9. Waag, W.; Fleischer, C.; Sauer, D.U. On-line estimation of lithium-ion battery impedance parameters using a novel varied-parameters approach. *J. Power Sources* **2013**, *237*, 260–269. [CrossRef]
10. Schmidt, R. Impedance Spectroscopy of Electroceramics. In *Ceramic Materials Research Trends*; Lin, P.B., Aguiar, R., Eds.; Nova Science Publ.: New York, NY, USA, 2007.
11. Schönleber, M.; Klotz, D.; Ivers-Tiffée, E. A Method for Improving the Robustness of linear Kramers-Kronig Validity Tests. *Electrochim. Acta* **2014**, *131*, 20–27. [CrossRef]
12. Witzenhausen, H. Elektrische Batteriespeichermodelle: Modellbildung, Parameteridentifikation und Modellreduktion. Ph.D. Thesis, Rheinisch-Westfälischen Technischen Hochschule Aachen, Aachen, Germany, 2017.
13. Illig, J.; Ender, M.; Chrobak, T.; Schmidt, J.P.; Klotz, D.; Ivers-Tiffée, E. Separation of Charge Transfer and Contact Resistance in LiFePO4-Cathodes by Impedance Modeling. *J. Electrochem. Soc.* **2012**, *159*, A952–A960. [CrossRef]
14. Schmidt, J.P.; Berg, P.; Schönleber, M.; Weber, A.; Ivers-Tiffée, E. The distribution of relaxation times as basis for generalized time-domain models for Li-ion batteries. *J. Power Sources* **2013**, *221*, 70–77. [CrossRef]
15. Sabet, P.S.; Stahl, G.; Sauer, D.U. Non-invasive investigation of predominant processes in the impedance spectra of high energy lithium-ion batteries with Nickel-Cobalt-Aluminum cathodes. *J. Power Sources* **2018**, *406*, 185–193. [CrossRef]
16. Schichlein, H.; Müller, A.C.; Voigts, M.; Krügel, A.; Ivers-Tiffée, E. Deconvolution of electrochemical impedance spectra for the identification of electrode reaction mechanisms in solid oxide fuel cells. *J. Appl. Electrochem.* **2002**, *32*, 875–882. [CrossRef]
17. Hershkovitz, S.; Baltianski, S.; Tsur, Y. Harnessing evolutionary programming for impedance spectroscopy analysis: A case study of mixed ionic-electronic conductors. *Solid State Ionics* **2011**, *188*, 104–109. [CrossRef]
18. Goldammer, E.; Kowal, J. Determination of the Distribution of Relaxation Times by Means of Pulse Evaluation for Offline and Online Diagnosis of Lithium-Ion Batteries. *Batteries* **2021**, *7*, 36. [CrossRef]
19. Lain, M.J.; Brandon, J.; Kendrick, E. Design strategies for high power vs. High energy lithium ion cells. *Batteries* **2019**, *5*, 64. [CrossRef]
20. Schmidt, J.P. *Verfahren zur Charakterisierung und Modellierung von Lithium-Ionen Zellen*; Karlsruher Institut für Technologie: Karlsruhe, Germany, 2013.
21. Schmidt, J.P.; Ivers-Tiffée, E. Pulse-fitting—A novel method for the evaluation of pulse measurements, demonstrated for the low frequency behavior of lithium-ion cells. *J. Power Sources* **2016**, *315*, 316–323. [CrossRef]
22. Sturm, J.; Rheinfeld, A.; Zilberman, I.; Spingler, F.; Kosch, S.; Frie, F.; Jossen, A. Modeling and simulation of inhomogeneities in a 18650 nickel-rich, silicon-graphite lithium-ion cell during fast charging. *J. Power Sources* **2019**, *412*, 204–223. [CrossRef]
23. Klotz, D. *Characterization and Modeling of Electrochemical Energy Conversion Systems by Impedance Techniques*; KIT Scientific Publishing: Karlsruhe, Germany, 2012.
24. Schichlein, H. *Experimentelle Modellbildung für die Hochtemperatur-Brennstoffzelle SOFC*; Universität Karlsruhe (TH): Aachen, Germany, 2003.
25. Wan, T.H.; Saccoccio, M.; Chen, C.; Ciucci, F. Influence of the Discretization Methods on the Distribution of Relaxation Times Deconvolution: Implementing Radial Basis Functions with DRTtools. *Electrochim. Acta* **2015**, *184*, 483–499. [CrossRef]
26. Boukamp, B.A. A Linear Kronig-Kramers Transform Test for Immittance Data Validation. *J. Electrochem. Soc.* **1995**, *142*, 1885. [CrossRef]
27. Saccoccio, M.; Wan, T.H.; Chen, C.; Ciucci, F. Optimal Regularization in Distribution of Relaxation Times applied to Electrochemical Impedance Spectroscopy: Ridge and Lasso Regression Methods—A Theoretical and Experimental Study. *Electrochim. Acta* **2014**, *147*, 470–482. [CrossRef]
28. Tikhonov, A.N.; Goncharsky, A.V.; Hazewinkel, M. *Numerical Methods for the Solution of Ill-Posed Problems*; Springer: Dordrecht, The Netherlands, 2010.
29. Hahn, M.; Schindler, S.; Triebs, L.C.; Danzer, M.A. Optimized Process Parameters for a Reproducible Distribution of Relaxation Times Analysis of Electrochemical Systems. *Batteries* **2019**, *5*, 43. [CrossRef]
30. Hansen, P.C. Analysis of Discrete Ill-Posed Problems by Means of the L-Curve. *SIAM Rev.* **1992**, *34*, 561–580. [CrossRef]
31. Hansen, P.C. The L-Curve and Its Use in the Numerical Treatment of Inverse Problems. Available online: https://orbit.dtu.dk/en/publications/the-l-curve-and-its-use-in-the-numerical-treatment-of-inverse-pro-2 (accessed on 18 May 2021).
32. Choi, M.B.; Shin, J.; Ji, H.I.; Kim, H.; Son, J.W.; Lee, J.H.; Kim, B.K.; Lee, H.W.; Yoon, K.J. Interpretation of Impedance Spectra of Solid Oxide Fuel Cells: L-Curve Criterion for Determination of Regularization Parameter in Distribution Function of Relaxation Times Technique. *JOM* **2019**, *71*, 3825–3834. [CrossRef]
33. Press, W.H. *Numerical Recipes in C: The Art of Scientific Computing*, 2nd ed.; Reprinted with Corr. to Software Version 2.10; Cambridge University Press: Cambridge, UK, 2002.

34. The MathWorks Inc. MATLAB MultiStart. 2021. Available online: https://de.mathworks.com/help/gads/multistart.html (accessed on 5 May 2021).
35. Reiter, C.; Wassiliadis, N.; Wildfeuer, L.; Wurster, T.; Lienkamp, M. Range Extension of Electric Vehicles through Improved Battery Capacity Utilization: Potentials, Risks and Strategies. In Proceedings of the 2018 21st International Conference on Intelligent Transportation Systems (ITSC), Maui, HI, USA, 4–7 November 2018; pp. 321–326. [CrossRef]
36. Sonn, V.; Leonide, A.; Ivers-Tiffée, E. Combined deconvolution and CNLS fitting approach applied on the impedance response of technical Ni/ 8YSZ cermet electrodes. *J. Electrochem. Soc.* **2008**, *155*, B675–B679. [CrossRef]
37. Franklin, A.D.; de Bruin, H.J. The fourier analysis of impedance spectra for electroded solid electrolytes. *Phys. Status Solidi (a)* **1983**, *75*, 647–656. [CrossRef]
38. Hust, F.; Witzenhausen, H.; Sauer, D.U. Distribution of relaxation times for lithium-ion batteries. In Proceedings of the 9th International Symposium on Electrochemical Impedance Spectroscopy, Okinawa, Japan, 17–20 June 2013.
39. Tesler, A.B.; Lewin, D.R.; Baltianski, S.; Tsur, Y. Analyzing results of impedance spectroscopy using novel evolutionary programming techniques. *J. Electroceram.* **2010**, *24*, 245–260. [CrossRef]
40. Tuncer, E.; Macdonald, J.R. Comparison of methods for estimating continuous distributions of relaxation times. *J. Appl. Phys.* **2006**, *99*, 074106. [CrossRef]

2.2.2 Online Estimation of Resistance Parameters in Electric Vehicles

Once in operation within a BEV, the resistance of lithium-ion cells changes due to aging, and the extent, to which different kinetic loss processes are affected, depends on the aging domain and conditions. To accurately reflect the dynamic behavior during advanced aging, the RC parameters of a deployed ECM must be updated over time to maintain validity. The method presented in the previous section relies on specific test protocols and high-precision measurement equipment. In contrast, BEV operation profiles consist of a repetitive yet unpredictable sequence of charging, parking, and driving. Additionally, current and voltage sensors are of lower quality to save costs. This makes the previously proposed method based on the DRT inapplicable for the online application. Motivated by research question 2b), this section presents a new method for online parameterization of high- and low-frequency resistance, which works with arbitrary load profiles in BEVs. Figure 2.5 illustrates how the results and methods from the previous sections are utilized and provides an overview of the proposed method presented in Study III.

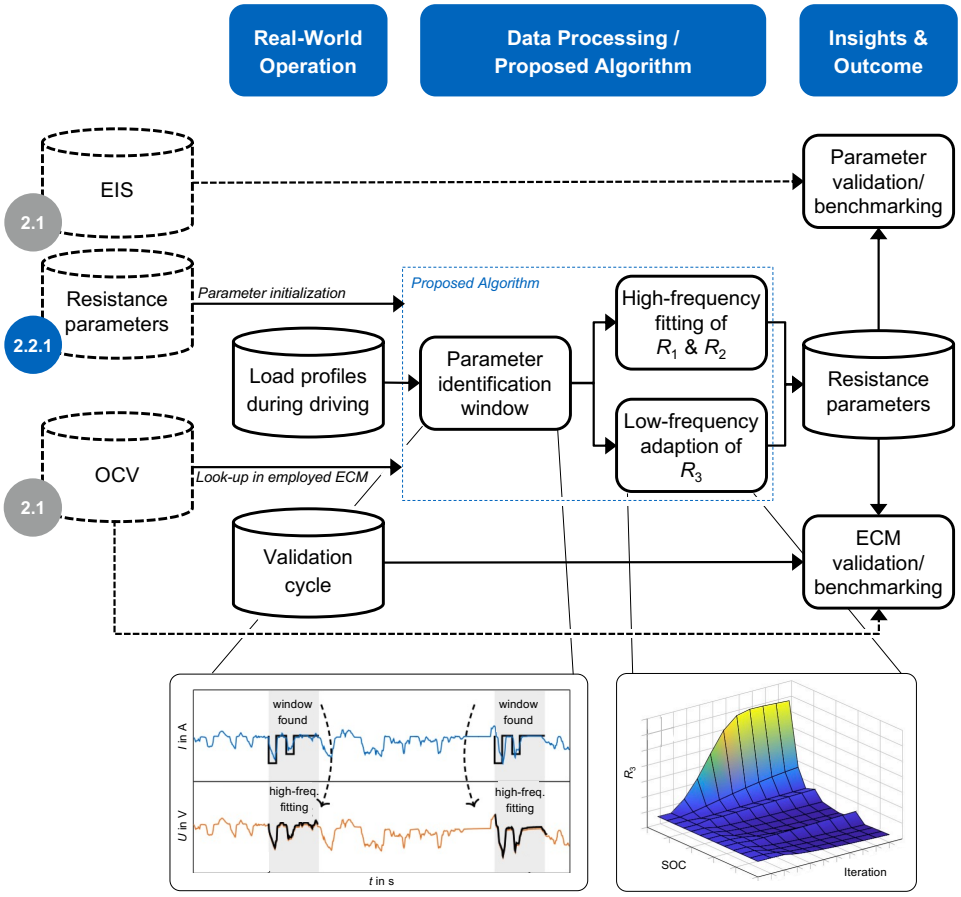

Figure 2.5: Graphical summary of Study III [3].

Despite its unpredictability, typical BEV load profiles contain valuable information to determine resistance parameters. Regenerative braking and subsequent acceleration at a traffic light, for example, excite the battery similarly to current pulses in the lab. The first step of the proposed algorithm is to detect suitable parameter identification windows, which fulfill certain requirements:

1. **Initiate the window** if the current remains below a certain threshold for a specified time.

2. **Accept the window** if the current remains above a certain threshold for a specified time.
3. **Terminate the window** if the amount of collected data exceeds the storage capacity of the computing hardware.

The design of the parameterization algorithm was further motivated based on theoretical considerations about the smallest and largest observable time constants in such parameter identification windows. The smallest observable time constant $\tau_{\mathrm{min}} = \Delta t / \pi$ is determined by the sampling rate Δt according to the Nyquist-Shannon theorem. Assuming a sampling rate of 100 ms, this means that distinct determination of the pure ohmic resistance R_{ohm} is not feasible. The extent to which R_{SEI} and R_{ct} can be separated depends on the cell type and operating conditions. The largest observable time constant τ_{max} is dependent on the measurement duration T_{meas} and determined as $\tau_{\mathrm{max}} = T_{\mathrm{meas}} / (2 \cdot \pi)$. Violating the criteria for the largest observable time constant can result in unrealistic resistance parameters with no physical relevance, which means that the low-frequency behavior cannot be captured reasonably within a parameter identification window.

The basic idea to overcome this challenge is to decouple the parameterization of the high-frequency and low-frequency resistance into a separate logic. Concretely, an ECM with 3 RC elements is employed out of which the first two RC elements are parameterized using a conventional non-recursive fitting algorithm during the identified windows. The third RC element, which should reflect the low-frequency behavior, is determined outside of the window by using a closed-loop feedback cycle. R_3 is adjusted iteratively by minimizing the remaining error of the simulated voltage in the parameter identification window with a proportional control algorithm. In this approach, all resistance parameters are either fitted or adapted and good starting values are beneficial for numerical stability. For this purpose, the parameters determined from the DRT can be used.

To test the algorithm, real-world operation was mimicked by scaling current profiles from vehicle measurements with a Volkswagen e-Golf to the cell level. Parameters obtained with this method were validated against measured impedance spectra. Furthermore, parameters were compared with the results of a benchmark algorithm, in which R_3 was determined within the parameter identification window rather than through out-of-window adaptation by the proposed observer logic. The presented algorithm delivers consistent and physically reasonable parameters and is superior compared to the benchmark algorithm, especially in the low-frequency region. Lastly, a similar validation cycle to that in the previous section was used to validate the obtained parameters in the time domain, i.e., when integrated into an ECM. Compared to the benchmark algorithm, the proposed algorithm achieved a considerably lower RMSE and less systematic error across all phases of the validation cycle.

Contribution

Alexander Karger and Leo Wildfeuer are shared first authors of the article.

Alexander Karger: Conceptualization, Methodology, Software, Data curation, Writing - original draft. Leo Wildfeuer: Conceptualization, Methodology, Investigation, Data curation, Writing - original draft. Arpit Maheshwari: Conceptualization, Writing - original draft. Nikolaos Wassiliadis: Writing - review & editing. Markus Lienkamp: Writing - review & editing, Supervision.

Novel method for the on-line estimation of low-frequency impedance of lithium-ion batteries

Alexander Karger*, Leo Wildfeuer*, Arpit Maheshwari, Nikolaos Wassiliadis and Markus Lienkamp
*Both authors contributed equally as first authors

Journal of Energy Storage, Volume 32, p. 101818, 2020
Digital Object Identifier: 10.1016/j.est.2020.101818
Permanent Weblink: https://doi.org/10.1016/j.est.2020.101818

Journal of Energy Storage 32 (2020) 101818

Contents lists available at ScienceDirect

Journal of Energy Storage

journal homepage: www.elsevier.com/locate/est

Novel method for the on-line estimation of low-frequency impedance of lithium-ion batteries

Alexander Karger[1,a], Leo Wildfeuer[*,1,a,b], Arpit Maheshwari[a], Nikolaos Wassiliadis[b], Markus Lienkamp[b]

[a] TWAICE Technologies GmbH, Munich, Germany
[b] Institute of Automotive Technology, Department of Mechanical Engineering, Technical University of Munich, Germany

ARTICLE INFO

Keywords:
Lithium-ion batteries
Impedance estimation
On-line algorithm
Equivalent circuit model
Low-frequency
Degradation diagnostics

ABSTRACT

Impedance is an important characteristic of lithium-ion batteries since it directly influences their power capability. However, battery impedance is highly dependent on the operating condition and increases over the lifetime of the battery, due to degradation of the latter. Continuous tracking of the impedance can hence provide meaningful insights into the aging status of a battery. However, the on-line determination of battery impedance parameters, especially for its low-frequency part, is a challenging task, which has not yet been solved unambiguously in literature. This work provides an algorithm for the on-line determination of battery impedance, which features a novel approach to quantifying the impedance caused by diffusion processes at low frequencies. The algorithm works by parameterizing an equivalent circuit model comprised of RC elements, which reproduces the Li-ion kinetics. The on-line functionality is enabled by parameterizing the model during parameter identification windows of battery operating data, which allow for the separation of high-frequency and low-frequency dynamics. The developed algorithm is designed in such a way that it can in future be embedded into a low-cost microcontroller by taking into account the relevant computational and memory limitations. During experimental validation with a commercial Li-ion battery, the root-mean-square error of the simulated voltage during diverse static and dynamic loads is reduced by over 50% compared to a benchmark algorithm without the proposed approach.

1. Introduction

1.1. Motivation

Car manufacturers are increasingly working on the development of battery electric vehicles (BEVs) to replace the traditional internal combustion engine vehicle, so as to reduce the greenhouse gas footprint of their range [1]. Lithium-ion batteries (LIBs) have so far been the first choice as the primary source of energy for BEVs due to their high power and energy densities [2]. Aging is an important concern, since the LIB represents the single largest cost factor for BEVs [3]. Crucially, all aging mechanisms evolve at substantially different rates depending on operating and storage conditions, and are specific to the battery chemistry [4]. Therefore, these mechanisms must be determined for each battery individually in order to estimate the remaining service life, to ensure safe operation and to permit decision making on second-life applications [5].

Determination of battery impedance can be used to non-destructively quantify the kinetics inside a cell, which is reflected in the dynamic relationship between the input current and the resulting battery voltage. Under laboratory conditions, prior to the deployment of the battery in the field, battery impedance can be determined from either time-domain measurements (e.g. current pulses [6]) or from frequency-domain measurements (e.g. by electrochemical impedance spectroscopy (EIS) [7]). Here, the cell is typically excited by specific, predefined excitation signals [8–13], which are designed in such a way that all electrochemical effects to be identified are clearly discernible.

However, such a priori characterization can only be employed on the pristine LIB, while impedance estimation over the service life of a LIB can provide meaningful insight into its aging state [14–18]. Therefore, on-line impedance estimation algorithms which run on the battery management system (BMS) are needed. Using updated impedance parameters also enhances important BMS functionalities such as the accurate estimation of the state of available power [19].

* Corresponding author:.
E-mail addresses: alexander.karger@tum.de (A. Karger), leo.wildfeuer@tum.de (L. Wildfeuer).
[1] A.K. & L.W. contributed equally as first authors.

https://doi.org/10.1016/j.est.2020.101818
Received 18 May 2020; Received in revised form 7 August 2020; Accepted 25 August 2020

Nomenclature

C_{max}	Maximum C-rate to be considered small enough for the search of parameter identification windows
C_{min}	Minimum C-rate to be considered large enough for the search of parameter identification windows
E_{RMS}	Root-mean-square error
U_{Error}	Model error voltage, equivalent to the difference between measured and simulated voltage
I_C	Current over a capacitance in an RC element
I_{meas}	Measured current
I_R	Current over a resistor in an RC element
N	Total number of sampling points in a time-discrete signal
$\mathbf{P}$	Parameter set for an equivalent circuit model
$\mathbf{P}_{reduced}$	Simplified parameter set for an equivalent circuit model
R_i	Resistance of the i-th RC element in an equivalent circuit model
R_{ct}	Current-dependent charge-transfer resistance of the first RC element in an equivalent circuit model
C_i	Capacitance of the i-th RC element in an equivalent circuit model
C_{nom}	Nominal cell capacity
T_{hc}	Time of sufficiently large current for the search of parameter identification windows
T_{meas}	Measurement duration
T_{relax}	Relaxation time before parameter identification window (PIW) initiation
U_{sim}	Terminal voltage in an equivalent circuit model, i.e. simulated battery voltage
U_i	Voltage over the i-th RC element in an equivalent circuit model
$U_{err,iRC}$	Error voltage for an i-RC equivalent circuit model
R_0	Resistance of the ohmic resistor
f_{cost}	Cost function, which is minimized during the search for optimal parameters
f_{max}	Maximum observable frequency
f_{min}	Minimum observable frequency
f_{meas}	Measurement frequency
f_{obs}	Observable frequency for a given measurement duration
n	Sampling point in a time-discrete signal
k_1	Currentdependence of the first RC element in an equivalent circuit model
τ_{max}	Largest observable time constant
τ_{min}	Smallest observable time constant
Δt_{meas}	Measurement sampling interval
t	Time

Depending on the application, the load profiles are typically unpredictable and contain a broad range of different dynamics, which makes on-line impedance estimation a challenging task.

The on-line estimation of battery impedance parameters has been the subject of many studies in the past. In the following subsection, an overview about different methods of on-line impedance parameter estimation is given. The main challenges posed by hardware limitations and unpredictable load profiles are presented and previous approaches to cope with these problems are summarized.

1.2. State of the art in on-Line impedance estimation

To separate the characteristic impedance parameters influencing the current-voltage relationship on-line, battery models are often deployed and continuously parameterized. On-line model parameterization algorithms must comply with strict hardware requirements, as the computational resources provided by the BMS are limited. Compared to physics-based and data-driven models, equivalent circuit models (ECMs) are the dominating technique for on-line applications due to their simplified mathematical and numerical approaches [19,20], which allow them to predict battery behavior in real time.

ECMs use passive electrical components, such as resistors and capacitors, to mimic the behavioral response of an LIB. ECMs are ideally designed in such a way that there is a strong physical relation between the model parameters and the underlying electrochemical processes within the cell. For battery applications, the simplest ECM is in the form of an ideal voltage source, modeling the open circuit behavior, in series with a resistor, which models the ohmic resistance caused by current collectors, active material, electrolyte and separator. However, this approach, typically referred to as the RINT-model [21], neglects dynamic effects inside the battery. More complex ECMs include resistor-capacitor (RC) elements to characterize the battery transient response as a result of the solid electrolyte interphase, the charge transfer and diffusion inside the active materials as well as in the electrolyte. In previous studies, the number of RC elements connected in series varied between one RC element [22–24], two RC elements [8,9] and higher numbers of RC elements [25,26]. The number of RC elements are typically chosen with respect to the dynamics of the load profile, the required modeling accuracy and the parameterization method.

Farmann and Sauer [27] showed in their review that models with more sophisticated ZARC elements have the potential for higher model accuracy. However, there is no transfer function from the frequency- to the time-domain for ZARC elements. Because of this, they are also typically approximated by a discrete number of serial RC elements in the time-domain. Other reviews of different ECM layouts have been conducted by Hu et al. [28] and Nejad et al. [20], where the trade-off between modeling accuracy and computational effort is highlighted.

It is not only with regard to the model structure, but also in terms of the chosen parametrization algorithm, that a large variety can be found in literature. Waag et al. [29] reviewed different algorithms for the on-line estimation of impedance parameters from time-domain data. In general, one can distinguish between two groups of estimation algorithms: recursive algorithms and non-recursive algorithms. Recursive algorithms include Kalman-filters and their derivate algorithms, such as employed in [30,31], as well as recursive least squares (RLS) approaches. The advantages of such algorithms are that, because of their recursive nature, little memory is needed, and computation times are fast [32]. However, this comes at the cost of possible divergence problems when the battery model inaccurately reproduces the behavior of the battery [30]. The stability of such approaches can be improved by introducing a sliding window, where the error squares are averaged over a pre-defined number of historical sampling points, such as employed in [33–35]. Whereas recursive methods can be improved by using more sampling points, non-recursive methods are explicitly designed to make use of such a batch of data [32]. Because parameters are iteratively searched using the same batch of data until convergence requirements are met, non-recursive methods provide higher stability and accuracy than recursive methods [29].

Waag et al. [36] and Farmann et al. [26] introduced systematic criteria for the initializiation and acceptance of these data batches used for parameter estimation. The definition of criteria for such parameter identification window (PIWs) is superior to the above-described sliding window approach, since meaningful impedance parameters can only be generated when, e.g., the initial voltage in the model capacitances are known [26]. Baumann et al. [5] expanded on this idea by proposing an impedance estimation algorithm, which searches for precisely defined patterns in the current profile to identify suitable PIWs. The goal was to find current profiles which resemble reproducible laboratory conditions to enable the consistent estimation of parameters during non-recursive fitting. The functional principle of a PIW search and subsequent ECM

parameter fitting is schematically presented in Fig. 1.

The memory and computational capability of a BMS narrow down the degrees of freedom in designing a PIW, as they limit the maximum length of the PIW and the data sampling rate, respectively. The influence of the sampling rate on the quality of identified parameters was previously studied by Gu et al. [37], who found that the accuracy of a 2RC ECM can be greatly improved when the sampling frequency is increased from 0.2 Hz to 10 Hz during parameter estimation. This result is expected, because the sampling rate dictates the upper limit in the observable spectrum of the estimated impedance. Lower sampling rates reduce the visibility of high-frequency (HF) dynamics, i.e., ohmic, solid electrolyte interphase and charge-transfer resistances. The influence of the window was studied by Huai et al. [32]. They investigated window sizes between 30 s and 600 s, and found that a longer PIW is beneficial to the fitting accuracy of the model voltage. This is also expected, since the amount of data stored in a PIW dictates the lower limit in the observable spectrum of the estimated impedance. The longer the PIW, the more low-frequency (LF) dynamics, i.e., diffusion effects, become visible.

One could suggest increasing the sampling rate and window size until all impedance parameters of interest are identifiable. However, a higher sampling rate and longer window size lead to a higher demand of BMS memory and computational resources, which are limited in practice. Additionally, even if more hardware resources were available on a BMS, the parameterization of LF impedance from an ever longer PIW is difficult. This is because, under dynamic battery load, the voltage response is influenced by both HF dynamics, and LF dynamics. When fitting ECM parameters with different timescales simultaneously, optimization algorithms can suffer from numerical problems [38], as was illustrated in [39–41]. Furthermore, since the impedance is dependent on the SOC and temperature, larger window sizes increasingly violate the assumption of constant operating conditions. Thus, mapping a single set of impedance parameters to such windows becomes unreasonable.

In previous publications, these issues were often tackled by simply neglecting LF impedance parameters during on-line parameter estimation [29]. However, LF impedance contributes significantly to the absolute impedance of a LIB during real-world loading, and accurately estimating these diffusion characteristics can provide meaningful insights into the aging state.

A small number of approaches have already worked on algorithmic solutions to overcome these problems. Hu et al. [41] proposed a two-timescale scheme, where HF and LF dynamics were estimated individually. They assumed the HF and LF ranges to be far enough apart that they could be separated using linear high-pass and low-pass filters on the measurement data. They used an RLS estimation and parameterized a 2RC ECM from pulses of varying frequency, and found an accuracy improvement over a fitting approach without filtering.

Zhang et al. [39] expanded on [41] by employing non-linear filters that were iteratively applied to increase the modeling accuracy even further. They labeled their approach 'decoupled weighted RLS'.

Dai et al. [40] suggested a different method of estimating the battery dynamics on separate timescales. They also used a 2RC ECM, but only parameterized one RC element using RLS, while the LF RC element was adapted at specific timesteps by an extended Kalman-Filter, when the change in state of charge (SOC) was greater than 0.2%. This condition was chosen to be indicative of the excitation of diffusion processes. The experimental results demonstrated modeling accuracy improvement over a conventional RLS approach for both RC elements.

While these approaches are promising and show an improvement over estimation algorithms without separate timescales, they do not use the potential of employing a non-recursive algorithm, since they do not implement PIWs, which are designed on the basis of systematic criteria. Instead, they all employ RLS approaches, which can suffer from stability issues. In addition, using a filter to separate HF and LF frequencies carries the disadvantage of possibly missing the physical interpretability of impedance parameters when the cut-off frequency of a filter is chosen poorly.

1.3. Goal, novelty and outline of this work

Based on the review of the state of the art in on-line estimation of battery impedance, the following major conclusions can be drawn: i) ECMs seem to be the most suitable modeling approach for on-line applications due to their low computational effort. ii) To continuously update impedance parameters on-line, non-recursive algorithms are favorable over recursive algorithms, since they promise higher numerical stability when initiated incorrectly. iii) Non-recursive algorithms require suitable PIWs to find physically reasonable parameters. iv) There is a clear advantage in separating HF and LF impedance fitting in two different algorithms.

To the best of our knowledge, there is no approach in the literature which fulfills the aforementioned requirements for a robust and accurate on-line impedance estimation algorithm covering a broad range of impedance dynamics, and which also considers BMS hardware limitations.

Therefore, this work aims to systematically derive such an algorithm. In summary, the main contributions of this work are:

- **Provision of a theoretical background to the observable range of an impedance spectrum in a PIW:** Based on BMS limitations, the smallest and largest observable time constants in a window-based impedance estimation approach are reviewed and applied to impedance spectra of a commercial LIB under various conditions. Implications for observable processes are derived. (Section 2)
- **Presentation of a novel observer-based approach for an on-line impedance estimation:** Based on the theoretical findings of Section 2, the integer-order time-domain ECM to model the impedance is derived. Furthermore, design characteristics of the PIW used to parameterize the ECM are presented. The new parameterization method consists of two algorithms running in parallel and on separate timescales. A distinction is drawn between HF impedance, which is identified within the PIW, and low-frequency (LF) impedance, which is identified outside of the PIW. (Section 3)
- **Experimental validation of the novel algorithm with a commercial LIB:** The novel approach is deployed on measurements with

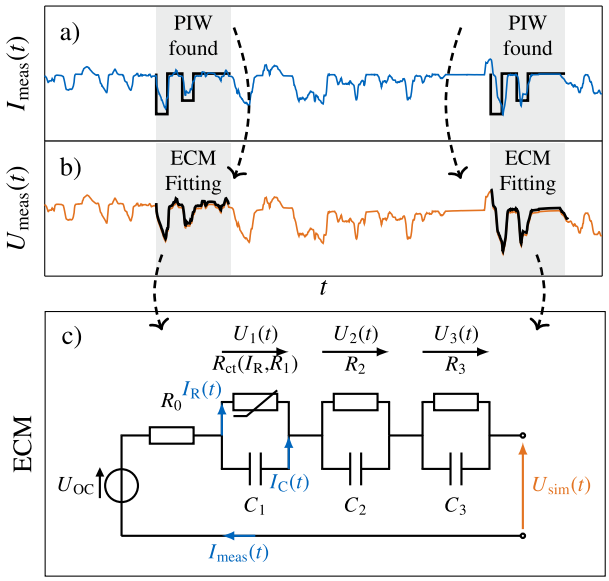

Fig. 1. Schematic representation of a) the parameter identification window (PIW) search, b) parameter fitting on the voltage signal and c) the employed ECM of the battery for the estimation of the battery impedance.

real driving cycles. The performance of the estimated impedance parameters is validated using a multi-step validation cycle and compared to a non-recursive benchmark algorithm. (Experimental methodology: Section 4, Validation results: Section 5)

The conclusions and the outlook for future work can be found in Section 6.

2. Theoretical considerations

2.1. Smallest observable time constants

The concept of a smallest observable time constant τ_{min} implies that all processes with a time constant smaller than τ_{min} cannot be modeled from measurement data [42]. The highest observable frequency of any time-discrete signal, such as a current and voltage signal measured by a BMS, is limited by the Nyquist-Shannon sampling theorem [43]. The theorem states that if a function contains no frequencies higher than the maximum observable frequency f_{max} Hz, it is completely determined by giving its ordinates at a series of points spaced $1/(2f_{max})$ s apart. By analogy, the inversion of this theorem states that for a given spacing of the sampling interval $\Delta t_{meas} = 1/f_{meas}$, the largest observable frequency is defined by

$$f_{obs} \leq \frac{f_{meas}}{2} = \frac{1}{2\Delta t_{meas}} \tag{1}$$

Using the definition of the time constant τ for an RC element, the smallest observable time constant can be calculated as [44]:

$$\tau_{min} = \frac{\Delta t_{meas}}{\pi} \tag{2}$$

However, the Nyquist-Shannon theorem holds for periodic signals only and for an infinite observation period. For a finite observation period, Schmidt et al. [12] claim that the smallest observable time constant for the laboratory-based parameter identification of lithium-ion cells with pulse measurements can be estimated by

$$\tau_{min,[12]} = \frac{100\Delta t_{meas}}{\pi}. \tag{3}$$

2.2. Largest observable time constants

Parameters for electrochemical processes with large time constants are typically determined from the relaxation behavior of the cell after a current pulse, since this allows for the largest observable timeframe of dynamic behavior without changing the SOC. For these types of relaxation measurements [44], there are again some empirical values derived from pulse measurements for the largest observable time constants based on the total measurement time T_{meas}. Klotz et al. [45] derive a value of

$$f_{obs} \geq \frac{4}{T_{meas}} \tag{4}$$

based on the relation of the width of a function in the time domain and the width of its spectrum in the frequency domain (leakage). This yields a largest observable time constant of

$$\tau_{max,[45]} = \frac{T_{meas}}{8\pi}. \tag{5}$$

Neglecting the effect of leakage yields the theoretically largest time constant under the assumption of one full excitation of a periodic process

$$\tau_{max,[44]} = \frac{T_{meas}}{2\pi}, \tag{6}$$

which is used by Schindler [44]. Violating the criterion for the largest observable time constant can lead to the formation of pseudo-processes with an unrealistically high resistance and which have no physical relevance. This happens because if model time constants are so large that they become unobservable, the algorithm can assign any arbitrary value without influencing the quality of the model fit. All of these limits are plotted for impedance spectra of a commercial 18650 cell of type US18650VTC5A by *Sony/Murata* (Section 4) at different temperatures and SOCs in Fig. 2 assuming $\Delta t_{meas} = 100$ms and $T_{meas} = 60$s. These values can be derived as typical limitations for a BMS [37].

2.3. Implications for observable processes

Within this work, HF impedance refers to the impedance at all frequencies above the inflection point at which the impedance changes

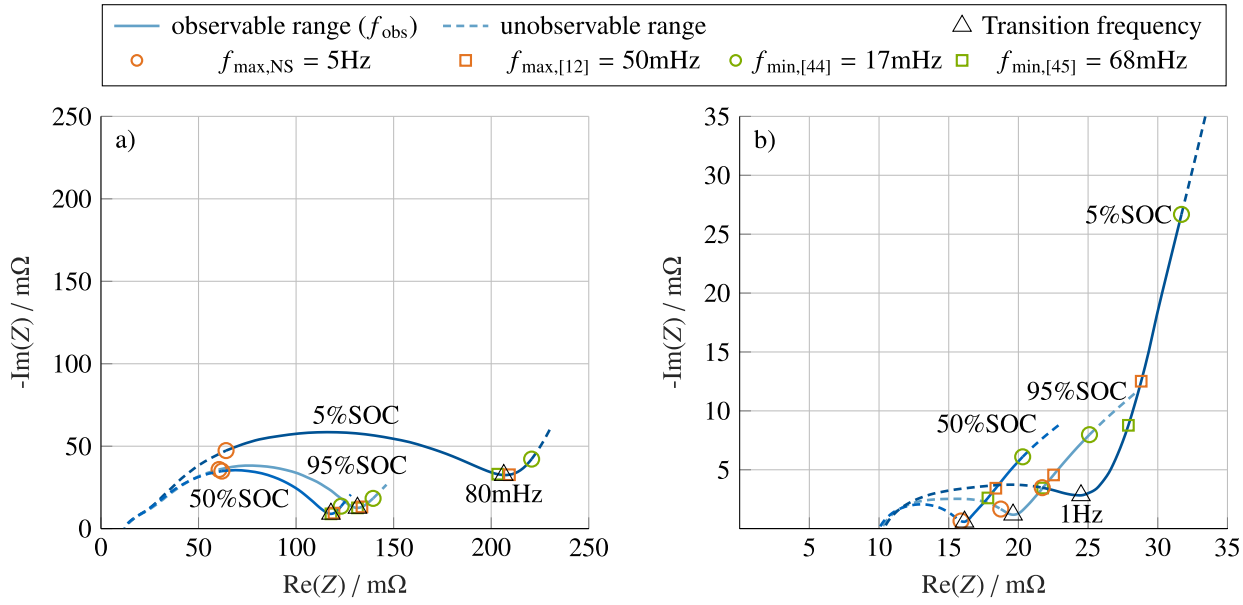

Fig. 2. Nyquist-Shannon limit and limit used by Schmidt [12] for the smallest observable time constant and limit used by Schindler [44] and Klotz et al. [45] for the largest observable time constant for the measured impedance spectrum of a commercial 18650 cell of type US18650VTC5A by *Sony/Murata* at different SOC at a) – 10°C ambient temperature and b) 20°C ambient temperature. Assumptions for calculation of the respective limits: $\Delta t_{meas} = 100$ms and $T_{meas} = 60$s.

to a quasi-linear behavior in a Nyquist plot, sometimes referred to as the transition frequency [46]. This transition frequency is marked by a black triangle in Fig. 2. LF impedance comprises the impedance at all frequencies below this transition frequency. The figure shows that the value of the transition frequency varies greatly between the different temperatures and SOCs. Hence, the electrochemical processes observable within the derived observable frequency range vary as well. Here we apply the more optimistic limit in either case. At 20°C, the observable range lies mostly within the LF region, while the HF region is mostly unobservable, even under the optimistic assumption of the Nyquist-Shannon limit. For LIBs, the semicircle in the HF region is typically associated with the charge transfer and double-layer capacitance at the electrodes [47]. If two semicircles are observable, they are typically attributed to the transport of ions across the solid electrolyte interface (SEI), which occurs at a higher frequency, and to the charge transfer and double-layer capacitance at the electrodes [48]. At − 10°C, the majority of the first semicircle is observable under the assumption of the Nyquist-Shannon limit. At all temperatures, under the optimistic assumption in [44], the observable range of LF impedance is comparable to the typical lowest frequency of EIS measurements (10 mHz). It is noticeable that the observable frequency range at − 10°C almost totally collapses when applying the more conservative limits presented in literature [12,45].

The full impedance spectrum of a nickel manganese cobalt oxide (NMC)-based lithium-ion cell is described in [11]. Schönleber describes that while the impedance changes significantly for the different SOCs, a subsequent analysis of the distribution of relaxation times reveals that the time constants of the LF processes stay approximately constant. Additionally, the distribution of relaxation times (DRT) reveals that the solid-state diffusion consists of two individual processes representing the solid-state diffusion of different particle sizes [11]. One of the two processes can be considered dominant in terms of the magnitude of the overvoltage, which is why the impedance spectrum approaches the form of a semicircle at the lowest frequencies. For the HF impedance however, SOC independence does not hold. Sabet et al. [49,50] reveal that, depending on the SOC, the charge transfer resistance is dominated by the charge transfer process of either the cathode or anode, leading to a shift in frequency over the SOC.

Based on the previous discussion of observable and real impedance spectra and the respective time constants, we can conclude the following: It is expedient to model three major kinetic properties of the battery on-line: charge-transfer, electrolyte diffusion and solid-state diffusion. With $T_{meas} = 60s$ however, the solid-state diffusion cannot be parametrized inside the PIW, even considering the less restrictive scenario given by Eq. (6). This demands a new method of parameterizing the LF impedance in the μHz-range outside of the PIW.

3. Proposed method

The functional principle of the observer algorithm, which is described in detail in the following section, is illustrated in Fig. 3. First, the employed ECM, which is used to describe the battery impedance, is derived. Afterwards, the design characteristics of the PIW, which triggers the two separate parameter estimation algorithms, are presented. Finally, the decoupled parametrization of HF impedance (HF fitting) and LF impedance (LF adaption) are described.

3.1. Employed ECM

Based on the findings in Section 2, the employed ECM consists of an ohmic resistance and 3 RC elements to model the three major kinetics (Fig. 1c)). Fractional-order models have recently attracted increasing interest in the field of on-line battery parameter identification [51,52]. For a behavioral battery model however, an integer-order ECM has proven sufficient for the real-time estimation of lithium-ion battery states [20]. Moreover, the novel method for the parametrization proposed in this work can be transformed to other ECM layouts without much effort.

In this model, the HF dynamics of the battery are modeled by the ohmic resistance and one current-dependent RC element. This ECM subset is identical to the proposed ECM in [36]. In particular, the term for the current-dependence of the charge transfer Eq. (9) is adopted from [36], where it is derived as a time-discrete formulation of the Butler-Volmer equation. The implementation of only one RC element for the HF dynamics is purposeful due to the derived limitation of the smallest observable time constant, which means that the SEI cannot be parametrized on-line under the assumption of typical BMS sampling rates. The LF impedance is modeled by the two remaining RC elements, which model electrolyte and solid-state diffusion respectively. One important thing to note is that parametrizing this ECM using any adapting algorithm neither guarantees nor necessitates that the parameters precisely reflect the intended physical effects in the battery. In fact, this model can never precisely reflect the intended physical effects, since RC elements can only approximate the impedance spectra of electro-chemical systems [53]. For a behavioral model however, only convergence to meaningful values must be ensured [29]. This convergence is maintained by having derived the model on the basis of a physical understanding of the battery.

For an on-line application, the described model can be described by the following set of discretized equations at sampling step n:

$$U_{\mathrm{sim},n} = U_{\mathrm{OC},n} + R_0 I_{\mathrm{meas},n} + U_{1,n} + U_{2,n} + U_{3,n} \tag{7}$$

with

$$U_{i,n} = U_{i,n-1} e^{\frac{-\Delta t_n}{R_{j,n} C_1}} + R_{j,n} \cdot I_{\mathrm{meas},n} \left(1 - e^{\frac{\Delta t_n}{R_{j,n} C_i}}\right) \tag{8}$$

with $i \in \{1, 2, 3\}$ and $j \in \{\mathrm{ct}, 2, 3\}$ using the term derived by Waag et al. [36]:

$$R_{\mathrm{ct},n} = R_1 \left(\frac{ln\left(k_1 (I_{\mathrm{meas},n} - I_{C,n-1}) + \sqrt{(k_1 (I_{\mathrm{meas},n} - I_{C,n-1}))^2 + 1}\right)}{k_1 (I_{\mathrm{meas},n} - I_{C,n-1})} \right) \tag{9}$$

using

$$I_{C,n} = I_{\mathrm{meas},n} - \frac{U_{1,n}}{R_{\mathrm{ct},n}}. \tag{10}$$

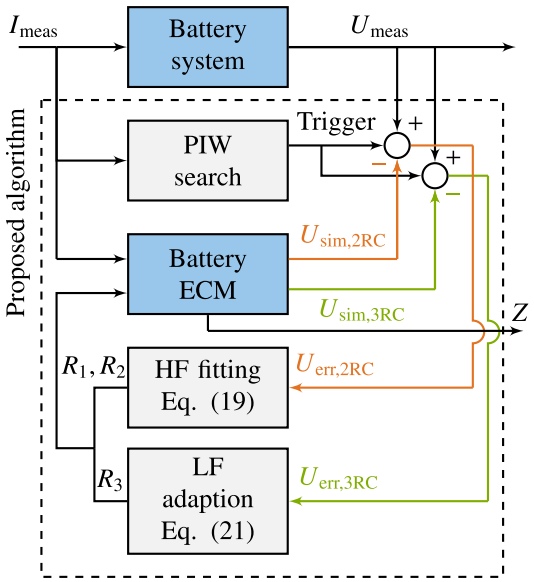

Fig. 3. Functional principle of the novel method for the on-line determination of RC elements with large time constants. The separate parameter estimation algortihms HF fitting and LF adaption are described in Sections 3.3 and 3.4 respectively.

In Eq. (9), k_1 is used as a factor that indicates the current-dependence of the charge-transfer process. The unit of k_1 is A^{-1}. Based on this set of equations, the model behavior is determined by the parameter set

$$\mathbf{P} = \{R_0, R_1, k_1, C_1, R_2, C_2, R_3, C_3\} \tag{11}$$

or, using $\tau = RC$, by

$$\mathbf{P} = \{R_0, R_1, k_1, \tau_1, R_2, \tau_2, R_3, \tau_3\}. \tag{12}$$

To increase the numerical stability of the system, it can be useful to refrain from determining the time constants during the model fit [11,12], which reduces the system's degrees of freedom. This approach may be motivated by the discussed consistency of diffusion time constants over the SOC. The model behavior is hence described by the reduced parameter set

$$\mathbf{P}_{\text{reduced}} = \{R_{\text{ohm}}, R_1, k_1, R_2, R_3\}. \tag{13}$$

For such a reduced parameter set, the time constants have to be selected a priori, for example, by analyzing the DRT for appropriate measurements. The assumption of constant τs over the aging of the cell should be further investigated in the future, and for each cell individually before application in the field, but has been found to hold reasonably well over the aging of NMC pouch cells [54].

3.2. Design characteristics of the PIW

There are three requirements which are used to characterize the initiation, termination and acceptance of a PIW:

- **The PIW should only be initiated after a certain period of low current:** The recursive characteristic of Eqs. (7)–(12) implies that all initialization values $U_{1,n}$, $U_{2,n}$ and $U_{3,n}$ must be known or equal to zero at the beginning of the PIW for the calculated overvoltages to be independent of the previous parameter set. Note that "recursive characteristic" in this context refers only to the characteristic of the equations and not to the design of the optimization algorithm, which operates non-recursively because the parameters are searched on a batch of data simultaneously. These initialization values approach zero when $I_{\text{meas},n} \approx 0$ and are below 36.8% of their maximum values $\lim_{n\to\infty} U_{i,n}(I_0)$ after τ seconds of zero current. This yields the condition for the initialization of the PIW, which is that it should only be initiated after a certain period T_{relax} of $I_{\text{meas},n} \approx 0$. Violating this condition means that the dynamics of the previous operating data, which cannot be influenced by the adaption of the new parameter set, are carried over into the PIW. This leads to inconsistent determination of parameter sets dependent on the previous operating data. Within this work, a zero current period of $T_{\text{relax}} > \tau_2$ proved to be sufficient for the consistent determination of parameter sets. The reason for the dependence of T_{relax} on τ_2 lies in the proposed parameterization procedure presented in the next subsection. This condition can be further accentuated by employing zero current periods of up to $5\tau_2$, where the overvoltage has dropped to $< 1\%$ of its maximum value. Because an exactly-zero current condition is non-practical, the condition is employed as

$$\left| \frac{I_{\text{meas},n}}{C_{\text{nom}}} \right| < C_{\max} \tag{14}$$

where $C_{\max}$ must be large enough for the condition to not be violated by measurement noise, and small enough to ensure that the influence of $I_{\text{meas},n}$ on the overvoltages is negligible. Sometimes, the more lax condition of $I_{\text{meas},n} = const.$ is employed as a condition for the initialization of a PIW [29]. With this condition, the initialization values approach $\lim_{n\to\infty} U_{i,n}(I_0)$ and become quasi-constant. The problem with this is that the maximum overvoltage $\lim_{n\to\infty} U_{i,n}(I_0)$ also changes if the parameters in the ECM change, so that the previous dynamics are not fully decoupled from the new PIW.
- **The PIW data cannot exceed the hardware storing capability:** The definition of the length of the PIW depends on the maximum number of storable datapoints. Dependent on the sampling frequency Δt_{meas}, this can be translated into a maximum measurement period T_{meas}. The search pattern for the PIW cannot be longer than T_{meas} but should be long enough to determine the largest time constant of the determined RC elements, in this case R_2.
- **The PIW should only be accepted if it contains a certain period above a threshold current:** The final requirement for the PIW is that all parametrized physical effects must be sufficiently excited. This can be guaranteed by introducing a minimum C-rate $C_{\min}$, which has to be surpassed for a minimum time T_{hc} (time of high current). The reasoning behind this condition can be easily understood by looking at the boundary case of $I_{\text{meas},n} \approx 0$ over the entire PIW. In this case, the algorithm can assign any arbitrary value without any impact on the quality of the fit.

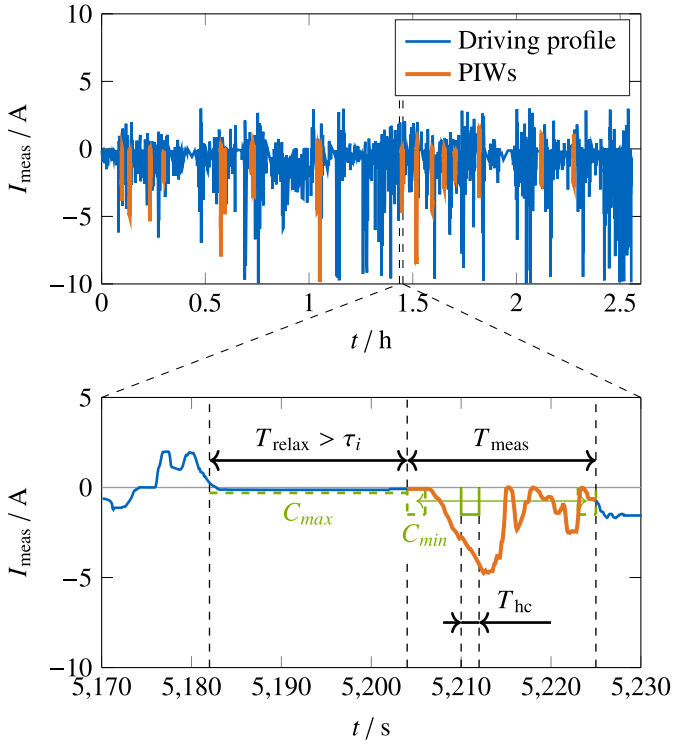

Fig. 4. Top: Current profile of a real driving cycle with identified parameter identification window (PIWs). Bottom: Schematic illustration of the characteristics of the PIWs.

The above-derived characteristics of the PIW search pattern are schematically illustrated in Fig. 4. This pattern allows for a separation between HF and LF impedance, since the HF dynamics are reasonably decayed at the beginning of the PIW. The number of integer-second sampling points in a PIW is henceforth denoted as N. The subscript n refers to the sampling steps inside a PIW.

The derived separation of HF and LF impedance means that the parameterization of the ECM can also be divided into two separate procedures. For this, the recursive Eqs. (7)–(12) are continuously calculated for the employed 3RC ECM at every sampling step ($U_{\text{sim,3RC}}$ in Fig. 3). Additionally, the model voltage without the overpotential of the third RC element ($U_{\text{sim,2RC}}$ in Fig. 3) is continuously calculated:

$$U_{\text{sim,2RC}} = U_{\text{sim,3RC}} - U_3 \tag{15}$$

Whenever a PIW is identified, two individual algorithms are executed.

3.3. HF Fitting

The HF fitting algorithm uses a non-recursive least-squares optimization to fit the parameters of the first and second RC element during the PIW. The goal of this optimization is to minimize the following cost function:

$$f_{\text{cost}} = \sum_{n=1}^{N} (U_{\text{meas},n} - U_{\text{sim,2RC},n} - U_{\text{err,2RC}})^2 \rightarrow min. \tag{16}$$

$U_{\text{sim,2RC},n}$ refers to the 2 RC model voltage inside a PIW, while $U_{\text{meas},n}$ is the corresponding measured voltage. The overvoltages in the two RC elements $U_{1,n=1}$ and $U_{2,n=1}$ at the beginning of the window are initialized as zero as a boundary condition for the optimization. This assumption is justified by the low-current period T_{relax} at the start of the PIW.

However, this is not true for $U_{3,n=1}$, which is not decayed after T_{relax} because of the higher time constant. This voltage difference at the beginning of the PIW, which is induced by LF overpotentials, must be taken into account. Subtracting $U_{3,n=1}$ is not suitable, because uncertainties of the estimated R_3 would be carried over into the fitting of R_1 and R_2.

This is why $U_{\text{err,2RC}}$ and $U_{\text{err,3RC}}$ are introduced and are defined as the difference between measured and simulated voltage at the first sampling step $n = 1$ of the PIW, respectively:

$$U_{\text{err,2RC}} = U_{\text{meas},n=1} - U_{\text{sim,2RC},n=1} \tag{17}$$

and

$$U_{\text{err,3RC}} = U_{\text{meas},n=1} - U_{\text{sim,3RC},n=1} \tag{18}$$

These two values are connected by the third RC element via

$$U_{\text{err,3RC}} = U_{\text{err,2RC}} - U_{3,n=1}. \tag{19}$$

$U_{\text{err,2RC}}$ is used in the cost function Eq. (16). This implies the assumption that the diffusion overvoltage is constant during the PIW, which is justified if the order of magnitude of the time constant of the third RC element is much greater than the order of magnitude of the time constant of the second RC element.

In this work, the non-recursive least-squares optimization is carried out by means of the *lsqnonlin* [55] in MATLAB. The *lsqnonlin* function employs a trust region-based algorithm to generate the optimal parameter set. A trust region is constructed around the initial parameter values and describes the region where the change of the cost function is predictable.

3.4. LF adaption

The third RC element representing the LF impedance is adjusted by using a closed-loop feedback circle. The input to this feedback loop is the $U_{\text{err,3RC}}$ introduced above. This variable represents the model error of $U_{\text{sim,3RC},n}$ caused by the third RC element, since the overvoltages $U_{1,n=1}$ and $U_{2,n=1}$ were previously assumed as zero. The output of the feedback loop is the adaption of R_3. Within this work, the adaption of R_3 is proportional to $U_{\text{err,3RC}}$

$$R_{3,\text{new}} = R_{3,\text{old}} + U_{\text{err,3RC}} R_{3,\text{old}} K_p, \tag{20}$$

which represents the basic equation of a proportional control algorithm. This classifies the feedback loop as a Luenberger observer [56]. R_3 is decreased or increased to minimize $U_{\text{err,3RC}}$ at every iteration. Changing R_3 changes the value of $U_{\text{err,3RC}}$ in the next iteration (Fig. 7a) so that R_3(SOC) converges towards a steady-state solution (Fig. 7b).

It should be noted that the behavior of $U_{\text{err,2RC}}$, which is used inside the HF fitting algorithm, is different to the plotted behavior of $U_{\text{err,3RC}}$ (Fig. 7a). $U_{\text{err,2RC}}$ is not intended to be minimized by the algorithm. It only shows how strongly the diffusion effects are excited, resulting in a difference of $U_{\text{sim,2RC},n}$ compared to U_{meas} even after the defined relaxation period at the beginning of the PIW.

Using this approach, R_3 can be adapted in intervals smaller than τ_3.

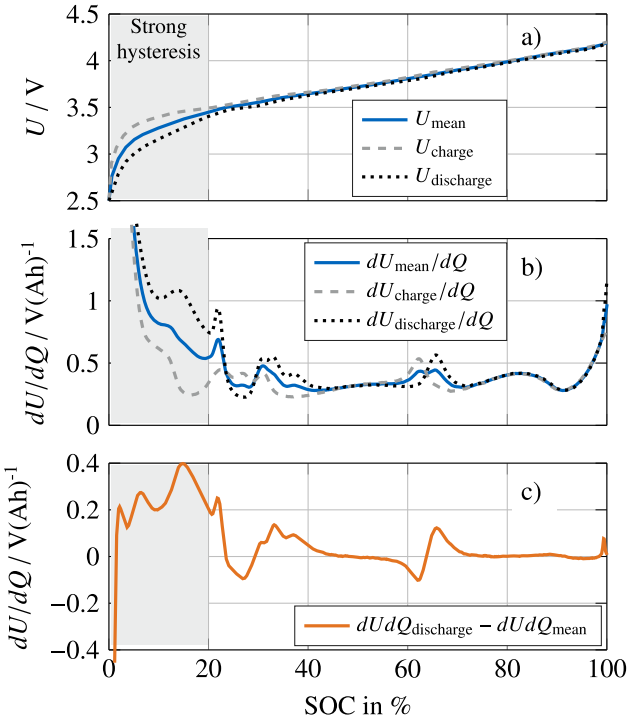

Fig. 5. a) Measured pseudo-OCV curve from C/50 charging and discharging at 20°C b) corresponding differential voltage of the charging, discharging and mean curves. Due to strong hysteresis in the low SOC area, validation results in Section 5 are presented separately from 100% to 20% SOC and 20% to 0% SOC.

Therefore R_3 can be expressed as a function of SOC, where the resolution is only limited by the time between two PIWs, which is not possible when fitting R_3 inside a PIW of size τ_3.

4. Experimental

The proposed algorithm is tested on a commercial 18650 cell of type US18650VTC5A by *Sony/Murata* with a rated capacity of C_{nom}=2.5 Ah. The anode active material consists of graphite with a small fraction of silicon added, whilst the cathode active material is nickel cobalt aluminum oxide (NCA) [57]. In the following, the current profiles used for parametrization and validation are introduced, respectively. Furthermore, tested configurations of the algorithms are presented.

4.1. Open-circuit potential

In our proposed algorithm, the open-circuit voltage (OCV) is not fitted but pre-determined and used as an input for the algorithm. In Fig. 5a), the pseudo-OCV obtained from averaging a charging and discharging curve with C/50 is shown. The corresponding differential voltage of the charging, discharging and mean curves is shown in Fig. 5b). Furthermore, the difference between the differential voltage of the mean and discharging curve is shown in Fig. 5c). It is noticeable that the location of the anode peaks at around 30% SOC and between 60% and 70% SOC is slightly shifted for charging and discharging curves, which is also reflected in a higher value for $dU_{\text{discharge}}/dQ - dU_{\text{mean}}/dQ$ in these ranges. Furthermore, it can be seen that the charging and discharging curves diverge strongly below 20% SOC to over 100 mV, which is assumed to be caused by the (de-)lithiation competition of graphite and silicon during charging and discharging in this SOC region [58]. Strong divergence between charging and discharging curves will cause high errors when averaging the two curves to a mean pseudo-OCV curve, which is used by the algorithms during parameterization and also during validation. This in turn might influence the parameter fitting and validation in these ranges, meaning

that this cell behavior must be kept in mind when analyzing the validation results. To account for this, we distinguish between the two SOC ranges (100% – 20% SOC and 20% – 0% SOC) during model validation in Section 5.

4.2. EIS

To validate whether the algorithm estimates physically reasonable parameters, validation is also carried out in the frequency-domain by comparing the estimated impedance parameters with the measured impedance spectra. Therefore, EIS measurements were performed at 20°C using a *Gamry Instruments Interface 5000*, whereby the hybrid EIS mode with an AC voltage of 10 mV rms, a frequency range of 5 kHz to 10 mHz and ten points per decade was used. EIS was performed every 5% SOC with a relaxation period of 3 h after discharging to the respective SOC.

4.3. Driving cycle for parameterization

The ECM parametrization is carried out with current profiles recorded during real driving cycles with a *Volkswagen eGolf*, which are concatenated so as to discharge the battery entirely. The employment of real driving profiles is crucial, in order to cover realistic frequency spectra of the load current [29] and to test the applicability of the PIW search pattern to real-world load. The sampling rate of this data is $f_{\text{meas}} = 10\text{Hz}$. One of the current profiles used is presented in Fig. 4, together with the PIWs identified by the window search algorithm. For the depicted current profile, the algorithm finds 13 PIWs, distributed over the entire SOC range.

4.4. Validation cycle

The validation is carried out by applying a defined current profile to the cell and to the parameterized ECM, and comparing the measured voltage with the simulated voltage. This specific current profile (Fig. 6), henceforth referred to as the validation cycle, consists of subsequent constant current (CC) charge (A) and discharge (B) phases with $C/5$, a repetitive synthetic profile (dynamic stress test (DST)) by means of discharging and charging current pulses between $-2C$ and $1C$ (C) and a dynamic driving profile (D), similar to the one used for the parameterization of the cells. Fig. 6 shows the validation cycle and the cell's voltage response, and highlights the respective regions evaluated during validation.

4.5. Configuration of the proposed algorithm

Table 1 lists the numerical values of the configuration parameters of the proposed algorithm. These parameters are: a) T_{relax} with C_{max}, which define the initiation condition for the PIW; b) T_{hc} with C_{min}, which define the acceptance condition for the PIW; c) K_p, which is the adaption parameter for R_3. These values can be used as an initial estimate when employing the described algorithm on different cell types. Table 2 lists the initial values used, as well as the lower and upper limits of the impedance parameters used as boundary conditions for the proposed algorithm.

The limits for the time constants are chosen with the following reasoning:

- $\tau_1 = 0.9\text{s}$ is chosen based on the calculation of the DRT of the impedance spectrum in Fig. 9 at 50% SOC. In this spectrum, $\tau = 0.005\text{s}$ is identified as the smallest time constant, which is, however, unobservable according to Eq. (1). Hence, R_1 can be interpreted as a blend between charge-transfer resistance and the resistance from ion transport through the SEI.
- $\tau_2 = 25\text{s}$ is also chosen based on the DRT, where a large peak appears at $\tau = 100\text{s}$. However, this peak appears mainly because of the EIS measurement limitations, where lower frequency processes cannot be distinguished from each other. Hence, R_2 can be interpreted as a blend of charge-transfer resistance and electrolyte diffusion resistance.
- $\tau_3 = 2000\text{s}$ is estimated from [11], where it is identified as the time constant of solid-state diffusion during low-frequency DRT. R_3 can be interpreted as a blend of electrolyte and solid-state diffusion.

This assignment of electrochemical effects is however only an approximation, since the kinetics of these effects change dramatically at different ambient temperatures (Fig. 2).

4.6. Benchmarking the algorithm

To assess the results of the proposed algorithm and the advantage of separating the fitting of the HF and LF impedance in two parallel algorithms (HF fitting and LF adaption in Fig. 3), a benchmark algorithm is needed. The configuration of this benchmark algorithm is also given in Table 1. The benchmark algorithm utilizes all described considerations about observable frequencies and the derived PIW pattern, meaning that it finds precisely the same PIWs as the proposed algorithm. However, R_3 is not adapted by the observer logic but instead also fitted inside the PIW. This is achieved by adding R_3 as a fitting parameter to the simplified parameter set from Eq. (12). This represents an equivalent implementation to the approach employed by Baumann [5]. Adding R_3 as a fitting parameter requires two adaptions to the parameterization procedure. Firstly, the cost function has to be adapted by a constant subtraction of $U_{\text{err,3RC}}$ instead of $U_{\text{err,2RC}}$:

$$f_{\text{cost}} = \sum_{n=1}^{N} (U_{\text{sim},n} - U_{\text{meas},n} - U_{\text{err,3RC}})^2 \rightarrow min. \tag{21}$$

This is required to compensate any difference in overvoltages between the model and the measurement at $n = 1$ resulting from incorrect diffusion parameters. Secondly, an initialization value for $U_3(n = 1)$ has to be defined. An initialization of $U_3(n = 1) = 0\text{V}$, equivalent to $U_1(n = 1)$ and $U_2(n = 1)$, is not practical, because the time-constant of R_3 is too large to allow for any significant change in U_3 over the course of the PIW. Hence, we initialize the overvoltage with the previous overvoltage so as to allow U_3 to change during a charge-throughput outside the PIW. As pointed out in Section 2, such an initialization is not desired, as the dynamics are then influenced by previously estimated parameters. However, it is required in order to benchmark the advantage of separate HF and LF impedance estimation.

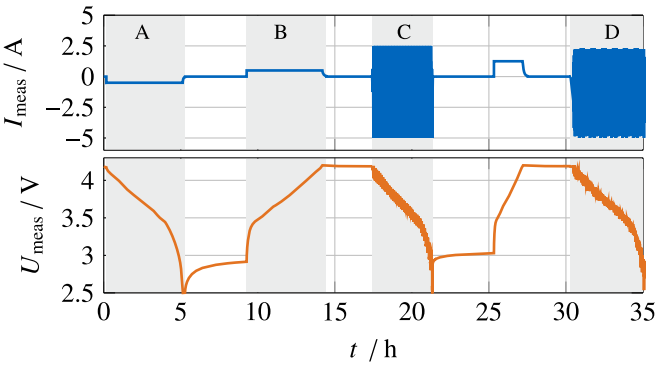

Fig. 6. Current profile (top) and voltage response (bottom) of the applied validation cycle at 20°C ambient temperature, used to validate the estimated impedance in the time domain. The validation cycle consists of a CC charge (A) and discharge (B) phase with $C/5$, a DST by means of discharging and charging current pulses between $-2C$ and $1C$ (C) and a dynamic driving profile (D).

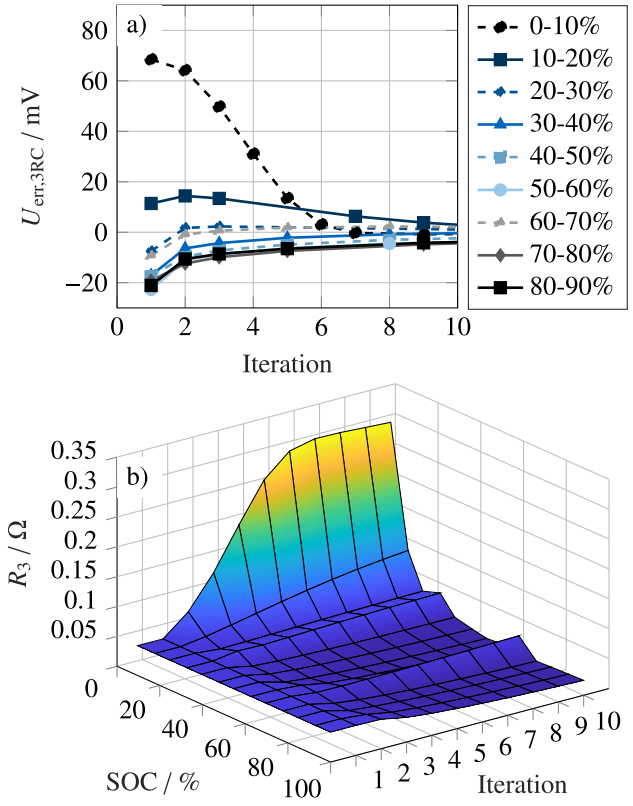

Fig. 7. a) Course of $U_{\mathrm{err,3RC}}$ using Eq. (20) during deployment of the algorithm on the real driving cycle for different SOCs. b) Corresponding adaption of R_3 for the PIWs found by the algorithm.

Table 1
Configuration parameters of the parameter identification window (PIW) applied for validation of the proposed and benchmark algorithm.

Purpose	Parameter	Proposed algorithm	Benchmark algorithm
Initiation of PIW			
	T_{relax} in s	$20 \approx \tau_2$	$20 \approx \tau_2$
	C_{max} in h^{-1}	0.1	0.1
Acceptance of PIW			
	T_{hc} in s	1	1
	C_{min} in h^{-1}	0.5	0.5
Initialization of PIW			
	$U_1(n=1)$ in V	0	0
	$U_2(n=1)$ in V	0	0
	$U_3(n=1)$ in V	-	$U_3(n=n-1)$
R_3 adaption	K_{p} in V^{-1}	0.5	-

Table 2
Initial values and lower and upper limits for the estimated impedance parameters used for the proposed algorithm.

	Initial value	Lower limit	Upper limit
R_0 in mΩ	20	0.1	250
R_1 in mΩ	5	0.1	150
k_1 in A^{-1}	0.01	0.01	0.01
R_2 in mΩ	20	0.1	150
R_3 in mΩ	50	1	900
τ_1 in s	0.9	0.9	0.9
τ_2 in s	25	25	25
τ_3 in s	2000	2000	2000

5. Model validation

5.1. Parameter identification

The parameterization is carried out by iteratively applying the algorithm to the same driving cycle for parameterization described in Section 4.3 until the value of $U_{\mathrm{err,3RC}}$ is reached, and R_3 therefore converges to a steady-state solution. This process is illustrated in Fig. 7, where a steady-state solution is achieved after around 10 iterations with the configuration in Table 1.

Fig. 7 a) shows the decreasing value of $U_{\mathrm{err,3RC}}$ over the course of the iterations and Fig. 7b) shows the corresponding course of R_3 for the different PIWs. After reaching a steady-state solution, the proper functioning of the algorithm is shown by a physically reasonable distribution of R_3 over the SOC range. A strong increase towards low SOCs and small peaks during the stage transitions of graphite between 20% SOC and 30% SOC and between 60% SOC and 70% SOC reflect the typical SOC dependency of the impedance [59–61].

Fig. 8 displays the parameterization results for all parameters with the proposed algorithm, as well as with the benchmark algorithm. One immediate result when comparing the parameter sets generated by the different algorithms is that the fitting of R_0 through R_2 is almost independent of the algorithm employed. This is expected, since the fitting procedure for these HF parameters is identical. The slight differences between these parameters result from the addition of R_3 during fitting with the benchmark algorithm.

The resistance R_3 on the other hand differs greatly between the two algorithms. The diffusion resistance is greatly underestimated with the benchmark algorithm, since R_3 is unobservable in the PIW according to Eqs. (5) and (6) and hence the benchmark algorithm always assigns the lower bound of 1 mΩ. This underestimation is also the reason why the calculated total resistance of the ECM is higher with the proposed algorithm.

There are two exceptions to this behavior, which are the PIWs at the two lowest SOCs. The reason for this is the discussed hysteresis of the tested cell at low SOCs. For the two mentioned PIWs, the difference between discharge and mean differential OCV (Fig. 5c) is greater than 0.2 V/Ah. During an exemplary PIW with a length of 20 s with an average current of the charge-throughput is around 14 mAh. This leads to a voltage error of 0.2 V/Ah $\cdot$ 14 mAh = 2.8 mV. This voltage difference is compensated for this exemplary current pulse by

$$R_3 = \frac{U_3}{I_0\left(1 - e^{\frac{-T_{\mathrm{meas}}}{\tau_3}}\right)} = 112.5\,\mathrm{m\Omega}, \tag{22}$$

which lies in the range of the values estimated by the benchmark algorithm for these PIWs. Hence, these values are attributed to the hysteresis of the OCV in this range and do not reflect a correctly estimated diffusion. With the proposed algorithm, this issue is circumvented, since R_3 is estimated outside of the PIW.

5.2. Validation in the frequency domain

In this section, the impedance parameters estimated by using the proposed algorithm are analyzed in the frequency domain and validated against impedance spectra experimentally determined via EIS measurements. In Fig. 9, impedance spectra are plotted for different SOCs, respectively. In the HF region, a small semi-circle resulting from R_1 at the fixed time constant of 0.9 s is visible. It covers the range until the diffusion processes start. The time constant was revealed by the DRT of the measured impedance spectra. The next semi-circle, resulting from R_2, coincides well with the diffusive branch of the measured impedance spectra. In the high SOC region however, R_2 seems to be slightly under-estimated. This might be due to the fact that, as the dynamic driving profile starts from a fully charged and relaxed state, diffusion is not yet excited as much in the first PIWs as it is during EIS

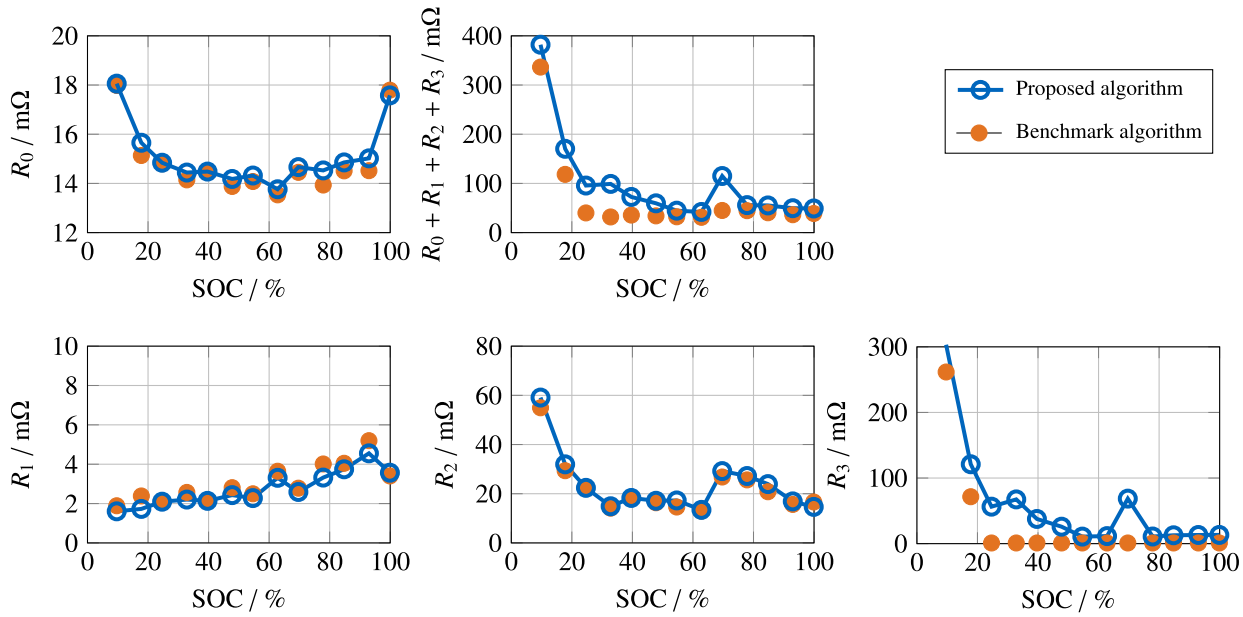

Fig. 8. Parameterization results with the proposed algorithm and the benchmark algorithm for the real driving cycle at 20°C.

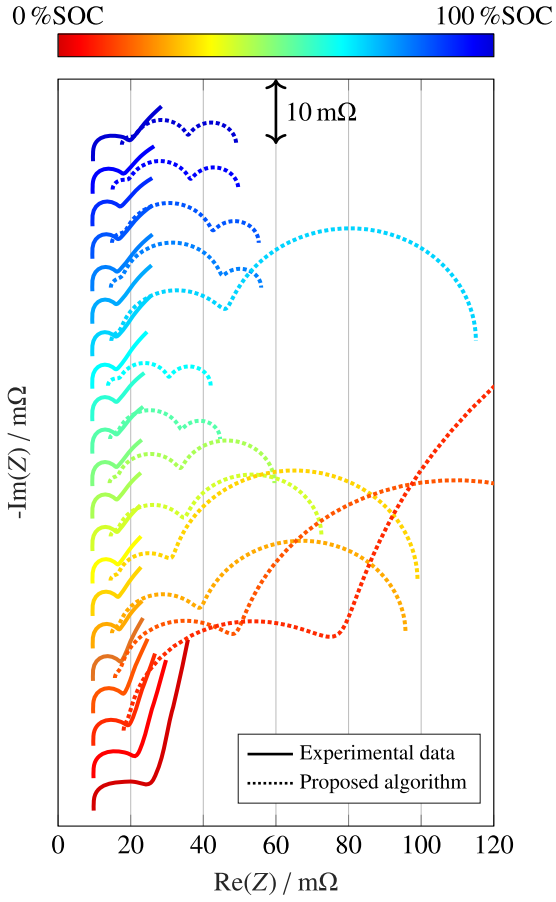

Fig. 9. Impedance spectra from EIS measurements (solid line) and impedance spectra estimated by the proposed algorithm (dotted line) for different SOC at 20°C. Impedance spectra are shifted in the y-direction according to the SOC, for the sake of better visibility (as seen in [49]).

measurements. In the overlapping region covering both measured frequency points from EIS and observable frequencies during a PIW, it can be concluded that the impedance spectra estimated by the proposed algorithm correspond reasonably well with the experimental data. In the frequency region below $f_{\text{min,EIS}}$ = 0.01 Hz, the impedance spectrum can no longer be compared with the experimental data.

5.3. Validation in the time domain

The validity of the identified impedance parameter in frequency ranges below that of the EIS measurements has to be investigated in the timedomain, which is described in the following. Only when the error between the simulated voltage and the measured voltage is low for a properly designed validation cycle, it can be assumed that the identified parameters are physically reasonable.

Table 3 lists the root-mean-square error (RMSE) and absolute maximum error of the modeled voltage in the validation cycle (Fig. 6) for the two different algorithms. In this table, the regions from Fig. 10 are further differentiated based on the SOC between 100% – 20% SOC and 20% – 0% SOC. This is because of the discussed large hysteresis below 20% SOC. As a result, the absolute maximum model errors in this region are high, irrespective of the algorithm used. However, the table still shows that in all regions of the validation cycle, the RMSE of the proposed algorithm is lower than for the benchmark algorithm. The same is true for the absolute maximum error, with the exception of the CC charge between 100% – 20% SOC.

Fig. 10 shows the changes in the model error for the respective

Table 3
Validation results with parameters from the proposed algorithm versus the benchmark algorithm at 20°C.

Regime	RMSE in mV		Abs. max. error in mV	
	Proposed	Benchmark	Proposed	Benchmark
A: CC discharge				
SOC 100% – 20%	8.17	20.46	22.74	42.89
SOC 20% – 0%	49.70	63.92	138.40	112.11
B: CC charge				
SOC 100% – 20%	13.34	14.47	42.78	39.34
SOC 20% – 0%	162.56	166.22	527.76	530.70
C: DST				
SOC 100% – 20%	6.82	15.99	30.40	40.02
SOC 20% – 0%	27.42	38.35	195.81	235.11
D: Driving profile				
SOC 100% – 20%	5.50	15.66	18.17	38.21
SOC 20% – 0%	28.25	53.01	235.89	265.71

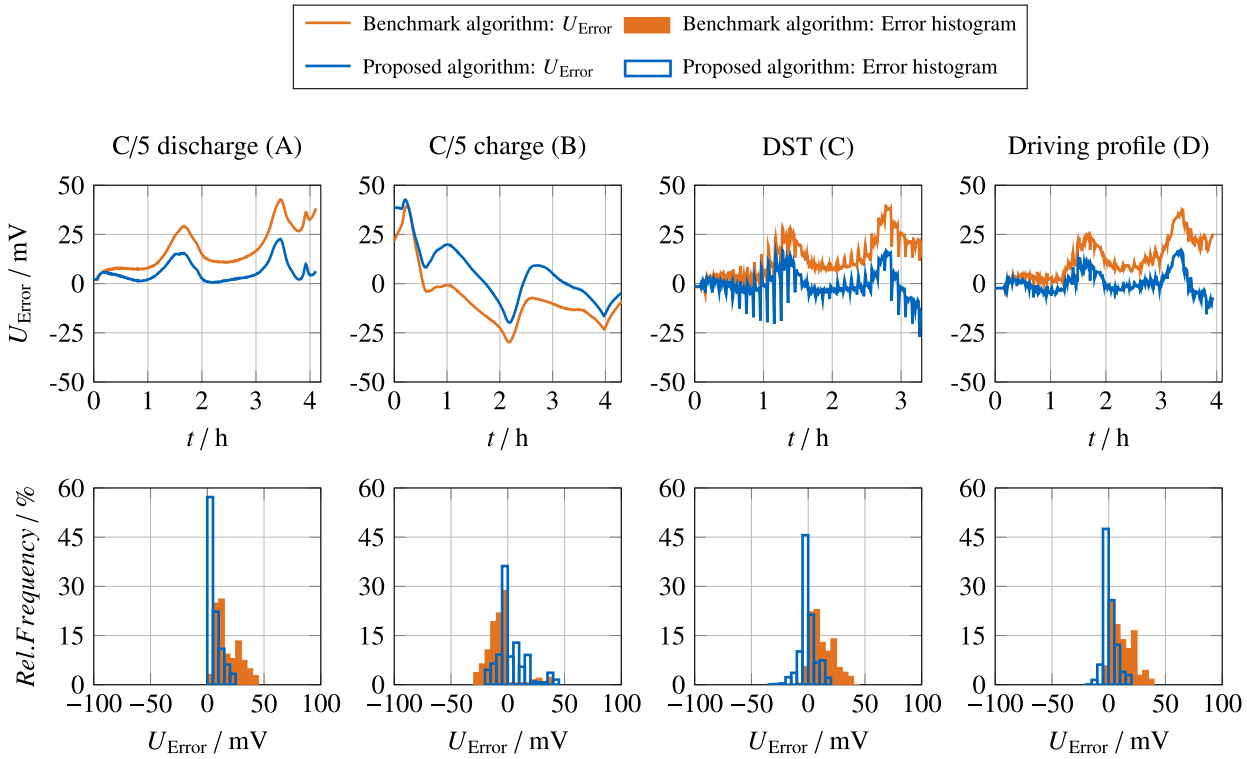

Fig. 10. Comparison of model error $U_{Error} = U_{meas} - U_{sim}$ with the proposed algorithm versus the benchmark algorithm at 20°C.

regions of Table 3 for the developed algorithm versus the benchmark approach. This figure reveals the reason why the maximum error is higher with the proposed algorithm during the CC charge than with the benchmark algorithm. This behavior results from the residual overvoltage in the third RC element due to the hysteresis-dominated low SOC-region, resulting in an initially higher voltage error. Other than that, the reduced error during the driving cycle is particularly noteworthy, since this represents the most realistic BEV use-case. A second result is that the model error during the CC charging and discharging phases shows a specific pattern. A likely explanation is that this pattern can also be ascribed to the aforementioned hysteresis behavior, where the OCV is different between charging and discharging. The most relevant result from the course of the model errors is that, while the model error of the benchmark algorithm grows over time during all discharge phases, it stays constant with the proposed algorithm. This result is also reflected in the error histograms, where the mean error is shifted towards zero compared to a constant positive error during discharge, and compared to a constant negative error during charge with the benchmark algorithm. This behavior can most likely be ascribed to the improved diffusion fitting developed in this work. An incorrect diffusion model results in a constant drift of the model voltage versus the measured voltage over continuous discharge or charge. The results presented are in accordance with those of previous studies [39,40], which also decoupled HF and LF impedance.

6. Conclusions

In this work, a novel method for the parameterization of an ECM-based impedance is presented. This method features a novel approach to parameterizing the low-frequency range by separating the fitting procedure into two individual algorithms. Thereby, high-frequency and low-frequency impedance are estimated separately, which was found to be necessary based on theoretical considerations regarding observable time-constants in parameter-identification windows.

Using this approach, R_3 can be adapted in intervals smaller than τ_3. Therefore R_3 can be expressed as a function of SOC, where the resolution is only limited by the time between two PIWs, which is not possible when fitting R_3 inside a PIW of size τ_3.

Ideally, the algorithm is initialized with an a priori laboratory measurement, which has only been considered for the HF impedance within the scope of this work. However, even without such measurements, the algorithm achieves an average voltage RMSE of 5.50 mV/$U_{nom} \approx 0.15\%$ during the driving profile for the tested NCA round-cell. This value is well below the error achieved with an identical algorithm without the developed novel approach. Because the reduced error is due to a reduced drift of the model voltage versus the measured voltage, it is ascribed to an improved low-frequency impedance determination.

Future work based on these results will involve the detection and quantification of aging mechanisms, such as lithium-plating, using the impedance parameters.

Ideas concerning the improvement of the developed algorithm should verify the possibility of employing a constant-phase element (CPE) instead of the RC elements, by means of a Fourier transform of the CPE [62]. Additionally, the novel method for the on-line determination of RC elements with large time constants can possibly be improved by using a PI or PID control loop instead of the proposed P control loop. Other future efforts should also focus on increasing convergence of the current-dependence factor k_1. This factor was fixed within the scope of this work to reduce the degrees of freedom of the ECM to increase the numerical stability. Additionally, in this work, we parameterize and validate the algorithm at only one temperature. While the assumption of constant time constants holds reasonably well there, these time constants are typically highly dependent on temperature. This issue can be tackled by either adding the time constants as fitting parameters during HF fitting at the cost of decreased numerical stability, or by estimating reasonable values for different temperature ranges a priori.

Patents

A.K., L.W., A.M. and others have filed a patent related to this work: DE Application No. 10 2020 105 349.5, dated 28 February 2020.

Contributions

As first authors, A.K. and L.W. contributed equally to the conceptualization and writing of the article. A.K. developed and implemented the presented method under the supervision of L.W. and A.M. L.W. conducted the experiments and A.K. analyzed the results. N.W. critically reviewed the paper and gave advice on the concept of observers. M.L. made an essential contribution to the conception of the research project and revised the paper critically for important intellectual content. M.L. gave final approval for the version to be published and agrees to all aspects of the work. As a guarantor, M.L. accepts responsibility for the overall integrity of the paper.

CRediT authorship contribution statement

Alexander Karger: Conceptualization, Methodology, Software, Data curation, Writing - original draft. **Leo Wildfeuer:** Conceptualization, Methodology, Investigation, Data curation, Writing - original draft. **Arpit Maheshwari:** Conceptualization, Writing - original draft. **Nikolaos Wassiliadis:** Writing - review & editing. **Markus Lienkamp:** Writing - review & editing, Supervision.

Declaration of Competing Interest

The authors declare the following financial interests/personal relationships which may be considered as potential competing interests: A.K., L.W., A.M. and others have filed a patent related to this work: DE Application No. 10 2020 105 349.5, dated 28 February 2020.

References

[1] J. González Palencia, T. Furubayashi, T. Nakata, Energy use and co2 emissions reduction potential in passenger car fleet using zero emission vehicles and lightweight materials, Energy 48 (2012) 548–565, https://doi.org/10.1016/j.energy.2012.09.041.

[2] Z. Cano, D. Banham, S. Ye, A. Hintennach, J. Lu, M. Fowler, Z. Chen, Batteries and fuel cells for emerging electric vehicle markets, Nat. Energy 3 (2018) 279–289, https://doi.org/10.1038/s41560-018-0108-1.

[3] M. Fries, M. Kerler, S. Rohr, M. Sinning, S. Schickram, M. Lienkamp, R. Kochhan, S. Fuchs, B. Reuter, P. Burda, S. Matz, An overview of costs for vehicle components, fuels, greenhouse gas emissions and total cost of ownership - update 2017, ResearchGate (2017) 1–26, https://doi.org/10.13140/RG.2.2.11685.40164.

[4] M.R. Palacín, A. de Guibert, Why do batteries fail? Science 351 (2016), https://doi.org/10.1126/science.1253292.

[5] M. Baumann, S. Rohr, M. Lienkamp, Cloud-connected battery management for decision making on second-life of electric vehicle batteries, 2018 13th International Conference on Ecological Vehicles and Renewabl-8e Energies (EVER), (2018), pp. 1–6, https://doi.org/10.1109/EVER.2018.8362355.

[6] S. Gantenbein, M. Weiss, E. Ivers-Tiffée, Impedance based time-domain modeling of lithium-ion batteries: part i, J. Power Sources 379 (2018) 317–327, https://doi.org/10.1016/j.jpowsour.2018.01.043.

[7] F. Ciucci, Modeling electrochemical impedance spectroscopy, Curr. Opin. Electrochem. 13 (2019) 132–139, https://doi.org/10.1016/j.coelec.2018.12.003.

[8] T. Kim, W. Qiao, A hybrid battery model capable of capturing dynamic circuit characteristics and nonlinear capacity effects, IEEE Trans. Energy Convers. 26 (2011) 1172–1180, https://doi.org/10.1109/TEC.2011.2167014.

[9] M. Sitterly, L.Y. Wang, G.G. Yin, C. Wang, Enhanced identification of battery models for real-time battery management, IEEE Trans. Sustainable Energy 2 (2011) 300–308, https://doi.org/10.1109/TSTE.2011.2116813.

[10] T. Huria, G. Ludovici, G. Lutzemberger, State of charge estimation of high power lithium iron phosphate cells, J. Power Sources 249 (2014) 92–102, https://doi.org/10.1016/j.jpowsour.2013.10.079.

[11] M. Schönleber, Verfahren zur Charakterisierung des Niederfrequenzverhaltens von Lithium-Ionen Batterien, Karlsruher Institut für Technologie (KIT), 2017 Dissertation.

[12] J. Schmidt, E. Ivers-Tiffée, Pulse-fitting - a novel method for the evaluation of pulse measurements, demonstrated for the low frequency behavior of lithium-ion cells, J. Power Sources 315 (2016) 316–323, https://doi.org/10.1016/j.jpowsour.2016.03.026.

[13] A.J. Fairweather, M.P. Foster, D.A. Stone, Modelling of VRLA batteries over operational temperature range using pseudo random binary sequences, J. Power Sources 207 (2012) 56–59, https://doi.org/10.1016/j.jpowsour.2012.02.024.

[14] C. Pastor-Fernández, T.F. Yu, W.D. Widanage, J. Marco, Critical review of non-invasive diagnosis techniques for quantification of degradation modes in lithium-ion batteries, Renewable Sustainable Energy Rev. 109 (2019) 138–159, https://doi.org/10.1016/j.rser.2019.03.060.

[15] C. Pastor-Fernández, W.D. Widanage, J. Marco, G.V. Miguel-Angel, G.H. Chouchelamane, Identification and Quantification of Ageing Mechanisms in Lithium-ion Batteries using the EIS technique, 2016 IEEE Transportation Electrification Conference and Expo (ITEC), (2016), pp. 1–6, https://doi.org/10.1109/ITEC.2016.7520198.

[16] K. Uddin, G.H. Chouchelamane, C. Pastor-Fernández, W.D. Widanage, J. Marco, A comparison between electrochemical impedance spectroscopy and incremental capacity-Differential voltage as li-ion diagnostic techniques to identify and quantify the effects of degradation modes within battery management systems, J. Power Sources 360 (2017) 301–318, https://doi.org/10.1016/j.jpowsour.2017.03.042.

[17] S. Schindler, M.A. Danzer, A novel mechanistic modeling framework for analysis of electrode balancing and degradation modes in commercial lithium-ion cells, J. Power Sources 343 (2017) 226–236, https://doi.org/10.1016/j.jpowsour.2017.01.026.

[18] S. Saxena, C. Le Floch, J. MacDonald, S. Moura, Quantifying EV battery end-of-life through analysis of travel needs with vehicle powertrain models, J. Power Sources 282 (2015) 265–276, https://doi.org/10.1016/j.jpowsour.2015.01.072.

[19] A. Farmann, D. Sauer, A comprehensive review of on-board state-of-available-power prediction techniques for lithium-ion batteries in electric vehicles, J. Power Sources 329 (2016) 123–137, https://doi.org/10.1016/j.jpowsour.2016.08.031.

[20] S. Nejad, D. Gladwin, D. Stone, A systematic review of lumped-parameter equivalent circuit models for real-time estimation of lithium-ion battery states, J. Power Sources 316 (2016) 183–196, https://doi.org/10.1016/j.jpowsour.2016.03.042.

[21] S.M. Mousavi G., M. Nikdel, Various battery models for various simulation studies and applications, Renewable Sustainable Energy Rev. 32 (2014) 477–485, https://doi.org/10.1016/j.rser.2014.01.048.

[22] Y.H. Chiang, W.Y. Sean, J.C. Ke, Online estimation of internal resistance and open-circuit voltage of lithium-ion batteries in electric vehicles, J. Power Sources 196 (2011) 3921–3932, https://doi.org/10.1016/j.jpowsour.2011.01.005.

[23] H. Rahimi-Eichi, F. Baronti, M.Y. Chow, Modeling and online parameter identification of li-Polymer battery cells for SOC estimation, IEEE Int. Sympos. Indus. Electron. (2012) 1336–1341, https://doi.org/10.1109/ISIE.2012.6237284.

[24] L. Zhou, L. He, Y. Zheng, X. Lai, M. Ouyang, L. Lu, Massive battery pack data compression and reconstruction using a frequency division model in battery management systems, J. Energy Storage 28 (2020) 101252, https://doi.org/10.1016/j.est.2020.101252.

[25] D. Andre, M. Meiler, K. Steiner, H. Walz, T. Soczka-Guth, D.U. Sauer, Characterization of high-power lithium-ion batteries by electrochemical impedance spectroscopy. II: modelling, J. Power Sources 196 (2011) 5349–5356, https://doi.org/10.1016/j.jpowsour.2010.07.071.

[26] A. Farmann, W. Waag, D.U. Sauer, Adaptive approach for on-board impedance parameters and voltage estimation of lithium-ion batteries in electric vehicles, J. Power Sources 299 (2015) 176–188, https://doi.org/10.1016/j.jpowsour.2015.08.087.

[27] A. Farmann, D.U. Sauer, Comparative study of reduced order equivalent circuit models for on-board state-of-available-power prediction of lithium-ion batteries in electric vehicles, Appl. Energy 225 (2018) 1102–1122, https://doi.org/10.1016/j.apenergy.2018.05.066.

[28] X. Hu, S. Li, H. Peng, A comparative study of equivalent circuit models for li-ion batteries, J. Power Sources 198 (2012) 359–367, https://doi.org/10.1016/j.jpowsour.2011.10.013.

[29] W. Waag, C. Fleischer, D.U. Sauer, Critical review of the methods for monitoring of lithium-ion batteries in electric and hybrid vehicles, J. Power Sources 258 (2014) 321–339, https://doi.org/10.1016/j.jpowsour.2014.02.064.

[30] N. Wassiliadis, J. Adermann, A. Frericks, M. Pak, C. Reiter, B. Lohmann, M. Lienkamp, Revisiting the dual extended kalman filter for battery state-of-charge and state-of-health estimation: a use-case life cycle analysis, Journal of Energy Storage 19 (2018) 73–87, https://doi.org/10.1016/j.est.2018.07.006.

[31] Y. Wang, R. Pan, C. Liu, Z. Chen, Q. Ling, Power capability evaluation for lithium iron phosphate batteries based on multi-parameter constraints estimation, J. Power Sources 374 (2018) 12–23, https://doi.org/10.1016/j.jpowsour.2017.11.019.

[32] R. Huai, Z. Yu, H. Li, Historical data demand in window-based battery parameter identification algorithm, J. Power Sources 433 (2019) 126686, https://doi.org/10.1016/j.jpowsour.2019.05.092.

[33] C.R. Gould, C.M. Bingham, D.A. Stone, P. Bentley, New battery model and state-of-health determination through subspace parameter estimation and state-observer techniques, IEEE Trans. Veh. Technol. 58 (2009) 3905–3916, https://doi.org/10.1109/TVT.2009.2028348.

[34] R. Morello, R. Di Rienzo, R. Roncella, R. Saletti, F. Baronti, Tuning of moving window least squares-based algorithm for online battery parameter estimation, 2017 14th International Conference on Synthesis, Modeling, Analysis and Simulation Methods and Applications to Circuit Design (SMACD), (2017), pp. 1–4, https://doi.org/10.1109/SMACD.2017.7981558.

[35] H. Rahimi-Eichi, F. Baronti, M. Chow, Online adaptive parameter identification and state-of-charge coestimation for lithium-polymer battery cells, IEEE Trans. Ind. Electron. 61 (2014) 2053–2061, https://doi.org/10.1109/TIE.2013.2263774.

[36] W. Waag, C. Fleischer, D.U. Sauer, On-line estimation of lithium-ion battery impedance parameters using a novel varied-parameters approach, J. Power Sources 237 (2013) 260–269, https://doi.org/10.1016/j.jpowsour.2013.03.034.

[37] P. Gu, Z. Zhou, S. Qu, C. Zhang, B. Duan, Influence analysis and optimization of sampling frequency on the accuracy of model and state-of-charge estimation for LiNCM battery, Energies 12 (2019), https://doi.org/10.3390/en12071205.

[38] H. Garnier, L. Wang, P.C. Young, Direct Identification of Continuous-time Models from Sampled Data: Issues, Basic Solutions and Relevance, Springer, London, pp. 1–29. 10.1007/978-1-84800-161-9_1.

[39] C. Zhang, W. Allafi, Q. Dinh, P. Ascencio, J. Marco, Online estimation of battery

equivalent circuit model parameters and state of charge using decoupled least squares technique, Energy 142 (2018) 678–688, https://doi.org/10.1016/j.energy.2017.10.043.
[40] H. Dai, T. Xu, L. Zhu, X. Wei, Z. Sun, Adaptive model parameter identification for large capacity li-ion batteries on separated time scales, Appl. Energy 184 (2016) 119–131, https://doi.org/10.1016/j.apenergy.2016.10.020.
[41] Y. Hu, Y.Y. Wang, Two time-Scaled battery model identification with application to battery state estimation, IEEE Trans. Control Syst. Technol. 23 (2015) 1180–1188, https://doi.org/10.1109/TCST.2014.2358846.
[42] A. Lievre, A. Sari, P. Venet, A. Hijazi, M. Brigaudet, S. Pelissier, Practical online estimation of lithium-ion battery apparent series resistance for mild hybrid vehicles, IEEE Trans. Veh. Technol. 65 (2015), https://doi.org/10.1109/TVT.2015.2446333 1–1.
[43] C.E. Shannon, Communication in the presence of noise, Proc. IRE 37 (1949) 10–21.
[44] S. Schindler, Diskrete elektrochemische Modellierung und experimentelle Identifikation von Lithium-Ionen-Zellen basierend auf Halbzellpotentialen, University of Bayreuth, 2018 Dissertation.
[45] D. Klotz, M. Schönleber, J. Schmidt, E. Ivers-Tiffée, New approach for the calculation of impedance spectra out of time domain data, Electrochimica Acta - ELECTROCHIM ACTA 56 (2011) 8763–8769, https://doi.org/10.1016/j.electacta.2011.07.096.
[46] U.R. Koleti, T.Q. Dinh, J. Marco, A new on-line method for lithium plating detection in lithium-ion batteries, J. Power Sources 451 (2020) 227798, https://doi.org/10.1016/j.jpowsour.2020.227798.
[47] S.M. Alavi, C.R. Birkl, D.A. Howey, Time-domain fitting of battery electrochemical impedance models, J. Power Sources 288 (2015) 345–352, https://doi.org/10.1016/j.jpowsour.2015.04.099.
[48] V.J. Ovejas, A. Cuadras, Impedance characterization of an LCO-NMC/graphite cell: ohmic conduction, sei transport and charge-transfer phenomenon, Batteries 4 (2018), https://doi.org/10.3390/batteries4030043.
[49] P. Shafiei Sabet, G. Stahl, D.U. Sauer, Non-invasive investigation of predominant processes in the impedance spectra of high energy lithium-ion batteries with nickel-Cobalt-Aluminum cathodes, J. Power Sources (2018), https://doi.org/10.1016/j.jpowsour.2018.10.024.
[50] P.S. Sabet, D.U. Sauer, Separation of predominant processes in electrochemical impedance spectra of lithium-ion batteries with nickelemanganeseecobalt cathodes, J. Power Sources 425 (2019) 121–129, https://doi.org/10.1016/j.jpowsour.2019.03.068.
[51] Q. Yang, J. Xu, B. Cao, X. Li, A simplified fractional order impedance model and parameter identification method for lithium-ion batteries, PLoS ONE 12 (2017) e0172424, https://doi.org/10.1371/journal.pone.0172424.
[52] Q. Zhang, Y. Shang, Y. Li, N. Cui, B. Duan, C. Zhang, A novel fractional variable-order equivalent circuit model and parameter identification of electric vehicle li-ion batteries, ISA Trans. (2019), https://doi.org/10.1016/j.isatra.2019.08.004.
[53] M. Schönleber, E. Ivers-Tiffée, Approximability of impedance spectra by RC elements and implications for impedance analysis, Electrochem. Commun. 58 (2015) 15–19, https://doi.org/10.1016/j.elecom.2015.05.018.
[54] X. Zhou, Z. Pan, X. Han, L. Lu, M. Ouyang, An easy-to-implement multi-point impedance technique for monitoring aging of lithium ion batteries, J. Power Sources (2018), https://doi.org/10.1016/j.jpowsour.2018.11.087.
[55] The MathWorks Inc, MATLAB lsqnonlin, 2019. https://de.mathworks.com/help/optim/ug/lsqnonlin.html.
[56] D.G. Luenberger, Observing the state of a linear system, IEEE Trans. Milit. Electron. 8 (1964) 74–80.
[57] M.J. Lain, J. Brandon, E. Kendrick, Design strategies for high power vs. high energy lithium ion cells, Batteries 5 (2019), https://doi.org/10.3390/batteries5040064.
[58] J. Sturm, A. Rheinfeld, I. Zilberman, F. Spingler, S. Kosch, F. Frie, A. Jossen, Modeling and simulation of inhomogeneities in a 18650 nickel-rich, silicon-graphite lithium-ion cell during fast charging, J. Power Sources 412 (2019) 204–223, https://doi.org/10.1016/j.jpowsour.2018.11.043.
[59] L. Wildfeuer, N. Wassiliadis, C. Reiter, M. Baumann, M. Lienkamp, Experimental characterization of li-ion battery resistance at the cell, module and pack level, 2019 14th International Conference on Ecological Vehicles and Renewable Energies (EVER), (2019), pp. 1–12, https://doi.org/10.1109/EVER.2019.8813578.
[60] J.P. Schmidt, Verfahren zur Charakterisierung und Modellierung von Lithium-Ionen Zellen, Karlsruher Institute of Technology, 2013 Dissertation.
[61] F.E. Hust, Physico-chemically motivated parameterization and modelling of real-time capable lithium-ion battery models : a case study on the Tesla Model S battery, RWTH Aachen, 2018 Dissertation.
[62] C.S. Cheng, H.S.H. Chung, R.W.H. Lau, Time-domain modeling of constant phase element for simulation of lithium batteries under arbitrary charging and discharging current profiles, 2017 IEEE Applied Power Electronics Conference and Exposition (APEC), (2017), pp. 985–992, https://doi.org/10.1109/APEC.2017.7930816.

2.3 Experimental Degradation Study

The electric behavior of lithium-ion batteries changes due to complex degradation mechanisms which eventually reduce the driving range and performance of BEVs. Targeting the third research question, this section provides the results of a large-scale experimental degradation study covering calendar aging and cycle aging under all main stress factors. Figure 2.6 gives an overview of the input from other sections, the performed measurements, the applied analysis techniques, and the results of the presented Study IV.

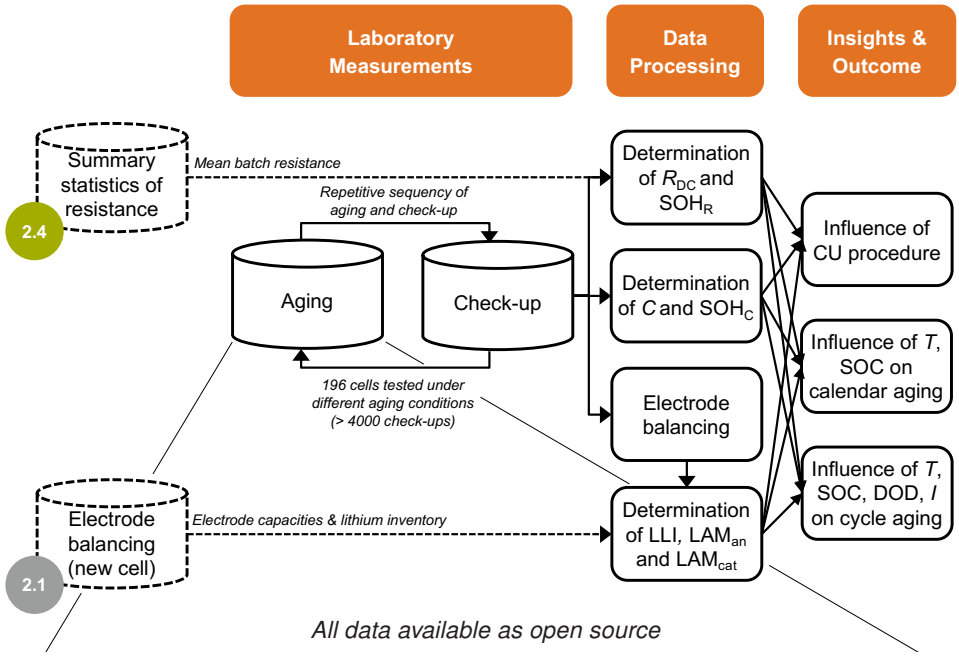

Group	Domain	Operation	Test points (ID)	Motivation & scope
A	Cyc	Check-up (CU) only	1 (1)	• Impact of check-up on aging
B	Cal	Constant (CU every 6 w.)	27 (2–28)	• Influence of T and SOC • Parameterization of calendar aging models
C	Cal	Constant (CU every 12 w.)	13 (29–41)	• Influence of check-up on calendar aging
D	Cal	Constant (CU after 96 w.)	7 (42–48)	• Influence of check-up on calendar aging
E	Cal	Constant (duplicate)	8 (49-56)	• Analysis of cell-to-cell aging variations
F	Cal	Alternating	16 (57–72)	• Analysis of path dependency • Validation of calendar aging models
G	Cal	Randomly changing	4 (73–76)	• Validation of calendar aging models
H	Cyc	Constant	72 (77–148)	• Influence of T, SOC, DOD, $I_{\text{discharge}}$, I_{charge} • Parameterization of cycle aging models
I	Cyc	Alternating	22 (149–170)	• Analysis of path dependency • Validation of cycle aging models
J	Cyc	Randomly changing	3 (171–173)	• Validation of cycle aging models
K	Cal/ Cyc	Alternating	6 (174–179)	• Analysis of path dependency • Validation of combined aging model
L	Cyc	Real-world driving profiles	10 (180–189)	• Validation of aging models
M	Cal/ Cyc	Real-world driving profiles	7 (190–196)	• Validation of aging models

Figure 2.6: Graphical summary of Study IV [4].

Aging tests were performed with a total number of 196 lithium-ion cells which are classified into 13 groups according to their aging domain and operation of stress factors. The check-up procedure was designed to enable regular tracking of aging effects and degradation modes. The capacity was measured during CCCV charging and discharging and $\mathrm{SOH_C}$ was calculated according to Eq. (1.21). To determine the resistance, discharge and charge pulses were performed at 100 % SOC, 50 % SOC, and 20 % SOC. The presented article evaluates the resistance $R_{\mathrm{DC,10\,s}}$ at 50% SOC. Since resistance measurements are prone to higher scattering due to small fluctuations of the ambient temperature during experiments (Section 2.4), the mean resistance of the batch of cells was used as R_{new} to calculate $\mathrm{SOH_R}$ according to Eq. (1.22).

As concluded in Section 2.1, CC measurements with a current rate of C/10 were observed to be suitable to identify the capacities of both electrodes and lithium inventory, which is why such a charging phase was incorporated into the check-up procedure. By performing the half-cell fitting on every check-up measurement, the degradation modes LLI, $\mathrm{LAM_{an}}$ and $\mathrm{LAM_{cat}}$ could be obtained according to Eq. (1.24–1.26). Hence, all aging effects and degradation modes could be calculated with a measurement duration of less than 24 h. This was important considering that over 4000 check-up measurements, all at 20 °C, were performed in this aging campaign.

The open source contains the raw cycling and check-up data of all groups [13]. In the presented article, the results of groups A, B, C, D, and H were investigated. One main outcome of this study is that a periodic check-up procedure significantly influences the aging rate compared to pure calendar aging. At 20 °C and 50 % SOC, for example, pure calendar aging led to a $\mathrm{SOH_C}$ of 96.6 % after 96 weeks. If a check-up measurement was performed every 6 weeks, the $\mathrm{SOH_C}$ was determined to be 5.4 % lower. This means that the capacity fade induced by the 15 additional check-ups was greater than the capacity fade due to pure calendar aging.

During cycle aging, $\mathrm{LAM_{an}}$ was significantly triggered at high DOD, which probably was caused by the increased degradation of silicon at low SOCs. For a DOD of 100 %, a knee point was observed. The influence of the discharge rate on cycle aging was dependent on the mean SOC and DOD and rapid degradation of the cathode was observed in certain SOC ranges. It is assumed, that $\mathrm{LAM_{cat}}$ increases when specific material phases are transitioned, which happens more heterogeneously at higher currents. Cells cycled with varying charging rates at low temperatures all experienced nonlinear aging but showed an unexpected trend because smaller charging currents led to an earlier onset of a knee-point. One reason for this behavior might be the additional self-heating induced by the higher currents. Overall, the presented study showed that the analysis of degradation modes enables deeper insights into the root causes of aging.

Contribution

Leo Wildfeuer is the first author of the article.

Leo Wildfeuer: Conceptualization, Methodology, Formal Analysis, Investigation, Visualization, Data curation, Software, Validation, Writing – original draft, Writing – review & editing. Alexander Karger: Formal Analysis, Software, Validation, Writing – original draft, Writing – review & editing. Deniz Aygül: Software, Investigation, Writing – review & editing. Nikolaos Wassiliadis: Investigation, Validation, Writing – review & editing. Andreas Jossen: Supervision, Writing – review & editing. Markus Lienkamp: Resources, Supervision, Writing – review & editing.

Experimental degradation study of a commercial lithium-ion battery

Leo Wildfeuer, Alexander Karger, Deniz Aygül, Nikolaos Wassiliadis, Andreas Jossen, Markus Lienkamp

Journal of Power Sources, Volume 560, p. 232498, 2023
Digital Object Identifier: 10.1016/j.jpowsour.2022.232498
Permanent Weblink: https://doi.org/10.1016/j.jpowsour.2022.232498

Journal of Power Sources 560 (2023) 232498

Contents lists available at ScienceDirect

Journal of Power Sources

journal homepage: www.elsevier.com/locate/jpowsour

Experimental degradation study of a commercial lithium-ion battery

Leo Wildfeuer [a,b,*], Alexander Karger [c,b], Deniz Aygül [a,b], Nikolaos Wassiliadis [a], Andreas Jossen [c,d], Markus Lienkamp [a]

[a] Technical University of Munich, School of Engineering and Design, Department of Mobility Systems Engineering, Institute of Automotive Technology, Boltzmannstr. 15, 85748 Garching, Germany
[b] TWAICE Technologies GmbH, Joseph-Dollinger-Bogen 26, 80807 Munich, Germany
[c] Technical University of Munich, School of Engineering and Design, Department of Energy and Process Engineering, Institute for Electrical Energy Storage Technology, Arcisstr. 21, 80333 Munich, Germany
[d] Technical University of Munich, Munich School of Engineering, Lichtenbergstr. 4a, 85748 Garching, Germany

HIGHLIGHTS

- Open source dataset with aging over wide operating conditions.
- Determination of capacity, resistance, LLI, and LAM during 4000 CU measurements.
- Periodic check-ups have significant influence on calendar aging.
- Depth-of-discharge has the highest influence on cycle aging rate.
- Low charging rates lead to early non-linear degradation.

ARTICLE INFO

Keywords:
Lithium-ion batteries
Aging
State-of-health
Degradation modes
Open-source data

ABSTRACT

In this study, we analyze data collected during the aging of 196 commercial lithium-ion cells with a silicon-doped graphite anode and nickel-rich NCA cathode. The cells are aged over a large range of calendar and cycle aging conditions. For different cells, these conditions are constant, alternating or randomly changing. The total test time and reached cycles are 697 days and 1500 equivalent full cycles for the calendar and cyclic aging tests respectively. A periodic check-up procedure was consistently performed at 20 °C controlled temperature, which allows for good comparability between different aging scenarios. In addition to capacity fade and resistance increase, we provide data of the degradation modes LLI, LAM_{NE}, and LAM_{PE} obtained from half-cell fitting of the full cell's and both electrode's differential voltage. During calendar aging, we quantify the influence of the check-up procedure, which significantly increases the aging observed after 697 days. For certain conditions, the degradation induced by the check-up even exceeds the pure calendar aging, which reveals that the lifetime of lithium-ion batteries was underestimated in previous studies and models. Fitting of the Arrhenius equation on calendar aging at four temperatures at different SOCs shows a varying activation energy, which lies between 23.6 kJ mol^{-1} and 29.9 kJ mol^{-1} for the capacity. The activation energy of resistance increase is almost twice as high. The influence of SOC on the calendar aging is highest at about 85% SOC, presumable due to a cathode-driven shuttle mechanism. Next to current rates, temperature and mean SOC, the depth-of-discharge has the highest impact on cycle aging. Additionally it is shown that lower charging rates favor the onset of accelerated aging in certain conditions. For all tests, the raw data is made publicly available, which fosters the development of data-based aging models or state-estimation algorithms.

* Corresponding author at: Technical University of Munich, School of Engineering and Design, Department of Mobility Systems Engineering, Institute of Automotive Technology, Boltzmannstr. 15, 85748 Garching, Germany.
E-mail address: leo.wildfeuer@tum.de (L. Wildfeuer).

https://doi.org/10.1016/j.jpowsour.2022.232498
Received 20 August 2022; Received in revised form 16 November 2022; Accepted 4 December 2022
Available online 21 January 2023

Acronyms

BoC	Beginning-of-charge
CC	Constant current
CCCV	Constant current constant voltage
CU	Check-up
DM	Degradation mode
DOD	Depth of discharge
EFC	Equivalent full cycles
EoC	End-of-charge
LAM	Loss of active material
LAM_{NE}	Loss of active material at the negative electrode
LAM_{PE}	Loss of active material at the positive electrode
LIB	Lithium-ion battery
LLI	Loss of lithium inventory
NCA	Nickel–cobalt–aluminum
NE	Negative electrode
OCP	Open-circuit potential
OCV	Open-circuit voltage
PE	Positive electrode
pOCP	Open-circuit potential
pOCV	Open-circuit voltage
SEI	Solid electrolyte interphase
SiG	Silicon–graphite
SOC	State of charge
SOH	Relative state of health
SOH_C	Relative state of health based on the capacity
SOH_{LI}	Relative state of health based on the lithium inventory
SOH_{NE}	Relative state of health based on LAM_{NE}
SOH_{PE}	Relative state of health based on LAM_{PE}
SOH_R	Relative state of health based on the resistance

1. Introduction

1.1. Motivation

Lithium-ion batteries are inevitable for the electrification of the mobility sector and renewable energy adoption. Lifetime and aging are key parameters for the economic and ecologic benefit of both battery electric vehicles as well as stationary electrical energy storage. To support important design and business decisions, it is therefore important to develop a good understanding of the aging behavior of a given battery type under different operating conditions and to develop accurate aging models for lifetime prediction. For use cases such as cell selection, dimensioning of a battery system and its peripheral components such as the cooling system, and optimization of operating strategies, (semi-)empirical aging models have long been a popular choice for battery engineers, due to their robust predictions and easy interpretability [1–4]. For in-life use cases such as predictive maintenance, warranty tracking or fleet optimization, machine learning models have recently gained increasing attraction, due to their ability of self-adaption with field data [5–8], and potentially higher accuracy [9].

Both model types are data-driven because they are built on data collected during the aging of batteries, which in the following is referred to as aging data. The aim of these models is to correlate operating conditions to aging effects extracted from the aging data, with the difference being that they employ different mathematical constructs for this correlation. (Semi-)empirical aging models employ analytic equations, which usually contain few parameters and thus require little data for parameterization. In these analytic equations, discrete stress factors, such as e.g., SOC or cell temperature, are correlated with discrete aging rates. Hence, they require aging data from experimental aging tests under defined conditions where these stress factors remain constant [1–4]. Machine-learning-based models on the other hand do not need constant aging conditions, allowing them to also be trained on real operating data [5]. However, this comes at the cost of an increased number of model parameters, which in turn increases the aging data required for training.

In the academic literature, many data-driven models are developed and tested with a relatively small number of cells only, since the collection of aging data is time- and cost-consuming. Typical numbers of cells incorporated in data-driven models varies between 30 [1] at the lower end and above 100 at the higher end of the spectrum [9–11]. The number of different test points is often even lower, since test points are repeated with multiple cells to identify statistical outliers.

Many yet unresolved research questions such as choosing an optimal design of experiments for new cell types, applying the right analytic model equations, selecting optimal features and machine learning architectures, and analyzing the transferability of aging models across different cell types could be tackled faster and better with more publicly available open-source aging datasets.

Recently, Dos Reis et al. [12] reviewed existing open-source datasets and showed how they vary with respect to cell chemistry, cell type, the number of tested cells, the testing conditions and the given data sensors. While they review over 30 datasets, the overall number of available aging data is still small with a total number of 1099 tested cells. Therefore, any new open-source dataset of aging data constitutes a significant improvement on the status quo. The usefulness of sets of aging data for future research is, however, not only characterized by the amount of data, but also by the actuality and relevance of the tested cell, the test conditions and the measured state of health parameters.

Many researchers, e.g., have used a dataset published by National Aeronautics and Space Administration (NASA) [13] to develop data-based models [14–18]. However, since this dataset was published over 10 years ago, the cell characteristics are outdated and researchers are starved for datasets with state-of-the-art cell design, material properties and production quality standards [19,20].

With regard to test conditions, aging data from both calendar, i.e. storing of the battery, and cycle aging, i.e. during operation, is desired. Furthermore, data gleaned under a wide range of stress factors is desirable [21]. Under laboratory conditions, stress factors often are kept constant over the test period. However, in real-world scenarios, the sequence of stress factors depends on the individual driving and charging behavior and changes in environmental conditions. In addition, small changes in the test procedure, such as the relaxation period between charge and discharge cycles, can have a big impact on the degradation behavior [22]. Therefore, aging data is needed for test scenarios where the stress factors are changing over time and where dynamic loads are applied.

Often, the lifetime of a battery is determined by the time or cycles until the capacity reaches a certain threshold, e.g. 80% or 70%. This is why the usable capacity, often represented as SOH_C, is the most popular parameter to be analyzed during aging experiments and is mostly used as the model target for lifetime prediction models. Moreover, the resistance increase over lifetime is also analyzed in many aging studies and is considered in aging models [23]. However, to better understand the cause-and-effect relationship of battery aging, the well-known degradation modes, namely loss of lithium inventory (LLI), loss of active anode material (LAM_{NE}) and loss of active cathode material (LAM_{PE}) have gained increased attention as a non-destructive method for lithium-ion cell aging characterization [24–28]. They can be seen as an aggregated form of the underlying fundamental degradation mechanisms such as SEI growth or particle cracking. Analyzing the degradation modes can therefore give meaningful insights between the aging stress factors on the one side and capacity fade and resistance increase on the other side. Hence, datasets which give information beyond capacity and resistance can help to track down the origins of the aging and support the development of advanced modeling approaches.

Table 1
Classification of all performed aging experiments according to the aging domain and operation of stress factors. Cal: storing under open-circuit conditions, only CU data at 20 °C available. Cyc: cycling with periodic CU at 20 °C, cycling and CU data available. Const: stress factors remain constant over test period. Alter: Stress factors alternate periodically between CU. Rand: Stress factors change randomly after CU. Dyn: Dynamic discharging using driving profiles. If not specified further, CUs are performed every 6 weeks. Otherwise, the CU interval is given in brackets after the test conditions. The number of cells is listed in the # cells column, where each cell underwent different test conditions (Besides group E, where cells are doubled test conditions from group B).

Group	Domain	Operation : Test variables	# Cells
A	Cyc	Const: CU only	1
B	Cal	Const: T, SOC	27
C	Cal	Const (12 w CU): T, SOC	13
D	Cal	Const (96 w CU): T, SOC	7
E	Cal	Const (doubled): T, SOC	8
F	Cal	Alter: T, SOC	16
G	Cal	Rand: T, SOC	4
H	Cyc	Const: T, SOC, DOD, C_{ch}, C_{dis}	72
I	Cyc	Alter: T, SOC, DOD, C_{ch}, C_{dis}	22
J	Cyc	Rand: T, SOC, DOD, C_{ch}, C_{dis}	3
K	Cal/Cyc	Alter: T, DOD	6
L	Cyc	Dyn: T, chrg & dschrg protocol	10
M	Cal/Cyc	Dyn: T, chrg & dschrg protocol	7

1.2. Contribution of this work

We performed a large aging campaign with 196 lithium-ion cells in total. The main contribution of the article is the open-source publication of the experimental data of the whole aging study, which can be accessed under [29]. The main characteristics of this dataset are:

- **Different aging domains and operation:** We performed calendar and cycle aging with constant, alternating and randomly changing operating conditions. Additionally, cells were tested with dynamic driving profiles.
- **Over 4000 check-up (CU) measurements:** The periodic CU procedure was consistently performed at 20 °C and allows for good comparability between different aging scenarios.
- **Five state of health parameters:** In addition to capacity fade and resistance increase, we provide data of the degradation modes LLI, LAM_{NE}, and LAM_{PE} obtained from half-cell fitting of the full cell's and both electrode's differential voltage.

In Table 1, all performed aging experiments are classified into 13 groups according to their aging domain and operation of stress factors. The open source contains the data of all groups. However, in this paper we only analyze the results of group A, B, C, D, and H (calendar and cycle aging with constant conditions). Cycle aging tests under alternating conditions (Group I) were already analyzed in [30] about modeling the capacity fade of lithium-ion batteries during dynamic cycling considering path dependence. The remaining groups will eventually be analyzed in future work.

In this article, the experimental procedures (Section 2) and the methods for determining the five health parameters, i.e. capacity fade, resistance increase and the degradation modes LLI, LAM_{NE} and LAM_{PE}, from the CU measurements (Section 3) are described. In Section 4, we present the results of all five health parameters for constant calendar and for a subset of constant cycle aging (groups A, B, C, D, H). While the main purpose of this aging campaign is the development of data-driven aging prediction models, this study focus on the analysis of the aging behavior of the different health parameters to provide labeled data for downstream modeling. The investigation consists of:

- **The CU influence on calendar aging:** By analyzing calendar aging with a periodic 6, 12, and 96-week CU interval, we demonstrate the significant effect of periodic CUs. (Section 4.1.1)
- **The Arrhenius dependency of calendar aging:** We analyze the temperature dependency by employing the Arrhenius equation at different SOC and different CU intervals. (Section 4.1.2)
- **The SOC dependency of calendar aging:** The SOC dependency of calendar aging is analyzed and linked to the electrode's material stages. (Section 4.1.3)
- **Factorial analysis of cycle aging:** The aging rate dependency on the main stress factors DOD, temperature, and current rates in charge and discharge direction are analyzed. (Section 4.2)

Table 2
Parameters of the investigated cell.

Parameter	Value
Manufacturer	Sony Murata
Cell type	US18650VTC5A
Anode material	SiG
Cathode material	NCA
Electrolyte material	n.a.
Nominal capacity	2.5 Ah
Nominal voltage	3.6 V
CCCV capacity[a]	2.53 Ah
10 s DC resistance[a]	32.42 mΩ
Weight[a]	47.65 g

[a]Experimentally determined in a previous study [31].

Table 3
Precision of the used measurement equipment.

Instrument	Variable	Precision	Range
BaSyTec CTS	Voltage	$\Delta U = \pm 1$ mV	$U \in [0\,V, 6\,V]$
	Current	$\Delta I = \pm 1$ mA	$I \in [300\,mA, 5\,A]$
	Current	$\Delta I = \pm 50$ µA	$I \in [15\,mA, 300\,mA]$
	Current	$\Delta I = \pm 2.5$ µA	$I \in [1\,mA, 15\,mA]$
	Current	$\Delta I = \pm 0.2$ µA	$I \in [0\,mA, 1\,mA]$
BaSyTec XCTS	Voltage	$\Delta U = \pm 1$ mV	$U \in [0\,V, 6\,V]$
	Current	$\Delta I = \pm 20$ mA	$I \in [20\,A, 40\,A]$
	Current	$\Delta I = \pm 10$ mA	$I \in [15\,A, 300\,A]$
NTC Sensor	Temperature	$\Delta T = \pm 0.25$ °C	T@25 °C

2. Experimental

2.1. Investigated cell and measurement equipment

196 cells from the same production batch of commercial 18650 cells of type US18650VTC5 A by *Sony/Murata* with a nominal capacity of 2.5 Ah were aged under different conditions. Table 2 summarizes the parameters of the investigated cell.

The anode active material is silicon-graphite (SiG) with 1.4 wt% silicon and the cathode active material is nickel-cobalt-aluminum (NCA) with the formulation $LiNi_{0.80}Co_{0.15}Al_{0.05}O$ [32]. The capacity, resistance and weight variation of a total of 600 cells of this production batch at beginning of life was examined in a previous study [31]. The second previous study described the tear-down, building of half-cells and characterization of the thermodynamic and kinetic behavior at a pristine state [33]. The corresponding data can be found under [34].

Fig. 2 shows the cell holder including cell connection and temperature sensing. Table 3 lists the precision of the respective measurement devices. All CU measurements were performed using BaSyTec cell test systems (CTS). Additionally, for cycling with higher currents, the BaSyTec XCTS MKII was used.

2.2. Check-up measurement

Fig. 1 gives an overview of the test protocols. At the beginning of the CU, cells rest for 3 h to precondition the cells to the desired temperature of 20 °C. Afterward, there is a second rest of 2 h, before the cells were constant current (CC) discharged ($I = 2.5$ A, $U_{min} = 2.5$ V) in order

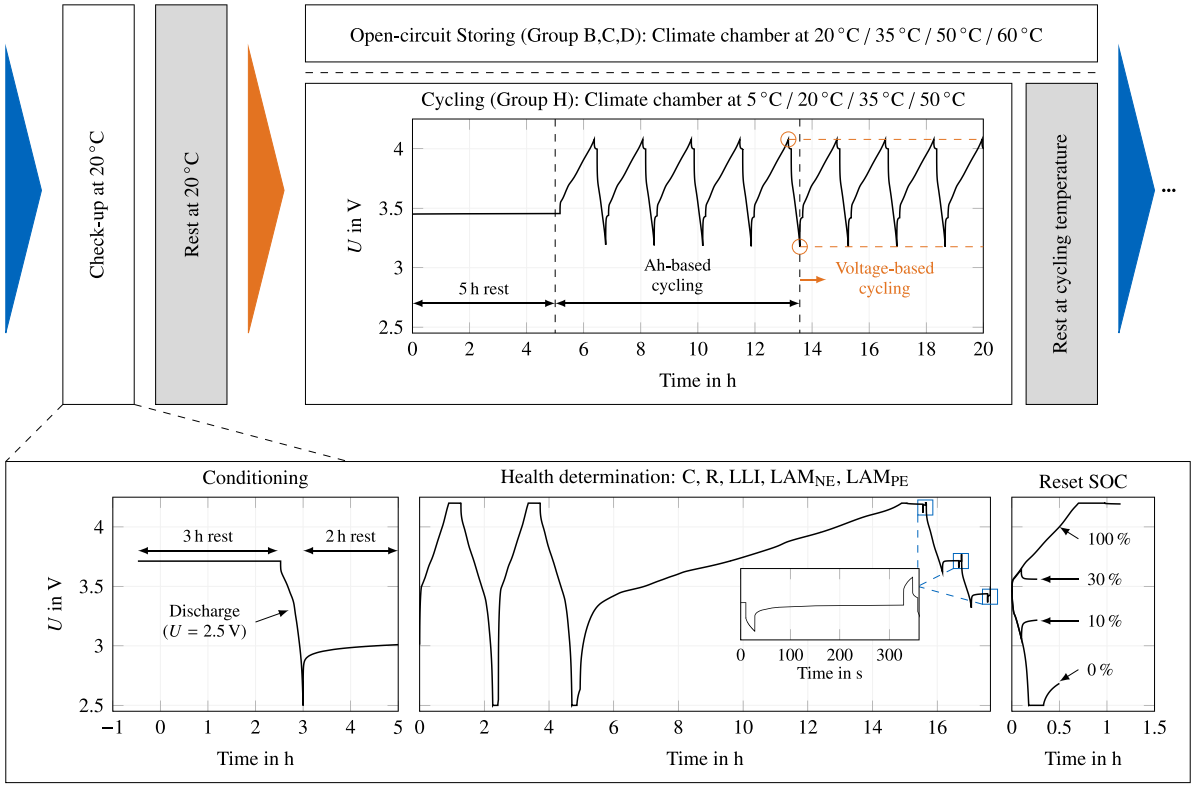

Fig. 1. Overview of the testing sequence. After the check-up, the cell was at rest at 20 °C until it was switched to the respective climate chamber for cyclic or calendaric aging. After the cycle protocol was finished, the cell was at rest at the respective climate chamber until it was switched to the designated climate chamber for check-up measurements.

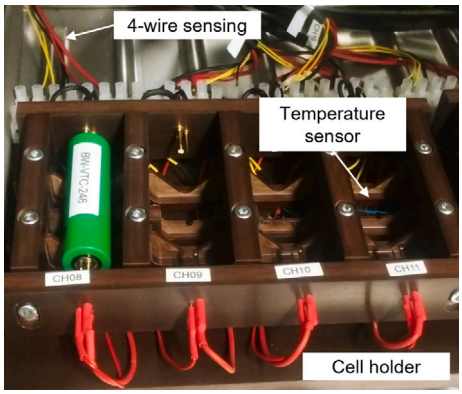

Fig. 2. Picture of the cell holder used for all experiments.

to achieve comparable starting conditions independent of the SOC at the end of cycling or storing.

To measure the cell's capacity, two consecutive constant current constant voltage (CCCV) charging and discharging cycles were performed (I = 2.5 A, U_{max} = 4.2 V, U_{min} = 2.5 V, $I_{cut,CV}$ = 0.02 C, $t_{cut,CV}$ = 1 h). Afterward, we performed a slow rate charging (I = 0.25 A, U_{max} = 4.2 V, $I_{cut,CV}$ = 0.02 C, $t_{cut,CV}$ = 1 h) to calculate the differential voltage and to perform the half-cell fitting for degradation mode detection. To calculate the DC resistance of the cell, we performed 18 s discharge and charge pulses with I = 2.5 A at 100% SOC, 50% SOC, and 20% SOC. The determination of state of health measures from this CU procedure is described in Section 3.

Next, the cells were brought to the desired Start-SOC by either charging or discharging them if the Start-SOC was >20% or <20% respectively. For calendar aging, the Start-SOC is the storage SOC. For cycle aging, the Start-SOC is SOC_{low}, which is calculated from the desired mean SOC and DOD. After the CU, cells were at rest at 20 °C ambient temperature until they were moved to their respective thermal chamber for cyclic or calendar aging. This time period could not be controlled perfectly due to resource availability, available test channels, etc.

2.3. Factorial design of experiments for calendar aging with different check-up interval

The rate of calendar aging with constant conditions depends on the cell's temperature and SOC during storing. The cells were stored at open-circuit conditions and were only connected to the test device for periodical CUs. Hence, the influence and cross dependencies of these stress factors can be investigated with a full-factorial design of experiments in the 2-dimensional T-SOC space with manageable testing effort. However, performing a CU during aging tests changes the aging condition. On the one hand, the calendar conditions are changed due to the change of temperature and SOC during CUs. On the other hand, the cells are charged and discharged for the capacity measurement during CUs inducing cyclic aging. The cycles performed during the CUs can trigger different aging mechanisms and lead to recovery effects due to the electrode overhang [35–37]. Thus, the degradation estimated during CUs might be biased by the CU procedure and frequency, i.e. at which intervals CUs are performed. Previous studies have already reported a significant influence of the CU on the observed aging [38,39], as well as the mutual influence between cycle and calendar aging [40]. Thus, choosing a CU interval is a compromise between minor influence caused by the periodic cycling and observed data points to generate a comprehensive data set for aging modeling. As shown in Fig. 3, three test matrices with different CU intervals were performed.

In the first test matrix (Group B), the CU was performed every 6 weeks. It is a full factorial test matrix that includes cross dependencies with four temperature levels (20 °C, 35 °C, 50 °C and 60 °C) and four SOCs (10%, 50%, 70% and 100%). Additional SOC levels were added at

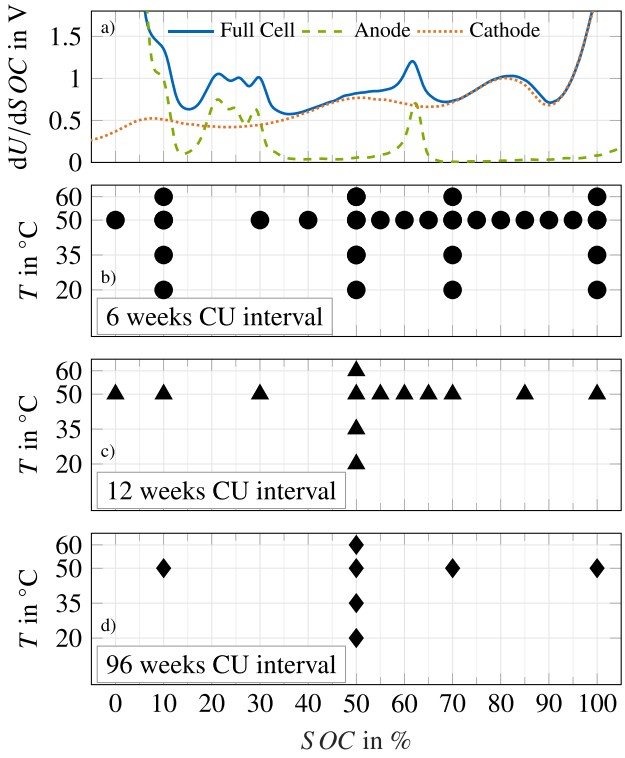

Fig. 3. Test matrix of the static calendar aging study. (a) differential voltage of pristine full-cell over SOC, as well as differential voltage of electrode potentials obtained from half-cell fitting. (b) Test points with 6 weeks CU interval. (c) Test points with 12 weeks CU interval. (d) Test points with no CU until the end-of-life of the corresponding cells with 12 week CU interval is reached or the study is terminated.

50 °C to capture a more distinct picture of the effect of electrode material stages on the reversible and irreversible calendar aging effects [41], leading to 27 test points with 1 tested cell per test point. The second test matrix (Group C) consists of a subset of test points (13 tested cells) where the only difference is the CU interval, which, with 12 weeks of storing before regular CU, was chosen to be twice as long as in the first test matrix. In the third test matrix (Group D, 7 cells), besides the initial CU, no CUs are performed at all. The second CU was performed when we terminated the aging study, which was after 96 weeks (672 days).

2.4. D-optimal design of experiments for cycle aging

In contrast to calendar aging, five stress factors influence the magnitude of cycle aging with constant conditions: temperature, ∅SOC, depth of discharge (DOD), and current rate in charge and discharge direction. A full factorial design of experiments would lead to an excessive number of test points. For example, only three factor levels of each stress factor would lead to $3^5 = 243$ test points. Since we wanted to cover a wide stress factor range, we applied a D-optimal design of experiments as a starting point to reduce the number of tests significantly, in theory without losing information of the underlying system. The software Visual-Xsel by CRGRAPH [42] was used. Table 4 lists the stress factor levels which were given as input into the D-optimal design of experiments and which resulted in 38 test points.

A D-optimal design of experiments comes with the disadvantage that the influence of individual stress factors cannot be analyzed phenomenologically without model parameterization. This is why we added additional factorial test points during the course of this aging study, where only one selected stress factor was varied at a time (34 additional test points). In total, we performed 72 aging tests with constant cycle aging conditions (Group H). All test conditions not specifically stated in this article can be found in the data repository.

Table 4
Stress factor levels as input for the D-optimal design of experiments.

Stress factor	Levels
Temperature in °C	[5, 20, 35, 50]
∅SOC in %	[10, 20, 30, 40, 50, 60, 80, 90]
DOD in %	[5, 20, 40, 60, 80, 100]
C_{charge} in 1/h	[0.5, 1, 1.5, 2]
$C_{discharge}$ in 1/h	[1, 2, 5, 10, 14]

At the beginning of the cycling procedure, cells were at rest for 5 h to reach the desired temperature. Then, starting at SOC_{low} = ∅SOC - DOD/2, the first cycles with the desired DOD were performed Ah-based, depending on the last measured capacity C_{new}. These initial cycles allowed temperature increase and cell polarization until cycling became quasi-stationary, i.e. temperature was not increasing across cycles. For certain conditions, e.g., low temperatures and high current rates, we increased the number of Ah-based cycles to 10 because we expected a longer necessary time-interval until quasi-stationary cycling. Then we switched to voltage- and current-based cycling. This means, that the lowest voltage of the discharge phase and the highest voltage of the charge phase remain constant over the remaining cycles. In the case of a CV phase at 2.5 V or 4.2 V during the initial Ah-based cycles, the cutoff current was set accordingly for the remaining cycles. This was done, because imperfect current integration can cause unintended drifts in the cycling conditions, i.e., the mean SOC, when cycling is performed Ah-based for a longer period of time. Same as for the DOD and the mean SOC, also the charging and discharging currents are adapted based on the new capacity C_{new}, measured during the last CU to assure a constant C-rate over the entire lifetime. In this study, we defined the C-rate as the charge and discharge current with respect to latest capacity measurement. This means that the absolute current rates were reduced over the lifetime. The pause between charging and discharging was set depending on the DOD to a maximum of 10 min according to $t_{Pause} = 600\,s \cdot DOD$. After the cycle protocol was finished, the cell was at rest at SOC_{low} at the respective climate chamber until it was moved to the designated climate chamber for CUs.

Here, the CU interval for most test points was 50 equivalent full cycles (EFCs), where 1 EFC is defined as the charge throughput during one full charge–discharge cycle based on the capacity measured at the last CU (C_{new}). As already discussed for calendar aging, the CU will also influence the aging behavior of cycled cells. Although we varied the CU interval for some cells, no systematic investigation as done for calendar aging was performed. Still, it has to be kept in mind that in the case of 50 EFCs between every CU, the share of charge throughput induced by the check-up corresponds to 3 EFC/50 EFC = 6%.

2.5. Cell-to-cell variations

In this study, a higher variety of stress factor combinations was chosen over testing multiple cells for one condition. Previous publications showed negligible variation in the aging rate [3]. We confirm this observation for 8 storing conditions (Group E), where the relative capacity difference is below 0.1 % for most cases and below 0.3 % for all cases. Furthermore, as elaborated in [31], the impact of external influencing factors such as temperature inhomogeneities inside the climate chamber is assumed to be dominant compared to the inherent variability due to the manufacturing process.

3. Determination of state of health parameters

3.1. Aging effects: capacity and resistance

In this study, the SOH with respect to the capacity is determined from the second CCCV discharging phase and is defined as:

$$SOH_{C,i} = \frac{C_{CCCV,\ Dis2,i}}{C_{CCCV,\ Dis2,0}}. \quad (1)$$

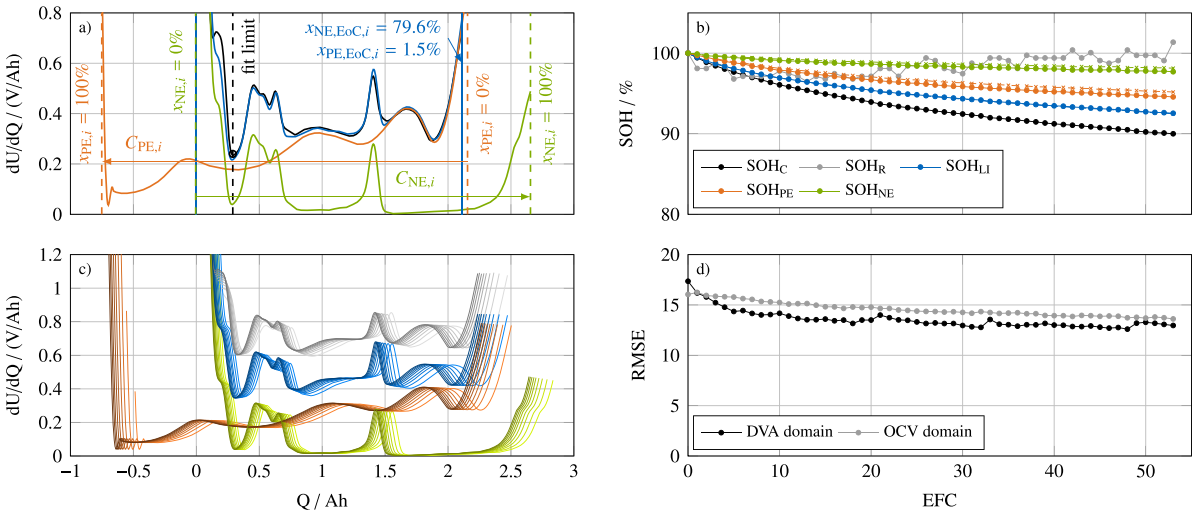

Fig. 4. Aging of cell with continuously repeated check up measurements. (a) Visualization of half-cell fitting and identified parameters used for calculation of degradation modes. The fit limit determined by the minimum (black circle) in the full-cell DVA is highlighted by a black dashed line. (b) Evolution of half-cell fitting over aging. Every 6th check up is plotted. (c) Evolution of the error of the half-cell fitting over aging. (c)–(e) are plotted over the number of check up's. One check up cycle corresponds to approx. 3 EFC. (c) Evolution of degradation modes. SOH_{LI}, SOH_{PE}, $SOH_{NE\text{-}C}$, and $SOH_{Ne\text{-}Si}$ are plotted absolute (dashed line; mark = x), and normalized to the initial full cell capacity (solid line; mark = *). (d) Evolution of the relative share of the degradation modes SOH_{LI}, SOH_{PE}, $SOH_{NE\text{-}C}$, and $SOH_{Ne\text{-}Si}$ with respect to SOH_{LI}. (e) Evolution of the fitting error in the OCV domain and in the DVA domain (= fitting domain). (For interpretation of the references to color in this figure legend, the reader is referred to the web version of this article.)

$C_{CCCV,\ Dis2,0}$ is the measured capacity at the initial check-up of an individual cell and $C_{CCCV,\ Dis2,i}$ is the measured capacity at check-up i. We chose the second discharge phase to reduce any potential effect from different stress factor combinations of individual cells.

The SOH with respect to the resistance is determined from the DC-resistance calculated after 10 s of the discharge pulse at 50% SOC according to Ohm's law. The SOH_R is defined as:

$$SOH_{R,i} = \frac{R_{10s,\ 50\%\ SOC,i}}{\frac{1}{N}\sum_{n=1}^{N=196} R_{10s,\ 50\%\ SOC,0}}. \quad (2)$$

Here, we use the mean of the initial resistances of all 196 cells as reference due to the higher non-inherent scattering of the resistance measurement compared to capacity measurements [31]. Using the initial resistance of individual cells for the calculation of SOH_R changes the results compared to the absolute resistance values because the starting value influences the resulting aging curve.

In contrast to the capacity definition, the chosen resistance definition has a high impact on the SOH_R. Choosing smaller time steps for evaluating Ohm's law, e.g. 1 s, leads to higher values for SOH_R, meaning that the aging rate of the resistance is slower. This is expected, since only a share of the individual contributors to the dynamic loss processes is observed, e.g. the solid electrolyte interphase (SEI) and charge-transfer resistance, and the other share is neglected, e.g. the electrolyte and solid-state diffusion [33]. But the SOC also strongly influences the observed aging rate. In our case, the resistance at 100% SOC increases slower, while the resistance at 20% SOC increases faster compared to 50% SOC. Different SOH definitions are included in the open-source dataset and can be analyzed in detail in the future.

In Fig. 4(b) , SOH_C and SOH_R are plotted over EFC for the cell, which was aged only with repeating CU measurements (group A). It can be seen that only after 50 CUs, the cell has lost 10% of its original capacity. The resistance decreases at the beginning of aging before the expected resistance increase starts to dominate the aging behavior. This can be explained by a break-in mechanism due to micro-cracks in the electrodes surfaces [23] or increased electrode wetting [23,43]. Both phenomena lead to an increase in electrode surface area and therefore to a decrease in internal resistance. For certain operating conditions, this effect dominates the resistance increase due to SEI growth at the beginning of aging.

3.2. Degradation modes: loss of lithium inventory and active material

In addition to capacity and resistance, we determine the three commonly reported degradation modes (DMs): loss of lithium inventory (LLI), loss of active cathode material (LAM_{PE}) and loss of active anode material (LAM_{NE}) [27]. In this study, we use the transformed expressions $SOH_{LI} = 100\% - LLI$, $SOH_{PE} = 100\% - LAM_{PE}$, and $SOH_{NE} = 100\% - LAM_{NE}$, respectively, to allow for better comparison with the other SOH measures.

SOH_{LI}, SOH_{NE} and SOH_{PE} become visible in the full cell open circuit voltage (OCV) due to a relative shift or scaling of the electrode open-circuit potentials (OCPs). To this end, many researches have employed different optimization algorithms where the OCPs curves of the electrodes are aligned to match the full cell OCV [24–26,33,44–54], hence allowing estimation of the DMs.

In this study, we track the DMs of all cells by using the C/10 differential pseudo-OCPs (pOCPs) during lithiation of the anode and delithiation of the cathode to reconstruct the full-cell differential C/10 pseudo-OCV (pOCV) during charging. The employed fitting algorithm is described in detail in a previous publication [33] where we also describe how the electrode potential curves were obtained. The algorithm is executed at every CU indexed i and yields a capacity for the negative electrode (NE) $C_{NE,i}$ and a capacity for the positive electrode (PE) $C_{NE,i}$. Comparing these capacities of the electrodes for an aged cell to the capacities of the electrodes for a pristine cell allows us to directly estimate the relative loss of active material and thus the SOH of the anode:

$$SOH_{NE,i} = \frac{C_{NE,i}}{C_{NE,0}} \quad (3)$$

and of the cathode:

$$SOH_{PE,i} = \frac{C_{PE,i}}{C_{PE,0}}. \quad (4)$$

To estimate LLI, we only consider the cyclable lithium intercalated in the electrodes and assume a constant concentration of solvent lithium-ions in the electrolyte over aging. The intercalated lithium in the negative and positive electrode is calculated by multiplying the electrode's states of charge $x_{NE,i}$ and $x_{PE,i}$ with the electrode's capacities $C_{NE,i}$ and $C_{PE,i}$ respectively. The electrode's states of charge $x_{NE,i}$ and $x_{PE,i}$ are defined as 0% and 100% at the upper and lower cut-off voltage of the manufactured half-cells [33]. The total intercalated lithium of the

full cell is the sum of the intercalated lithium of the electrodes, if $x_{NE,i}$ and $x_{PE,i}$ are taken for the same full cell SOC. This full-cell SOC can be any value between beginning-of-charge (BoC) and end-of-charge (EoC), which will only influence in which electrode the lithium is intercalated. Using, for example, the loading state of the electrodes at EoC yields the SOH of the lithium-inventory at CU i:

$$SOH_{LI,i} = \frac{x_{NE,EoC,i} \cdot C_{NE,i} + x_{PE,EoC,i} \cdot C_{PE,i}}{x_{NE,EoC,0} \cdot C_{NE,0} + x_{PE,EoC,0} \cdot C_{PE,0}} \quad (5)$$

During fitting, we always use the pristine electrode pOCPs, although a change in OCP for Si-C blend-electrodes was reported due to the faster aging of the silicon share compared to the graphite [55]. We assume that the electrochemical activity of the silicon share in the anode is highest in the low SOC region of the full cell, because of the higher potential of silicon compared to graphite against metallic lithium. Thus, to ensure accurate tracking of the characteristic features of the full cell with pristine electrode pOCPs, we always exclude a low SOC region from fitting, which is already discussed in [33]. The boundary for this low SOC region is determined by automatic identification of the first minimum in the full-cell charge pOCV.

Fig. 4(a) illustrates the estimation of DMs over aging for the cell, which was cycled only with periodic repetition of the check-up procedure. The measures used in Eqs. (3), (4) and (5) and the minimum defining the fitting range are also marked. Below the measured curve, the fitted differential voltage, composed of the fitted PE and fitted NE curves, is visualized, which shows the shifting and scaling of the electrode potential curves over aging. Fig. 4(b) shows the resulting SOH_{LI}, SOH_{PE}, and SOH_{NE} together with the other SOH measures. Fig. 4(d) shows the RMSE of the difference between the modeled pOCV and measured pOCV (OCV domain) and modeled differential pOCVs measured differential pOCV (DVA domain) for these CUs.

For some aged cells, the fitting procedure fails, i.e. the algorithm is not able to align the electrode pOCP curves in such a way that the peaks in the differential pOCV curve of the full cell are reconstructed. This happens if peaks in the full cell differential pOCV disappear, or if additional peaks appear. Such appearing or disappearing of peaks in the differential voltage has been previously reported in other studies [56,57] and is typically associated with inhomogeneous electrode degradation. While fitting is performed in the DVA domain, the failing of the fitting algorithm can be detected by a sudden increase in RMSE in the OCV domain. For CUs, where the algorithm failed, we cannot report the values for SOH_{LI}, SOH_{NE} and SOH_{PE}.

All data analysis was performed with MATLAB by MathWorks®.

4. Results

4.1. Calendar aging

In Fig. 5, the five health parameters (Fig. 5, five rows) are plotted for the full-factorial test matrix of calendar aging under constant conditions with 6 weeks CU interval (Group B). The four columns show the four storing SOCs and the different colors represent the different temperatures. In addition, where applicable, the test point with a larger CU interval are shown by different markers (Group C with 12 weeks CU interval and Group D with 96 weeks CU interval).

4.1.1. Influence of the check-up procedure

After 96 weeks, the state of health of the cells subjected to the same calendar aging conditions but with different CU intervals are compared. An influence of the CU procedure on the capacity fade estimation during calendar storage has been previously reported in the literature. However, the CUs caused increased capacity fade in one study [38], while leading to reduced capacity fade in another study [39]. For the cells stored at 50% SOC, the state of health estimations after 96 weeks are compared in the enlarged sections in the middle of Fig. 5. When interpreting these results, the state of health estimation of the cells with 96 week CU interval can be interpreted as the result of the degradation due to "pure" calendar aging, while the state of health values for the other cells are influenced by the CU procedure. In Fig. 6, the absolute difference of state of health between the cells subjected to "pure" calendar aging and the cells subjected to CUs every 6 weeks and 12 weeks is shown.

The determined capacity is significantly lower for an increasing number of CUs. Exemplary, for the cells stored at 20 °C, the absolute difference for the 6 week CU interval and 12 week CU interval is 5.4 % and 2.9 % compared to the "pure" calendar aging (SOH_C= 96.6 %), respectively. This translates to a relative difference of additional capacity fade of 158.8 % and 85.3 %, which means that for these conditions, the degradation induced by the 15 additional CUs over 96 weeks is greater than the degradation due to "pure" calendar aging.

The additional capacity fade observed in the cells subjected to additional CUs increases when the temperature during storage increases. This can be seen in Fig. 6. However, there is no clear trend of increased capacity fade when the SOC during storage increases. Note that we cannot compare the CU influence for the cells stored at 100% SOC, since the cells subjected to additional CUs dropped to 0 V after around 500 days.

At 50 °C and 60 °C ambient temperature during storage, the influence of the CU procedure on resistance increase is qualitatively similar to the influence on capacity fade, i.e. the cells subjected to more CUs show increased degradation in the form of increased SOH_R. However, for the cells stored at 20 °C and 35 °C, the trend is reversed and SOH_R is lowest after 96 weeks for the cells subjected to the highest number of additional CUs. We assume that this happens since the resistance decreases during the first cycles for this cell type, which can be seen in Fig. 9. Fig. 6 reveals that, analogous to the capacity fade, there is a clear trend of increased CU influence on resistance increase with increasing storage temperature, but no trend with increasing SOC.

The estimated loss of lithium inventory, indicated by a reduction of SOH_{LI}, is influenced similarly by the CU as SOH_C. We assume that the reason is that capacity fade is mainly driven by SEI growth during calendar aging, reducing lithium inventory in the process. This, in turn, leads to a strong correlation between SOH_C and SOH_{LI} and thus also to a similar CU influence on both values.

The CU influence on loss of active material at the positive and negative electrode is qualitatively similar to the CU influence on capacity fade. However, for the positive electrode, the CU influence is lower at 35 °C compared to 20 °C, but they are close to each other and we assume that this is not statistically significant. At the negative electrode, SOH_{NE} of the cell with 96 weeks CU interval stored at 35 °C is higher compared to the cell stored at 20 °C. However, this might also be a statistical outlier, since only one cell is used per test point and due to the overall lower values of SOH_{NE} compared to SOH_{LI} and SOH_{PE}.

To summarize, the CU influence on the various state of health estimations across different storage conditions depends significantly on the storage conditions. Hence, we assume that the additional aging seen in the groups with higher CU intervals does not only result from the aging induced during the CU itself. This assumption is strengthened by the fact that the additional aging observed in the 6 weeks CU group is much smaller than two times the additional aging observed in the 12 weeks CU group, although there are exactly two times as many additional CUs. We believe that a reason for this might be that the CU causes accelerated aging in the subsequent calendar phases, possibly by cracking of the electrodes induced during the CUs, causing additional SEI formation during the subsequent open-circuit phase.

A possibly complementary, model-based explanation, can be derived from [30]. In this study, we showed that, at a given aging state, the subsequent capacity fade is mostly determined by the current capacity and not the elapsed time or charge-throughput. In this model-based explanation, the CU can be seen as periodic switching between two aging conditions. Thus, a possible explanation for the higher absolute capacity fade induced by the CU at higher temperatures is that the aging induced by the CU accelerates below a certain SOH_C, past what is commonly referred to as a "knee"-point [58].

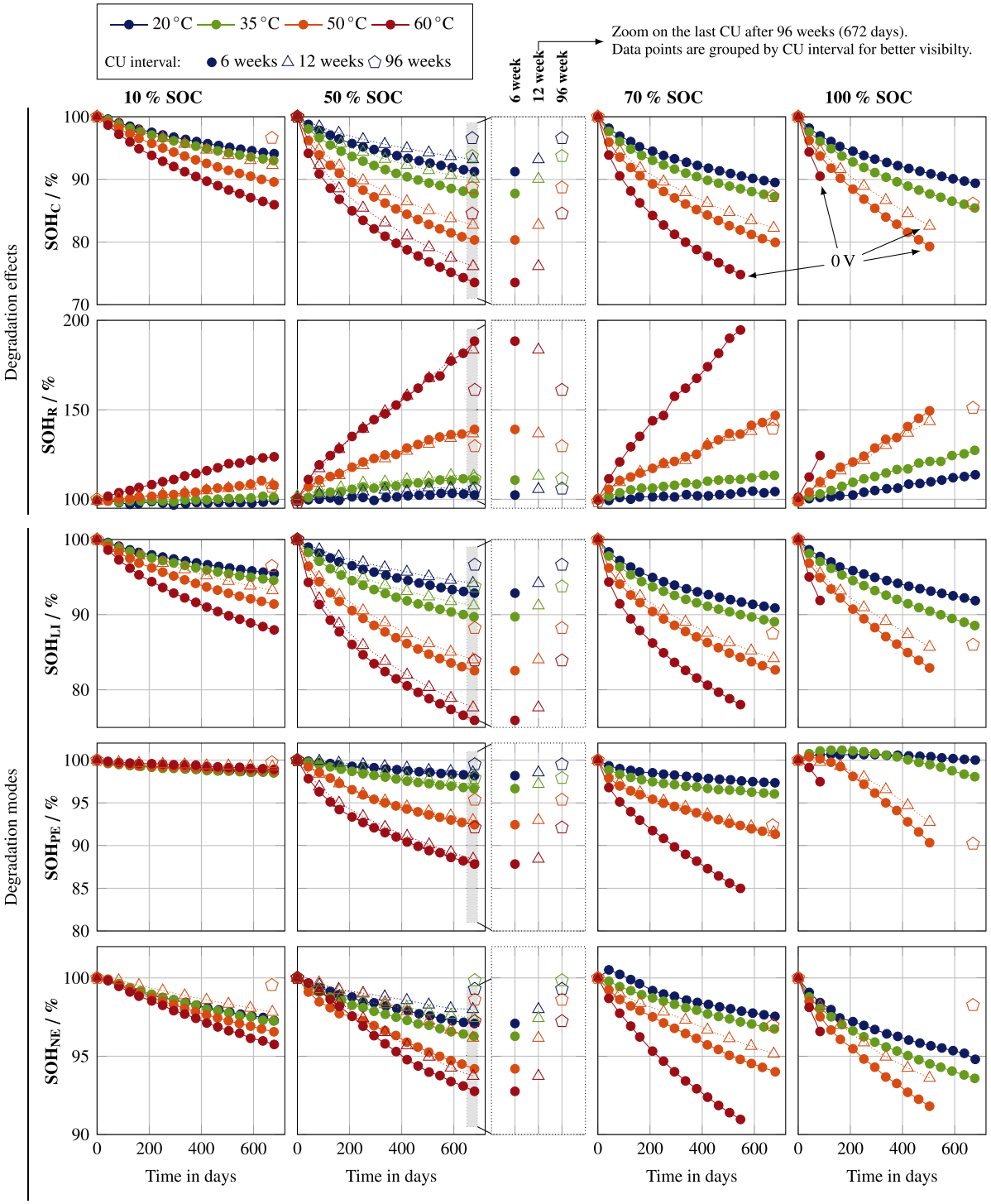

Fig. 5. Health parameters estimated during CUs of calendar aged cells over a timeframe of 96 weeks (672 days). The different rows show the state of health estimations for capacity, resistance, lithium inventory, positive electrode and negative electrode, from top to bottom respectively. The different columns show groups of cells stored at the same SOC, to avoid overplotting. Cells are tested with different CU intervals of 6 weeks, 12 weeks and 96 weeks to quantify the influence of the CU on calendar aging. The zoomed section in the middle shows the data collected during the last CU of all cells stored at 50% SOC.

4.1.2. Influence of the temperature

To analyze the temperature dependency of health parameters, we evaluate the Arrhenius equation:

$$\kappa(T_{\text{amb}}) = \kappa_0 \cdot e^{\frac{E_A}{R_{\text{gas}} \cdot T_{\text{amb}}}} \tag{6}$$

for all SOH parameters. In this equation, κ is the aging rate and calculated as the respective ΔSOH from BOL until the last recorded CU, normalized by the storing time until the last CU. R is the universal gas constant, E_A is the activation energy, and κ_0 is a constant prefactor. In Fig. 7, the logarithm of the five health parameters is plotted over the inverse temperature for different SOCs and different CU intervals to check for the Arrhenius dependency. The regression lines are constructed as follows. To compare the slopes of the regression lines, the aging rates are normalized to $\ln(\Delta\text{SOH}) = 0$ at 60 °C, by subtracting the aging rate at 60 °C for every health parameter. Moreover, the linear

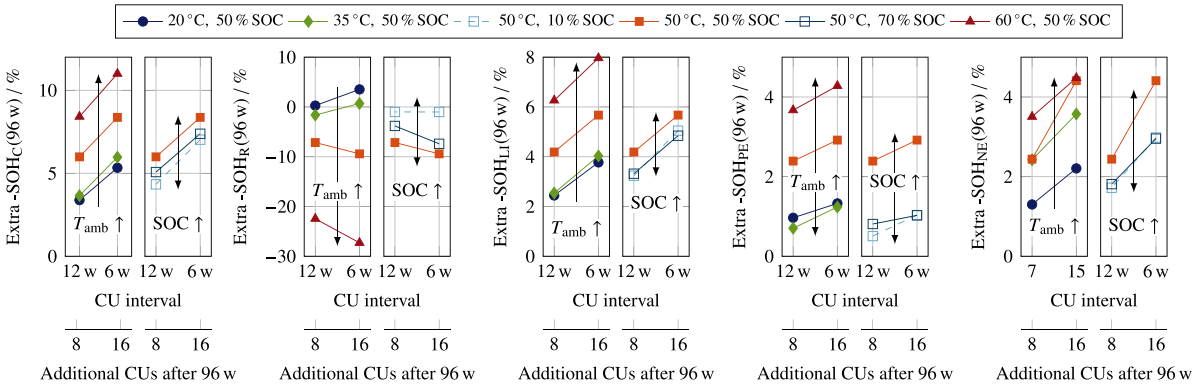

Fig. 6. Absolute difference of state of health after 96 weeks between the cells subjected to "pure" calendar aging (96 weeks CU interval) and the cells subjected to CUs every 6 weeks and 12 weeks. The extra loss of state of health correlates positively with increasing ambient storage temperature T_{amb} for all SOHs, indicated by the one-headed arrow. Only extra -SOH_{PE}96 w is smaller at 35 °C than at 20 °C, indicated by the double-headed arrow. There is no correlation of extra loss of state of health with increasing SOC, indicated by the double-headed arrow. The extra loss of state of health from 16 additional CUs after 96 weeks is always smaller than two times the extra loss of state of health from 8 additional CUs after 96 weeks, indicating that the extra loss of state of health does not result from the CU itself, but rather accelerates aging during the subsequent open-circuit phase.

regression lines are only fitted to the aging rates at 35 °C, 50 °C, and 60 °C, since the aging rate at 20 °C distorted the regression fit for most cases. We assume that a reason for this might be that at 20 °C, the relative influence of the CU on the state of health parameters is larger. In addition to the Arrhenius plot, we show the activation energy E_A and the R^2 as a measure of the goodness of the regression fit.

The R^2 of SOH_C and SOH_R is above 0.99 for all cases, which confirms the expected Arrhenius dependency of capacity fade and resistance increase. The activation energy increases for higher SOC from 23.6 kJ mol^{-1} to 29.9 kJ mol^{-1}. The increased capacity fade observed in the cells subjected to a larger number of CUs leads to an underestimation of the activation energy by 15% (26.3 kJ mol^{-1} with 6 week CU interval compared to 30.9 kJ mol^{-1} with 96 week CU interval).

For the resistance, the trend is again reversed due to the above discussed break-in mechanism. The underestimation of the resistance increase at lower temperatures and the overestimation of the resistance increase at higher temperatures leads to an overestimation of activation energy and thus, of temperature dependence. With 56.8 kJ mol^{-1} at 50% SOC and 96 weeks CU interval, the activation energy of resistance increase is almost twice as high compared to the activation energy of capacity fade.

Since LLI is the dominating degradation mode, the temperature dependence behaves similar to the dependence of capacity fade with $R^2 > 0.99$ for all cases. For the active material loss, results are more ambiguous. For SOH_{PE}, the R^2 at 50% SOC and 70% SOC is above 0.99. At 100% SOC, however, the Arrhenius equation fails to describe the data due to increasing values of SOH_{PE}. It is not clear why SOH_{PE} is increasing for this case. Possible reasons include particle cracking leading to increased accessibility of active material [59], electrode overhang effects leading to lithium transport into or out of the electrodes [60] or aging-induced changes in the open-circuit potentials [55,61]. The latter seems likely, due to the silicon–graphite anode of the cell, where the open-circuit potential is reported to change significantly in shape during aging, due to the faster degradation of silicon compared to graphite [28,61,62]. We want to validate this assumption in a future study. At 10% SOC, the calculated activation energy is negative. We assume however, that this is only an artifact and no real effect, since SOH_{PE} only reduces negligibly for all cases ($SOH_{PE} > 98.5$ % for all temperatures).

For SOH_{NE}, the R^2 is slightly lower compared to the other health parameters, but still high at >96%. There is a trend towards lower activation energies with increasing number of CU. With SOC, the activation is highest at 70% and decreases towards higher and lower SOCs. This dependence of SOH_{NE} on SOC is discussed in the following subsection.

4.1.3. Influence of the storage SOC

Fig. 8 shows the SOH estimations for the cells stored at 50 °C, now plotted over storage SOC. At 50 °C, cells were stored over the largest range of SOCs, thus revealing the dependency of calendar degradation on storage SOC. Again, the SOH estimations of the cells stored with 12 weeks CU interval and 96 weeks CU interval are plotted, but in this subsection, only the results of the cells subjected to CUs every 6 weeks are discussed.

The observed capacity fade generally increases with higher storage SOCs but for the cells stored between 40% and 65% storage SOC, capacity fade is very similar. We assume that this results from the quasi-constant anode potential in this SOC region, driving SEI formation at a similar rate. Between 70% and 85% storage SOC, capacity fade rapidly accelerates, which coincides with the reduced anode potential at SOCs above the transition from LiC_{12} to LiC_6, which can be seen by the characteristic peak in the differential voltage at the bottom of Fig. 8. However, above 85% storage SOC, capacity fade reduces slightly. This results in a spoon-shaped graph of capacity fade over SOC for the first 5 CUs, which was previously reported by Zülke et al. [63] for a similar 21700 cylindrical cell with, also, an NCA cathode and a silicon-doped graphite anode. They hypothesized that capacity fade was higher between 80% and 90% compared to 100% SOC, due to a cathode-driven shuttle mechanism at higher storage SOCs that alleviates loss of lithium to the (re)formation of SEI. Similar observations have also been reported for other cell types [39], where capacity fade during calendar storage was the same at 70% and 90% storage SOC for an NMC/graphite pouch cell. However, capacity fade between CU 0 and CU 1 is much higher compared to the other CUs. This might be an indication that passive electrode effects [60] influence the capacities measured at the beginning of life, thus distorting the dependence of capacity fade on storage SOC, which should be investigated in the future. Moreover, the spoon shape of SOH_C over storage SOC gets distorted after 6 CUs, corresponding to 30 weeks of storing. After this time, capacity fade at 100% accelerates, leading to a kink at the tip of the figurative "spoon". This might be an indication, that capacity fade enters a non-linear regime, although it is not visible in the capacity fade curve in Fig. 5.

The resistance increase also correlates with increasing storage SOC. Furthermore, the different stages of the anode potential also correlate with different levels of resistance increase, i.e. resistance increase is similar between 40% and 65% storage SOC, but increases at higher storage SOCs. Because of this correlation with anode potential, we assume that SOH_R increase is primarily driven by the growth of the SEI and thus, by an increase in charge-transfer resistance. The noise of SOH_R estimation is generally higher than the noise of SOH_C estimation, because of the higher sensitivity to temperature variations and higher

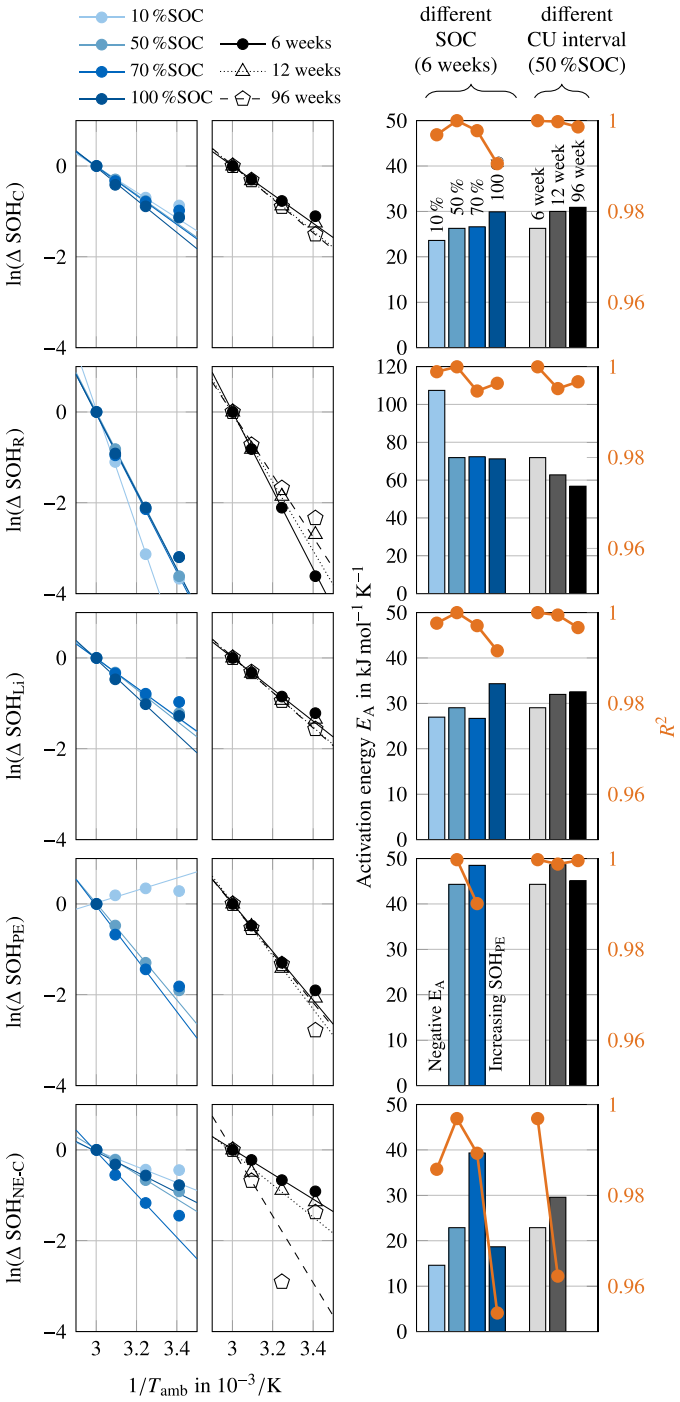

Fig. 7. Temperature dependence of state of health measures during calendar aging. Left side: aging rate ΔSOH over storage temperature T_{amb}. Aging rates are normalized to ln(ΔSOH) = 0 at 60 °C, by subtracting the aging rate at 60 °C for every health parameter. Linear regression lines are fitted to the aging rates at 35 °C, 50 °C, and 60 °C. Right side: calculated activation energy E_A and R^2 as a measure of the goodness of the regression fit. R^2 shows the Arrhenius dependence of the different state of health measures.

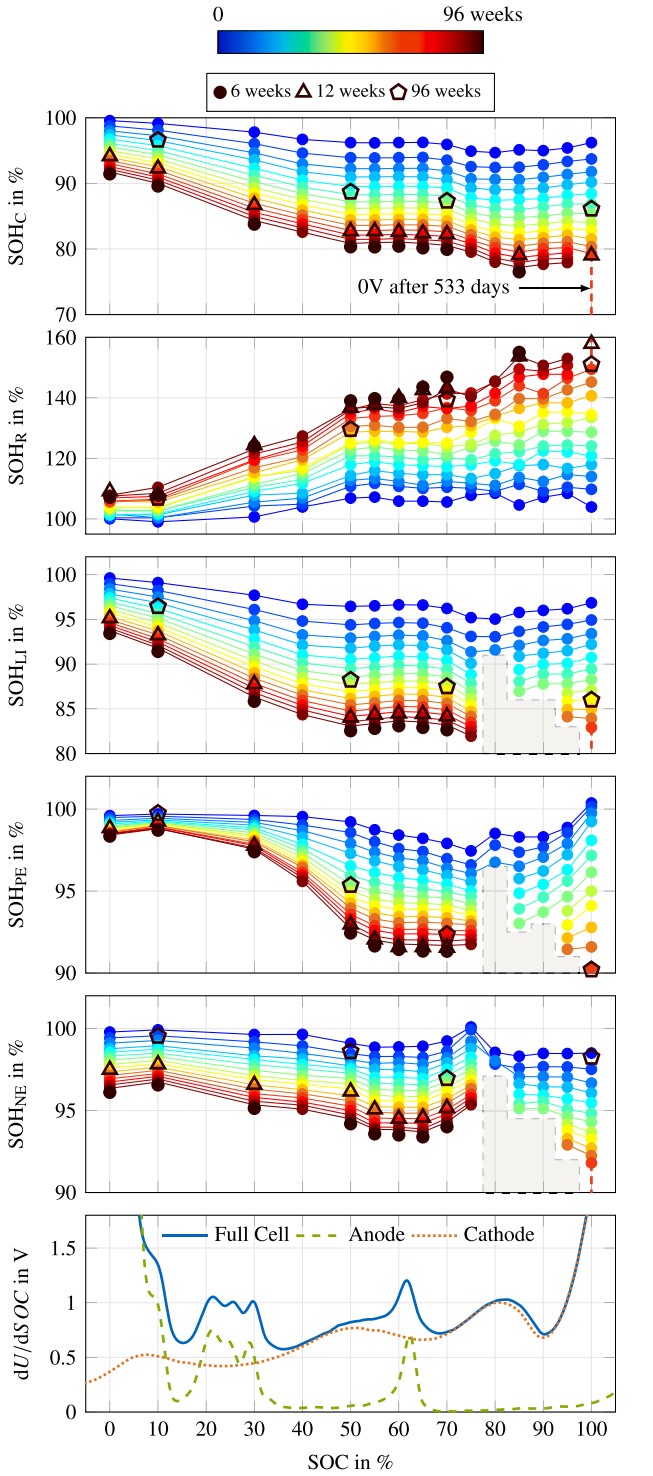

Fig. 8. Evolution of state of health measures for the calendar aged cells, plotted over storage SOC. The grey area in the subplots of SOH_{LI}, SOH_{PE} and SOH_{NE} represents the region, where half-cell fitting failed. The bottom plot shows the differential voltage signature of a pristine cell, to highlight the correlation of state of health evolution with phase transitions in the electrodes. It can be seen, that there is a correlation of SOH_C and anode potential, and that SOH_C follows a characteristic spoon shape over storage SOC for the first 6 CUs. (For interpretation of the references to color in this figure legend, the reader is referred to the web version of this article.)

demand on measurement accuracy [31]. Hence, it remains unclear from this data, if resistance increase generally decreases at storage SOCs above 85% and if it follows a spoon shape over storage SOC, similar to the spoon shape observed for the capacity fade.

The state of health measures of lithium inventory and the electrodes could be extracted for all cells for the first 3 CUs, but for the cells stored at SOCs between 80% and 95%, the half-cell fitting gradually fails. The failing occurs after 3 CUs for the cell stored at 80% SOC, after 7 CUs for the cells stored at 85% and 90% SOC and after 10 CUs for the cell stored at 95% SOC. The reason for the failing of the half-cell fitting is that an additional peak in the C/10 charge differential voltage starts to emerge

for these storage conditions, located at around 70% SOC. This peak, likely resulting from inhomogeneous aging of the electrodes, cannot be reproduced by shifting and scaling of the half-cell OCPs, thus leading to a sudden increase in RMSE in the OCV domain.

Analyzing the results, where the half-cell fitting could be performed successfully reveals that SOH_{LI} depends similarly on SOC as SOH_C. This is expected, since we assume that degradation is mostly driven by SEI growth during calendar aging. SOH_{PE}, however, depends differently on SOC. At low SOCs, SOH_{PE} remains almost constant over the entire 96 weeks. Between 30% and 50% storage SOC, there is a sudden increase in degradation at the positive electrode, which coincides with the occurrence of the monoclinic phase in NCA, which can be seen at the bottom of Fig. 8. At higher storage SOCs, the degradation at the positive electrode reduces, suggesting it to be the culprit of the spoon shape of SOH_C. However, with increasing CUs, SOH_{PE} drops dramatically at the high storage SOCs. SOH_{NE}, again, increase with increasing storage SOC. However, different to any of the other health parameters, there is a local minimum of degradation of the cell stored at 35% SOC. At higher storage SOCs, degradation increases and there is no spoon shape of SOH_{NE} with respect to storage SOC.

4.2. Cycle aging

In Fig. 9, the five health parameters (five rows) are plotted for a selection of cells from the cyclic D-optimal test matrix. For this comparison, we selected cells, where only one of the stress factors T_{amb}, ∅SOC, DOD, I_{ch} or I_{dis} is changed versus other cells, to evaluate the effect of the individual stress factors on degradation.

Across most test conditions, the cycle life of the tested cell type well exceeds 1000 EFC when using SOH_C<80% as the end-of-life criterium. The resistance increase is in the same order of magnitude, and SOH_R does not exceed 120% before 1000 EFC for most cells. Also across most test conditions, there is an initial reduction in SOH_R, which was discussed above for the influence of the CU procedure on calendar aging. Similar resistance break-in during initial cycling has been reported in the literature [43,64–66]. Authors assume that the resistance decreases due to an increased active surface at the anode, either through particle cracking [65,66], or through increased pressure, which in turn improves the wetting with electrolyte [43].

The degradation modes, calculated from the half-cell fitting procedure, reveal that the dominant degradation mode during cyclic aging of this cell type is LLI. In the following, the individual influence of the different stress factors on degradation is discussed.

4.2.1. Influence of depth of discharge

The influence of the depth of discharge on degradation is visible in the subfigures in the left column of Fig. 9. Here, 5 cells are compared, where the DOD was varied between 20% and 100%. The other stress factors were kept constant and the values can be taken from the respective legend in Fig. 9. Degradation increases with increasing DOD. However, the correlation between DOD and degradation is not linear: SOH_C evolves similarly, i.e. it decreases sublinearly with charge-throughput, for the four cells at 20%, 40%, 60% and 80% DOD and capacity fade increases slightly with increasing DOD. The evolution of SOH_R between these four cells is even indistinguishable. However, the degradation of the cell cycled with 100% DOD is different, both qualitatively and quantitatively. For this cell, capacity fade evolves at a much higher rate during early cycling and even accelerates past a knee-point after around 500 EFC. Even before this knee-point, SOH_R increases at a higher rate.

The degradation modes reveal that the accelerated capacity fade and resistance increase is mostly driven by LLI and LAM_{NE}, which evolve differently for this cell compared to the cells cycled at lower DODs. A possible explanation for this increased degradation at high DODs might be that at high and low SOCs, the cell active materials undergo additional phase transitions during lithiation and delithiation. For NCA, the phase transition from monoclinic to hexagonal-2 at high potential causes a volume reduction, which has been reported to cause subsequent microcracks in the material [59]. For silicon–graphite compounds, the silicon only becomes electrochemically active at high potentials, i.e. low SOCs of the full cell, leading to accelerated silicon degradation, when cycling at low SOCs [67].

4.2.2. Influence of temperature

The influence of the temperature on degradation is visible in the subfigures in the second to left column of Fig. 9. We compare three cells cycled with a low discharge rate of 1 C at 20 °C, 35 °C and 50 °C ambient temperature, as well as two cells cycled with a high discharge rate of 10 °C at 20 °C and 35 °C ambient temperature.

For the three cells cycled with a low discharge rate, an increase in ambient temperature correlates with increase capacity fade and resistance increase. However, the increase in capacity fade and resistance is larger between 35 °C and 50 °C than between 20 °C and 35 °C, suggesting that the correlation between temperature and degradation during cycling is non-linear. SOH_{LI}, again, correlates strongly with SOH_C. The degradation of the electrodes also show a dependence on temperature, but this dependence is more pronounced in SOH_{PE} than in SOH_{NE}. In fact, SOH_{NE} of the cells cycled at 20 °C and 35 °C ambient temperature are indistinguishable from one another.

For the two cells cycled with a higher discharged rate, degradation is higher overall compared to the same test points with a low discharge rate. However, the temperature dependence of the state of health parameters is qualitatively the same.

4.2.3. Influence of discharging rates

The influence of the discharge rate on degradation is visible in the subfigures in the second-to-right column of Fig. 9. We compare two cells cycled with a low DOD of only 5% with 1 C and 10 C discharge current, as well as two cells cycled with a higher DOD of 30% with 1 C and 10 C discharge current.

For the two cells cycled with the low DOD, the influence of the discharge current on degradation is comparatively small. SOH_C degrades slightly faster at the higher discharge current, but SOH_R is indistinguishable between both cells. The degradation modes reveal the reason for the difference in SOH_C. The electrodes states of health SOH_{PE} and SOH_{NE} evolve indistinguishably for these conditions and are not influenced by the increased discharge rates. SOH_{LI}, however, correlates with SOH_C, suggesting that LLI is the main reason for accelerated capacity fade at the higher discharge rate.

For the two cells cycled with the higher DOD, however, the influence of the discharge current on degradation is significantly higher. In this case, the difference in SOH_C after 1000 EFC is close to 10% and SOH_C of the cell cycled with the high discharge rate has already dropped to about 80%, commonly used as the end-of-life criterium. The degradation modes reveal the cause for this higher dependence on discharge rate. Compared to the cells cycled with the low DOD, where no dependence of electrode degradation on discharge rate was present, SOH_{PE} rapidly decreases for the cell cycled with the high discharge rate, compared to the cell cycled with the low discharge rate. In fact, degradation at the positive electrode is so rapid, that half-cell fitting fails after around 900 EFC. We assume that this high dependence of SOH_{PE} on discharge rate for these conditions is due to the SOC range during cycling. With a mean SOC of 60% and a DOD of 30%, the cells are always cycled across the phase transition between the hexagonal-1 and the monoclinic phase. At the higher discharge rate, we assume that this phase transition occurs more heterogeneously across the electrode. This leads to a higher stress between the active particles due to the heterogeneous volume change during phase-transition and thus, to a higher loss of active material due to a loss of electric contact.

To summarize, these results suggest that the influence of the discharge current on aging strongly depends on the SOCs range during cycling.

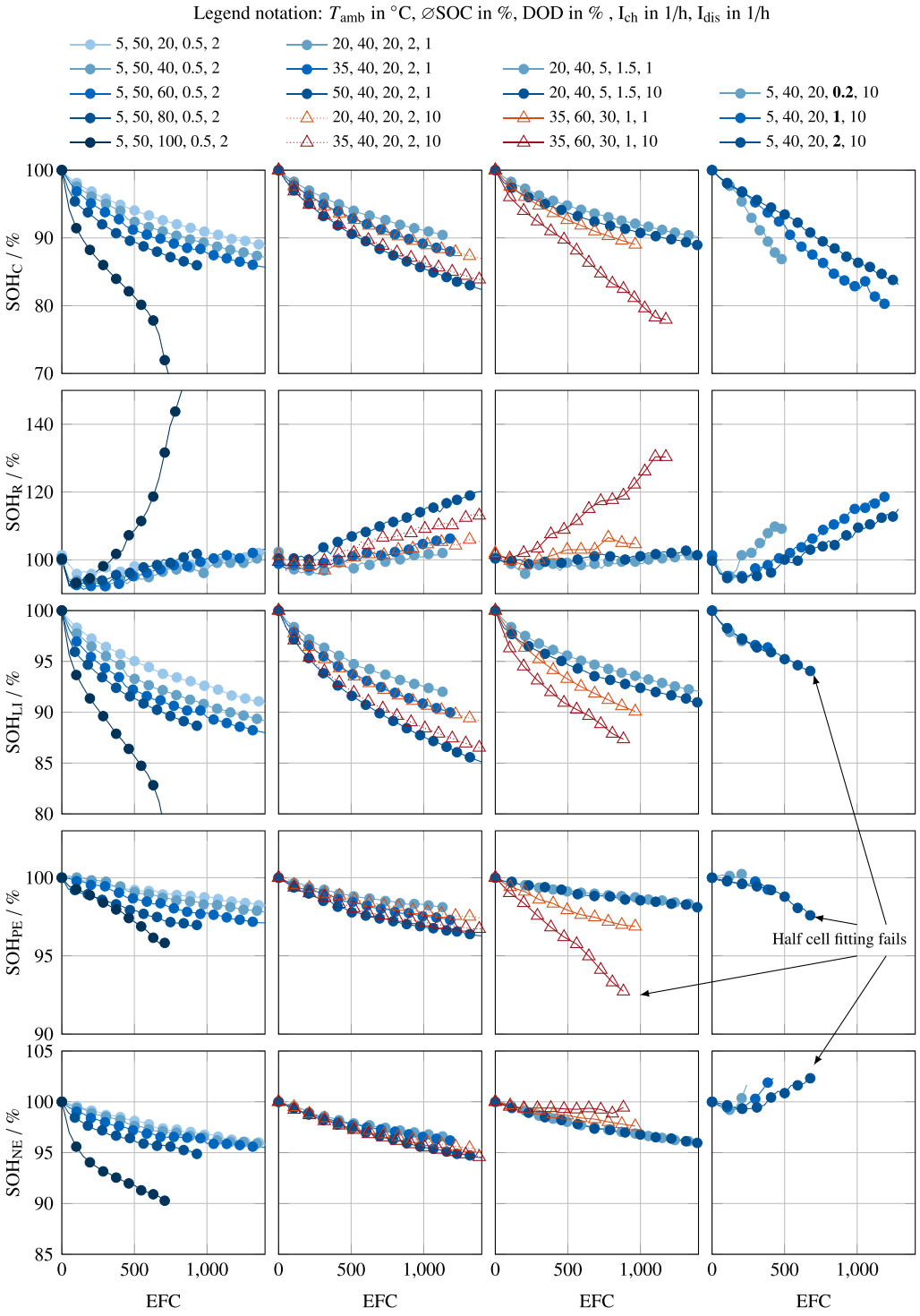

Fig. 9. Health parameters estimated during CUs of cycle aged cells over 1500 EFC. The different rows show the state of health estimations for capacity, resistance, lithium inventory, positive electrode and negative electrode, from top to bottom respectively. The different columns show groups of cells, where only one stress factor was changed to reveal the influence of temperature, mean cyclic SOC, DOD, charge current and discharge current, from left to right respectively.

4.2.4. Influence of charging rates

The influence of the charge rate on degradation is visible in the subfigures in the right column of Fig. 9. We compare three cells cycled at 5 °C ambient temperature, with charge rates of 0.2 C, 1 C and 2 C. In contrast to all other described cells, with the exception of the cell cycled with high discharge currents with a high DOD, these are the only three cells, where SOH_C does not evolve sublinearly. Instead, capacity fade accelerates after a certain point, which is at around 500 EFC for the two cells charged with 1 C and 2 C and at around 200 EFC for the cell charged with 0.2 C. A likely explanation for the occurrence of accelerated capacity fade in these three cells is that the high charge currents in combination with the low ambient temperature facilitate lithium plating, which is often associated with superlinear capacity fade [58]. Usually, higher charge rates are reported to result in an increase of lithium plating [68]. However, in our tests, capacity fades most rapid for the cell charged with 0.2 C. A possible explanation for this observation might be that the cells charged with higher currents are less prone to lithium plating due to the additional heating induced

by the higher currents, such as suggested in [69]. Moreover, due to the lower overpotentials during charging with lower current rate, the cell charged with 0.2 C reaches the CV phase during discharging. This is not the case for the higher charging rates, thus resulting in faster cycles and less time to cool down after discharging.

The resistance increase follows the same trend, and the cell charged with the lowest current shows the highest increase in SOH_R. For the degradation modes, we have only limited data available, since the half-cell fitting failed for all cells after a certain amount of degradation. And even before the half-cell fitting fails per our definition described earlier, the results from half-cell fitting are not physical; e.g. SOH_{NE} increases for all cells.

5. Summary

We aged 196 commercial lithium-ion cells with a silicon-doped graphite anode and nickel-rich NCA cathode during a variety of different cycle and calendar aging conditions. For all test conditions, we performed periodic check-ups to measure capacity fade, resistance increase, loss of lithium inventory, loss of active material at the anode and loss of active material at the cathode.

During calendar aging, we quantify the influence of the check-up on aging by comparing degradation of cells subjected to CUs at different frequencies, while being stored at the same ambient temperature and SOC. We show that the CU influence on degradation depends significantly on the storage conditions and thus, we assume that the additional aging seen in the groups with higher CU intervals results from accelerated aging in the subsequent calendar phases.

Capacity fade during calendar aging increases with SOC and temperature and LLI is the dominating degradation mechanism. The cells stored at 60 °C and 50 °C with 100% SOC and at 60 °C with 70% failed (0 V) before the end of testing after 697 days. During cyclic aging, the influence of DOD, temperature, charge rate and discharge rate are compared. DOD has the highest influence on capacity fade and resistance increase, while the influence of the discharge rate on capacity fade and resistance increase depends on the cycling SOC window. During cycling at high SOCs, capacity fade is accelerated and we assume that particle cracking in the cathode is the primary cause, which is visible in an accelerated fade of SOH_{PE}. For the cells cycled with different charging rates at 5 °C, half-cell fitting fails after few CUs and the capacity fades non-linearly. We assume that lithium plating is the primary cause for this. However, capacity fade is highest at low charge currents, which we ascribe to self-heating of the cells at higher charge currents.

Further investigations are required for the state of health measures of lithium inventory and the electrodes, due to inhomogeneous electrode degradation, resulting in a failing of the half-cell fitting algorithm. In the future, we want to develop a model that can reflect the inhomogeneous electrode degradation, by combining multiple pristine electrode curves, representing different regions of the electrodes.

CRediT authorship contribution statement

Leo Wildfeuer: Conceptualization, Methodology, Formal Analysis, Investigation, Visualization, Data curation, Software, Validation, Writing – original draft, Writing – review & editing. **Alexander Karger:** Formal Analysis, Software, Validation, Writing – original draft, Writing – review & editing. **Deniz Aygül:** Software, Investigation, Writing – review & editing. **Nikolaos Wassiliadis:** Investigation, Validation, Writing – review & editing. **Andreas Jossen:** Supervision, Writing – review & editing. **Markus Lienkamp:** Resources, Supervision, Writing – review & editing.

Declaration of competing interest

The authors declare that they have no known competing financial interests or personal relationships that could have appeared to influence the work reported in this paper.

Data availability

Data is accessible under [29].

Acknowledgments

The authors want to acknowledge the Bavarian Ministry of Economic Affairs, Regional Development and Energy, Germany for funding the project bawaii —- battery analytics with artificial intelligence (IUK-1808-0013).

References

[1] M. Ecker, J.B. Gerschler, J. Vogel, S. Käbitz, F. Hust, P. Dechent, D.U. Sauer, Development of a lifetime prediction model for lithium-ion batteries based on extended accelerated aging test data, J. Power Sources 215 (2012) 248–257, http://dx.doi.org/10.1016/j.jpowsour.2012.05.012.

[2] J. Schmalstieg, S. Käbitz, M. Ecker, D.U. Sauer, A holistic aging model for Li(NiMnCo)O2 based 18650 lithium-ion batteries, J. Power Sources 257 (2014) 325–334, http://dx.doi.org/10.1016/j.jpowsour.2014.02.012.

[3] M. Naumann, M. Schimpe, P. Keil, H.C. Hesse, A. Jossen, Analysis and modeling of calendar aging of a commercial LiFePO4/graphite cell, J. Energy Storage 17 (2018) 153–169, http://dx.doi.org/10.1016/j.est.2018.01.019.

[4] M. Naumann, F.B. Spingler, A. Jossen, Analysis and modeling of cycle aging of a commercial LiFePO4/graphite cell, J. Power Sources 451 (2020) 227666, http://dx.doi.org/10.1016/j.jpowsour.2019.227666.

[5] M. Lucu, E. Martinez-Laserna, I. Gandiaga, H. Camblong, A critical review on self-adaptive Li-ion battery ageing models, J. Power Sources 401 (2018) 85–101, http://dx.doi.org/10.1016/j.jpowsour.2018.08.064.

[6] M. Lucu, E. Martinez-Laserna, I. Gandiaga, K. Liu, H. Camblong, W. Widanage, J. Marco, Data-driven nonparametric Li-ion battery ageing model aiming at learning from real operation data – Part A: Storage operation, J. Energy Storage 30 (2020) 101409, http://dx.doi.org/10.1016/j.est.2020.101409.

[7] M. Lucu, E. Martinez-Laserna, I. Gandiaga, K. Liu, H. Camblong, W. Widanage, J. Marco, Data-driven nonparametric Li-ion battery ageing model aiming at learning from real operation data -Part B: Cycling operation, J. Energy Storage 30 (2020) 101410, http://dx.doi.org/10.1016/j.est.2020.101410.

[8] D. Burzyński, L. Kasprzyk, A novel method for the modeling of the state of health of lithium-ion cells using machine learning for practical applications, Knowl.-Based Syst. 219 (2021) 106900, http://dx.doi.org/10.1016/j.knosys.2021.106900.

[9] L. Su, M. Wu, Z. Li, J. Zhang, Cycle life prediction of lithium-ion batteries based on data-driven methods, eTransportation 10 (2021) 100137, http://dx.doi.org/10.1016/j.etran.2021.100137.

[10] J. Zhu, Y. Wang, Y. Huang, R. Bhushan Gopaluni, Y. Cao, M. Heere, M.J. Mühlbauer, L. Mereacre, H. Dai, X. Liu, A. Senyshyn, X. Wei, M. Knapp, H. Ehrenberg, Data-driven capacity estimation of commercial lithium-ion batteries from voltage relaxation, Nature Commun. 13 (1) (2022) 2261, http://dx.doi.org/10.1038/s41467-022-29837-w.

[11] N.H. Paulson, J. Kubal, L. Ward, S. Saxena, W. Lu, S.J. Babinec, Feature engineering for machine learning enabled early prediction of battery lifetime, J. Power Sources 527 (2022) 231127, http://dx.doi.org/10.1016/j.jpowsour.2022.231127.

[12] G. dos Reis, C. Strange, M. Yadav, S. Li, Lithium-ion battery data and where to find it, Energy AI 5 (2021) http://dx.doi.org/10.1016/j.egyai.2021.100081.

[13] B. Bole, C. Kulkarni, M. Daigle, Randomized battery usage data set, NASA AMES Prognostics Data Repository, NASA Ames Research Center, Moffett Field, CA.

[14] S.S. Ng, Y. Xing, K.L. Tsui, A naive Bayes model for robust remaining useful life prediction of lithium-ion battery, Appl. Energy 118 (2014) 114–123, http://dx.doi.org/10.1016/j.apenergy.2013.12.020.

[15] X. Lu, H. Li, N. Chen, An indicator for the electrode aging of lithium-ion batteries using a fractional variable order model, Electrochim. Acta 299 (2019) 378–387, http://dx.doi.org/10.1016/j.electacta.2018.12.097.

[16] X. Tang, K. Liu, X. Wang, B. Liu, F. Gao, W.D. Widanage, Real-time aging trajectory prediction using a base model-oriented gradient-correction particle filter for lithium-ion batteries, J. Power Sources 440 (2019) 227118, http://dx.doi.org/10.1016/j.jpowsour.2019.227118.

[17] B. Zhou, C. Cheng, G. Ma, Y. Zhang, Remaining useful life prediction of lithium-ion battery based on attention mechanism with positional encoding, IOP Conf. Ser.: Mater. Sci. Eng. 895 (1) (2020) 012006, http://dx.doi.org/10.1088/1757-899x/895/1/012006.

[18] X. Li, C. Yuan, Z. Wang, J. He, S. Yu, Lithium battery state-of-health estimation and remaining useful lifetime prediction based on non-parametric aging model and particle filter algorithm, eTransportation 11 (2022) 100156, http://dx.doi.org/10.1016/j.etran.2022.100156.

[19] F.J. Günter, N. Wassiliadis, State of the art of lithium-ion pouch cells in automotive applications: Cell teardown and characterization, J. Electrochem. Soc. 169 (3) (2022) 030515, http://dx.doi.org/10.1149/1945-7111/ac4e11.

[20] N. Wassiliadis, M. Steinsträter, M. Schreiber, P. Rosner, L. Nicoletti, F. Schmid, M. Ank, O. Teichert, L. Wildfeuer, J. Schneider, A. Koch, A. König, A. Glatz, J. Gandlgruber, T. Kröger, X. Lin, M. Lienkamp, Quantifying the state of the art of electric powertrains in battery electric vehicles: Range, efficiency, and lifetime from component to system level of the Volkswagen ID.3, eTransportation 12 (2022) 100167, http://dx.doi.org/10.1016/j.etran.2022.100167.

[21] M. Aykol, C.B. Gopal, A. Anapolsky, P.K. Herring, B. van Vlijmen, M.D. Berliner, M.Z. Bazant, R.D. Braatz, W.C. Chueh, B.D. Storey, Perspective—combining physics and machine learning to predict battery lifetime, J. Electrochem. Soc. 168 (3) (2021) 030525, http://dx.doi.org/10.1149/1945-7111/abec55.

[22] J. Keil, N. Paul, V. Baran, P. Keil, R. Gilles, A. Jossen, Linear and nonlinear aging of lithium-ion cells investigated by electrochemical analysis and in-situ neutron diffraction, J. Electrochem. Soc. 166 (16) (2019) A3908–A3917, http://dx.doi.org/10.1149/2.1271915jes.

[23] K. Smith, A. Saxon, M. Keyser, B. Lundstrom, Z. Cao, A. Roc, Life prediction model for grid-connected Li-ion battery energy storage system, Tech. Rep., 2017, pp. 4062–4068, http://dx.doi.org/10.23919/ACC.2017.7963578.

[24] X. Jia, C. Zhang, L.Y. Wang, L. Zhang, W. Zhang, The degradation characteristics and mechanism of Li[Ni0.5Co0.2Mn0.3]O2 batteries at different temperatures and discharge current rates, J. Electrochem. Soc. 167 (2) (2020) 020503, http://dx.doi.org/10.1149/1945-7111/ab61e9.

[25] S. Lee, P. Mohtat, J.B. Siegel, A.G. Stefanopoulou, J.-W. Lee, T.-K. Lee, Estimation error bound of battery electrode parameters with limited data window, IEEE Trans. Ind. Inform. 16 (5) (2020) 3376–3386, http://dx.doi.org/10.1109/TII.2019.2952066.

[26] S. Lee, J.B. Siegel, A.G. Stefanopoulou, J.-W. Lee, T.-K. Lee, Electrode state of health estimation for lithium ion batteries considering half-cell potential change due to aging, J. Electrochem. Soc. 167 (9) (2020) 090531, http://dx.doi.org/10.1149/1945-7111/ab8c83.

[27] J.S. Edge, S. O'Kane, R. Prosser, N.D. Kirkaldy, A.N. Patel, A. Hales, A. Ghosh, W. Ai, J. Chen, J. Yang, S. Li, M.-C. Pang, L. Bravo Diaz, A. Tomaszewska, M.W. Marzook, K.N. Radhakrishnan, H. Wang, Y. Patel, B. Wu, G.J. Offer, Lithium ion battery degradation: What you need to know, Phys. Chem. Chem. Phys. 23 (2021) 8200–8221, http://dx.doi.org/10.1039/D1CP00359C.

[28] J. Schmitt, M. Schindler, A. Oberbauer, A. Jossen, Determination of degradation modes of lithium-ion batteries considering aging-induced changes in the half-cell open-circuit potential curve of silicon–graphite, J. Power Sources 532 (2022) 231296, http://dx.doi.org/10.1016/j.jpowsour.2022.231296.

[29] L. Wildfeuer, A. Karger, D. Aygül, N. Wasiiliadis, A. Jossen, M. Lienkamp, Experimental degradation study of a commercial lithium-ion battery, 2023, http://dx.doi.org/10.14459/2023mp1713382, https://mediatum.ub.tum.de/1713382.

[30] A. Karger, L. Wildfeuer, D. Aygül, A. Maheshwari, J.P. Singer, A. Jossen, Modeling capacity fade of lithium-ion batteries during dynamic cycling considering path dependence, J. Energy Storage 52 (2022) 104718, http://dx.doi.org/10.1016/j.est.2022.104718.

[31] L. Wildfeuer, M. Lienkamp, Quantifiability of inherent cell-to-cell variations of commercial lithium-ion batteries, eTransportation 9 (2021) 100129, http://dx.doi.org/10.1016/j.etran.2021.100129.

[32] M.J. Lain, J. Brandon, E. Kendrick, Design strategies for high power vs. High energy lithium ion cells, Batteries 5 (4) (2019) 1–13, http://dx.doi.org/10.3390/batteries5040064.

[33] L. Wildfeuer, N. Wassiliadis, A. Karger, F. Bauer, M. Lienkamp, Teardown analysis and characterization of a commercial lithium-ion battery for advanced algorithms in battery electric vehicles, J. Energy Storage 48 (December 2021) (2022) 103909, http://dx.doi.org/10.1016/j.est.2021.103909.

[34] L. Wildfeuer, N. Wassiliadis, A. Karger, F. Bauer, M. Lienkamp, Teardown analysis and characterization of a commercial lithium-ion battery for advanced algorithms in battery electric vehicles, 2022, http://dx.doi.org/10.14459/2022mp1639153, Technical University of Munich.

[35] M. Lewerenz, P. Dechent, D.U. Sauer, Investigation of capacity recovery during rest period at different states-of-charge after cycle life test for prismatic Li(Ni 1/3 Mn 1/3 Co 1/3)O 2 -graphite cells, J. Energy Storage 21 (January) (2019) 680–690, http://dx.doi.org/10.1016/j.est.2019.01.004.

[36] M. Lewerenz, D.U. Sauer, Evaluation of cyclic aging tests of prismatic automotive LiNiMnCoO2-Graphite cells considering influence of homogeneity and anode overhang, J. Energy Storage 18 (January) (2018) 421–434, http://dx.doi.org/10.1016/j.est.2018.06.003.

[37] T. Hüfner, M. Oldenburger, B. Bedürftig, A. Gruhle, Lithium flow between active area and overhang of graphite anodes as a function of temperature and overhang geometry, J. Energy Storage 24 (May) (2019) 100790, http://dx.doi.org/10.1016/j.est.2019.100790.

[38] J. Schmitt, A. Maheshwari, M. Heck, S. Lux, M. Vetter, Impedance change and capacity fade of lithium nickel manganese cobalt oxide-based batteries during calendar aging, J. Power Sources 353 (2017) 183–194, http://dx.doi.org/10.1016/j.jpowsour.2017.03.090.

[39] A. Krupp, R. Beckmann, T. Diekmann, E. Ferg, F. Schuldt, C. Agert, Calendar aging model for lithium-ion batteries considering the influence of cell characterization, J. Energy Storage 45 (2022) 103506, http://dx.doi.org/10.1016/j.est.2021.103506.

[40] W.-F. Cai, K.-C. Chen, Influence of the calendar aging on the cycle aging of LiNiMnCoO2 lithium-ion batteries, J. Electrochem. Soc. 168 (12) (2021) 120525, http://dx.doi.org/10.1149/1945-7111/ac405a.

[41] M. Lewerenz, G. Fuchs, L. Becker, D.U. Sauer, Irreversible calendar aging and quantification of the reversible capacity loss caused by anode overhang, J. Energy Storage 18 (2018) 149–159, http://dx.doi.org/10.1016/j.est.2018.04.029.

[42] CRGRAPH, Visual-XSel, URL https://crgraph.de/visual-xsel-software/.

[43] K.W. Knehr, T. Hodson, C. Bommier, G. Davies, A. Kim, D.A. Steingart, Understanding full-cell evolution and non-chemical electrode crosstalk of Li-ion batteries, Joule 2 (6) (2018) 1146–1159, http://dx.doi.org/10.1016/j.joule.2018.03.016.

[44] M. Dubarry, C. Truchot, B.Y. Liaw, Synthesize battery degradation modes via a diagnostic and prognostic model, J. Power Sources 219 (2012) 204–216, http://dx.doi.org/10.1016/j.jpowsour.2012.07.016.

[45] J.P. Schmidt, H.Y. Tran, J. Richter, E. Ivers-Tiffée, M. Wohlfahrt-Mehrens, Analysis and prediction of the open circuit potential of lithium-ion cells, J. Power Sources 239 (2013) 696–704, http://dx.doi.org/10.1016/j.jpowsour.2012.11.101.

[46] X. Han, M. Ouyang, L. Lu, J. Li, Y. Zheng, Z. Li, A comparative study of commercial lithium ion battery cycle life in electrical vehicle: Aging mechanism identification, J. Power Sources 251 (2014) 38–54, http://dx.doi.org/10.1016/j.jpowsour.2013.11.029.

[47] K. Honkura, T. Horiba, Study of the deterioration mechanism of LiCoO2/graphite cells in charge/discharge cycles using the discharge curve analysis, J. Power Sources 264 (2014) 140–146, http://dx.doi.org/10.1016/j.jpowsour.2014.04.036.

[48] C.R. Birkl, E. McTurk, M.R. Roberts, P.G. Bruce, D.A. Howey, A parametric open circuit voltage model for lithium ion batteries, J. Electrochem. Soc. 162 (12) (2015) A2271–A2280, http://dx.doi.org/10.1149/2.0331512jes.

[49] A. Marongiu, N. Nlandi, Y. Rong, D.U. Sauer, On-board capacity estimation of lithium iron phosphate batteries by means of half-cell curves, J. Power Sources 324 (2016) 158–169, http://dx.doi.org/10.1016/j.jpowsour.2016.05.041.

[50] C.R. Birkl, M.R. Roberts, E. McTurk, P.G. Bruce, D.A. Howey, Degradation diagnostics for lithium ion cells, J. Power Sources 341 (2017) 373–386, http://dx.doi.org/10.1016/j.jpowsour.2016.12.011.

[51] C.R. Birkl, E. McTurk, S. Zekoll, F.H. Richter, M.R. Roberts, P.G. Bruce, D.A. Howey, Degradation diagnostics for commercial lithium-ion cells tested at - 10°C, J. Electrochem. Soc. 164 (12) (2017) A2644–A2653, http://dx.doi.org/10.1149/2.1401712jes.

[52] S. Schindler, M.A. Danzer, A novel mechanistic modeling framework for analysis of electrode balancing and degradation modes in commercial lithium-ion cells, J. Power Sources 343 (2017) 226–236, http://dx.doi.org/10.1016/j.jpowsour.2017.01.026.

[53] Y. Gao, J. Jiang, C. Zhang, W. Zhang, Y. Jiang, Aging mechanisms under different state-of-charge ranges and the multi-indicators system of state-of-health for lithium-ion battery with Li(NiMnCo)O2 cathode, J. Power Sources 400 (2018) 641–651, http://dx.doi.org/10.1016/j.jpowsour.2018.07.018.

[54] Z. Ma, Z. Wang, R. Xiong, J. Jiang, A mechanism identification model based state-of-health diagnosis of lithium-ion batteries for energy storage applications, J. Clean. Prod. 193 (2018) 379–390, http://dx.doi.org/10.1016/j.jclepro.2018.05.074.

[55] J. Schmitt, M. Schindler, A. Jossen, Change in the half-cell open-circuit potential curves of silicon–graphite and nickel-rich lithium nickel manganese cobalt oxide during cycle aging, J. Power Sources 506 (2021) 230240, http://dx.doi.org/10.1016/j.jpowsour.2021.230240.

[56] L. Cai, K. An, Z. Feng, C. Liang, S.J. Harris, In-situ observation of inhomogeneous degradation in large format Li-ion cells by neutron diffraction, J. Power Sources 236 (2013) 163–168, http://dx.doi.org/10.1016/j.jpowsour.2013.02.066.

[57] J.P. Fath, D. Dragicevic, L. Bittel, A. Nuhic, J. Sieg, S. Hahn, L. Alsheimer, B. Spier, T. Wetzel, Quantification of aging mechanisms and inhomogeneity in cycled lithium-ion cells by differential voltage analysis, J. Energy Storage 25 (2019) 100813, http://dx.doi.org/10.1016/j.est.2019.100813.

[58] P.M. Attia, A. Bills, F.B. Planella, P. Dechent, G. dos Reis, M. Dubarry, P. Gasper, R. Gilchrist, S. Greenbank, D. Howey, O. Liu, E. Khoo, Y. Preger, A. Soni, S. Sripad, A.G. Stefanopoulou, V. Sulzer, Review—"knees" in lithium-ion battery aging trajectories, J. Electrochem. Soc. 169 (6) (2022) 060517, http://dx.doi.org/10.1149/1945-7111/ac6d13.

[59] K.-J. Park, J.-Y. Hwang, H.-H. Ryu, F. Maglia, S.-J. Kim, P. Lamp, C.S. Yoon, Y.-K. Sun, Degradation mechanism of Ni-enriched NCA cathode for lithium batteries: Are microcracks really critical? ACS Energy Lett. 4 (6) (2019) 1394–1400, http://dx.doi.org/10.1021/acsenergylett.9b00733.

[60] T. Bank, J. Feldmann, S. Klamor, S. Bihn, D.U. Sauer, Extensive aging analysis of high-power lithium titanate oxide batteries: Impact of the passive electrode effect, J. Power Sources 473 (2020) 228566, http://dx.doi.org/10.1016/j.jpowsour.2020.228566.

[61] X. Li, A.M. Colclasure, D.P. Finegan, D. Ren, Y. Shi, X. Feng, L. Cao, Y. Yang, K. Smith, Degradation mechanisms of high capacity 18650 cells containing Si-graphite anode and nickel-rich NMC cathode, Electrochim. Acta 297 (2019) 1109–1120, http://dx.doi.org/10.1016/j.electacta.2018.11.194.

[62] M. Wetjen, D. Pritzl, R. Jung, S. Solchenbach, R. Ghadimi, H.A. Gasteiger, Differentiating the degradation phenomena in silicon-graphite electrodes for lithium-ion batteries, J. Electrochem. Soc. 164 (12) (2017) A2840–A2852, http://dx.doi.org/10.1149/2.1921712jes.

[63] A. Zülke, Y. Li, P. Keil, R. Burrell, S. Belaisch, M. Nagarathinam, M.P. Mercer, H.E. Hoster, High-energy nickel-cobalt-aluminium oxide (NCA) cells on idle: Anode- versus cathode-driven side reactions, Batteries Supercaps 4 (6) (2021) 849, http://dx.doi.org/10.1002/batt.202100101.

[64] J. Zhou, P. Notten, Studies on the degradation of Li-ion batteries by the use of microreference electrodes, J. Power Sources 177 (2) (2008) 553–560, http://dx.doi.org/10.1016/j.jpowsour.2007.11.032.

[65] B. Stiaszny, J.C. Ziegler, E.E. Krauß, J.P. Schmidt, E. Ivers-Tiffée, Electrochemical characterization and post-mortem analysis of aged LiMn2O4–Li(Ni0.5Mn0.3Co0.2)O2/graphite lithium ion batteries. Part I: Cycle aging, J. Power Sources 251 (2014) 439–450, http://dx.doi.org/10.1016/j.jpowsour.2013.11.080.

[66] T. Goh, M. Park, M. Seo, J.G. Kim, S.W. Kim, Capacity estimation algorithm with a second-order differential voltage curve for Li-ion batteries with NMC cathodes, Energy 135 (2017) 257–268, http://dx.doi.org/10.1016/j.energy.2017.06.141.

[67] N. Kirkaldy, M.A. Samieian, G.J. Offer, M. Marinescu, Y. Patel, Lithium-ion battery degradation: Measuring rapid loss of active silicon in silicon-graphite composite electrodes, 2022, http://dx.doi.org/10.26434/chemrxiv-2022-j2rnd, ChemRxiv.

[68] C. von Lüders, V. Zinth, S.V. Erhard, P.J. Osswald, M. Hofmann, R. Gilles, A. Jossen, Lithium plating in lithium-ion batteries investigated by voltage relaxation and in situ neutron diffraction, J. Power Sources 342 (2017) 17–23, http://dx.doi.org/10.1016/j.jpowsour.2016.12.032.

[69] I.D. Campbell, M. Marzook, M. Marinescu, G.J. Offer, How observable is lithium plating? Differential voltage analysis to identify and quantify lithium plating following fast charging of cold lithium-ion batteries, J. Electrochem. Soc. 166 (4) (2019) A725–A739, http://dx.doi.org/10.1149/2.0821904jes.

2.4 Quantification of Inherent Cell-to-Cell Parameter Variations

Inhomogeneities in lithium-ion battery packs can reduce their performance and increase the risk of system failure. Multiple origins of inhomogeneities trigger a complex cause-and-effect chain with mutual interactions. This section analyses the initial point of this chain and quantifies inherent cell-to-cell variations of commercial lithium-ion cells aimed at answering research question 4. Figure 2.7 gives an overview of measurements, data processing, and investigations performed in the presented Study V. The processed data has been made publicly available as open source [14].

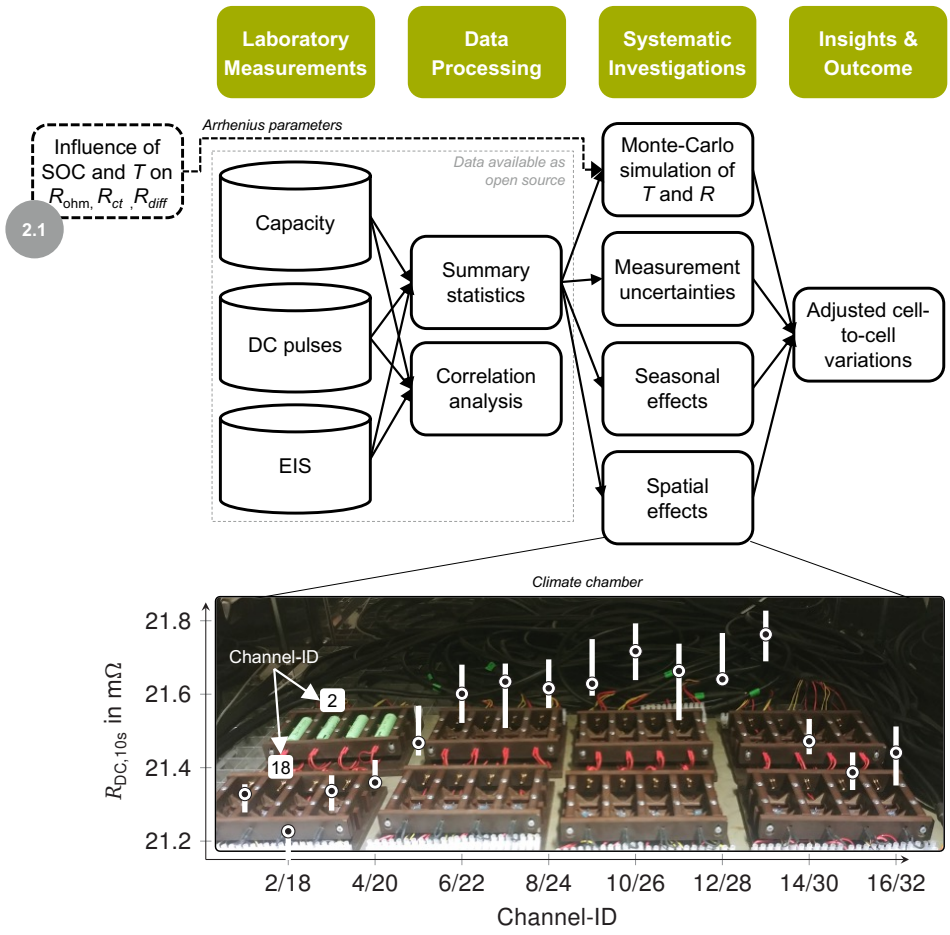

Figure 2.7: Graphical summary of Study V [5].

A total of 600 fresh cells from the same production batch were weighed and tested using an initial check-up procedure to determine their capacity and the DC resistance at a controlled ambient temperature of 20 °C. Additionally, EIS was performed on 100 of these cells. Calculation of the summary statistics revealed low coefficients of variations for the mass (0.11 %), the OCV (0.06 %), the capacity (0.22 %), and the resistance (0.86 % for $R_{\mathrm{DC,10\,s}}$, 0.46 % for R_{ohm}, and 1.64 % for R_{ct}).

As in previous studies, the resistance variation was greater than the capacity variation—approximately five times greater in this case. Already the fact that R_{ct} scattered 3 times more than R_{ohm} was suspicious having in mind that the influence of temperature on R_{ct} is of magnitudes higher compared to R_{ohm}. Moreover, a correlation analysis revealed inconsistent results.

Correlation coefficients of resistance parameters among each other were strongly dependent on the measurement method and the chronology of measurements yielded contradictory correlation coefficients. Therefore, several possible sources of misinterpretation were systematically investigated.

Firstly, it was shown that measurement uncertainties caused by sensor tolerances of the testing equipment are significantly higher for resistance measurements (75 % in this study) compared to capacity measurements (<2 % in this study) because they are calculated differently from the current and voltage sensor data.

Secondly, a Monte Carlo simulation was performed to investigate the mutual influences of temperature and resistance. The Arrhenius equation was used to simulate the effect of temperature variation on resistance and a simple thermal mass model, considering irreversible heat generation, was used to simulate the effect of resistance variation on cell temperature. It was demonstrated that elevated resistance variation is more likely caused by extrinsic temperature variation, rather than the other way around. While resistance variation in the order of 1 % leads to temperature variations in the order of 0.03 °C, temperature variation of 0.5 °C leads to a resistance variation of 1.5 %.

Thirdly, it was shown that temporal effects significantly impacted the results, as a clear trend over time was observed. Since only 32 cells were tested at a time, this was explained by manual processes involved in the experiments, which are handled differently by different people and faster over time.

Systematic spatial distortion of the measurement results was the last hypothesis tested. A picture of said 32 test channels inside the climate chamber is shown in Figure 2.7, and the mean and standard deviation of resistance measurements are plotted on top. The resistance shows a clear pattern which is in accordance with a complementary pattern of temperature and can be explained by an uneven temperature distribution within the climate chamber. Interestingly, analysis of data from a previous publication [197] revealed a similar pattern.

Based on described seasonal and spatial effects, the coefficients of variation could be systematically adjusted leading to a relative reduction of up to 50 % for the resistance and a coefficient of variation of 0.17 % for the capacity and 0.45 % for the resistance $R_{\mathrm{DC,10\,s}}$. Taking into account the higher measurement uncertainties, this study showed that the magnitude of inherent resistance variation of commercial lithium-ion cells caused by production tolerances was well overestimated in the past. It was concluded that compared to other origins of parameter variations, inherent cell-to-cell variations are negligible in the context of scaling the electric behavior of individual cells to battery packs in BEVs.

Contribution

Leo Wildfeuer is the first author of the article.

Leo Wildfeuer: Conceptualization, Methodology, Formal Analysis, Investigation, Visualization, Data curation, Software, Validation, Writing - original draft, Writing - review & editing. Markus Lienkamp: Resources, Supervision, Writing - review & editing.

Quantifiability of inherent cell-to-cell variations of commercial lithium-ion batteries

Leo Wildfeuer, Markus Lienkamp

eTransportation, Volume 9, p. 100129, 2021
Digital Object Identifier: 10.1016/j.etran.2021.100129
Permanent Weblink: https://doi.org/10.1016/j.etran.2021.100129

eTransportation 9 (2021) 100129

Contents lists available at ScienceDirect

eTransportation

journal homepage: www.journals.elsevier.com/etransportation

Quantifiability of inherent cell-to-cell variations of commercial lithium-ion batteries

Leo Wildfeuer [a, b, *], Markus Lienkamp [a]

[a] Institute of Automotive Technology, Department of Mechanical Engineering, Technical University of Munich, Germany
[b] TWAICE Technologies GmbH, Germany

ARTICLE INFO

Article history:
Received 4 May 2021
Received in revised form
29 June 2021
Accepted 13 July 2021
Available online 16 July 2021

Keywords:
Lithium-ion batteries
Cell-to-cell variations
Correlation analysis
Capacity
Electrochemical impedance spectroscopy
Charge transfer resistance

ABSTRACT

Parameter variations of lithium-ion batteries are an important concern because they can reduce the performance of a battery pack. To quantify inherent variations due to production tolerances, battery parameters of a batch of individual cells are experimentally determined and the latest studies show capacity variations of 0.2 %–0.3 % and impedance variations of 0.7 %–3.8 %. Motivated by the question of why impedance variation is consistently reported to be higher than the variation of other parameters, we show that measuring inherent parameter variations caused by production tolerances is superimposed by effects of an imperfect measurement setup. By breaking down external influence factors on own experimental results of a batch of 600 commercial lithium-ion cells as well as a previously published data set, we found that in fact parameter variations are substantially biased by temporal and spatial temperature inhomogeneities during the experiments. By systematically compensating these effects, resistance variation is reduced by almost 50 % to only 0.45 %, which is the smallest value reported so far and closer to the variation of capacity (0.17 %) and mass (0.11 %) in our case. Compensation is justified by a Monte-Carlo simulation of the charge-transfer resistance and the cell temperature to investigate the mutual interaction between resistance and temperature variation. Our results show that extrinsic temperature deviations of only 0.5°C can lead to resistance variations of more than 1.5 %. Based on our findings, we recommend incorporating more restrained initial parameter variations into system simulation models and setting the focus on external origins of parameter variations such as temperature inhomogeneities.

1. Introduction

1.1. Motivation

Parameter variations among individual lithium-ion batteries are an important concern because they can reduce the performance of a battery pack consisting of hundreds or thousands of single cells [1]. As assessed in Ref. [2], multiple origins can cause parameter variations before and during battery pack operation. They can be originated from production tolerances, the system assembly process, or can be a result of inhomogeneous operating conditions such as imperfect cooling of the battery pack. For battery system manufacturers, it is important to gain knowledge about the magnitude of all types of occurring parameter variations for quality management reasons and optimal product design. When they purchase individual cells from cell manufacturers, non-influenceable and thus inherent variations resulting from the cell manufacturing process and the supply chain until the cells arrive at the customer are of particular interest.

1.2. State of the art

In Table 1, previous studies, which experimentally quantified inherent parameter variations, are listed in ascending order according to their year of publication. Accompanying in Table 2, the stated variations alongside the applied measurement procedure is listed for capacity C, DC-resistance R_{DC}, AC-resistance R_{AC} and mass m, respectively. For comparability reasons, the variation of a parameter X is listed relative as $\kappa_X = \sigma_X/\mu_X$ with the coefficient of variation κ, the standard deviation σ, and the mean μ. Additionally, we list the ratio of resistance variation compared to capacity variation with the factor κ_R / κ_C.

* Corresponding author. Institute of Automotive Technology, Department of Mechanical Engineering, Technical University of Munich, Germany
E-mail address: leo.wildfeuer@tum.de (L. Wildfeuer).

https://doi.org/10.1016/j.etran.2021.100129
2590-1168/

Table 1
Overview of existing studies quantifying parameter variations within multiple lithium-ion cells.

Reference	Year	Cells	C_N / Ah	Manufacturer	Cell Model	Chemistry	Format
Dubarry et al. [3]	2009	100	0.3	*commercial*	–	C – LiCoO2	AAA
Zheng et al. [4]	2013	96	70	*commercial*	–	C – LiFePO4	Prismatic
Rothgang et al. [5]	2014	700	5	–	–	C - NMC	Prismatic
Schuster et al. [6]	2015	484	1.95	E-one Moli	IHR18650A	C - NMC	18650
Devie et al. [7]	2016	100	3.35	Panasonic	NCR 18650B	C - NCA	18650
Campestrini et al. [8]	2016	250	2.8	Panasonic	NCR 18650PD	C - NCA	18650
Fang et al. [9]	2017	138	2.9	Panasonic	NCR18650PF	C - NCA	18650
Rumpf et al. [10]	2017	1100	3	Sony/Murata	US26650FTC1	C – LiFePO4	26650
Barreras et al. [11]	2017	> 200	53	Kokam	SLPB 120216216	C - NMC	Pouch
Devie et al. [12]	2018	51	2.8	LG Chem	ICR18650C2	C – LiCoO2/NMC	18650
Baumann et al. [2]	2018	164	2.9	Panasonic	NCR18650PF	C - NCA	18650
Zilberman et al. [13]	2019	48	3.5	LG Chem	INR18650-MJ1	SiC - NMC	18650
Schindler et al. [14]	2021	160	3.35	LG Chem	INR18650-MJ1	SiC - NMC	18650
This study	2021	600	2.5	Sony/Murata	US18650VTC5A	SiC - NCA	18650

Table 2
Overview of stated parameter variations within existing literature. *Data was obtained extracting the raw data of Fig. 5 from Ref. [9] using the WebPlotDigitizer [15]. **The values of two batches (600 and 500 cells, respectively) were averaged. *** The first tested batch is identical with [13], which is why we listed results of the second batch.

	Factor	Capacity		DC-Resistance		AC-Impedance		Mass
Reference	κ_R / κ_C	Method	κ_C	Method	κ_R	Method	κ_Z	κ_m
Dubarry et al. [3]		$CC_{0.5C}$	1.90 %					1.70 %
Zheng et al. [4]						Z_{ohm}	19.47 %	
Rothgang et al. [5]	1.2	CC_{1C}	2.36 %	$R_{4C,\ 10\ s}$	2.87 %			
Schuster et al. [6]	2.4	$CC_{1C}CV_{I\ <\ C/20}$	0.80 %			Z_{ohm}	1.94 %	
Devie et al. [7]	3.7	$CC_{0.5C}$	0.80 %	$R_{0.5C,\ 1st\ point}$	2.95 %			0.16 %
Campestrini et al. [8]	4.5	$CC_{1C}CV_{I\ <\ C/30}$	0.16 %			Z_{ohm}	0.72 %	
Fang et al. [9]*	3.7	$CC_{0.2C}$	1.03 %	$R_{1C,\ 18\ s}$	3.78 %			
Rumpf et al. [10]**	4.8	$CC_{1C}CV_{I\ <\ C/20}$	0.28 %	$R_{CI,\ 10\ s}$	1.33 %	Z_{ohm}	1.28 %	0.10 %
Barreras et al. [11]	16.6	CC_{1C}	0.35 %	$R_{1C,\ 1st\ point}$	5.80 %			
Devie et al. [12]	9.0	$CC_{0.2C}$	0.40 %	$R_{0.2C,\ 1st\ point}$	3.60 %			0.20 %
Baumann et al. [2]	2.6	$CC_{1C}CV_{I\ <\ C/20}$	0.35 %	$R_{1C,\ 2\ s}$	0.92 %			
Zilberman et al. [13]	3.4	$CC_{0.2C}CV_{I\ <\ C/70}$	0.20 %	$R_{1C,\ 10\ s}$	0.68 %			
Schindler et al. [14]***	2.3	$CC_{0.2C}CV_{I\ <\ C/70}$	0.40 %			Z_{ohm}	0.90 %	
This study	3.9	$CC_{1C}CV_{I\ <\ C/25}$	0.22 %	$R_{1C,\ 10\ s}$	0.86 %	Z_{ohm}	0.46 %	0.11 %

Dubarry et al. [3] were one of the first authors to experimentally determine parameter variations for the purpose of system modeling and analyzed the capacity and weight variation of 100 AAA cells. Subsequently, over the time span of more than a decade, many researchers followed and experimentally quantified the variation of various cell characteristics for production new cell batches. Among them, the most comprehensive study in terms of number of tested cells and parameters was performed by Rumpf et al. [10], who investigated two batches (600 and 500 cells, respectively) of LFP 26650 cells and analyzed the distribution and correlation of mass and various capacity and impedance parameters. Besides capacity and impedance parameters, Zilberman et al. [13] also analyzed the variation of characteristic points in the differential voltage curve of 48 nickel-rich, silicon-graphite 18650 lithium-ion cells. Since they found no correlation between capacity or resistance and any characteristic peak in the differential voltage curve, they concluded that the capacity variation does not depend on either material parameters, manufacturing processes, cell assembly, or cell finishing [13]. Using the same cell as in [13], Schindler et al. [14] most recently investigated the evolution of initial cell-to-cell variations during a three-year production cycle with three batches (48, 160, and 200 cells, respectively) and found significant differences in initial cell-to-cell variations.

It is noticeable that over the years, with exceptions, the reported relative capacity variations have converged to smaller values below 0.4 % with the smallest (κ_C =0.16 %) reported by Campestrini et al. [8]. On the one hand, this can be traced back to the increased demand and thus the increased production quality of lithium-ion cells. On the other hand, the accuracy of test equipment and professionalization of academia's battery labs also evolved during that time, allowing for more precise measurement setups and test procedures. Rothgang et al. [5], e.g., found a comparably moderate value for κ_R, but they report a relatively high coefficient of variation for the capacity compared to the other studies following in the years after (2.36 % for 1C discharge). Most probably, this can be linked to their test procedure as they measured the capacity inside a limited voltage window between 4.1 V and 2.7 V with only CC discharging and hence no equalization of varying polarization, which would happen during a CV discharge step, took place.

In general, all studies consistently report higher relative variations of impedance parameters compared to the capacity, as represented by the factor κ_R / κ_C. Some authors explain this by the fact that the production process and cell sorting is optimized to reach small capacity variations, since it is the most commonly used characteristic by cell manufacturers [14,16].

In particular, Zheng et al. [4] report an unexpected high variation in the distribution of ohmic resistances (19.47 %) obtained from 96 cells using electrochemical impedance spectroscopy (EIS) measurements. One reason could be that they performed their experiments at room temperature instead of a temperature controlled climate chamber. Experiments performed by Barreras et al. [11] and Devie et al. [12] also show ambiguous results. Whereas the capacity variation lies within the range of other studies, the resistance shows a much higher relative variation (κ_R/κ_C > 9.0). Both used the first point of the discharge phase for the calculation of the resistance; however, they do not specify the exact time step. Depending on the measurement equipment, slightly

different time intervals to set the specified current may lead to higher measurement uncertainties. In addition, Barreras et al. [11] found a correlation between the resistance and temperature measurements and corrected the resistance by a linear gain factor. The resulting coefficient of variation, however, remained almost unaffected. Baumann et al. [2] and Fang et al. [9] used the same cell model for their investigations, whereby Baumann et al. report much lower parameter variations. This deviation might be caused by numerous reasons such as different test procedures, accuracy of measurement equipment, and batch quality.

Overall, the cell's mass shows the lowest variations below 0.2 %. This is particularly noticeable, since in contrast to electrochemical parameters such as capacity and impedance, which are prone to be strongly dependent on operating conditions such as temperature, the mass of a cell can simply be determined by weighing, where ambient conditions do not play a significant role.

Based on this literature overview, we conclude that there are various reasons for the different magnitudes of stated inherent parameter variations such as production year, cell type, cell chemistry, batch quality, etc. However, there is no physically motivated theory of why impedance variations are inherently higher compared to other parameters such as mass and capacity. This leads to the assumption that external factors such as the measurement setup and test procedure could be the reason for this discrepancy.

1.3. Goal and outline of this work

Reasonable quantification of inherent parameter variations is important, since these results are often incorporated into battery system simulation models to investigate various aspects of the influence of these parameter variations on the battery pack performance [17,18], e.g., on the current distribution inside parallel connections [19–21]. This in turn means that the simulation results and conclusions drawn by these studies are to a greater or lesser extent affected by the assumptions made for initial parameter variations. It is therefore of interest for different fields of lithium-ion battery research to critically re-evaluate the quantifiability of inherent parameter variations. Thus, we set up the hypothesis that the stated values for parameter variations in existing studies are biased by the measurement itself. The main contributions of this paper are as follows:

- **Experimental investigation of a batch of 600 commercial lithium-ion cells:** The mass and different capacities, DC-resistances and AC-impedances are experimentally determined via initial checkup (CU) measurements and electrochemical impedance spectroscopy and their variation and correlation is analyzed (Section 3.1).
- **Monte-Carlo simulation of the mutual interaction of cell temperature and resistance:** The influence of cell temperature on the resistance variation is simulated using the Arrhenius dependency of the charge transfer resistance and the influence of the resistance on the cell temperature is investigated by employing a simple thermal model (Section 3.3).
- **Analysis of external influence factors on parameter variations:** The influence of spatial and temporal temperature inhomogeneities on the investigated parameters is examined. This is also done for a previously published dataset. Thereupon, parameters are systematically adjusted and the coefficient of variation is re-evaluated (Section 3.4 and 3.5).

The experimental details are described in Section 2 and a conclusion is given in Section 4. The experimental dataset can be downloaded under [22].

2. Experimental

In this study, a full batch of commercial 18650 cells of type Sony US18650VTC5A with a nominal capacity of 2.5 Ah is examined. The anode active material consists of graphite with a small share of silicon added and the cathode active material is NCA [23]. In total, 600 cells from the same production batch are experimentally investigated in this study.

2.1. Measurement sequence

From the individual cell label by the manufacturer, the production date was determined as being January 12, 2019. The batch of cells arrived in one single package consisting of 12 boxes with 50 cells each on May 20, 2019. To investigate the batch's mass variation, the 600 cells (#1–#600) were weighed one at a time on June 5, 2019 at controlled room temperature ($\approx$ 20°C) using a high-precision balance (XP2004S by Mettler Toledo). The initial checkup (CU) of all cells was performed between the 6th and 13th of June 2019. EIS of 100 cells (#51–#150) was performed between the 11th and 13th of June 2019 with one cell tested at a time and a minimum pause of four days between the end of CU and EIS.

2.2. Initial checkup (CU)

Initial CU measurements were performed with all 600 cells sequentially, with 32 cells tested simultaneously, using a 32-channel BaSyTec cell test system inside a VC^3 4100 - S climate chamber by the Voetsch Industrietechnik GmbH set to 20°C. In Table 3, the precision of the respective measurement devices are listed.

During one set of CUs, there was a malfunction of the measurement equipment (CU-ID: 18; cells #545–#576), wherefore 32 cells have to be excluded from the analysis. We adopted the test procedure from Rumpf et al. [10] (Fig. 1a). Thus, the same parameters could be calculated, guaranteeing a good comparability. In this procedure, the resistance was calculated at current interruption after charging the cell to 50 % SOC (referred to as current interruption (CI) in this study). In addition, we applied a 30 s discharge pulse at the beginning of the measurement in order to calculate the DC-resistance before any cycling of the cells (referred to as pulse (P)). We calculated the resistance after 100 ms, 1 s, and 10 s.

2.3. EIS measurements

After the initial CU, 100 cells were used to perform EIS (packaging Box-ID 2 and 3, cell #51–#150), again at 20°C. EIS-measurements were performed using a Gamry Instruments Interface 5000, whereby the hybrid EIS mode with an AC voltage of 10 mV rms, a frequency range of 5 kHz to 100 mHz, and ten points per decade was used (Fig. 1b). Same as in Ref. [10], we calculated

Table 3
Precision of the used measurement equipment.

Instrument	Variable	Precision	Range
BaSyTec CTS	Voltage	$\Delta U = \pm 0.3$ mV	$U \in$ [0 V,6 V]
	Current	$\Delta I = \pm 200$ µA	$I \in$ [300 mA,5 A]
	Current	$\Delta I = \pm 10$ µA	$I \in$ [15 mA,300 mA]
	Current	$\Delta I = \pm 0.5$ µA	$I \in$ [1 mA,15 mA]
	Current	$\Delta I = \pm 0.05$ µA	$I \in$ [0 mA,1 mA]
NTC	Temperature	$\Delta T = \pm 0.25$ K	T @ 20°C
Gamry Interface 5000	Impedance	$\Delta Z = \pm 0.5$ %	$f \in$ [10 µHz,5 kHz]
Metler Toledo	Mass	$\Delta m = \pm 0.1$ mg	$m \in$ [0 g,2300 g]

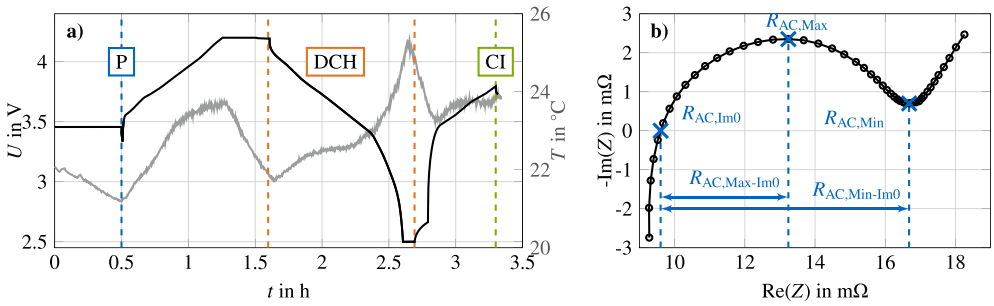

Fig. 1. Test procedures applied in this study: a) Voltage and temperature during the initial checkup (CU) with the initial discharge pulse (P) marked in blue, the CCCV discharge (DCH) marked in orange and current interruption (CI) marked in green. b) Impedance spectrum and characteristic parameters determined during EIS. (For interpretation of the references to color in this figure legend, the reader is referred to the Web version of this article.)

three characteristic points from the measured impedance spectra to characterize the AC impedance. $R_{AC,Im0}$ was defined as the zero crossing and was determined at the interpolated frequency $f_{AC,Im0}$, where the imaginary part equals zero. The mean value of $f_{AC,Im0}$ was determined to 1802 Hz with a small relative variation of 1.45 %. $R_{AC,Max}$ was defined as the local maximum of the semi-circle and consistently was determined at a frequency $f_{AC,Max}$ of 125.56 Hz. $R_{AC,Min}$ was defined as the local minimum after the semi-circle and was found to lie at a frequency $f_{AC,Min}$ of either 1.58 Hz, 2.00 Hz, 2.49 Hz, or 3.18 Hz. Interpolating the impedance spectra did not change the resulting coefficient of variation, wherefore the measured frequencies are reported. Subtracting $R_{AC,Im0}$ from $R_{AC,Max}$ and $R_{AC,Min}$ yields the parameters $R_{AC,Max-Im0}$ and $R_{AC,Min-Im0}$, which are used in this paper to characterize the variation of the dynamic loss processes.

Table 4
Univariate statistics of the experimental results of the initial CU (32 cells out of 600 cells had to be excluded) and EIS (100 cells). κ = coefficient of variation; μ = mean; σ = standard deviation; s = skewness, a measure of the asymmetry of the probability distribution ($s = 0$ for a normal distribution); k = kurtosis, a measure of the peakedness of the probability distribution ($k = 3$ for a normal distribution).

Parameter	Unit	$\kappa = \sigma/\mu$	μ	σ	s	k
Weighing						
Mass	g	0.11 %	47.652	0.054	−0.505	2.925
CU: Capacities from CCCV discharge (DCH)						
C_{CC}(DCH)	Ah	0.23 %	2.475	0.006	−0.381	4.038
C_{CV}(DCH)	Ah	2.45 %	0.052	0.001	−0.116	2.158
C_{CCCV}(DCH)	Ah	0.22 %	2.527	0.006	−0.253	3.772
T_{Mean}(DCH)	°C	1.67 %	22.768	0.38	0.167	3.038
CU: DC Resistances from initial discharge pulse (P)						
Voltage	V	0.06 %	3.459	0.002	−0.779	5.255
$R_{DC,100\ ms}$(P)	mΩ	1.11 %	20.237	0.224	0.012	3.321
$R_{DC,1s}$(P)	mΩ	1.06 %	22.004	0.234	0.023	3.382
$R_{DC,10s}$(P)	mΩ	1.10 %	32.423	0.356	0.106	3.741
T_{Start}(P)	°C	1.14 %	20.899	0.239	0.645	3.579
CU: DC Resistances from current interruption (CI) at 50 % SOC						
$R_{DC,100\ ms}$(CI)	mΩ	1.28 %	13.769	0.177	−0.118	2.603
$R_{DC,1s}$(CI)	mΩ	1.13 %	15.238	0.172	−0.055	2.486
$R_{DC,10s}$(CI)	mΩ	0.86 %	21.502	0.185	−0.044	2.146
T_{Start}(CI)	°C	2.25 %	23.625	0.532	0.189	2.843
EIS: AC Resistances						
$R_{AC,Im0}$	mΩ	0.46 %	9.577	0.044	−0.384	2.962
$R_{AC,Max-Im0}$	mΩ	1.62 %	3.670	0.060	0.620	2.467
$R_{AC,Min-Im0}$	mΩ	1.64 %	7.090	0.116	0.182	2.593

3. Results and discussion

3.1. Summary statistics and correlation analysis

The summary statistics of the main investigated parameters are listed in Table 4 and selected histograms are plotted in Fig. 2. The respective correlation coefficients are visualized in Fig. 3. The experimental data of all investigated parameters can be downloaded under [22].

The capacity C_{CCCV} has a relative variation of 0.22 % and the distribution is slightly left-skewed. Whereas the distribution of C_{CC} has a higher kurtosis than a normal distribution ($k_{Normal} = 3$), the distribution of C_{CV} has a smaller kurtosis with no distinct peak close to the mean value. Deviation from a normal distribution is not surprising per se, but should be investigated further since it can be a result of a systematic drift or external influence factor.

The coefficient of variation of the initial voltage, which was measured at the beginning of the checkup, is the smallest with 0.06 %. This means that the variation of R_{DC}(P) at the beginning of the CU is not distorted by the SOC dependency of the resistance [24]. In fact, resistance variations determined during the discharge pulse P are in the same range compared to R_{DC}(CI) determined at the current interruption at 50 % SOC. Resistance variations are in the same range compared to recent literature and almost constant for the different pulse lengths of R_{DC}(P), whereas R_{DC}(CI) shows slightly decreasing variation for increased pulse lengths. The different mean values of R_{DC}(P) and R_{DC}(CI) are expected due to the differences in SOC (≈ 20 % SOC vs. 50 % SOC), temperature (at 20.9°C vs. 23.6°C), and measurement method (discharge pulse vs. current interruption).

For C_{CV}, a strong positive correlation is found for R_{DC}(CI) and a moderate correlation for R_{DC}(P). This is expected since a higher

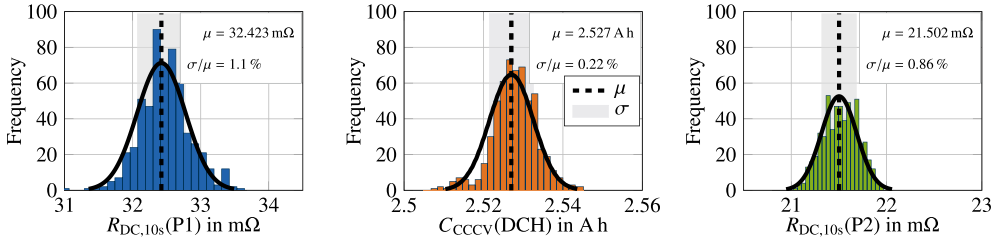

Fig. 2. Histograms of $R_{DC,\ 10s}$(P), C_{CCCV}(DCH), and $R_{DC,\ 10s}$(CI) determined during the initial CU.

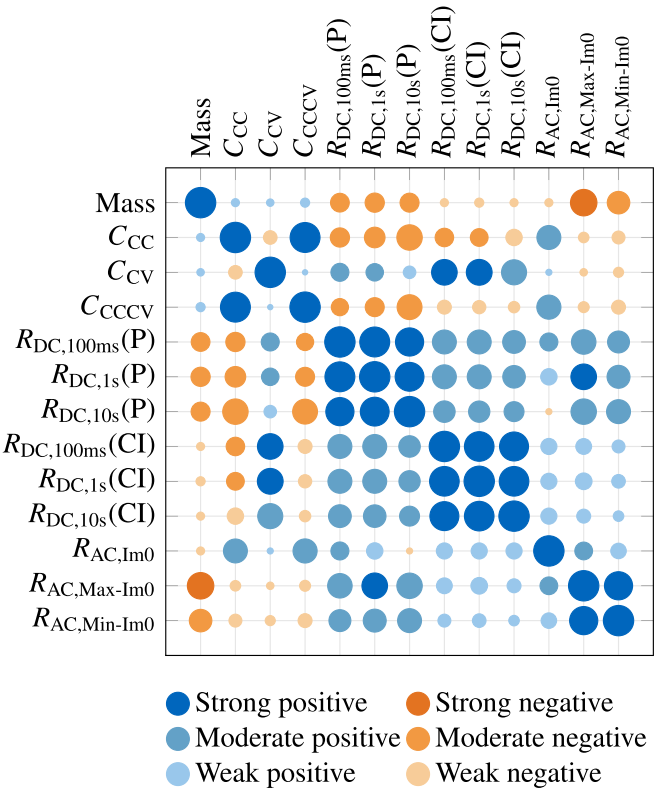

Fig. 3. Correlation matrix of the investigated parameters. The color indicates the classification of correlation coefficients into weak ($|p| \leq 0.3$), moderate ($0.3 < |p| \leq 0.7$), and strong ($0.7 < |p|$). Additionally, the bubbles size is scaled with the respective correlation coefficients. (For interpretation of the references to color in this figure legend, the reader is referred to the Web version of this article.)

resistance leads to higher over-potentials during the CC discharge and the lower cut-off voltage is reached earlier. This results in a longer CV phase (with higher Ah-throughput) where the remaining capacity is discharged. Following this argument, C_{CC} is expected to correlate negatively with C_{CV} and the resistance. Dubarry et al. [25] introduced two additional attributes, the rate capability and the capacity ration, and discuss the complex inter-dependency between capacity and resistance in more detail. In our case, only a moderate to weak negative correlation between the capacity C_{CC} is observed for R_{DC}(CI) and a moderate negative correlation is observed for R_{DC}(P). Furthermore, there is only a weak negative correlation between C_{CC} and C_{CV} ($p = -0.2$).

The AC impedances, where one cell was tested at a time, show lower coefficients of variation compared to the literature. The variation of the ohmic resistance $R_{AC,Im0}$ (0.46 %) is also smaller compared to the DC-resistances obtained from the initial CU. When taking into account dynamic loss processes such as the solid electrolyte interphase (SEI) and the charge-transfer, which together become visible as a semi-circle in the impedance spectrum, the coefficient of variation slightly increases (0.64 % for $R_{AC,Max}$ and 0.81 % for $R_{AC,Min}$).

Here, only a weak correlation with C_{CV} is present for any characteristic resistance value. In contrast, the ohmic resistance $R_{AC,Im0}$ shows a moderate positive correlation with C_{CC} and C_{CCCV}. These contradictory observations are also reflected in the correlation between all three differently determined resistances, since only a moderate or weak correlation is observed between R_{DC}(P), R_{DC}(CI), and R_{AC}(EIS), respectively. One exception is the strong positive correlation between $R_{DC,1s}$(P) and $R_{AC,Max-Im0}$.

As the AC impedances, the mass was measured for one cell at a time and the resulting coefficient of variation is 0.11 %. A positive correlation of the mass with the capacity due to a different amount of active material would theoretically make sense. However, since we only observe a weak correlation ($p = 0.09$ with C_{CCCV}), the variation of the cell's mass is more a result of other cell components such as housing or the measurement procedures of weighing and CU are not comparable. A moderate negative correlation is observed for R_{DC}(P), a weak negative correlation for R_{DC}(CI), and a negative correlation with varying strength for R_{AC}(EIS) (with the highest correlation of $p = -0.76$ for $R_{AC,Max-Im0}$ and the mass). A potential explanation could be that higher weight of the cell housing leads to a higher thermal mass and hence slower cooling of the cell core to the desired temperature inside the climate chamber. Thus, the cell's core temperature is still higher, leading to a lower resistance during the experiment.

In addition to the investigated parameters, summary statistics of the temperature are listed in Table 4. We analyzed the values right before the resistance measurements (T_{Start}(P) and T_{Start}(CI)) and the mean temperature during the CCCV discharge to determine the capacity C_{CCCV} (T_{Mean}(DCH)). We note that temperature variation increases during the course of the CU (1.14 % at the start of the pulse P, 1.67 % during the capacity measurement and 2.25 % at the start of CI). During EIS, no temperature was recorded.

3.2. Possible sources of misinterpretation

In general, the coefficients of variation are in good accordance with the values reported in recent literature. However, experimental results must be critically analyzed with respect to measurement errors [26]. Taylor et al. [26] investigated the errors and uncertainty of characterization experiments with respect to researcher variation, experimental rig design, and test chamber variation. They revealed systematic measurement errors and concluded that certain errors can be accounted for by carefully evaluating the testing process and the measurement data.

We follow this example and first analyze the measurement uncertainty due to the limited accuracy of the measurement equipment. Using the stated tolerances of the basic measured quantities in Table 3, the measurement uncertainty $u(x)$ can be calculated in the same way as described by Rumpf et al. [10]. For the DC-resistance, which is calculated according to Ohm's law, the propagation of errors of the basic quantities voltage and current can be determined as:

$$u(R) = \sqrt{\left(\frac{\partial R}{\partial \Delta U}\right)^2 \cdot u^2(\Delta U) + \left(\frac{\partial R}{\partial I}\right)^2 \cdot u^2(I)}, \tag{1}$$

using the partial derivatives of $R = \Delta U/I$. For the uncertainty of the voltage drop ΔU, the voltage tolerance has to be considered twice. The relative measurement uncertainty $u(R)/\sigma_R$ of $R_{DC,10s}$(CI) was determined to lie at 75 %. Hence, in the worst case, 75 % of the determined resistance variation might be due to tolerances of the voltage and current sensor. This value is much higher compared to the determined relative measurement uncertainty in Ref. [10] (28 %), which can be explained by two reasons. First, the standard deviation of $R_{DC,10s}$(CI) is much lower in our case (0.185 mΩ compared to 0.407 mΩ). Thus, the same voltage and current tolerances lead to higher relative measurement uncertainties. Second, the voltage drop ΔU is smaller, which also leads to a smaller absolute resistance $R_{DC,10s}$(CI) (21.502 mΩ compared to 28.485 mΩ). Again, according to Eq. (1), this leads to higher relative measurement uncertainties.

Furthermore it is noticeable that the relative measurement uncertainties of the resistance parameters are much higher compared to the capacities, which are below 2 % [10]. This again can be explained by two reasons. First, resistance and capacity are calculated differently from the basic measured quantities current and voltage. The voltage sensor tolerance does not affect the current integration for determining the capacity but strongly influences the measurement uncertainty of the voltage drop ΔU during the resistance determination. The second reason is the magnitude of the standard deviation, which is roughly one order smaller for the resistance compared to the capacity. Therefore, the same sensor tolerance has a higher influence on the relative measurement uncertainty $u(x)/\sigma_x$. It can be concluded that systematic higher measurement uncertainties are one reason for the higher resistance variation.

However, in addition to measurement uncertainties, the following observations motivate further investigations concerning systematic bias in the quantification of parameter variations:

- There is no argument of why resistance variations are higher than the variations of other parameters. As described above, higher values might be a result of higher measurement uncertainties due to the equipment's precision. The influence of limited accuracy of the measurement devices is expected to result in a noise with normal distribution [10]. However, measured parameters show a deviation from a normal distribution to a greater or lesser extent (as revealed by the skewness and kurtosis), which might be a result of other external influencing factors during the experiment.
- The determined coefficients of variation of resistance parameters and correlation coefficients of these parameters among each other depend strongly on the measurement method (discharge pulse, current interruption, EIS) and the chronology of the measurements (reflected in the increased variation of the measured temperature) and show contradictory behavior for some measurements.
- The variation of the ohmic resistance $R_{AC,Im0}$ is roughly three times lower compared to the polarization resistances due the charge transfer ($R_{AC,Max\text{-}Im0}$ and $R_{AC,Min\text{-}Im0}$). In Ref. [10], this observation was explained by the limited number of measured frequencies during EIS. However, since the charge transfer resistance shows a higher temperature dependency than the ohmic resistance [27], temperature variations during the measurement also cannot be excluded as a reason for this behavior. Inconclusive results of correlation analysis with other parameters further substantiate the suspicion of external factors influencing the measurement.

Therefore, we analyze the measurement data with respect to several influencing factors that could potentially bias the statistical analysis. First, the cell number (Cell-ID) could influence the measured parameters caused by drifts in process parameters during cell production. Second, the box (Box-ID) in which the cells have been shipped could have an impact due to their respective position in the package and varying temperatures during shipping. Mentioned factors occur before the cells' arrival and lead to non-influenceable (from the perspective of a customer) and therefore inherent parameter variations within a batch of lithium-ion cells. However, the sequence number of the CU (CU-ID) was also examined to reveal potential trends within the sequential measurements of 32 cells at a time. Furthermore, we analyzed the influence of the test channel during the CU (Channel-ID), which in turn represents a certain position inside the climate chamber, and potential temperature inhomogeneities can be revealed.

The mutual interaction between temperature and resistance is complex and it is not easy to fully distinguish between cause and effect. A difference in cell temperature will lead to different resistances, while two cells with different resistance, if subjected to an identical current, will acquire different cell temperatures. Therefore, in the next section we evaluate the mutual interaction between cell temperature and resistance in more detail with a set of Monte-Carlo simulations to provide a foundation for interpreting the results in the following sections.

3.3. Monte-Carlo simulation of the mutual interaction of cell temperature and resistance

As discussed earlier, the relative variation of the pure charge-transfer resistance R_{ct}, defined as $R_{AC,Min} - R_{AC,Im0}$, is observed to be more than three times as high as for the pure ohmic resistance $R_{AC,Im0}$ and might result from a higher dependency of the ambient temperature during the experiment. The question arises, whether it is physically reasonable that small deviations of the ambient temperature are responsible for the variation of the charge transfer resistance or whether this results from inherent parameter variations due to different characteristics on cell material level.

To answer this question and to investigate the mutual interaction of resistance and temperature in more detail, we performed a simple set of simulations. Since especially R_{ct} strongly depends on the temperature, we chose the Arrhenius dependency of R_{ct} (Eq. (2)) to estimate the influence of temperature deviations on the resistance measurement.

$$R_{ct}(T) = A \cdot e^{\frac{E_A}{R_{gas} \cdot \underbrace{(\mu_T + \mathrm{randn} \cdot \sigma_T)}_{T}}}. \tag{2}$$

R is the universal gas constant, E_A is the activation energy, and A is the amplitude. The term $(\mu_T + \mathrm{randn} \cdot \sigma_T)$ gives a random temperature value from a normal distribution with the mean temperature μ_T and the standard deviation σ_T using Matlab's RANDN [28]. Here, we use the absolute variation σ_T and we assume the temperature deviation inside a climate chamber to be constant over the whole temperature range. To see the effect of temperature deviations over a wide temperature range, we vary the mean ambient temperature μ_T between 0°C and 40°C in 5°C steps. Furthermore, we analyze the effect of different temperature variations σ_T in 0.1°C

Table 5
Parameters for Monte-Carlo simulation of the cell temperature for varying resistances. * The values for E_A and A have been determined at 50 %SOC based on EIS at six temperature levels between −10°C and 60°C. ** The specific heat capacity was determined analytically according to the mass and thermal properties of the individual cell components after cell opening, analogous to Ref. [29].

Parameter	Symbol	Unit	Value
General			
Ambient temperature	μ_T	°C	[0 : 5 : 40]
Ohmic resistance	R_{ohm}	mΩ	9.577
Arrhenius equation			
Temperature variation	σ_T	°C	[0 : 0.1 : 1]
Amplitude*	A	–	$2.0975 \cdot 10^{13}$
Activation energy*	E_A	kJ mol^{-1}	61.990
Universal gas constant	R_{gas}	J mol^{-1} K^{-1}	8.314
Lumped mass model			
Resistance variation	$\kappa_{R_{tot}}$	%	[0 : 0.2 : 2]
Cell mass	m	g	47.652
Specific heat capacity**	c_p	J kg^{-1} K^{-1}	845
Current	I	A	2.5
Simulation time	dt	s	1800

steps until 1°C. The respective parameters used for this simulation study are listed in Table 5.

For better comparability with the effect of resistance variation on the temperature variation, which is described below, we use the sum of ohmic and charge transfer resistance according to

$$R_{\text{tot}}(T) = R_{\text{ohm}} + R_{\text{ct}}(T). \tag{3}$$

whereby the ohmic resistance R_{ohm}, which has a much lower temperature dependency compared to R_{ct}, is assumed to be constant over the whole temperature range for reasons of simplicity. For each combination of the ambient temperature μ_T and different magnitudes of temperature variations σ_T, the coefficient of variation $\kappa_{R\text{tot}}$ is calculated from 10,000 simulations of R_{tot}. Results are shown in Fig. 4, where the green to blue color coding represents the different magnitudes of temperature variation.

For μ_T =20°C and σ_T =0.5°C, which was observed during our experiments, $\kappa_{R_{\text{tot}}}$ lies at 1.53 %. The pure charge transfer resistance at these conditions even shows a variation of 4.30 %.

In order to interpret the results with respect to the mutual interaction of temperature and resistance, we additionally estimate the opposite effect of resistance variation on the heat generation and cell temperature variation. Therefore, we use a simplified thermal mass model, only considering the irreversible heat generation $Q_{\text{irr}} = I \cdot U_{R_{\text{tot}}}$ with the current I and the overpotentials due to the superimposed ohmic and charge transfer resistance $U_{R_{\text{tot}}}$. For R_{tot} (Eq. (3)), we use the mean value of the previous simulation results for the different ambient temperatures μ_T, respectively. Since the purpose of the model is to estimate the impact of resistance scattering on the cell heating, we do not consider any dynamics of the cell's kinetic behavior. Furthermore, any additional effects on the cell's temperature such as reversible heat generation, thermal radiation, and dissipation of heat due to free and forced convection are neglected. The cell temperature T_{cell} after a simulation time dt under constant current load I at ambient temperature μ_T can be calculated according to

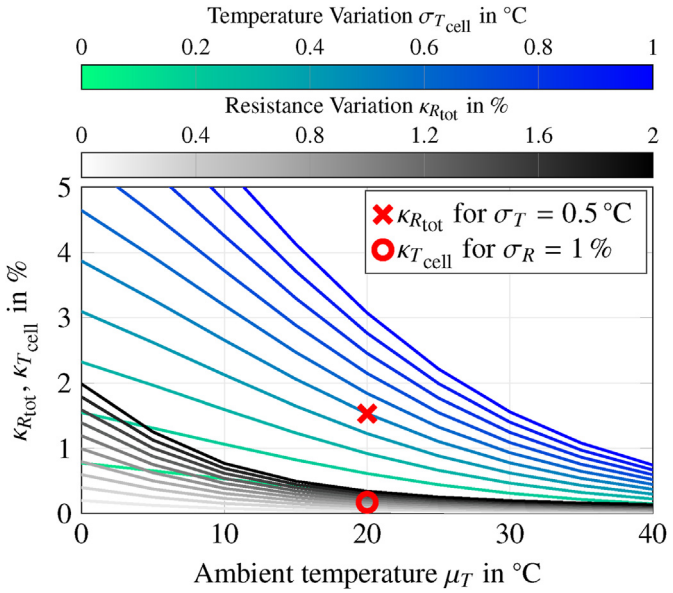

Fig. 4. Monte-Carlo simulation results for 1) Relative resistance variation $\kappa_{R\text{tot}}$ due to different magnitudes of temperature variations, represented by the color coding from green to blue. 2) Relative temperature variation $\kappa_{T\text{cell}}$ due to different magnitudes of resistance variations, represented by the color coding from white to black. (For interpretation of the references to color in this figure legend, the reader is referred to the Web version of this article.)

$$T_{\text{cell}} = \mu_T + \frac{\overbrace{\left(\mu_{R_{\text{tot}}} + \text{randn} \cdot \kappa_{R_{\text{tot}}}/\mu_{R_{\text{tot}}}\right)}^{R} \cdot I^2}{m \cdot c_p} \cdot dt. \tag{4}$$

m and c_p display the cell's mass and heat capacity, respectively. Again, the term $(\mu_{R_{\text{tot}}} + \text{randn} \cdot \kappa_{R_{\text{tot}}}/\mu_{R_{\text{tot}}})$ gives a random resistance from the normal distribution with mean resistance $\mu_{R_{\text{tot}}}$, which changes with ambient temperature and the standard deviation $\kappa_{R_{\text{tot}}}/\mu_{R_{\text{tot}}}$. We analyze the effect of different resistance variations $\kappa_{R_{\text{tot}}}$ in 0.2 % steps until 2 %. For each ambient temperature, the coefficient of variation $\kappa_{T_{\text{cell}}}$ due to different magnitudes of resistance variations $\kappa_{R_{\text{tot}}}$ is calculated from 10,000 simulations of T_{cell}. Results are additionally plotted in Fig. 4, where the white to black color coding represents the different magnitude of resistance variation. For μ_T =20°C and $\kappa_{R_{\text{tot}}}$ =1 %, which was observed during our experiments, $\kappa_{T\text{cell}}$ lies at 0.17 %.

Comparing the results of $\kappa_{R_{\text{tot}}}$ and $\kappa_{T_{\text{cell}}}$ from these simplified simulations, we conclude that it is much more likely that the observed resistance variation is a result of extrinsic temperature variation than vice versa. Based on these findings, we assume that for other studies also the share of observed resistance variation caused by extrinsic temperature variation is higher than the share of observed temperature variation due to inherent resistance variation. In our experiments, we observed a resistance variation of roughly 1 % and a temperature variation of 0.5°C. Since from the Arrhenius dependency we would expect even higher resistance variations, we must keep in mind that the temperature is measured only at the cell's surface and the variation of the cell core temperature might be smaller due to the cell's thermal mass.

After revealing the mutual cause and effect chain of temperature and resistance variation, we analyze the measurement data with respect to seasonal, i.e., in which order the cells were tested, and spatial, i.e., at which location the cells were tested, temperature inhomogeneities.

3.4. Seasonal effects: influence of the Cell-ID, Box-ID, and CU-ID

Fig. 5 shows the parameters $R_{\text{DC, 10s}}$(P) (left column), C_{CCCV} (medium column),and $R_{\text{DC, 10s}}$(CI) (right column) plotted over the cell number. In the same column, below the parameters itself, the temperature just before (in the case of the resistance) and the mean value during (in case of the capacity) their measurement is plotted in the same manner. As elaborated in the previous section, it is important to keep in mind that the temperature is measured only at the cell's surface.

$R_{\text{DC, 10s}}$(P) shows a drift towards lower resistances for increasing cell numbers. The corresponding temperature T_{Start}(P) shows no obvious drift in the observed direction, except for the last sequence of CUs and some minor seasonal fluctuations. C_{CCCV}, with some exceptions, shows a drift towards higher capacities for increasing cell numbers. The corresponding temperature T_{Mean}(DCH) shows only a minimal drift in the opposite direction. $R_{\text{DC, 10s}}$(CI), determined from the current interruption at 50 % SOC, shows a slight drift towards lower resistances for increasing cell numbers, which are, however, smaller in magnitude compared to $R_{\text{DC, 10s}}$(P), determined during the initial pulse. The corresponding temperature T_{Start}(CI) behaves similarly to the capacity.

There are three possible explanations for the observed parameter drifts, which are discussed in the following. First, differences in the Cell-ID, e.g., due to changes during the production process, might be the cause for inherent parameter variations. In our opinion, this is rather unlikely because the cells originated from the same production lot and were produced on the same day. Also, no

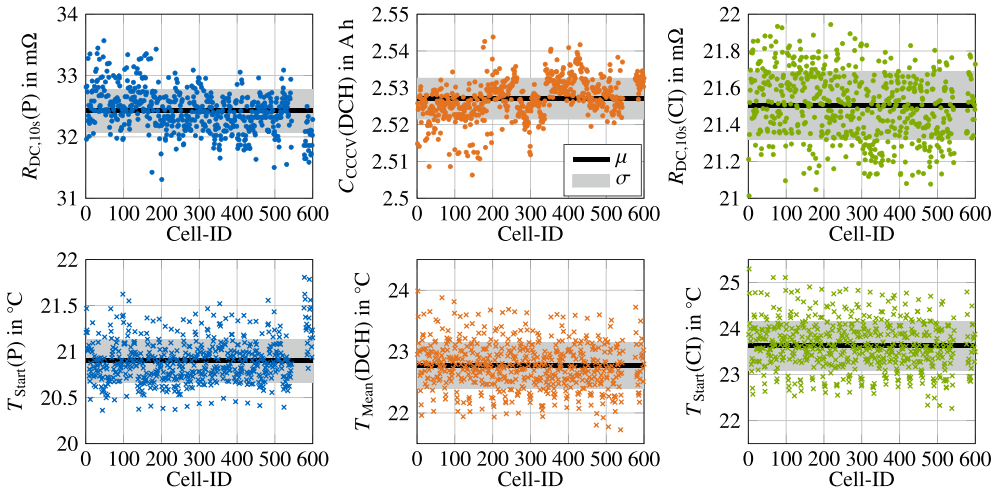

Fig. 5. R_{DC}(P), C_{CCCV}, and R_{DC}(CI) plotted over the cell number (1st row). Additionally, the corresponding temperatures just before the resistance measurements (T_{Start}(P) and T_{Start}(CI)) and during the CCCV discharge (T_{Mean}(DCH) are plotted (2nd row).

drift in the Cell-ID was observed in Ref. [10], which analyzed cells from the same manufacturer. Second, the Box-ID could lead to this drift due to inhomogeneous temperature stress during shipping. However, this also is rather unlikely for a package with the size of roughly 50 cm × 50 cm x 50 cm. The fact that the drift is much less pronounced for $R_{DC,\ 10s}$(P) compared to $R_{DC,\ 10s}$(CI) also speaks against the two previous arguments.

Third, this drift might be a result of the sequential testing process and occurring temperature deviations over the consecutive experiments of 32 cells at a time (CU-ID). Two people were involved in placing the cells into the cell holders, closing and starting the climate chamber, and starting the tests in the test software. Such processes are handled faster with time, which reduces the time to cool the cells from room temperature to the desired temperature of 20°C. Since the test plan included a pause of only 15 min before the initial discharge pulse was performed, just small time differences in the process before the test is started can have an impact on cell temperature.

Potentially, the cell's core temperature at the beginning of the pulse P was still deviating from the measured temperature at the cell's surface and was larger for the later CU-IDs, which leads to the lower resistances $R_{DC,\ 10s}$(P) for increasing Cell-ID. A higher core temperature would also result in a higher capacity C_{CCCV}, which in fact is observed for increasing cell numbers. After the capacity is determined, the cell is charged to 50 % SOC and the resistance is determined during the current interruption (CI). For $R_{DC,\ 10s}$(CI), the decreasing trend towards higher cell numbers and the distinct group building of the last CU-ID apparently vanished during the course of the CU. It appears that deviations of the cell core temperature resulting from differences at the beginning of the sequential number of CU disappeared gradually during the CU duration of roughly 3 h.

From the previous observations, an externally induced drift due to variations of the core temperature over the consecutive CU measurements is more likely than any inherent parameter variation, in our opinion, and we conclude that the actual inherent variation of capacity and resistance are smaller than experimentally quantified. By calculating the mean of a parameter X for each CU-ID separately, we can compensate this drift and adjust the respective parameters according to

$$X_{CU-ID} = X - (\mu_{X(CU-ID)} - \mu_X) \tag{5}$$

with $X_{CU\text{-}ID}$ as the adjusted parameter, X as the experimentally determined parameter, $\mu_{X(CU\text{-}ID)}$ as the separate mean over each CU-ID, and μ_X as the mean over the whole dataset. The resulting coefficients of variation (Table 6) slightly decrease for every parameter, e.g., for $R_{DC,\ 10s}$(P) at the beginning of the CU the variation is reduced by 15 % relative to the raw experimental results. The small reduction of only 6 % for $R_{DC,\ 10s}$(CI) reveals the decreased influence of seasonal temperature effects during the course of the CU.

3.5. Spatial effects: influence of the Channel-ID

In addition to the seasonal drift over CU-ID, there is also a noticeable temperature variation within individual CU-IDs, where the measurement data is analyzed in more detail with respect to spatial patterns. By plotting the cell's parameters over the respective Channel-ID, inhomogeneities regarding the position inside the

Table 6
Parameter variations after the systematic adjustment of measured parameters due to seasonal (CU-ID) and spatial (Channel-ID) temperature inhomogeneities. Additionally, the relative reduction of the coefficient of variation compared to measured parameters is given.

		Pulse P		CCCV Discharge				Current Interrupt CI	
Adjustment	Variable	$R_{DC,10s}$(P1)	T_{Start}(P1)	C_{CC}	C_{CV}	C_{CCCV}	T_{Mean}(DCH)	$R_{DC,10s}$(P2)	T_{Start}(P2)
Original:	κ_X in %	1.10	1.14	0.23	2.45	0.22	1.67	0.86	2.25
Seasonal:	$\kappa_{X_{CU-ID}}$ in %	0.94 / **−15 %**	1.01 / **−12 %**	0.19 / **−17 %**	2.38 / **−3 %**	0.18 / **−20 %**	1.64 / **−2 %**	0.81 / **−6 %**	2.23 / **−1 %**
Spatial:	$\kappa_{X_{Channel-ID}}$ in %	1.01 / **−8 %**	0.57 / **−50 %**	0.21 / **−7 %**	1.16 / **−53 %**	0.21 / **−3 %**	0.67 / **−60 %**	0.54 / **−38 %**	0.83 / **−63 %**
Both:	$\kappa_{X_{Channel-ID,channel-ID}}$ in %	0.84 / **−24 %**	0.23 / **−80 %**	0.17 / **−26 %**	1.01 / **−59 %**	0.17 / **−24 %**	0.58 / **−65 %**	0.45 / **−48 %**	0.74 / **−67 %**

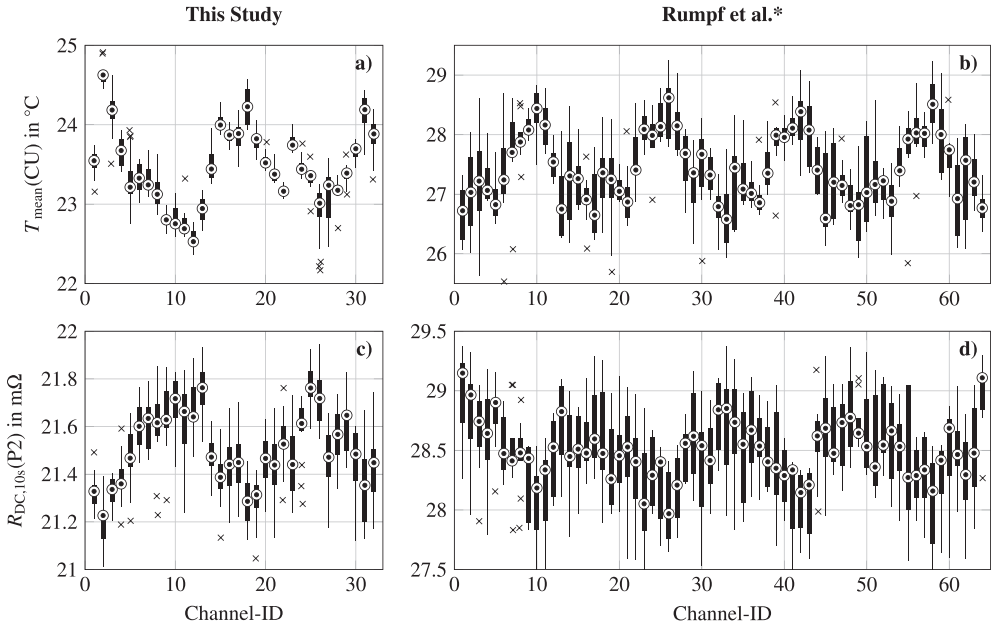

Fig. 6. Influence of the temperature gradient inside the climate chamber on the measured resistance. Left side: Temperature (a) and resistance (c) over Channel-ID for every tested cell in this study. Right side: Temperature (b) and resistance (d) over Channel-ID for the published data set (Batch 1) by Rumpf et al. [10]. *Since the Channel ID was not explicitly reported, it is counted repetitively from 1 to 64, as they used a 64-channel cell test system.

climate chamber and corresponding spatial temperature inhomogeneities can be revealed.

Fig. 6a) shows the mean temperature over the whole CU procedure T_{mean}(CU) as a boxplot for each Channel-ID. T_{mean}(CU) was chosen to make the analysis comparable with Rumpf et al. [10]. A distinct pattern is observed, which can be attributed to temperature inhomogeneities inside the climate chamber. In fact, the picture fits well to the positioning of the cell holders inside the climate chamber, which were placed in two rows with 16 neighboring cells behind each other. Apparently, cells at the edge of the chamber were warmer during the CU, whereas cells placed in the middle of the chamber experienced a better conductive cooling by the chamber's fan.

Since the resistance decreases with higher temperatures due to the Arrhenius dependency of the charge transfer resistance and the solid state diffusion [27], we observe an inverse pattern for $R_{DC,10s}$(CI) (Fig. 6c)). Since R_{DC}(CI) correlates strongly with C_{CV}, the same pattern is also observed here.

Fig. 6b) and Fig. 6d) show the same parameters for the published dataset by Rumpf et al. [10]. Here, we see a similar pattern, which we assume to also result from temperature inhomogeneities inside the climate chamber. From their way of plotting the data (over Cell-ID), the authors concluded that errors within parametric variations due to the temperature can be excluded [10]. While this may be true regarding seasonal drifts between the groups of 64 cells that have been tested at the same time, it is not true for spatial drifts within one group of 64 cells.

Analogous to the CU-ID, we can adjust the respective parameters according to

$$X_{\text{Channel-ID}} = X - (\mu_{X_{(\text{Channel-ID})}} - \mu_X) \tag{6}$$

with $\mu_{X(\text{Channel-ID})}$ as the mean calculated separately over each Channel-ID. The resulting coefficients of variation are additionally listed in Table 6, once with sole adjustment of the Channel-ID and once with combined adjustment of the CU-ID and Channel-ID.

In contrast to the seasonal adjustment, the spatial adjustment leads to a much higher relative reduction of resistance variation for $R_{DC,10s}$(CI) (38 %) compared to $R_{DC,10s}$(P) (8 %). This makes sense, since the cells are subjected to inhomogeneous cooling inside the climate chamber for a longer period of time during the course of the CU. Since the temperature is measured at the cell's surface, the adjustment of temperature is in a similar range for T_{Start}(P), T_{Mean}(DCH), and T_{Start}(CI) (50 %–63 %). The effect of adjusting the capacity parameters C_{CC} and C_{CV} seems to counterbalance and the reduction of the variation for C_{CCCV} is only 3 %. Combining seasonal and spatial parameter adjustment leads to a relative reduction of parameter variations of up to 48 % for $R_{DC,10s}$(CI). The resulting coefficient of variation is 0.45 %, which is almost equal to the variation of the ohmic resistance $R_{AC,Im0}$ (0.45 %) and much closer to the variation of other parameters such as mass and capacity.

4. Conclusion

In this study, we experimentally investigated cell-to-cell variations of various characteristic parameters of a batch of 600 commercial lithium-ion cells. As in all previous studies which quantified cell-to-cell variations, our experimental results revealed higher scattering of the resistance compared to the capacity and mass. However, we observed inconclusive summary statistics and contradictory correlation between some of the measured parameters and there is no physically motivated explanation for higher resistance variation. Therefore, we analyzed our data as well as a previously published data set with respect to systematic trends and confirmed the hypothesis that quantification of cell-to-cell variations is substantially biased by the measurement procedure itself. Our observations allow the conclusion that the inherent resistance variation is smaller than consistently reported in the literature and closer to the relative variation of other characteristic parameters such as weight or capacity.

In particular, we found that seasonal and temporal temperature inhomogeneities are a major reason for biased experimental results. By compensating the measurement data for these effects, we re-calculated the cell-to-cell variations and found a significant

reduction of resistance variation ($R_{DC,\ 10s}$) by 48 % and capacity variation (C_{CCCV}) by 24 %, leading to a coefficient of variation of 0.45 % and 0.17 %, respectively. Compensation was justified with a simple set of Monte-Carlo simulations where we showed that the effect of resistance variation caused by extrinsic temperature variation is much higher than the effect of temperature variation due to inherent resistance variation. Still, the ratio of capacity and resistance variation is 1:2.65, but with the smallest reported values for capacity and resistance variation so far. It has to be noted that we did not compensate the parameter variations with respect to the measurement uncertainties, which are much higher for the resistance (75 %) compared to the capacity (< 2 %) and could explain the higher coefficient of variation of the resistance.

Based on our findings, we assume that the relatively higher resistance scattering is mainly due to the fact, that the experimental setup has a much higher influence on measuring impedance parameters and that the measurement uncertainty due to the limited accuracy of the measurement equipment is much higher for resistance calculation compared to other parameters such as mass and capacity. Hence, due to the small magnitude of cell-to-cell variations of high-quality commercial lithium-ion cells, quantifying the true inherent variation is a challenging task. High-precision measurement equipment is needed and the influence of seasonal and spatial temperature inhomogeneities and other distorting factors must be reduced to a minimum. This can be done by performing the experiments with only one cell tested a time, with long relaxation times to reach thermal and electrochemical equilibrium, and a highly standardized process before and during the experiment. It is preferable to choose the ohmic resistance from EIS or the DC-resistance evaluated at short time intervals in the range of ms and to perform the experiments at higher temperatures. Thereby, due to the exponential Arrhenius dependency of the charge transfer resistance, the influence of the environmental temperature on the measured resistance variation can be reduced.

Compared to other origins of parameter variations which occur during the system assembly process (e.g., variations of the contact resistance) or during operation of the battery pack (e.g., temperature variations due to inhomogeneous cooling), inherent cell-to-cell variations caused by production tolerances are assumed to be negligible. This should be taken into account in future modeling efforts, where inherent variations should be induced with more caution so as not come to misleading conclusions. Furthermore, the results of this study can also be transferred to the statistical variation of the degradation rate of lithium-ion cells aged with the same load profile under laboratory conditions. It can be assumed that previous reported divergence of individual lithium-ion cells is more likely due to non-identical experimental conditions than due to statistical variation. However, further investigations are needed in the future.

CRediT authors contribution statement

L. Wildfeuer: Conceptualization, Methodology, Formal Analysis, Investigation, Visualization, Data curation, Software, Validation, Writing - original draft, Writing - review & editing. L.W. is the first author. **M. Lienkamp:** Resources, Supervision, Writing - review & editing.

Declaration of competing interest

The authors declare that they have no known competing financial interests or personal relationships that could have appeared to influence the work reported in this paper.

Acknowledgements

The authors want to acknowledge the Bavarian Ministry of Economic Affairs, Regional Development and Energy for funding the project bawaii battery analytics with artificial intelligence (IUK-1808-0013). The fruitful discussions with Nikolaos Wassiliadis (TUM) and Alexander Karger (TWAICE) are gratefully acknowledged.

References

[1] Rothgang S, Baumhöfer T, van Hoek H, Lange T, De Doncker RW, Sauer DU. Modular battery design for reliable, flexible and multi-technology energy storage systems. Appl. Energy 2015;137:931–7. https://doi.org/10.1016/j.apenergy.2014.06.069.

[2] Baumann M, Wildfeuer L, Rohr S, Lienkamp M. Parameter variations within li-ion battery packs – theoretical investigations and experimental quantification. J. Energy Storage 2018;18:295–307. https://doi.org/10.1016/j.est.2018.04.031.

[3] Dubarry M, Vuillaume N, Liaw BY. From single cell model to battery pack simulation for Li-ion batteries. J Power Sources 2009;186(2):500–7. https://doi.org/10.1016/j.jpowsour.2008.10.051.

[4] Zheng Y, Han X, Lu L, Li J, Ouyang M. Lithium ion battery pack power fade fault identification based on Shannon entropy in electric vehicles. J Power Sources 2013. https://doi.org/10.1016/j.jpowsour.2012.09.015.

[5] Rothgang S, Baumhofer T, Sauer DU. Diversion of aging of battery cells in automotive systems. In: IEEE vehicle power and propulsion conference (VPPC). IEEE; 2014. p. 1–6. https://doi.org/10.1109/VPPC.2014.7007050.

[6] Schuster SF, Brand MJ, Berg P, Gleissenberger M, Jossen A. Lithium-ion cell-to-cell variation during battery electric vehicle operation. J Power Sources 2015;297:242–51. https://doi.org/10.1016/j.jpowsour.2015.08.001. doi: 10.1016/j.jpowsour.2015.08.001. URL.

[7] Devie A, Dubarry M. Durability and reliability of electric vehicle batteries under electric utility grid operations. Part 1: cell-to-cell variations and preliminary testing. Batteries 2016;2(3):1–13. https://doi.org/10.3390/batteries2030028.

[8] Campestrini C, Keil P, Schuster SF, Jossen A. Ageing of lithium-ion battery modules with dissipative balancing compared with single-cell ageing. J. Energy Storage 2016;6:142–52. https://doi.org/10.1016/j.est.2016.03.004.

[9] Fang Q, Wei X, Dai H. A study of parameter inconsistency evolution pattern in parallel-connected battery modules. SAE Technical Paper; 2017. https://doi.org/10.4271/2017-01-1194.

[10] Rumpf K, Naumann M, Jossen A. Experimental investigation of parametric cell-to-cell variation and correlation based on 1100 commercial lithium-ion cells. J. Energy Storage 2017;14:224–43. https://doi.org/10.1016/j.est.2017.09.010.

[11] Barreras JV, Raj T, Howey DA, Schaltz E. Results of screening over 200 pristine lithium-ion cells. In: 2017 IEEE vehicle power and propulsion conference, (VPPC). IEEE; 2018. p. 1–6. https://doi.org/10.1109/VPPC.2017.8331054.

[12] Devie A, Baure G, Dubarry M. Intrinsic variability in the degradation of a batch of commercial 18650 lithium-ion cells. Energies 2018;11(5):1–14. https://doi.org/10.3390/en11051031.

[13] Zilberman I, Ludwig S, Jossen A. Cell-to-cell variation of calendar aging and reversible self-discharge in 18650 nickel-rich, silicon–graphite lithium-ion cells. J. Energy Storage 2019;26(August):100900. https://doi.org/10.1016/j.est.2019.100900.

[14] Schindler M, Sturm J, Ludwig S, Schmitt J, Jossen A. Evolution of initial cell-to-cell variations during a three-year production cycle. eTransportation 2021;8(March):100102. https://doi.org/10.1016/j.etran.2020.100102.

[15] Rohatgi A. Webplotdigitizer: Version 4.4. URL, https://automeris.io/WebPlotDigitizer; 2020.

[16] An F, Huang J, Wang C, Li Z, Zhang J, Wang S, et al. Cell sorting for parallel lithium-ion battery systems: evaluation based on an electric circuit model. J. Energy Storage 2016;6:195–203. https://doi.org/10.1016/j.est.2016.04.007.

[17] Dubarry M, Pastor-Fernández C, Baure G, Yu TF, Dhammika Widanage W, Marco J. Battery energy storage system modeling: investigation of intrinsic cell-to-cell variations. J. Energy Storage 2019. https://doi.org/10.1016/j.est.2019.02.016.

[18] Rumpf K, Rheinfeld A, Schindler M, Keil J, Schua T, Jossen A. Influence of cell-to-cell variations on the inhomogeneity of lithium-ion battery modules. J Electrochem Soc 2018;165(11). https://doi.org/10.1149/2.0111811jes.

[19] Hofmann MH, Czyrka K, Brand MJ, Steinhardt M, Noel A, Spingler FB, Jossen A. Dynamics of current distribution within battery cells connected in parallel. J. Energy Storage 2018;20(August):120–33. https://doi.org/10.1016/j.est.2018.08.013. doi:10.1016/j.est.2018.08.013. URL.

[20] Fill A, Koch S, Pott A, Birke K-P. Current distribution of parallel-connected cells in dependence of cell resistance, capacity and number of parallel cells. J Power Sources 2018;407:147–52. https://doi.org/10.1016/j.jpowsour.2018.10.061.

[21] Reiter C, Wildfeuer L, Wassiliadis N, Krahl T, Dirnecker J, Lienkamp M. A holistic approach for simulation and evaluation of electrical and thermal loads in lithium-ion battery systems. In: 2019 14th international conference

on ecological vehicles and renewable energies (EVER). IEEE; 2019. https://doi.org/10.1109/EVER.2019.8813640.
[22] Wildfeuer Leo, Lienkamp Markus. Quantifiability of inherent cell-to-cell variations of commercial lithium-ion batteries - Dataset. ResearchGate 2021. https://doi.org/10.13140/RG.2.2.31720.60160.
[23] Lain MJ, Brandon J, Kendrick E. Design strategies for high power vs. High energy lithium ion cells. Batteries 2019;5(4). https://doi.org/10.3390/batteries5040064.
[24] Wildfeuer L, Wassiliadis N, Reiter C, Baumann M, Lienkamp M. Experimental characterization of Li-ion battery resistance at the cell , module and pack level. In: 2019 fourteenth international conference on ecological vehicles and renewable energies (EVER). IEEE; 2019. p. 1–12. https://doi.org/10.1109/EVER.2019.8813578.
[25] Dubarry M, Baure G. Perspective on commercial Li-ion battery testing, best practices for simple and effective protocols. Electronics (Switzerland) 2020;9(1). https://doi.org/10.3390/electronics9010152.
[26] Taylor J, Barai A, Ashwin TR, Guo Y, Amor-Segan M, Marco J. An insight into the errors and uncertainty of the lithium-ion battery characterisation experiments. J. Energy Storage 2019;24. https://doi.org/10.1016/j.est.2019.100761.
[27] Mertens A, Vinke IC, Tempel H, Kungl H, de Haart LGJ, Eichel R-A, Granwehr J. Quantitative analysis of time-domain supported electrochemical impedance spectroscopy data of Li-ion batteries: reliable activation energy determination at low frequencies. J Electrochem Soc 2016;163(7). https://doi.org/10.1149/2.0511607jes. H521–H527.
[28] The MathWorks inc, MATLAB randn. URL, https://de.mathworks.com/help/matlab/ref/randn.html; 2021.
[29] Bolsinger C, Birke KP. Effect of different cooling configurations on thermal gradients inside cylindrical battery cells. J. Energy Storage 2019;21:222–30. https://doi.org/10.1016/j.est.2018.11.030.

3 Discussion

This chapter discusses the results of the presented studies. A general limitation of this thesis is that all investigations were performed on a single cell type. The transferability to other cell types was not explored and could be addressed in future studies. However, since the investigated cell type features a silicon-doped anode and a high-nickel cathode—both material trends in the automotive industry—many of the presented processing methods and insights can be applied to automotive batteries with similar material compositions.

3.1 Leveraging Half-Cell Measurements

Understanding the *electric behavior* was the entry point in this work and the primary electrical parameters were introduced. Study I presented the methodology of building half-cells and the results of an in-depth half-cell and full-cell characterization to answer the following research question:

1 *Can half-cell measurements enhance the parameterization of electric models and facilitate the identification of degradation modes during aging studies?*

Half cells ≠ half full cells
Mini-pouch bags were built out of electrodes harvested from the full cell. Besides the electrode material, however, half cells have little in common with the original commercial cell. A different counter electrode, separator, electrolyte, and different current collectors were built into a different cell format with different mechanical compression. These discrepancies significantly influence the kinetic loss process, which impacts the measurement of OCV and resistance to varying degrees. An improved process of constructing the half cells [96] or a three-electrode setup [175] can reduce these differences to some extent, but transferring the results to the full-cell level remains challenging.

Some tweaks were needed to enable tracking of degradation modes
When applying the vanilla version of the mechanistic OCV model as described in Eq. (1.5), superimposition of half-cell curves couldn't reconstruct the full-cell OCV in a physically meaningful way due to the described differences between half cells and full cells. The phase transitions of anode and cathode were not matched and the RMSE between simulated and measured full-cell voltages was high. Eventually, this could be circumvented by extending the mechanistic OCV model in two ways. Firstly, a vertical adjustment parameter was introduced to account for impedance differences between half cells and full cells. Secondly, the low SOC range was excluded from half-cell fitting. This way, the full cell could be reconstructed with an RMSE of 1.3 mV within the fitting range and the capacities of electrodes and lithium inventory could be determined.

Parts of silicon's contribution to the anode capacity could not be captured
Excluding the low SOC range has broader implications, which are discussed in more detail. Stepwise increase of the lower SOC fitting boundary showed that scaling and alignment parameters converged at approximately 12–15 % SOC. Since lithiation of the silicon mainly takes place in the low SOC area [173], a potential explanation is that silicon behaved differently in the constructed half cells compared to the full cell. In fact, previous investigations demonstrated that the shape of the OCP curve of silicon–graphite anodes can change significantly during cycle aging and that this can be attributed to a decreased contribution of silicon to the blended anode capacity [173]. Thus, the assumption that the change in OCV over aging can be described purely with a change of shifting and alignment parameters does not hold for silicon-doped anodes. In this case, apparently, silicon behaved differently even for fresh half cells. On the one hand, excluding the lower SOC range made half-cell fitting feasible because the area where the half-cell OCP curve behaved differently is ignored. On the other hand, this means that parts of the silicon's contribution to the anode capacity C_{an} are not captured. The reconstructed full cell was not defined below approx. 2 % SOC. To avoid these pitfalls, the presented method could be extended by modeling U_{an} with a blend-electrode model [16, 17, 223–225].

A qualitative assignment of full-cell processes to half cells was feasible – a quantitative was not
The described discrepancies between mini-pouch bags and cylindrical cells made a quantitative superimposition of half-cell impedances to the full-cell level impossible. Half-cell measurements revealed an additional process attributed to the lithium counter electrode, which could be circumvented by utilizing a three-electrode setup instead of half cells. Still, the full-cell processes could be qualitatively assigned to either electrode by evaluating the DRT, which enabled physically meaningful parameterization of the high-frequency RC parameters of ECM. Future work should include pulse-relaxation measurements into the half-cell characterization procedure to investigate the low-frequency behavior of both electrodes.

3.2 Parameterizing Resistance Throughout Development and Operation of BEVs

To address shortcomings of conventional fitting algorithms in the time domain or frequency domain, the goal of this work in the *modeling* dimension was to provide solutions for determining high- and low-frequency resistance parameters so that kinetic loss processes are reflected in a physically meaningful way. Study I presented a method to combine frequency-domain and time-domain measurements to cover dynamic effects with time constants over a broad spectrum. Study II built on that and proposed a decoupled parameterization method for high- and low-frequency resistance based on real-world operation. Together, Studies II and III wanted to answer the following research question:

2 *How can high- and low-frequency resistance be parameterized to represent kinetic loss processes in a physically meaningful way:*
a) Pre-life (during the development phase) under laboratory conditions?
b) In-life (in electric vehicles) under real operating conditions?

DRT is a powerful tool – but has its own challenges
The DRT gives valuable insights into the kinetic loss processes and allows the determination of physically meaningful resistance parameters. The main challenge, however, lies in the de-

convolution of the measurement data to obtain the DRT in the first place because results are sensitive to the quality of the measurement data. Pulse relaxation measurements, in particular, can be distorted by effects such as self-discharge, which necessitates careful design of the test procedure. To check impedance spectra for validity, it is recommended to evaluate the Kramers-Kronig relationship. Moreover, optimizing the respective equations to compute the DRT requires mathematical stabilization. Tikhonov regularization [116] was applied in this case. Here, the chosen regularization factor and regularization term have a major influence on the solution. An attempt to reduce as many tuning parameters as possible has been made by using the L-curve method for an automatic determination of the regularization factor. Still, the argument can be made that computing the DRT is of similar complexity as the iterative process of adjusting starting and boundary values of conventional fitting algorithms. However, once computed, analyzing the DRT provides powerful insights that surpass the conventional analysis of the underlying data. Optimizing the measurement and calculation methods should be the focus of future research [116].

Impact of temperature on OCV should be investigated further
The impact of temperature on the OCV was small over the vast majority of the SOC range. Therefore, the presented ECMs were parameterized with OCV look-up tables at 20 °C only. A considerable systematic difference greater than a few mV was found at low SOC, where silicon is most active. It is not clear, however, whether this is caused by temperature-dependent material properties or higher kinetic loss processes distorting the measurement. Further investigations are needed before adding complexity to ECMs by implementing a temperature-dependent OCV is justified.

OCV hysteresis cannot be neglected, especially for silicon-doped anodes
Section 2.1 presented OCV curves measured in charge direction only. For OCV look-up tables in ECMs, also discharge measurements were evaluated and a mean OCV, U_{mean}, was calculated. Thereby, the effect of voltage hysteresis was observed to have a great impact on U_{OCV}. Figure 3.1 shows the difference between the OCV measured in charge direction, U_{charge}, and discharge direction, $U_{\mathrm{discharge}}$, together with the differential voltage. Strong divergence is observed in SOC areas of stage transitions of the anode. The magnitude of voltage hysteresis is particularly high in the low SOC range, where it is assumed to be caused by the (de-)lithiation competition of

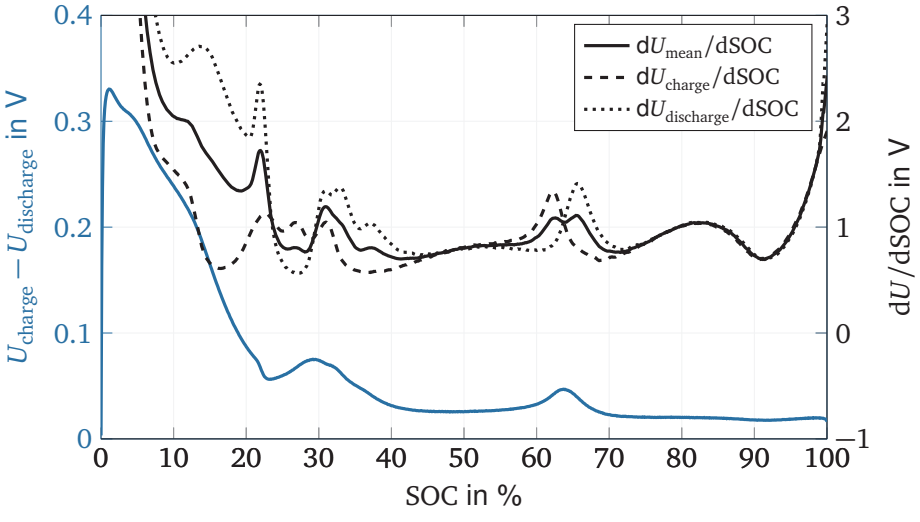

Figure 3.1: OCV hysteresis measured as the difference between constant current measurement with C/50 in charge direction (U_{charge}) and discharge direction ($U_{\mathrm{discharge}}$). Additionally, the differential voltage of the charge, discharge, and mean curve is plotted.

graphite and silicon [228]. The observed hysteresis effect was not analyzed in more detail in this thesis. However, due to the considerable voltage difference in certain SOC ranges, it significantly impacts model accuracy. Therefore, voltage hysteresis should be part of future investigations and half-cell measurements can build the foundation to develop modeling approaches.

3.3 Impact of Aging on SOH_C, SOH_R, LLI, LAM_{an}, and LAM_{cat}

The goal of this work in the *aging* dimension was to gain a deeper understanding of how degradation mechanisms impact electric behavior. Study IV presented the results of a large-scale aging campaign covering calendar aging and cycle aging under all main stress factors. These experiments were performed to answer the following research question:

3 *How do different aging domains and drivers influence SOH_C, SOH_R, LLI, LAM_{an}, and LAM_{cat}? The experimental results should support the development of data-driven aging models.*

Degradation modes were successfully determined – with some exceptions
Half-cell fitting was successfully applied to fresh cells following systematic modifications to the mechanistic OCV model. The same configuration of the algorithm was applied to every check-up measurement, and, with some exceptions, degradation modes were determined with consistent fitting results across the entire aging dataset. Half-cell fitting failed for a few cells subjected to extreme aging conditions such as high temperature and high SOC, or low temperature and high current. In these cases, characteristic peaks in the differential voltage became less pronounced after advanced aging, likely due to inhomogeneous aging of the electrodes. Consequently, the full-cell OCV could no longer be reconstructed from the pristine half-cell OCPs. The relatively high current rate of C/10 might have amplified this issue and a lower current rate could be chosen in future studies at the cost of a longer check-up. As discussed previously, degradation of silicon was not captured fully while tracking C_{an} over aging because of the reduced fitting range. This means that $\mathrm{LAM}_{\mathrm{an}}$ does not represent loss of active material of the whole anode. In future studies, the determination of degradation modes could be enhanced by utilizing blend-electrode models that account for the effects of inhomogeneously aged electrodes [229]. In the presented article, only $R_{\mathrm{DC,10\,s}}$ at 50% SOC was evaluated. The dataset, however, contains different SOCs and pulse durations which can be evaluated in more detail in the future, e.g., to investigate the influence of different aging conditions on the SOC dependency of various kinetic loss processes.

Calendar aging was overestimated in the past
During aging studies, periodic check-up measurements were performed. Calendar aging tests with different check-up intervals revealed that their influence on the aging rate is immense. As the integration of check-up measurements into aging studies is a common approach among researchers, it can be concluded that the calendar life of lithium-ion cells has been significantly underestimated in the past. The extent to which cycle aging experiments are affected depends on the specific combination of stress factors. The check-up procedure, which in this case consisted of three full cycles between 0–100 % SOC, poses significant aging stress on the cell, suggesting a considerable influence on cycle aging tests as well. When designing future aging campaigns, the influence of check-up measurements must be taken into account carefully. One potential measure would be to perform aging tests on multiple individual cells, so that only one check-up procedure is performed on each cell, respectively. This, however, would increase testing costs

significantly. A more economical approach would be to systematically compensate for the effect. Figure 3.2 shows a first heuristic attempt that uses the measurement data with the different check-up intervals [44]. Due to path dependency [15], however, calendar aging and cycle aging do not simply add up [230]. Therefore, Karger et al. went one step further and developed a model based on the theory of SEI growth on cracks in the active material particles, which can describe the influence of check-up measurement using the same experimental data [230].

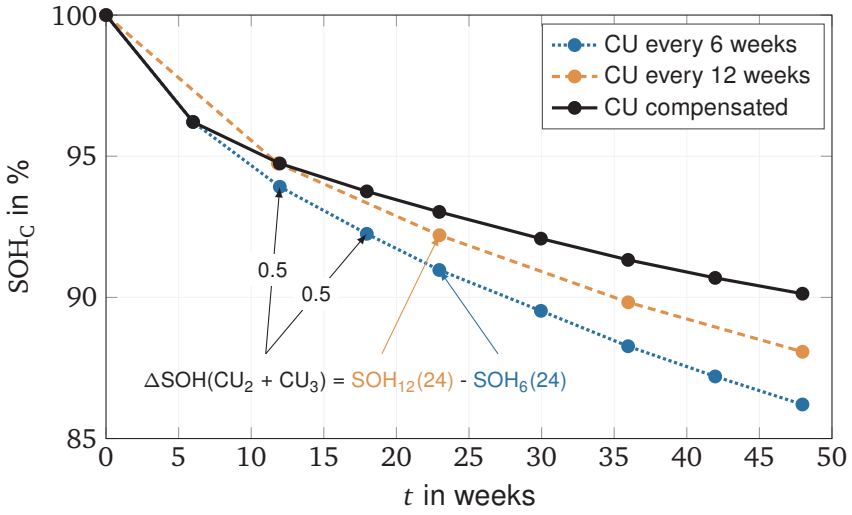

Figure 3.2: Illustration of a heuristic approach to compensate the influence of check-up measurements and results for calendar aging at 50 °C and 50 % SOC. After 24 weeks, the cell with a 6-week interval underwent 4 check-up procedures and the cell with a 12-week interval has only seen 2 check-up procedures (both without the initial check-up). The difference between $\mathrm{SOH_C}$ after 24 weeks is attributed to the two additional check-ups. As a first step, $\Delta\mathrm{SOH_C}$ was distributed equally. The approach was presented in the Semester Thesis of Deniz Aygül [44].

3.4 Role of Inherent Cell-to-Cell Variations in Battery Packs of BEVs

The goal of this work in the *system design* dimension was to understand the occurring effects when scaling electric parameters from cell level to pack level. Study V, presented in Section 2.4, provided statistical results of the experimental characterization of 600 fresh lithium-ion cells to answer the research question:

4 *Why are resistance variations greater than capacity variations, and how significant are initial cell-to-cell variations overall?*

Cell-to-cell resistance variation is not greater than capacity variation

It was shown that measurement uncertainties and external influences during the experiments could explain the greater relative variation of resistance parameters. Temperature variations were identified as the main distorting factor during the test procedures. Systematic adjustment of seasonal and spatial effects reduced the coefficient of variation of the resistance $R_{\mathrm{DC,10\,s}}$ by 50 %, which partly compensated the differences to the capacity variation. Taking into account the greater measurement uncertainties of experimental resistance determination, enough justifiable indicators hint that inherent resistance variation is not greater than capacity variation.

Cell-to-cell variations caused by production tolerances have minor significance
The study revealed low variations of 0.17 % for the capacity and 0.45 % for the resistance $R_{\mathrm{DC,10\,s}}$. Such small variations were considered negligible compared to extrinsic origins of inhomogeneities such as temperature gradients. A Monte Carlo simulation showed, that resistance variations in the order of 1 % lead to temperature variations in the order of only 0.03 °C, but that a temperature variation of 0.5 °C can lead to resistance variations of 1.5 %. Despite active cooling, battery packs in BEVs can suffer from an uneven temperature distribution and extreme operating conditions such as fast charging can easily result in a temperature spread of several degrees Celsius [232]. This has a much greater impact on electrical performance than initial parameter variations of lithium-ion cells produced for the automotive industry under high-quality standards. Hence, the conclusion that inherent cell-to-cell variations are of minor significance is legitimate.

Inherent cell-to-cell variations of aging rates also play a minor role
Additionally, it was hypothesized that variations in the aging rate due to production tolerances are also negligible. High variations reported in previous studies might also have been influenced by temperature variations during the aging experiments [188, 221]. To give preliminary insights, the duplicate test points of calendar aging tests under different conditions are evaluated in Figure 3.3. The biggest difference of $\mathrm{SOH_C}$, for example, is 0.13 % after a capacity fade of over

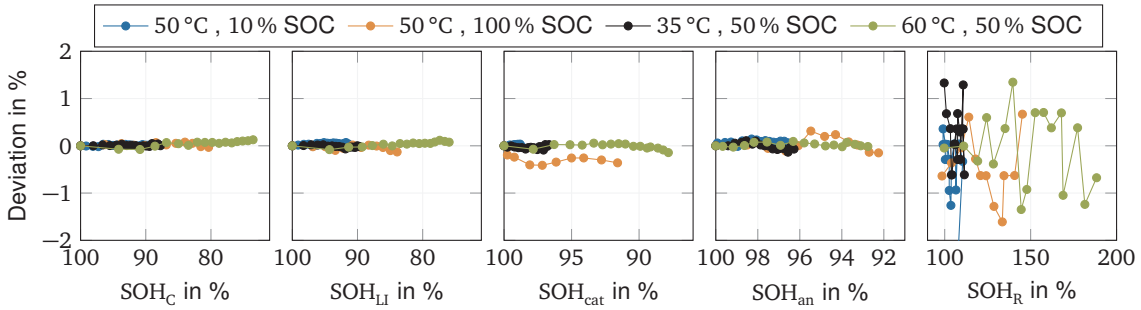

Figure 3.3: Cell-to-cell variations during calendar aging (measurement group E of the aging study presented in Section 2.3). The absolute difference of all five health parameters between two tested cells is plotted over their mean value, respectively.

26 %. This translates to a relative deviation of 0.005 %. Slightly higher relative deviations of the degradation modes might be due to noise in the half-cell fitting and, again, the influence of temperature variations on the resistance measurement. This is a first indication that intrinsic aging rate variations of commercial lithium-ion cells can be considered negligible compared to the total capacity fade. Similar observations were made in [233].

4 Conclusion

To achieve the goal of decarbonizing the mobility sector, the market share of BEVs must increase in the future. This thesis aimed to develop methods and present findings that help overcome purchasing barriers preventing customers from adopting BEVs. These barriers—such as long charging times and limited battery lifespan—prompted research into the dimensions of *modeling*, *aging*, and *system design*, all within the context of the *electric behavior* of lithium-ion batteries. Based on the current state of the art in these areas, specific research questions were formulated. To address these questions, five studies focused on optimizing the development and operation of lithium-ion batteries in electric vehicles were presented and discussed. This chapter concludes the thesis by summarizing how the experimental results and analytical methods presented enable OEMs to bring new BEVs to market more quickly and make them more appealing to customers. Additionally, proposals for future work are outlined. Figure 4.1 brings the individual studies into the context of the broader objectives of this thesis.

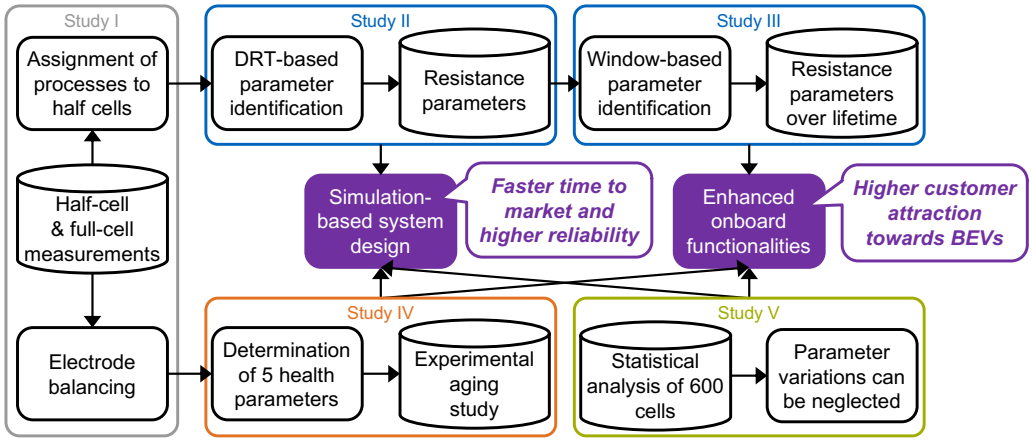

Figure 4.1: Contextualization of the presented studies within the broader objectives of this thesis.

Study I-III present a framework that enables resistance parameterization across the development and operation of BEVs. The first step is to assign the kinetic processes on the full-cell level to either electrode by calculating the DRT from half-cell and full-cell measurements (Study I). Thereby, EIS can capture the high-frequency behavior and pulse-relaxation measurements can identify the low-frequency effects. Both methods can be coupled with one of the presented merging approaches (Study II). Based on these results, an appropriate number of RC elements that represent specific kinetic loss processes can be chosen. The next step is to determine RC parameters directly from the DRT. The resulting parameters can be incorporated into simulation models, such as the holistic simulation framework presented in [21]. Thereby, simulative investigations must eventually consider the whole battery pack instead of individual cells. Study V demonstrated that parameter variations due to production tolerances are negligible compared to extrinsic origins of inhomogeneities such as temperature gradients and can be neglected when scaling the behavior of individual cells to the pack level.

The parameters further serve as starting values for the proposed online algorithm that works on field data (Study III). One use case of the proposed algorithm is the estimation of a pack-level resistance for accurate range estimation over lifetime [70]. In this case, resistance parameters determined for a single cell have to be scaled to pack level, and system-level voltage and current sensor data are used as input to the algorithm. Again, cell-to-cell variations due to production tolerances can be neglected (Study V). Another use case is anomaly detection of individual cells within the battery pack to prevent cell failures from causing thermal runaways [226]. For this purpose, the algorithm can be fed with cell-level sensors. In the future, the presented parameterization approaches can be extended to model anode and cathode separately, e.g., to monitor the anode potential during model-based fast charging control strategies [73, 227].

Beyond accurate electrical parameters, accounting for battery aging is equally crucial to maintaining model validity throughout its lifetime. Study I laid the foundation to leverage the benefits of analyzing the evolution of degradation modes LLI, $\mathrm{LAM_{an}}$ and $\mathrm{LAM_{cat}}$ alongside the tracking of capacity fade and resistance increase. In the experimental aging series presented in Study IV, data with constant aging conditions was collected. Thereby, all main stress factors for calendar aging (as part of a full-factorial design of experiments) and cycle aging (as part of a D-optimal design of experiments) have been varied. These measurements build the foundation for developing (semi-)empirical aging models, where either of the five health parameters can be chosen as target variable [36–45]. Additionally, tests with alternating and randomly changing stress factors, and tests with dynamic automotive load profiles were performed. These kinds of tests allow for thorough validation of developed models.

Because of the high number of 196 tested cells and a great variety of load profiles and their sequence, this open source data set is a valuable resource to develop machine learning aging models as well [46–53]. Over 4000 available check-up measurements can be used to generate labeled data, such as the presented degradation modes and effects. The corresponding cycling data can be used to develop suitable features which can predict different aging trajectories. Such models can be continuously re-trained with field data collected during the operation of BEVs. Under real operating conditions in mobility applications, however, phases with a small constant current over the full SOC range, which are needed to determine degradation modes via the mechanistic OCV model, typically don't occur. Thus, new methods are needed to determine OCV curves from field data to leverage the benefits of degradation modes for enhanced health monitoring and prediction of a BEV fleet [86, 231]. Moreover, as the static behavior of lithium-ion batteries can change significantly, OCV tracking over lifetime would complement the proposed resistance estimation algorithm to enable accurate electric model parameters for aged batteries.

Previous conclusions on the negligible magnitude of production tolerances do not imply that monitoring production processes is not important. On the contrary, quality assurance of lithium-ion cell production becomes more and more relevant to meet the expected ramp-up of electrification in the mobility sector in the upcoming years [234, 235]. On the one hand, the outcome of Study V suggests that production quality requirements could be reasonably lowered to reduce costs [236]. On the other hand, impurities in the raw materials and cell defects can lead to extreme outliers which can reduce the performance of battery packs and in the worst case cause safety critical incidents [226, 237]. As concerns about battery safety are one of the purchasing barriers preventing customers from buying BEVs, future research activities should focus on early detection of cell anomalies [179, 238] and the development of measures to prevent such incidents in order to make battery systems even more reliable in the future.

List of Figures

Figure 1.1: BEV sales share in Europe, China, and USA. 1
Figure 1.2: Overview of the pursued research dimensions. 3
Figure 1.3: Structure of this thesis. 4
Figure 1.4: CCCV measurement procedure to determine the capacity. 6
Figure 1.5: Open-circuit voltage and differential voltage of half cells and full cell. 7
Figure 1.6: Dynamic voltage response to a current pulse. 9
Figure 1.7: Resistance measurement in the time domain and frequency domain. 10
Figure 1.8: Impedance spectrum and Kramers-Kronig relationship. 11
Figure 1.9: Influence of operating conditions on resistance. 12
Figure 1.10: Principle structure of an equivalent circuit model. 14
Figure 1.11: Relationship between cause and effect of aging. 16
Figure 1.12: Origins and effects of inhomogeneities within battery packs. 21
Figure 1.13: Cell-to-cell parameter variations reported in literature. 21
Figure 1.14: Overview of the research questions along the pursued research dimensions. 23
Figure 2.1: Overview of the presented studies along the pursued research dimensions. 25
Figure 2.2: Main parameters of the investigated lithium-ion cell type. 25
Figure 2.3: Graphical summary of Study I. 26
Figure 2.4: Graphical summary of Study II. 44
Figure 2.5: Graphical summary of Study III. 70
Figure 2.6: Graphical summary of Study IV. 86
Figure 2.7: Graphical summary of Study V. 104
Figure 3.1: OCV hysteresis for cells with silicon-doped anodes. 121
Figure 3.2: Heuristic approach to compensate the influence of check-ups. 123
Figure 3.3: Cell-to-cell variations during calendar aging 124
Figure 4.1: Contextualization of the presented studies within the broader objectives. 125

Bibliography

[1] L. Wildfeuer, N. Wassiliadis, A. Karger, F. Bauer and M. Lienkamp, “Teardown analysis and characterization of a commercial lithium-ion battery for advanced algorithms in battery electric vehicles," *Journal of Energy Storage*, vol. 48, no. December 2021, p. 103909, 2022, DOI: 10.1016/j.est.2021.103909.

[2] L. Wildfeuer, P. Gieler and A. Karger, “Combining the Distribution of Relaxation Times from EIS and Time-Domain Data for Parameterizing Equivalent Circuit Models of Lithium-Ion Batteries," *Batteries*, vol. 7, no. 3, pp. 1–23, 2021, DOI: 10.3390/batteries7030052.

[3] A. Karger, L. Wildfeuer, A. Maheshwari, N. Wassiliadis and M. Lienkamp, “Novel method for the on-line estimation of low-frequency impedance of lithium-ion batteries," *Journal of Energy Storage*, vol. 32, no. August, p. 101818, 2020, DOI: 10.1016/j.est.2020.101818.

[4] L. Wildfeuer, A. Karger, D. Aygül, N. Wassiliadis, A. Jossen and M. Lienkamp, “Experimental degradation study of a commercial lithium-ion battery," *Journal of Power Sources*, vol. 560, p. 232498, 2023, DOI: 10.1016/j.jpowsour.2022.232498.

[5] L. Wildfeuer and M. Lienkamp, “Quantifiability of inherent cell-to-cell variations of commercial lithium-ion batteries," *eTransportation*, vol. 9, p. 100129, 2021, DOI: 10.1016/j.etran.2021.100129.

[6] M. Baumann, L. Wildfeuer, S. Rohr and M. Lienkamp, “Parameter variations within Li-Ion battery packs – Theoretical investigations and experimental quantification," *Journal of Energy Storage*, vol. 18, 2018, DOI: 10.1016/j.est.2018.04.031.

[7] L. Wildfeuer, N. Wassiliadis, C. Reiter, M. Baumann and M. Lienkamp, “Experimental Characterization of Li-Ion Battery Resistance at the Cell, Module and Pack Level," in *2019 Fourteenth International Conference on Ecological Vehicles and Renewable Energies (EVER)*, 2019, pp. 1–12, DOI: 10.1109/EVER.2019.8813578.

[8] L. Wildfeuer, “Investigation on the Aging Behavior of Li-Ion Battery Packs Compared to Single Cells," Semester Thesis, Technical University of Munich, 2016.

[9] L. Wildfeuer, “Investigation of the Influence of Parameter Variations in Parallel Connections on the Electrical, Thermal and Aging Behavior of Lithium-Ion Battery Packs," Master’s Thesis, Technical University of Munich, 2017.

[10] L. Wildfeuer, M. Baumann and M. Lienkamp. “*Concept for a hybrid semi-empirical and data-based model for state-of-health monitoring and aging prediction of li-ion battery packs*," Poster. at: *Advanced Automotive Battery Conference (AABC) Europe*, Strasbourg, France. 2019.

[11] L. Wildfeuer, N. Wassiliadis, C. Reiter, M. Baumann and M. Lienkamp. “*Experimental Characterization of Li-Ion Battery Resistance at the Cell, Module and Pack Level*," Dataset. 2019. DOI: 10.13140/RG.2.2.12299.75047.

[12] L. Wildfeuer, N. Wassiliadis, A. Karger, F. Bauer and M. Lienkamp. "*Teardown analysis and characterization of a commercial lithium-ion battery for advanced algorithms in battery electric vehicles*," Dataset. 2022. DOI: 10.14459/2022mp1639153.

[13] L. Wildfeuer, A. Karger, D. Aygül, N. Wasiiliadis, A. Jossen and M. Lienkamp. "*Experimental degradation study of a commercial lithium-ion battery*," Dataset. 2023. DOI: 10.14459/2023mp1713382.

[14] L. Wildfeuer and M. Lienkamp. "*Quantifiability of inherent cell-to-cell variations of commercial lithium-ion batteries*," Dataset. 2023. DOI: 10.13140/RG.2.2.31720.60160.

[15] A. Karger, L. Wildfeuer, D. Aygül, A. Maheshwari, J. P. Singer and A. Jossen, "Modeling capacity fade of lithium-ion batteries during dynamic cycling considering path dependence," *Journal of Energy Storage*, vol. 52, p. 104718, 2022, DOI: 10.1016/j.est.2022.104718.

[16] A. Karger, J. Schmitt, C. Kirst, J. P. Singer, L. Wildfeuer and A. Jossen, "Mechanistic calendar aging model for lithium-ion batteries," *Journal of Power Sources*, vol. 578, p. 233208, 2023, DOI: 10.1016/j.jpowsour.2023.233208.

[17] A. Karger, J. Schmitt, C. Kirst, J. P. Singer, L. Wildfeuer and A. Jossen, "Mechanistic cycle aging model for the open-circuit voltage curve of lithium-ion batteries," *Journal of Power Sources*, vol. 593, p. 233947, 2024, DOI: 10.1016/j.jpowsour.2023.233947.

[18] A. Karger, L. Wildfeuer and A. Jossen. "*Using degradation modes for large-scale capacity and power fade diagnostics*," Poster. at: *Advanced Battery Power*, Münster, Germany. 2022.

[19] A. Karger, J. Schmitt, C. Kirst, J. P. Singer, L. Wildfeuer and A. Jossen. "*Empirical modeling of degradation mode evolution during calendar aging of lithium-ion batteries*," Poster. at: *Advanced Battery Power*, Münster, Germany. 2023.

[20] C. Reiter, N. Wassiliadis, L. Wildfeuer, T. Wurster and M. Lienkamp, "Range extension of electric vehicles through improved battery capacity utilization: Potentials, risks and strategies," in *2018 21st International Conference on Intelligent Transportation Systems (ITSC)*, 2018, pp. 321–326, DOI: 10.1109/ITSC.2018.8569455.

[21] C. Reiter, L. Wildfeuer, N. Wassiliadis, T. Krahl, J. Dirnecker and M. Lienkamp, "A holistic approach for simulation and evaluation of electrical and thermal loads in lithium-ion battery systems," in *2019 Fourteenth International Conference on Ecological Vehicles and Renewable Energies (EVER)*, 2019, pp. 1–17, DOI: 10.1109/EVER.2019.8813640.

[22] W. Schmid, L. Wildfeuer, J. Kreibich, R. Büechl, M. Schuller and M. Lienkamp, "A Longitudinal Simulation Model for a Fuel Cell Hybrid Vehicle: Experimental Parameterization and Validation with a Production Car," in *2019 Fourteenth International Conference on Ecological Vehicles and Renewable Energies (EVER)*, 2019, pp. 1–13, DOI: 10.1109/EVER.2019.8813648.

[23] N. Wassiliadis, T. Herrmann, L. Wildfeuer, C. Reiter and M. Lienkamp, "Comparative Study of State-Of-Charge Estimation with Recurrent Neural Networks," in *2019 IEEE Transportation Electrification Conference and Expo (ITEC)*, 2019, pp. 1–6, DOI: 10.1109/ITEC.2019.8790597.

[24] T. Gewald, A. Candussio, L. Wildfeuer, D. Lehmkuhl, A. Hahn and M. Lienkamp, "Accelerated Aging Characterization of Lithium-ion Cells: Using Sensitivity Analysis to Identify the Stress Factors Relevant to Cyclic Aging," *Batteries*, vol. 6, no. 1, 2020, DOI: 10.3390/batteries6010006.

[25] N. Wassiliadis, M. Ank, L. Wildfeuer, M. K. Kick and M. Lienkamp, “Experimental investigation of the influence of electrical contact resistance on lithium-ion battery testing for fast-charge applications," *Applied Energy*, vol. 295, p. 117064, 2021, DOI: 10.1016/j.apenergy.2021.117064.

[26] N. Wassiliadis, J. Schneider, A. Frank, L. Wildfeuer, X. Lin, A. Jossen and M. Lienkamp, “Review of fast charging strategies for lithium-ion battery systems and their applicability for battery electric vehicles," *Journal of Energy Storage*, vol. 44, p. 103306, 2021, DOI: 10.1016/j.est.2021.103306.

[27] N. Wassiliadis, M. Steinsträter, M. Schreiber, P. Rosner, L. Nicoletti, et al., “Quantifying the state of the art of electric powertrains in battery electric vehicles: Range, efficiency, and lifetime from component to system level of the Volkswagen ID.3," *eTransportation*, vol. 12, p. 100167, 2022, DOI: 10.1016/j.etran.2022.100167.

[28] P. Gries, “Emission Reduction Potential of Predictive Battery Analytics along the Lithium-Ion Battery Lifecycle," Master’s Thesis, Technical University of Munich, 2021.

[29] E. Fischer, “Konstruktion einer Temperaturkammer für Batterieversuche," Bachelor’s Thesis, Technical University of Munich, 2019.

[30] P. Gieler, “Implementierung und Analyse eines Algorithmus zur Parameterbestimmung von Lithium-Ionen-Zellen," Bachelor’s Thesis, Technical University of Munich, 2019.

[31] P. Gieler, “Parameterizing Equivalent Circuit Models of Lithium-Ion Batteries with the Distribution of Relaxation Times," Semester’s Thesis, Technical University of Munich, 2020.

[32] A. Karger, “Impedance Determination of Lithium-Ion Batteries during Vehicle Operation," Semester Thesis, Technical University of Munich, 2019.

[33] L. Reinfeld, “Parametrization of Thermal Equivalent Circuit Models for Lithium-Ion Batteries," Master’s Thesis, Technical University of Munich, 2020.

[34] J. Schürmer, “Detektion und Quantifizierung von Lithium-Plating in Batteriepacks von Elek- trofahrzeugen," Semester Thesis, Technical University of Munich, 2019.

[35] A. Karger, “Detection of Lithium Plating in Lithium-Ion Batteries," Master’s Thesis, Technical University of Munich, 2020.

[36] M. Keßler, “Untersuchung und Implementierung von Methoden zur Belastungscharakterisierung von Lithium-Ionen-Batteriesystemen," Master’s Thesis, Technical University of Munich, 2018.

[37] A. Swierstra, “Experimentelle Untersuchung über das Superpositionsverhalten von kalendarischer und zyklischer Alterung bei Lithium-Ionen Batterien," Semester Thesis, Technical University of Munich, 2019.

[38] D. Ostilla, “Modelling of Superposition Principles of Lithium-Ion Cell Aging Mechanisms," Master’s Thesis, Technical University of Munich, 2020.

[39] K. Waldher, “Untersuchung neuartiger Methoden zur semi-empirischen Alterungsmodellierung von Lithium-Ionen-Zellen," Master’s Thesis, Technical University of Munich, 2019.

[40] S. Erkilic, “Implementierung und Analyse eines Algorithmus zur Parameterbestimmung von Lithium-Ionen-Zellen," Master’s Thesis, Technical University of Munich, 2019.

[41] N. Rücker, “Experimental Investigation and Modelling of Superposition Principles of Lithium-Ion Cell Aging Mechanisms," Master’s Thesis, Technical University of Munich, 2019.

[42] J. Schürmer, “Entwicklung eines semi-empirischen Alterungsmodells für Lithium-Ionen Batterien," Master’s Thesis, Technical University of Munich, 2020.

[43] D. Schmitt, “Entwicklung generischer, semi-empirische Alterungsmodelle für LIB," Semester Thesis, Technical University of Munich, 2020.

[44] D. Aygül, “Analysis of Parameterization Approaches for Aging Modeling of Lithium-Ion Batteries," Semester Thesis, Technical University of Munich, 2020.

[45] D. Schmitt, “Entwicklung eines Alterungsmodells zur Vorhersage des Widerstands für Lithium-Ionen Batterien," Master’s Thesis, Technical University of Munich, 2021.

[46] M. Wanisch, “Lebensdauerprädiktion von Li-Ionen Batterien mittels künstlicher Intelligenz," Master’s Thesis, Technical University of Munich, 2019.

[47] C. Kirst, “Data-Based Aging Modeling of Li-Ion Batteries," Semester Thesis, Technical University of Munich, 2019.

[48] F. Näher, “Datenbasierte Alterungsmodellierung von Lithium-Ionen-Batterien mittels künstlicher neuronaler Netze," Master’s Thesis, Technical University of Munich, 2020.

[49] P. Bilfinger, “Implementation of Transfer Machine Learning Methods for the Aging Prediction of Li-Ion Batteries," Master’s Thesis, Technical University of Munich, 2020.

[50] R. Droop, “Architekturen Künstlicher Neuronaler Netze zur Alterungsmodellierung von Architectures of artificial neural networks for modeling," Semester Thesis, Technical University of Munich, 2020.

[51] D. Weinzierl, “Integration of external knowledge in deep learning methods for the life time prediction of Li-Ion batteries," Master’s Thesis, Technical University of Munich, 2020.

[52] F. Diller, “Entwicklung eines stressfaktorbasierten Alterungsmodells von Lithium-Ionen Batterien mittels maschinellen Lernens," Semester Thesis, Technical University of Munich, 2021.

[53] D. Aygül, “Development of a Hybrid Semi-Empirical and Data-Based Aging Model for Li-Ion Batteries," Master’s Thesis, Technical University of Munich, 2021.

[54] J. Niedermayer, “Analyse und Simulation von Betriebsstrategien für Brennstoffzellenfahrzeuge," Semester Thesis, Technical University of Munich, 2019.

[55] J. Buberger, “Modellierung, Parametrierung und Validierung der Brennstoffzelle in der Längsdynamiksimulation eines Brennstoffzellenfahrzeugs," Semester Thesis, Technical University of Munich, 2019.

[56] P. Rosner, “Experimentelle Analyse des Betriebsverhaltens eines Brennstoffzellen - Elektrofahrzeuges," Semester Thesis, Technical University of Munich, 2019.

[57] R. Büechl, “Modellierung, Parametrierung und Validierung der Längsdynamiksimulation eines Brennstoffzellenfahrzeugs anhand realer Fahrzyklen," Master’s Thesis, Technical University of Munich, 2019.

[58] G. Inc. “*Grammarly: Writing Assistant*," Version used: November 2024. 2024. Available: https://www.grammarly.com.

[59] OpenAI. “*ChatGPT-4*," https://openai.com. Version used: November 2024. 2024.

[60] NASA. "*There is unequivocal evidence that Earth is warming at an unprecedented rate.*" Available: https://science.nasa.gov/climate-change/evidence/ [visited on 10/02/2024].

[61] United Nations Treaty Collection, Chapter XXVII 7. d. "*Paris Agreement*," 2015. Available: https://treaties.un.org/pages/ViewDetails.aspx?src=TREATY&mtdsg_no=XXVII-7-d&chapter=27&clang=_en [visited on 10/02/2024].

[62] S. Schlacke, H. Wentzien, E.-M. Thierjung and M. Köster, "Implementing the EU Climate Law via the 'Fit for 55' package," *Oxford Open Energy*, vol. 1, oiab002, 2022, DOI: 10.1093/ooenergy/oiab002.

[63] IEA, "Global EV Outlook 2024," IEA, Paris, 2024. Available: https://www.iea.org/reports/global-ev-outlook-2024 [visited on 10/02/2024].

[64] German National Academy of Science and Engineering. "*Mobilitätsmonitor 2024*," 2024. Available: https://www.acatech.de/mobilitaetsmonitor/ [visited on 10/02/2024].

[65] McKinsey & Company. "*How European consumers perceive electric vehicles*," 2024. Available: https://www.mckinsey.com/industries/automotive-and-assembly/our-insights/how-european-consumers-perceive-electric-vehicles#/ [visited on 10/02/2024].

[66] O. Teichert, S. Link, J. Schneider, S. Wolff and M. Lienkamp, "Techno-economic cell selection for battery-electric long-haul trucks," *eTransportation*, vol. 16, p. 100225, 2023, DOI: 10.1016/j.etran.2022.100225.

[67] M. Ank, A. Sommer, K. Abo Gamra, J. Schöberl, M. Leeb, et al., "Lithium-Ion Cells in Automotive Applications: Tesla 4680 Cylindrical Cell Teardown and Characterization," *Journal of The Electrochemical Society*, vol. 170, no. 12, p. 120536, 2023, DOI: 10.1149/1945-7111/ad14d0.

[68] F. J. Günter and N. Wassiliadis, "State of the Art of Lithium-Ion Pouch Cells in Automotive Applications: Cell Teardown and Characterization," *Journal of The Electrochemical Society*, vol. 169, no. 3, p. 030515, 2022, DOI: 10.1149/1945-7111/ac4e11.

[69] T. Gewald, "Beschleunigte Alterungscharakterisierung von Lithium-Ionen-Zellen in der Fahrzeuganwendung," PhD thesis, Technical University of Munich, 2021.

[70] N. Wassiliadis, J. Adermann, A. Frericks, M. Pak, C. Reiter, B. Lohmann and M. Lienkamp, "Revisiting the dual extended Kalman filter for battery state-of-charge and state-of-health estimation: A use-case life cycle analysis," *Journal of Energy Storage*, vol. 19, pp. 73–87, 2018, DOI: 10.1016/j.est.2018.07.006.

[71] N. Wassiliadis, "Model-Based Fast Charging Control of Lithium-Ion Batteries in Electric Vehicles," PhD thesis, Technical University of Munich, 2024.

[72] P. Keil and A. Jossen, "Charging protocols for lithium-ion batteries and their impact on cycle life-An experimental study with different 18650 high-power cells," *Journal of Energy Storage*, vol. 6, pp. 125–141, 2016, DOI: 10.1016/j.est.2016.02.005.

[73] N. Wassiliadis, J. Kriegler, K. A. Gamra and M. Lienkamp, "Model-based health-aware fast charging to mitigate the risk of lithium plating and prolong the cycle life of lithium-ion batteries in electric vehicles," *Journal of Power Sources*, vol. 561, p. 232586, 2023, DOI: 10.1016/j.jpowsour.2022.232586.

[74] C. Reiter, "Thermische Vorauslegung hochbelasteter Batteriesysteme für Elektrofahrzeuge in der Konzeptphase," PhD thesis, Technical University of Munich, 2020.

[75] M. S. Whittingham, "Lithium Batteries and Cathode Materials," *Chemical Reviews*, vol. 104, no. 10, pp. 4271–4302, 2004, DOI: 10.1021/cr020731c.

[76] M. J. Lain, J. Brandon and E. Kendrick, “Design strategies for high power vs. High energy lithium ion cells," *Batteries*, vol. 5, 2019, DOI: 10.3390/batteries5040064.

[77] P. Nzereogu, A. Omah, F. Ezema, E. Iwuoha and A. Nwanya, “Anode materials for lithium-ion batteries: A review," *Applied Surface Science Advances*, vol. 9, p. 100233, 2022, DOI: https://doi.org/10.1016/j.apsadv.2022.100233.

[78] W. M. Dose, M. J. Piernas-Muñoz, V. A. Maroni, S. E. Trask, I. Bloom and C. S. Johnson, “Capacity fade in high energy silicon-graphite electrodes for lithium-ion batteries," *Chem. Commun.*, vol. 54, pp. 3586–3589, 2018, DOI: 10.1039/C8CC00456K.

[79] H. Cheng, J. G. Shapter, Y. Li and G. Gao, “Recent progress of advanced anode materials of lithium-ion batteries," *Journal of Energy Chemistry*, vol. 57, pp. 451–468, 2021, DOI: https://doi.org/10.1016/j.jechem.2020.08.056.

[80] P. Keil, “Aging of Lithium-Ion Batteries in Electric Vehicles," PhD thesis, Technical University of Munich, 2017.

[81] Q.-Q. Yu, R. Xiong, L.-Y. Wang and C. Lin, “A Comparative Study on Open Circuit Voltage Models for Lithium-ion Batteries," *Chinese Journal of Mechanical Engineering*, vol. 31, no. 1, p. 65, 2018, DOI: 10.1186/s10033-018-0268-8.

[82] I. Bloom, J. P. Christophersen, D. P. Abraham and K. L. Gering, “Differential voltage analyses of high-power lithium-ion cells: 3. Another anode phenomenon," *Journal of Power Sources*, vol. 157, no. 1, pp. 537–542, 2006, DOI: 10.1016/j.jpowsour.2005.07.054.

[83] A. Adam, E. Knobbe, J. Wandt and A. Kwade, “Application of the differential charging voltage analysis to determine the onset of lithium-plating during fast charging of lithium-ion cells," *Journal of Power Sources*, vol. 495, p. 229794, 2021, DOI: 10.1016/j.jpowsour.2021.229794.

[84] L. Wang, C. Pan, L. Liu, Y. Cheng and X. Zhao, “On-board state of health estimation of LiFePO4 battery pack through differential voltage analysis," *Applied Energy*, vol. 168, pp. 465–472, 2016, DOI: 10.1016/j.apenergy.2016.01.125.

[85] K. Uddin, G. H. Chouchelamane, C. Pastor-Fernández, W. D. Widanage and J. Marco, “A Comparison between Electrochemical Impedance Spectroscopy and Incremental Capacity-Differential Voltage as Li-ion Diagnostic Techniques to Identify and Quantify the Effects of Degradation Modes within Battery Management Systems," *Journal of Power Sources*, vol. 360, pp. 301–318, 2017, DOI: 10.1016/j.jpowsour.2017.03.042.

[86] P. Bilfinger, P. Rosner, M. Schreiber, T. Kröger, K. A. Gamra, M. Ank, N. Wassiliadis, B. Dietermann and M. Lienkamp, “Battery pack diagnostics for electric vehicles: Transfer of differential voltage and incremental capacity analysis from cell to vehicle level," *eTransportation*, vol. 22, p. 100356, 2024, DOI: 10.1016/j.etran.2024.100356.

[87] M. Hess, “Kinetics and stage transitions of graphite for lithium-ion batteries," PhD thesis, ETH / PSI, ETH Zürich, Zürich, 2013, DOI: 10.3929/ethz-a-010000442.

[88] F. Friedrich, S. Pieper and H. A. Gasteiger, “Entropy measurements of Li-ion battery cells with Li-and Mn-rich layered transition metal oxides via linear temperature variation," *Journal of The Electrochemical Society*, vol. 168, no. 12, p. 120502, 2021.

[89] K. Takano, Y. Saito, K. Kanari, K. Nozaki, K. Kato, A. Negishi and T. Kato, “Entropy change in lithium ion cells on charge and discharge," *Journal of Applied Electrochemistry*, vol. 32, pp. 251–258, 2002.

[90] R. Zhang, B. Xia, B. Li, L. Cao, Y. Lai, W. Zheng, H. Wang, W. Wang and M. Wang, “A Study on the Open Circuit Voltage and State of Charge Characterization of High Capacity Lithium-Ion Battery Under Different Temperature," *Energies*, vol. 11, no. 9, p. 2408, 2018, DOI: 10.3390/en11092408.

[91] F. Zheng, Y. Xing, J. Jiang, B. Sun, J. Kim and M. Pecht, “Influence of different open circuit voltage tests on state of charge online estimation for lithium-ion batteries," *Applied Energy*, vol. 183, pp. 513–525, 2016, DOI: 10.1016/j.apenergy.2016.09.010.

[92] J. P. Schmidt, “Verfahren zur Charakterisierung und Modellierung von Lithium-Ionen Zellen," PhD thesis, Karlsruher Institute of Technology, 2013, DOI: 10.5445/KSP/1000036622.

[93] A. Nickol, T. Schied, C. Heubner, M. Schneider, A. Michaelis, M. Bobeth and G. Cuniberti, “GITT analysis of lithium insertion cathodes for determining the lithium diffusion coefficient at low temperature: challenges and pitfalls," *Journal of The Electrochemical Society*, vol. 167, no. 9, p. 090546, 2020.

[94] J. Schmitt, “State of health estimation for lithium-ion batteries," PhD thesis, Technical University of Munich, 2023.

[95] M. Baumann, “Methode zur Parameterbestimmung und -prädiktion von Lithium-Ionen-Traktionsbatterien," Dissertation, Technical University of Munich, 2019.

[96] A. U. Schmid, M. Kurka and K. P. Birke, “Reproducibility of Li-ion cell reassembling processes and their influence on coin cell aging," *Journal of Energy Storage*, vol. 24, p. 100732, 2019, DOI: 10.1016/j.est.2019.04.006.

[97] C. R. Birkl, M. R. Roberts, E. McTurk, P. G. Bruce and D. A. Howey, “Degradation diagnostics for lithium ion cells," *Journal of Power Sources*, vol. 341, pp. 373–386, 2017, DOI: 10.1016/j.jpowsour.2016.12.011.

[98] S. Schindler and M. A. Danzer, “A novel mechanistic modeling framework for analysis of electrode balancing and degradation modes in commercial lithium-ion cells," *Journal of Power Sources*, vol. 343, pp. 226–236, 2017, DOI: 10.1016/j.jpowsour.2017.01.026.

[99] M. Dubarry, C. Truchot and B. Y. Liaw, “Synthesize battery degradation modes via a diagnostic and prognostic model," *Journal of Power Sources*, vol. 219, pp. 204–216, 2012, DOI: 10.1016/j.jpowsour.2012.07.016.

[100] A. Jossen, “Fundamentals of battery dynamics," *Journal of Power Sources*, vol. 154, no. 2, pp. 530–538, 2006, DOI: 10.1016/j.jpowsour.2005.10.041.

[101] P. Verma, P. Maire and P. Novák, “A review of the features and analyses of the solid electrolyte interphase in Li-ion batteries," *Electrochimica Acta*, vol. 55, no. 22, pp. 6332–6341, 2010, DOI: 10.1016/j.electacta.2010.05.072.

[102] T. R. Jow, S. A. Delp, J. L. Allen, J.-P. Jones and M. C. Smart, “Factors Limiting Li+ Charge Transfer Kinetics in Li-Ion Batteries," *Journal of The Electrochemical Society*, vol. 165, no. 2, A361, 2018, DOI: 10.1149/2.1221802jes.

[103] M.-T. von Srbik, M. Marinescu, R. F. Martinez-Botas and G. J. Offer, “A physically meaningful equivalent circuit network model of a lithium-ion battery accounting for local electrochemical and thermal behaviour, variable double layer capacitance and degradation," *Journal of Power Sources*, vol. 325, pp. 171–184, 2016, DOI: 10.1016/j.jpowsour.2016.05.051.

[104] M. Schönleber, “Verfahren zur Charakterisierung des Niederfrequenzverhaltens von Lithium-Ionen Batterien," PhD thesis, KIT Scientific Publishing, Karlsruher Institut für Technologie (KIT), 2017, DOI: 10.5445/KSP/1000070943.

[105] A. Barai, K. Uddin, W. D. Widanage, A. McGordon and P. Jennings, “A study of the influence of measurement timescale on internal resistance characterisation methodologies for lithium-ion cells," *Scientific Reports*, vol. 8, no. 1, p. 21, 2018, DOI: 10.1038/s41598-017-18424-5.

[106] M. A. Roscher, O. Bohlen and J. Vetter, “OCV hysteresis in Li-Ion batteries including two-phase transition materials," *International Journal of Electrochemistry*, vol. 2011, no. 1, p. 984320, 2011.

[107] A. Sleigh, J. Murray and W. McKinnon, “Memory effects due to phase conversion and hysteresis in Li/LixMnO2 cells," *Electrochimica Acta*, vol. 36, no. 9, pp. 1469–1474, 1991, DOI: 10.1016/0013-4686(91)85336-6.

[108] G. Piłatowicz, A. Marongiu, J. Drillkens, P. Sinhuber and D. U. Sauer, “A critical overview of definitions and determination techniques of the internal resistance using lithium-ion, lead-acid, nickel metal-hydride batteries and electrochemical double-layer capacitors as examples," *Journal of Power Sources*, vol. 296, pp. 365–376, 2015, DOI: 10.1016/j.jpowsour.2015.07.073.

[109] H.-G. Schweiger, O. Obeidi, O. Komesker, A. Raschke, M. Schiemann, C. Zehner, M. Gehnen, M. Keller and P. Birke, “Comparison of several methods for determining the internal resistance of lithium ion cells," *Sensors*, vol. 10, no. 6, pp. 5604–5625, 2010.

[110] S. Zhao, F. Wu, L. Yang, L. Gao and A. F. Burke, “A measurement method for determination of dc internal resistance of batteries and supercapacitors," *Electrochemistry Communications*, vol. 12, no. 2, pp. 242–245, 2010, DOI: 10.1016/j.elecom.2009.12.004.

[111] W. Waag, “Adaptive algorithms for monitoring of lithium-ion batteries in electric vehicles," PhD thesis, Shaker, RWTH Aachen, 2014.

[112] A. Barai, G. H. Chouchelamane, Y. Guo, A. McGordon and P. Jennings, “A study on the impact of lithium-ion cell relaxation on electrochemical impedance spectroscopy," *Journal of Power Sources*, vol. 280, pp. 74–80, 2015, DOI: 10.1016/j.jpowsour.2015.01.097.

[113] D. Qu, G. Wang, J. Kafle, J. Harris, L. Crain, Z. Jin and D. Zheng, “Electrochemical Impedance and its Applications in Energy-Storage Systems," *Small Methods*, vol. 2, p. 1700342, 2018, DOI: 10.1002/smtd.201700342.

[114] Michael Schönleber, “Kramers-Kronig Validity Test Lin-KK for Impedance Spectra," *Karlsruhe Institute of Technology, Materials for Electrical and Electronic*.

[115] M. Schönleber, D. Klotz and E. Ivers-Tiffée, “A Method for Improving the Robustness of linear Kramers-Kronig Validity Tests," *"Electrochimica Acta*, vol. 131, pp. 20–27, 2014, DOI: 10.1016/j.electacta.2014.01.034.

[116] C. Plank, T. Rüther, L. Jahn, M. Schamel, J. P. Schmidt, F. Ciucci and M. A. Danzer, “A review on the distribution of relaxation times analysis: A powerful tool for process identification of electrochemical systems," *Journal of Power Sources*, vol. 594, p. 233845, 2024, DOI: https://doi.org/10.1016/j.jpowsour.2023.233845.

[117] T. Momma, M. Matsunaga, D. Mukoyama and T. Osaka, “Ac impedance analysis of lithium ion battery under temperature control," *Journal of Power Sources*, vol. 216, pp. 304–307, 2012, DOI: 10.1016/j.jpowsour.2012.05.095.

[118] W. Waag, S. Käbitz and D. U. Sauer, “Experimental investigation of the lithium-ion battery impedance characteristic at various conditions and aging states and its influence on the application," *Applied Energy*, vol. 102, pp. 885–897, 2013, DOI: 10.1016/j.apenergy.2012.09.030.

[119] P. Shafiei Sabet, G. Stahl and D. U. Sauer, “Non-invasive investigation of predominant processes in the impedance spectra of high energy lithium-ion batteries with Nickel-Cobalt-Aluminum cathodes," *Journal of Power Sources*, 2018, DOI: 10.1016/j.jpowsour.2018.10.024.

[120] P. S. Sabet and D. U. Sauer, “Separation of predominant processes in electrochemical impedance spectra of lithium-ion batteries with nickelemanganeseecobalt cathodes," *Journal of Power Sources*, vol. 425, pp. 121–129, 2019, DOI: 10.1016/j.jpowsour.2019.03.068.

[121] S. Gantenbein, M. Weiss and E. Ivers-Tiffée, “Impedance based time-domain modeling of lithium-ion batteries: Part I," *Journal of Power Sources*, vol. 379, pp. 317–327, 2018, DOI: 10.1016/j.jpowsour.2018.01.043.

[122] F. E. Hust, “Physico-chemically motivated parameterization and modelling of real-time capable lithium-ion battery models : a case study on the Tesla Model S battery," Dissertation, ISEA, RWTH Aachen, Aachen, 2018, DOI: 10.18154/RWTH-2019-00249.

[123] A. Mertens, I. C. Vinke, H. Tempel, H. Kungl, L. G. J. de Haart, R.-A. Eichel and J. Granwehr, “Quantitative Analysis of Time-Domain Supported Electrochemical Impedance Spectroscopy Data of Li-Ion Batteries: Reliable Activation Energy Determination at Low Frequencies," *Journal of The Electrochemical Society*, vol. 163, no. 7, H521–H527, 2016, DOI: 10.1149/2.0511607jes.

[124] A. J. Bard and L. R. Faulkner, *Electrochemical methods: fundamentals and applications*, 2. edition, New York Weinheim, Wiley, 2001.

[125] N. Nieto, L. Díaz, J. Gastelurrutia, I. Alava, F. Blanco, J. Carlos Ramos and A. Rivas, “Thermal Modeling of Large Format Lithium-Ion Cells," *Journal of The Electrochemical Society*, vol. 160, no. 2, A212–A217, 2013, DOI: 10.1149/2.042302jes.

[126] C. Reiter, N. Wassiliadis and M. Lienkamp, “Design of Thermal Management Systems for Battery Electric Vehicles," in *2019 Fourteenth International Conference on Ecological Vehicles and Renewable Energies (EVER)*, 2019, pp. 1–10, DOI: 10.1109/EVER.2019.8813671.

[127] Y. Ye, Y. Shi, N. Cai, J. Lee and X. He, “Electro-thermal modeling and experimental validation for lithium ion battery," *Journal of Power Sources*, vol. 199, pp. 227–238, 2012, DOI: 10.1016/j.jpowsour.2011.10.027.

[128] C. Forgez, D. Vinh Do, G. Friedrich, M. Morcrette and C. Delacourt, “Thermal modeling of a cylindrical LiFePO4/graphite lithium-ion battery," *Journal of Power Sources*, vol. 195, no. 9, pp. 2961–2968, 2010, DOI: 10.1016/j.jpowsour.2009.10.105.

[129] J. Schmalstieg, S. Käbitz, M. Ecker and D. U. Sauer, “A holistic aging model for Li(NiMnCo)O2 based 18650 lithium-ion batteries," *Journal of Power Sources*, vol. 257, pp. 325–334, 2014, DOI: 10.1016/j.jpowsour.2014.02.012.

[130] M. Naumann, M. Schimpe, P. Keil, H. C. Hesse and A. Jossen, “Analysis and modeling of calendar aging of a commercial LiFePO4/graphite cell," *Journal of Energy Storage*, vol. 17, pp. 153–169, 2018, DOI: 10.1016/j.est.2018.01.019.

[131] M. Naumann, F. Spingler and A. Jossen, “Analysis and modeling of cycle aging of a commercial LiFePO4/graphite cell," *Journal of Power Sources*, vol. 451, p. 227666, 2020, DOI: 10.1016/j.jpowsour.2019.227666.

[132] M. Johnen, S. Pitzen, U. Kamps, M. Kateri, P. Dechent and D. U. Sauer, “Modeling long-term capacity degradation of lithium-ion batteries," *Journal of Energy Storage*, vol. 34, p. 102011, 2021, DOI: 10.1016/j.est.2020.102011.

[133] E. Redondo-Iglesias, P. Venet and S. Pelissier, “Modelling lithium-ion battery ageing in electric vehicle applications—calendar and cycling ageing combination effects," *Batteries*, vol. 6, pp. 1–18, 2020, DOI: 10.3390/batteries6010014.

[134] S. E. O’Kane, W. Ai, G. Madabattula, D. Alonso-Alvarez, R. Timms, V. Sulzer, J. S. Edge, B. Wu, G. J. Offer and M. Marinescu, “Lithium-ion battery degradation: how to model it," *Physical Chemistry Chemical Physics*, vol. 24, no. 13, pp. 7909–7922, 2022.

[135] H. Ruan, J. V. Barreras, T. Engstrom, Y. Merla, R. Millar and B. Wu, “Lithium-ion battery lifetime extension: A review of derating methods," *Journal of Power Sources*, vol. 563, p. 232805, 2023, DOI: https://doi.org/10.1016/j.jpowsour.2023.232805.

[136] M. Safari and C. Delacourt, “Modeling of a Commercial Graphite/LiFePO4 Cell," *Journal of The Electrochemical Society*, vol. 158, no. 5, A562, 2011, DOI: 10.1149/1.3567007.

[137] M. Doyle, T. F. Fuller and J. Newman, “Modeling of Galvanostatic Charge and Discharge of the Lithium/Polymer/Insertion Cell," *Journal of The Electrochemical Society*, vol. 140, no. 6, pp. 1526–1533, 1993, DOI: 10.1149/1.2221597/XML.

[138] G. L. Plett, “Extended Kalman filtering for battery management systems of LiPB-based HEV battery packs: Part 1. Background," *Journal of Power Sources*, vol. 134, no. 2, pp. 252–261, 2004, DOI: 10.1016/j.jpowsour.2004.02.031.

[139] X. Hu, S. Li and H. Peng, “A comparative study of equivalent circuit models for Li-ion batteries," *Journal of Power Sources*, vol. 198, pp. 359–367, 2012, DOI: 10.1016/j.jpowsour.2011.10.013.

[140] M. K. Tran, M. Mathew, S. Janhunen, S. Panchal, K. Raahemifar, R. Fraser and M. Fowler, “A comprehensive equivalent circuit model for lithium-ion batteries, incorporating the effects of state of health, state of charge, and temperature on model parameters," *Journal of Energy Storage*, vol. 43, no. May, p. 103252, 2021, DOI: 10.1016/j.est.2021.103252.

[141] M. Hossain Lipu, M. Hannan, A. Hussain, A. Ayob, M. H. Saad, T. F. Karim and D. N. How, “Data-driven state of charge estimation of lithium-ion batteries: Algorithms, implementation factors, limitations and future trends," *Journal of Cleaner Production*, vol. 277, p. 124110, 2020, DOI: 10.1016/j.jclepro.2020.124110.

[142] A. Farmann and D. Sauer, “A comprehensive review of on-board State-of-Available-Power prediction techniques for lithium-ion batteries in electric vehicles," *Journal of Power Sources*, vol. 329, pp. 123–137, 2016, DOI: 10.1016/j.jpowsour.2016.08.031.

[143] S. Nejad, D. Gladwin and D. Stone, “A systematic review of lumped-parameter equivalent circuit models for real-time estimation of lithium-ion battery states," *Journal of Power Sources*, vol. 316, pp. 183–196, 2016, DOI: 10.1016/j.jpowsour.2016.03.042.

[144] M.-K. Tran and M. Fowler, “A Review of Lithium-Ion Battery Fault Diagnostic Algorithms: Current Progress and Future Challenges," *Algorithms*, vol. 13, no. 3, 2020, DOI: 10.3390/a13030062.

[145] C. Reiter. “*sim_battery_system - A simulation framework for lithium-ion battery systems*," Software. 2019. Available: https://github.com/TUMFTM/sim_battery_system.

[146] S. M. Mousavi G. and M. Nikdel, “Various battery models for various simulation studies and applications," *Renewable and Sustainable Energy Reviews*, vol. 32, pp. 477–485, 2014, DOI: 10.1016/j.rser.2014.01.048.

[147] Y. H. Chiang, W. Y. Sean and J. C. Ke, “Online estimation of internal resistance and open-circuit voltage of lithium-ion batteries in electric vehicles," *Journal of Power Sources*, vol. 196, pp. 3921–3932, 2011, DOI: 10.1016/j.jpowsour.2011.01.005.

[148] H. Rahimi-Eichi, F. Baronti and M. Y. Chow, “Modeling and online parameter identification of Li-Polymer battery cells for SOC estimation," *IEEE International Symposium on Industrial Electronics*, pp. 1336–1341, 2012, DOI: 10.1109/ISIE.2012.6237284.

[149] L. Zhou, L. He, Y. Zheng, X. Lai, M. Ouyang and L. Lu, “Massive battery pack data compression and reconstruction using a frequency division model in battery management systems," *Journal of Energy Storage*, vol. 28, p. 101252, 2020, DOI: 10.1016/j.est.2020.101252.

[150] M. Sitterly, L. Y. Wang, G. G. Yin and C. Wang, “Enhanced identification of battery models for real-time battery management," *IEEE Transactions on Sustainable Energy*, vol. 2, pp. 300–308, 2011, DOI: 10.1109/TSTE.2011.2116813.

[151] T. Kim and W. Qiao, “A hybrid battery model capable of capturing dynamic circuit characteristics and nonlinear capacity effects," *IEEE Transactions on Energy Conversion*, vol. 26, pp. 1172–1180, 2011, DOI: 10.1109/TEC.2011.2167014.

[152] D. Andre, M. Meiler, K. Steiner, H. Walz, T. Soczka-Guth and D. U. Sauer, “Characterization of high-power lithium-ion batteries by electrochemical impedance spectroscopy. II: Modelling," *Journal of Power Sources*, vol. 196, pp. 5349–5356, 2011, DOI: 10.1016/j.jpowsour.2010.07.071.

[153] A. Farmann, W. Waag and D. U. Sauer, “Adaptive approach for on-board impedance parameters and voltage estimation of lithium-ion batteries in electric vehicles," *Journal of Power Sources*, vol. 299, pp. 176–188, 2015, DOI: 10.1016/j.jpowsour.2015.08.087.

[154] A. Farmann and D. U. Sauer, “Comparative study of reduced order equivalent circuit models for on-board state-of-available-power prediction of lithium-ion batteries in electric vehicles," *Applied Energy*, vol. 225, pp. 1102–1122, 2018, DOI: 10.1016/j.apenergy.2018.05.066.

[155] T. Heil and A. Jossen, “Continuous approximation of the ZARC element with passive components," *Measurement Science and Technology*, vol. 32, no. 10, p. 104011, 2021, DOI: 10.1088/1361-6501/ac0466.

[156] T. Handschuh, “Untersuchung des Betriebs-und Alterungsverhaltens von Blei-Säure-Akkumulatoren bei für Hybridantriebssysteme typischen Belastungen," PhD thesis, Universität Ulm, 2007.

[157] J. S. Edge, S. O’Kane, R. Prosser, N. D. Kirkaldy, A. N. Patel, et al., “Lithium ion battery degradation: what you need to know," *Physical Chemistry Chemical Physics*, vol. 23, no. 14, pp. 8200–8221, 2021, DOI: 10.1039/D1CP00359C.

[158] A. Barré, B. Deguilhem, S. Grolleau, M. Gérard, F. Suard and D. Riu, “A review on lithium-ion battery ageing mechanisms and estimations for automotive applications," *Journal of Power Sources*, vol. 241, pp. 680–689, 2013, DOI: 10.1016/j.jpowsour.2013.05.040.

[159] Y. Gao, J. Jiang, C. Zhang, W. Zhang and Y. Jiang, “Aging mechanisms under different state-of-charge ranges and the multi-indicators system of state-of-health for lithium-ion battery with Li(NiMnCo)O2 cathode," *Journal of Power Sources*, vol. 400, pp. 641–651, 2018, DOI: 10.1016/j.jpowsour.2018.07.018.

[160] S. Barcellona and L. Piegari, “Effect of current on cycle aging of lithium ion batteries," *Journal of Energy Storage*, vol. 29, p. 101310, 2020, DOI: 10.1016/j.est.2020.101310.

[161] Z. Ma, J. Jiang, W. Shi, W. Zhang and C. C. Mi, “Investigation of path dependence in commercial lithium-ion cells for pure electric bus applications: Aging mechanism identification," *Journal of Power Sources*, vol. 274, pp. 29–40, 2015, DOI: 10.1016/j.jpowsour.2014.10.006.

[162] K. L. Gering, S. V. Sazhin, D. K. Jamison, C. J. Michelbacher, B. Y. Liaw, M. Dubarry and M. Cugnet, “Investigation of path dependence in commercial lithium-ion cells chosen for plug-in hybrid vehicle duty cycle protocols," *Journal of Power Sources*, vol. 196, pp. 3395–3403, 2011, DOI: 10.1016/j.jpowsour.2010.05.058.

[163] J. Vetter, P. Novák, M. R. Wagner, C. Veit, K.-C. Möller, J. O. Besenhard, M. Winter, M. Wohlfahrt-Mehrens, C. Vogler and A. Hammouche, “Ageing mechanisms in lithium-ion batteries," *Journal of Power Sources*, vol. 147, no. 1–2, pp. 269–281, 2005, DOI: 10.1016/j.jpowsour.2005.01.006.

[164] X. Han, L. Lu, Y. Zheng, X. Feng, Z. Li, J. Li and M. Ouyang, “A review on the key issues of the lithium ion battery degradation among the whole life cycle," *eTransportation*, vol. 1, p. 100005, 2019, DOI: 10.1016/j.etran.2019.100005.

[165] S. J. An, J. Li, C. Daniel, D. Mohanty, S. Nagpure and D. L. Wood, “The state of understanding of the lithium-ion-battery graphite solid electrolyte interphase (SEI) and its relationship to formation cycling," *Carbon*, vol. 105, pp. 52–76, 2016, DOI: 10.1016/j.carbon.2016.04.008.

[166] P. M. Attia, W. C. Chueh and S. J. Harris, “Revisiting the t 0.5 Dependence of SEI Growth," *Journal of The Electrochemical Society*, vol. 167, p. 090535, 2020, DOI: 10.1149/1945-7111/ab8ce4.

[167] T. Waldmann, B.-I. Hogg and M. Wohlfahrt-Mehrens, “Li plating as unwanted side reaction in commercial Li-ion cells – A review," *Journal of Power Sources*, vol. 384, pp. 107–124, 2018, DOI: 10.1016/j.jpowsour.2018.02.063.

[168] C. Von Lüders, J. Keil, M. Webersberger and A. Jossen, “Modeling of lithium plating and lithium stripping in lithium-ion batteries," *Journal of Power Sources*, vol. 414, pp. 41–47, 2019, DOI: 10.1016/j.jpowsour.2018.12.084.

[169] J. Keil, N. Paul, V. Baran, P. Keil, R. Gilles and A. Jossen, “Linear and Nonlinear Aging of Lithium-Ion Cells Investigated by Electrochemical Analysis and In-Situ Neutron Diffraction," *Journal of The Electrochemical Society*, vol. 166, A3908–A3917, 2019, DOI: 10.1149/2.1271915jes.

[170] P. Fermín-Cueto, E. McTurk, M. Allerhand, E. Medina-Lopez, M. F. Anjos, J. Sylvester and G. Dos Reis, “Identification and machine learning prediction of knee-point and knee-onset in capacity degradation curves of lithium-ion cells," *Energy and AI*, vol. 1, p. 100006, 2020, DOI: 10.1016/j.egyai.2020.100006.

[171] C. Pastor-Fernández, T. F. Yu, W. D. Widanage and J. Marco, “Critical review of non-invasive diagnosis techniques for quantification of degradation modes in lithium-ion batteries," *Renewable and Sustainable Energy Reviews*, vol. 109, pp. 138–159, 2019, DOI: 10.1016/j.rser.2019.03.060.

[172] M. Dubarry and D. Anseán, “Best practices for incremental capacity analysis," *Frontiers in Energy Research*, vol. 10, p. 1023555, 2022, DOI: 10.3389/fenrg.2022.1023555.

[173] J. Schmitt, M. Schindler and A. Jossen, “Change in the half-cell open-circuit potential curves of silicon–graphite and nickel-rich lithium nickel manganese cobalt oxide during cycle aging," *Journal of Power Sources*, vol. 506, p. 230240, 2021, DOI: 10.1016/j.jpowsour.2021.230240.

[174] K. G. Gallagher and P. A. Nelson, “6 - Manufacturing Costs of Batteries for Electric Vehicles," in *Lithium-Ion Batteries*, G. Pistoia, ed. Amsterdam: Elsevier, 2014, pp. 97–126, DOI: 10.1016/B978-0-444-59513-3.00006-6.

[175] S. Stock, J. Hagemeister, S. Grabmann, J. Kriegler, J. Keilhofer, et al., “Cell teardown and characterization of an automotive prismatic LFP battery," *Electrochimica Acta*, vol. 471, p. 143341, 2023, DOI: 10.1016/j.electacta.2023.143341.

[176] S. Rothgang, T. Baumhöfer, H. van Hoek, T. Lange, R. W. De Doncker and D. U. Sauer, “Modular battery design for reliable, flexible and multi-technology energy storage systems," *Applied Energy*, vol. 137, pp. 931–937, 2015.

[177] A. Perner and J. Vetter, “8 - Lithium-ion batteries for hybrid electric vehicles and battery electric vehicles," in *Advances in Battery Technologies for Electric Vehicles* (Woodhead Publishing Series in Energy), B. Scrosati, J. Garche and W. Tillmetz, ed. Woodhead Publishing, 2015, pp. 173–190, DOI: 10.1016/B978-1-78242-377-5.00008-X.

[178] S. Lee, T. H. Kim, S. Jack Hu, W. Cai and J. A. Abell, “Joining Technologies for Automotive Lithium-Ion Battery Manufacturing: A Review," *ASME 2010 International Manufacturing Science and Engineering Conference*, vol. 1, 2010, DOI: 10.1115/MSEC2010-34168.

[179] M. Ank, T. Brehler and M. Lienkamp, “Wire bond contact defect identification in battery modules of electric vehicles using pulses and differential voltage analysis," *eTransportation*, vol. 18, p. 100284, 2023.

[180] V. Müller, R.-G. Scurtu, M. Memm, M. A. Danzer and M. Wohlfahrt-Mehrens, “Study of the influence of mechanical pressure on the performance and aging of Lithium-ion battery cells," *Journal of Power Sources*, vol. 440, p. 227148, 2019, DOI: 10.1016/j.jpowsour.2019.227148.

[181] M. J. Brand, P. A. Schmidt, M. F. Zaeh and A. Jossen, “Welding techniques for battery cells and resulting electrical contact resistances," *Journal of Energy Storage*, vol. 1, pp. 7–14, 2015, DOI: 10.1016/j.est.2015.04.001.

[182] M. J. Brand, E. I. Kolp, P. Berg, T. Bach, P. Schmidt and A. Jossen, “Electrical resistances of soldered battery cell connections," *Journal of Energy Storage*, vol. 12, pp. 45–54, 2017, DOI: 10.1016/j.est.2017.03.019.

[183] M. J. Brand, P. Berg, E. I. Kolp, T. Bach, P. Schmidt and A. Jossen, “Detachable electrical connection of battery cells by press contacts," *Journal of Energy Storage*, vol. 8, pp. 69–77, 2016, DOI: 10.1016/j.est.2016.09.011.

[184] X. Gong, R. Xiong and C. C. Mi, “Study of the Characteristics of Battery Packs in Electric Vehicles With Parallel-Connected Lithium-Ion Battery Cells," *IEEE Transactions on Industry Applications*, vol. 51, no. 2, pp. 1872–1879, 2015, DOI: 10.1109/TIA.2014.2345951.

[185] S. Santhanagopalan and R. E. White, “Quantifying Cell-to-Cell Variations in Lithium Ion Batteries," *International Journal of Electrochemistry*, vol. 2012, no. 12, pp. 1–10, 2012, DOI: 10.1155/2012/395838.

[186] M. Dubarry, N. Vuillaume and B. Y. Liaw, “Origins and accommodation of cell variations in Li-ion battery pack modeling," *International Journal of Energy Research*, vol. 34, no. 2, pp. 216–231, 2010, DOI: 10.1002/er.1668.

[187] B. Kenney, K. Darcovich, D. D. MacNeil and I. J. Davidson, “Modelling the impact of variations in electrode manufacturing on lithium-ion battery modules," *Journal of Power Sources*, vol. 213, pp. 391–401, 2012, DOI: 10.1016/j.jpowsour.2012.03.065.

[188] S. Paul, C. Diegelmann, H. Kabza and W. Tillmetz, “Analysis of ageing inhomogeneities in lithium-ion battery systems," *Journal of Power Sources*, vol. 239, pp. 642–650, 2013, DOI: 10.1016/j.jpowsour.2013.01.068.

[189] S. Müller, J. Eller, M. Ebner, C. Burns, J. Dahn and V. Wood, “Quantifying Inhomogeneity of Lithium Ion Battery Electrodes and Its Influence on Electrochemical Performance," *Journal of The Electrochemical Society*, vol. 165, no. 2, A339, 2018, DOI: 10.1149/2.0311802jes.

[190] M. Dubarry and B. Y. Liaw, “Identify capacity fading mechanism in a commercial LiFePO4 cell," *Journal of Power Sources*, vol. 194, no. 1, pp. 541–549, 2009, DOI: 10.1016/j.jpowsour.2009.05.036.

[191] Y. Zheng, X. Han, L. Lu, J. Li and M. Ouyang, “Lithium ion battery pack power fade fault identification based on Shannon entropy in electric vehicles," *Journal of Power Sources*, 2013, DOI: 10.1016/j.jpowsour.2012.09.015.

[192] S. Rothgang, T. Baumhofer and D. U. Sauer, “Diversion of Aging of Battery Cells in Automotive Systems," in *2014 IEEE Vehicle Power and Propulsion Conference (VPPC)*, 2014, pp. 1–6, DOI: 10.1109/VPPC.2014.7007050.

[193] S. F. Schuster, M. J. Brand, P. Berg, M. Gleissenberger and A. Jossen, “Lithium-ion cell-to-cell variation during battery electric vehicle operation," *Journal of Power Sources*, vol. 297, pp. 242–251, 2015, DOI: 10.1016/j.jpowsour.2015.08.001.

[194] A. Devie and M. Dubarry, “Durability and reliability of electric vehicle batteries under electric utility grid operations. Part 1: Cell-to-cell variations and preliminary testing," *Batteries*, vol. 2, no. 3, 2016, DOI: 10.3390/batteries2030028.

[195] C. Campestrini, P. Keil, S. F. Schuster and A. Jossen, “Ageing of lithium-ion battery modules with dissipative balancing compared with single-cell ageing," *Journal of Energy Storage*, vol. 6, pp. 142–152, 2016, DOI: 10.1016/j.est.2016.03.004.

[196] Q. Fang, X. Wei and H. Dai, “A Study of Parameter Inconsistency Evolution Pattern in Parallel-Connected Battery Modules," *SAE Technical Paper*, 2017, DOI: 10.4271/2017-01-1194.

[197] K. Rumpf, M. Naumann and A. Jossen, “Experimental investigation of parametric cell-to-cell variation and correlation based on 1100 commercial lithium-ion cells," *Journal of Energy Storage*, vol. 14, pp. 224–243, 2017, DOI: 10.1016/j.est.2017.09.010.

[198] J. V. Barreras, T. Raj, D. A. Howey and E. Schaltz, “Results of screening over 200 pristine lithium-ion cells," *2017 IEEE Vehicle Power and Propulsion Conference, VPPC 2017 - Proceedings*, vol. 2018-Janua, no. Cccv, pp. 1–6, 2018, DOI: 10.1109/VPPC.2017.8331054.

[199] A. Devie, G. Baure and M. Dubarry, “Intrinsic variability in the degradation of a batch of commercial 18650 lithium-ion cells," *Energies*, vol. 11, no. 5, pp. 1–14, 2018, DOI: 10.3390/en11051031.

[200] M. Baumann, S. Rohr and M. Lienkamp, “Cloud-connected battery management for decision making on second-life of electric vehicle batteries," in *2018 13th International Conference on Ecological Vehicles and Renewable Energies (EVER)*, 2018, pp. 1–6, DOI: 10.1109/EVER.2018.8362355.

[201] I. Zilberman, S. Ludwig and A. Jossen, “Cell-to-cell variation of calendar aging and reversible self-discharge in 18650 nickel-rich, silicon–graphite lithium-ion cells," *Journal of Energy Storage*, vol. 26, no. August, p. 100900, 2019, DOI: 10.1016/j.est.2019.100900.

[202] M. Schindler, J. Sturm, S. Ludwig, J. Schmitt and A. Jossen, “Evolution of Initial Cell-to-Cell Variations During a Three-Year Production Cycle," *eTransportation*, vol. 8, no. March, p. 100102, 2021, DOI: 10.1016/j.etran.2020.100102.

[203] D. Evans, D. M. Brieske, C. Tebruegge and J. Kowal, “Analysis of the impact of manufacturing-induced cell-to-cell variation for high-power applications," *Journal of Power Sources*, vol. 614, p. 235001, 2024, DOI: 10.1016/j.jpowsour.2024.235001.

[204] W. Li, L. Kang, X. Guo and Y. Yao, “Multi-Objective Predictive Balancing Control of Battery Packs Based on Predictive Current," *Energies*, vol. 9, no. 4, p. 298, 2016, DOI: 10.3390/en9040298.

[205] M. J. Brand, M. H. Hofmann, M. Steinhardt, S. F. Schuster and A. Jossen, “Current distribution within parallel-connected battery cells," *Journal of Power Sources*, vol. 334, pp. 202–212, 2016, DOI: 10.1016/j.jpowsour.2016.10.010.

[206] C. Bolsinger, M. Zorn and K. P. Birke, “Electrical contact resistance measurements of clamped battery cell connectors for cylindrical 18650 battery cells," *Journal of Energy Storage*, vol. 12, pp. 29–36, 2017, DOI: 10.1016/j.est.2017.04.001.

[207] U. Khayam, B. Sutrisno, M. Fauzan, Suwarno and A. Risdiyanto, “Measurement and analysis of contact resistance of new designed battery connection," in *Proceeding, Joint International Conference on Electric Vehicular Technology and Industrial, Mechanical, Electrical and Chemical Engineering (ICEVT & IMECE)*, 2015, pp. 22–27, DOI: 10.1109/ICEVTIMECE.2015.7496641.

[208] P. A. Schmidt, P. Schmitz and M. F. Zaeh, “Laser beam welding of electrical contacts for the application in stationary energy storage devices," *Journal of Laser Applications*, vol. 28, no. 2, p. 022423, 2016, DOI: 10.2351/1.4943908.

[209] P. Schmidt, “Laserstrahlschweißen elektrischer Kontakte von Lithium-Ionen-Batterien in Elektro- und Hybridfahrzeugen," Dissertation, Technical University of Munich, 2015.

[210] P. Taheri, S. Hsieh and M. Bahrami, “Investigating electrical contact resistance losses in lithium-ion battery assemblies for hybrid and electric vehicles," *Journal of Power Sources*, vol. 196, no. 15, pp. 6525–6533, 2011, DOI: 10.1016/j.jpowsour.2011.03.056.

[211] G. J. Offer, V. Yufit, D. A. Howey, B. Wu and N. P. Brandon, “Module design and fault diagnosis in electric vehicle batteries," *Journal of Power Sources*, vol. 206, pp. 383–392, 2012, DOI: 10.1016/j.jpowsour.2012.01.087.

[212] B. Wu, V. Yufit, M. Marinescu, G. J. Offer, R. F. Martinez-Botas and N. P. Brandon, “Coupled thermal–electrochemical modelling of uneven heat generation in lithium-ion battery packs," *Journal of Power Sources*, vol. 243, pp. 544–554, 2013, DOI: 10.1016/j.jpowsour.2013.05.164.

[213] R. Gogoana, M. B. Pinson, M. Z. Bazant and S. E. Sarma, “Internal resistance matching for parallel-connected lithium-ion cells and impacts on battery pack cycle life," *Journal of Power Sources*, vol. 252, pp. 8–13, 2014, DOI: 10.1016/j.jpowsour.2013.11.101.

[214] T. Bruen and J. Marco, “Modelling and experimental evaluation of parallel connected lithium ion cells for an electric vehicle battery system," *Journal of Power Sources*, vol. 310, pp. 91–101, 2016, DOI: 10.1016/j.jpowsour.2016.01.001.

[215] M.-S. Wu, C.-Y. Lin, Y.-Y. Wang, C.-C. Wan and C. R. Yang, “Numerical simulation for the discharge behaviors of batteries in series and/or parallel-connected battery pack," *Electrochimica Acta*, vol. 52, no. 3, pp. 1349–1357, 2006, DOI: 10.1016/j.electacta.2006.07.036.

[216] N. Yang, X. Zhang, B. Shang and G. Li, “Unbalanced discharging and aging due to temperature differences among the cells in a lithium-ion battery pack with parallel combination," *Journal of Power Sources*, vol. 306, pp. 733–741, 2016, DOI: 10.1016/j.jpowsour.2015.12.079.

[217] M. Fleckenstein, O. Bohlen, M. A. Roscher and B. Bäker, “Current density and state of charge inhomogeneities in Li-ion battery cells with LiFePO4 as cathode material due to temperature gradients," *Journal of Power Sources*, vol. 196, no. 10, pp. 4769–4778, 2011, DOI: 10.1016/j.jpowsour.2011.01.043.

[218] Y. Zhang, R. Zhao, J. Dubie, T. Jahns and L. Juang, “Investigation of current sharing and heat dissipation in parallel-connected lithium-ion battery packs," in *2016 IEEE Energy Conversion Congress and Exposition (ECCE)*, 2016, pp. 1–8, DOI: 10.1109/ECCE.2016.7855217.

[219] Y. Zheng, M. Ouyang, L. Lu and J. Li, “Understanding aging mechanisms in lithium-ion battery packs: From cell capacity loss to pack capacity evolution," *Journal of Power Sources*, vol. 278, pp. 287–295, 2015, DOI: 10.1016/j.jpowsour.2014.12.105.

[220] C. Pastor-Fernández, T. Bruen, W. D. Widanage, M. A. Gama-Valdez and J. Marco, “A Study of Cell-to-Cell Interactions and Degradation in Parallel Strings: Implications for the Battery Management System," *Journal of Power Sources*, vol. 329, pp. 574–585, 2016, DOI: 10.1016/j.jpowsour.2016.07.121.

[221] T. Baumhöfer, M. Brühl, S. Rothgang and D. U. Sauer, “Production caused variation in capacity aging trend and correlation to initial cell performance," *Journal of Power Sources*, vol. 247, pp. 332–338, 2014, DOI: 10.1016/j.jpowsour.2013.08.108.

[222] Datasheet. “*Product Specifications US18659VTC5A*," 2024. Available: https://enerpower.de/wp/wp-content/uploads/2016/04/Specification-US18650VTC5A.pdf [visited on 10/24/2024].

[223] J. Schmitt, M. Schindler, A. Oberbauer and A. Jossen, “Determination of degradation modes of lithium-ion batteries considering aging-induced changes in the half-cell open-circuit potential curve of silicon–graphite," *Journal of Power Sources*, vol. 532, p. 231296, 2022, DOI: https://doi.org/10.1016/j.jpowsour.2022.231296.

[224] D. Anseán, G. Baure, M. González, I. Cameán, A. García and M. Dubarry, “Mechanistic investigation of silicon-graphite/LiNi0.8Mn0.1Co0.1O2 commercial cells for non-intrusive diagnosis and prognosis," *Journal of Power Sources*, vol. 459, p. 227882, 2020, DOI: https://doi.org/10.1016/j.jpowsour.2020.227882.

[225] W. Ai, N. Kirkaldy, Y. Jiang, G. Offer, H. Wang and B. Wu, “A composite electrode model for lithium-ion batteries with silicon/graphite negative electrodes," *Journal of Power Sources*, vol. 527, p. 231142, 2022, DOI: https://doi.org/10.1016/j.jpowsour.2022.231142.

[226] Y. Pan, X. Han, X. Kong, L. Lu, M. Ouyang, J. Zhang, Y. Wang and H. Zheng, “Lithium plating induced by anode tab tearing in lithium-ion batteries: An experimental and modeling study," *Journal of Energy Storage*, vol. 73, p. 109176, 2023, DOI: 10.1016/j.est.2023.109176. Available: https://linkinghub.elsevier.com/retrieve/pii/S2352152X23025744 [visited on 10/23/2024].

[227] N. Wassiliadis, M. Ank, A. Bach, M. Wanzel, A.-S. Zollner, K. A. Gamra and M. Lienkamp, “A systematic approach for the parameter identification of electrochemical battery models enabling health-aware fast charging control of battery electric vehicles," *Journal of Energy Storage*, vol. 56, p. 105951, 2022, DOI: https://doi.org/10.1016/j.est.2022.105951.

[228] J. Sturm, A. Rheinfeld, I. Zilberman, F. Spingler, S. Kosch, F. Frie and A. Jossen, “Modeling and simulation of inhomogeneities in a 18650 nickel-rich, silicon-graphite lithium-ion cell during fast charging," *Journal of Power Sources*, vol. 412, pp. 204–223, 2019, DOI: https://doi.org/10.1016/j.jpowsour.2018.11.043.

[229] M. Dubarry and D. Beck, “Investigation of the impact of different electrode inhomogeneities on the voltage response of Li-ion batteries," *Cell Reports Physical Science*, vol. 5, no. 8, p. 102138, 2024, DOI: https://doi.org/10.1016/j.xcrp.2024.102138.

[230] A. Karger, S. E. J. O’Kane, M. Rogge, C. Kirst, J. P. Singer, M. Marinescu, G. J. Offer and A. Jossen, “Modeling Particle Versus SEI Cracking in Lithium-Ion Battery Degradation: Why Calendar and Cycle Aging Cannot Simply be Added," *Journal of The Electrochemical Society*, vol. 171, no. 9, p. 090512, 2024, DOI: 10.1149/1945-7111/ad76da.

[231] T. Hofmann, J. Li, J. Hamar, S. Erhard and J. P. Schmidt, “The deltaQ-method: State of health and degradation mode estimation for lithium-ion batteries using a mechanistic model with relaxed voltage points," *Journal of Power Sources*, vol. 596, p. 234107, 2024, DOI: https://doi.org/10.1016/j.jpowsour.2024.234107.

[232] X. Liu, W. Ai, M. Naylor Marlow, Y. Patel and B. Wu, “The effect of cell-to-cell variations and thermal gradients on the performance and degradation of lithium-ion battery packs," *Applied Energy*, vol. 248, pp. 489–499, 2019, DOI: https://doi.org/10.1016/j.apenergy.2019.04.108.

[233] C. Geisbauer, K. Wöhrl, D. Koch, G. Wilhelm, G. Schneider and H.-G. Schweiger, “Comparative Study on the Calendar Aging Behavior of Six Different Lithium-Ion Cell Chemistries in Terms of Parameter Variation," *Energies*, vol. 14, no. 11, p. 3358, 2021, DOI: 10.3390/en14113358.

[234] M. Ank, S. Stock, N. Wassiliadis, T. Burger, R. Daub and M. Lienkamp, “Influence analysis of production defects of lithium-ion cells using single-cell and multi-cell characterization," *Journal of Energy Storage*, vol. 62, p. 106938, 2023.

[235] M. Ank, T. Kröger, M. Schreiber and M. Lienkamp, “Experimental analysis of lithium-ion cell procurement: Quality differences, correlations, and importance of cell characterization," *Journal of Energy Storage*, vol. 66, p. 107430, 2023.

[236] E. Barbers, F. E. Hust, F. E. A. Hildenbrand, F. Frie, K. L. Quade, S. Bihn, D. U. Sauer and P. Dechent, “Exploring the effects of cell-to-cell variability on battery aging through stochastic simulation techniques," *Journal of Energy Storage*, vol. 84, p. 110851, 2024, DOI: https://doi.org/10.1016/j.est.2024.110851.

[237] J. Schöberl, M. Ank, M. Schreiber, N. Wassiliadis and M. Lienkamp, “Thermal runaway propagation in automotive lithium-ion batteries with NMC-811 and LFP cathodes: Safety requirements and impact on system integration," *Etransportation*, vol. 19, p. 100305, 2024.

[238] M. Ank, J. Göhmann and M. Lienkamp, “Multi-Cell Testing Topologies for Defect Detection Using Electrochemical Impedance Spectroscopy: A Combinatorial Experiment-Based Analysis," *Batteries*, vol. 9, no. 8, p. 415, 2023.

Prior Publications

During the development of this dissertation, publications and student theses were written in which partial aspects of this work were presented.

Journals; Scopus/Web of Science listed (peer-reviewed)

[1] L. Wildfeuer, N. Wassiliadis, A. Karger, F. Bauer and M. Lienkamp, “Teardown analysis and characterization of a commercial lithium-ion battery for advanced algorithms in battery electric vehicles," *Journal of Energy Storage*, vol. 48, no. December 2021, p. 103909, 2022, DOI: 10.1016/j.est.2021.103909.

[2] L. Wildfeuer, P. Gieler and A. Karger, “Combining the Distribution of Relaxation Times from EIS and Time-Domain Data for Parameterizing Equivalent Circuit Models of Lithium-Ion Batteries," *Batteries*, vol. 7, no. 3, pp. 1–23, 2021, DOI: 10.3390/batteries7030052.

[3] A. Karger, L. Wildfeuer, A. Maheshwari, N. Wassiliadis and M. Lienkamp, “Novel method for the on-line estimation of low-frequency impedance of lithium-ion batteries," *Journal of Energy Storage*, vol. 32, no. August, p. 101818, 2020, DOI: 10.1016/j.est.2020.101818.

[4] L. Wildfeuer, A. Karger, D. Aygül, N. Wassiliadis, A. Jossen and M. Lienkamp, “Experimental degradation study of a commercial lithium-ion battery," *Journal of Power Sources*, vol. 560, p. 232498, 2023, DOI: 10.1016/j.jpowsour.2022.232498.

[5] L. Wildfeuer and M. Lienkamp, “Quantifiability of inherent cell-to-cell variations of commercial lithium-ion batteries," *eTransportation*, vol. 9, p. 100129, 2021, DOI: 10.1016/j.etran.2021.100129.

[6] M. Baumann, L. Wildfeuer, S. Rohr and M. Lienkamp, “Parameter variations within Li-Ion battery packs – Theoretical investigations and experimental quantification," *Journal of Energy Storage*, vol. 18, 2018, DOI: 10.1016/j.est.2018.04.031.

[15] A. Karger, L. Wildfeuer, D. Aygül, A. Maheshwari, J. P. Singer and A. Jossen, “Modeling capacity fade of lithium-ion batteries during dynamic cycling considering path dependence," *Journal of Energy Storage*, vol. 52, p. 104718, 2022, DOI: 10.1016/j.est.2022.104718.

[16] A. Karger, J. Schmitt, C. Kirst, J. P. Singer, L. Wildfeuer and A. Jossen, “Mechanistic calendar aging model for lithium-ion batteries," *Journal of Power Sources*, vol. 578, p. 233208, 2023, DOI: 10.1016/j.jpowsour.2023.233208.

[17] A. Karger, J. Schmitt, C. Kirst, J. P. Singer, L. Wildfeuer and A. Jossen, “Mechanistic cycle aging model for the open-circuit voltage curve of lithium-ion batteries," *Journal of Power Sources*, vol. 593, p. 233947, 2024, DOI: 10.1016/j.jpowsour.2023.233947.

[24] T. Gewald, A. Candussio, L. Wildfeuer, D. Lehmkuhl, A. Hahn and M. Lienkamp, “Accelerated Aging Characterization of Lithium-ion Cells: Using Sensitivity Analysis to Identify the Stress Factors Relevant to Cyclic Aging," *Batteries*, vol. 6, no. 1, 2020, DOI: 10.3390/batteries6010006.

[25] N. Wassiliadis, M. Ank, L. Wildfeuer, M. K. Kick and M. Lienkamp, “Experimental investigation of the influence of electrical contact resistance on lithium-ion battery testing for fast-charge applications," *Applied Energy*, vol. 295, p. 117064, 2021, DOI: 10.1016/j.apenergy.2021.117064.

[26] N. Wassiliadis, J. Schneider, A. Frank, L. Wildfeuer, X. Lin, A. Jossen and M. Lienkamp, “Review of fast charging strategies for lithium-ion battery systems and their applicability for battery electric vehicles," *Journal of Energy Storage*, vol. 44, p. 103306, 2021, DOI: 10.1016/j.est.2021.103306.

[27] N. Wassiliadis, M. Steinsträter, M. Schreiber, P. Rosner, L. Nicoletti, et al., “Quantifying the state of the art of electric powertrains in battery electric vehicles: Range, efficiency, and lifetime from component to system level of the Volkswagen ID.3," *eTransportation*, vol. 12, p. 100167, 2022, DOI: 10.1016/j.etran.2022.100167.

Conferences; Scopus/Web of Science listed (peer-reviewed)

[7] L. Wildfeuer, N. Wassiliadis, C. Reiter, M. Baumann and M. Lienkamp, “Experimental Characterization of Li-Ion Battery Resistance at the Cell, Module and Pack Level," in *2019 Fourteenth International Conference on Ecological Vehicles and Renewable Energies (EVER)*, 2019, pp. 1–12, DOI: 10.1109/EVER.2019.8813578.

[20] C. Reiter, N. Wassiliadis, L. Wildfeuer, T. Wurster and M. Lienkamp, “Range extension of electric vehicles through improved battery capacity utilization: Potentials, risks and strategies," in *2018 21st International Conference on Intelligent Transportation Systems (ITSC)*, 2018, pp. 321–326, DOI: 10.1109/ITSC.2018.8569455.

[21] C. Reiter, L. Wildfeuer, N. Wassiliadis, T. Krahl, J. Dirnecker and M. Lienkamp, “A holistic approach for simulation and evaluation of electrical and thermal loads in lithium-ion battery systems," in *2019 Fourteenth International Conference on Ecological Vehicles and Renewable Energies (EVER)*, 2019, pp. 1–17, DOI: 10.1109/EVER.2019.8813640.

[22] W. Schmid, L. Wildfeuer, J. Kreibich, R. Büechl, M. Schuller and M. Lienkamp, “A Longitudinal Simulation Model for a Fuel Cell Hybrid Vehicle: Experimental Parameterization and Validation with a Production Car," in *2019 Fourteenth International Conference on Ecological Vehicles and Renewable Energies (EVER)*, 2019, pp. 1–13, DOI: 10.1109/EVER.2019.8813648.

[23] N. Wassiliadis, T. Herrmann, L. Wildfeuer, C. Reiter and M. Lienkamp, “Comparative Study of State-Of-Charge Estimation with Recurrent Neural Networks," in *2019 IEEE Transportation Electrification Conference and Expo (ITEC)*, 2019, pp. 1–6, DOI: 10.1109/ITEC.2019.8790597.

Poster; not Scopus/Web of Science listed

[10] L. Wildfeuer, M. Baumann and M. Lienkamp. "*Concept for a hybrid semi-empirical and data-based model for state-of-health monitoring and aging prediction of li-ion battery packs*," Poster. at: *Advanced Automotive Battery Conference (AABC) Europe*, Strasbourg, France. 2019.

[18] A. Karger, L. Wildfeuer and A. Jossen. "*Using degradation modes for large-scale capacity and power fade diagnostics*," Poster. at: *Advanced Battery Power*, Münster, Germany. 2022.

[19] A. Karger, J. Schmitt, C. Kirst, J. P. Singer, L. Wildfeuer and A. Jossen. "*Empirical modeling of degradation mode evolution during calendar aging of lithium-ion batteries*," Poster. at: *Advanced Battery Power*, Münster, Germany. 2023.

Thesis-relevant open-source data

[11] L. Wildfeuer, N. Wassiliadis, C. Reiter, M. Baumann and M. Lienkamp. "*Experimental Characterization of Li-Ion Battery Resistance at the Cell, Module and Pack Level*," Dataset. 2019. DOI: 10.13140/RG.2.2.12299.75047.

[12] L. Wildfeuer, N. Wassiliadis, A. Karger, F. Bauer and M. Lienkamp. "*Teardown analysis and characterization of a commercial lithium-ion battery for advanced algorithms in battery electric vehicles*," Dataset. 2022. DOI: 10.14459/2022mp1639153.

[13] L. Wildfeuer, A. Karger, D. Aygül, N. Wasiiliadis, A. Jossen and M. Lienkamp. "*Experimental degradation study of a commercial lithium-ion battery*," Dataset. 2023. DOI: 10.14459/2023mp1713382.

[14] L. Wildfeuer and M. Lienkamp. "*Quantifiability of inherent cell-to-cell variations of commercial lithium-ion batteries*," Dataset. 2023. DOI: 10.13140/RG.2.2.31720.60160.

Supervised Student Theses

The following student theses were written within the framework of the dissertation under the supervision of the author in terms of content, technical and scientific support as well as under relevant guidance of the author. In the following, the bachelor, semester and master theses relevant and related to this dissertation are listed. Many thanks to the authors of these theses for their extensive support within the framework of this research project.

[28] P. Gries, “Emission Reduction Potential of Predictive Battery Analytics along the Lithium-Ion Battery Lifecycle," Master’s Thesis, Technical University of Munich, 2021.

[29] E. Fischer, “Konstruktion einer Temperaturkammer für Batterieversuche," Bachelor’s Thesis, Technical University of Munich, 2019.

[30] P. Gieler, “Implementierung und Analyse eines Algorithmus zur Parameterbestimmung von Lithium-Ionen-Zellen," Bachelor’s Thesis, Technical University of Munich, 2019.

[31] P. Gieler, “Parameterizing Equivalent Circuit Models of Lithium-Ion Batteries with the Distribution of Relaxation Times," Semester’s Thesis, Technical University of Munich, 2020.

[32] A. Karger, “Impedance Determination of Lithium-Ion Batteries during Vehicle Operation," Semester Thesis, Technical University of Munich, 2019.

[33] L. Reinfeld, “Parametrization of Thermal Equivalent Circuit Models for Lithium-Ion Batteries," Master’s Thesis, Technical University of Munich, 2020.

[34] J. Schürmer, “Detektion und Quantifizierung von Lithium-Plating in Batteriepacks von Elek- trofahrzeugen," Semester Thesis, Technical University of Munich, 2019.

[35] A. Karger, “Detection of Lithium Plating in Lithium-Ion Batteries," Master’s Thesis, Technical University of Munich, 2020.

[36] M. Keßler, “Untersuchung und Implementierung von Methoden zur Belastungscharakterisierung von Lithium-Ionen-Batteriesystemen," Master’s Thesis, Technical University of Munich, 2018.

[37] A. Swierstra, “Experimentelle Untersuchung über das Superpositionsverhalten von kalendarischer und zyklischer Alterung bei Lithium-Ionen Batterien," Semester Thesis, Technical University of Munich, 2019.

[38] D. Ostilla, “Modelling of Superposition Principles of Lithium-Ion Cell Aging Mechanisms," Master’s Thesis, Technical University of Munich, 2020.

[39] K. Waldher, “Untersuchung neuartiger Methoden zur semi-empirischen Alterungsmodellierung von Lithium-Ionen-Zellen," Master’s Thesis, Technical University of Munich, 2019.

[40] S. Erkilic, “Implementierung und Analyse eines Algorithmus zur Parameterbestimmung von Lithium-Ionen-Zellen," Master’s Thesis, Technical University of Munich, 2019.

[41] N. Rücker, “Experimental Investigation and Modelling of Superposition Principles of Lithium-Ion Cell Aging Mechanisms," Master’s Thesis, Technical University of Munich, 2019.

[42] J. Schürmer, “Entwicklung eines semi-empirischen Alterungsmodells für Lithium-Ionen Batterien," Master’s Thesis, Technical University of Munich, 2020.

[43] D. Schmitt, “Entwicklung generischer, semi-empirische Alterungsmodelle für LIB," Semester Thesis, Technical University of Munich, 2020.

[44] D. Aygül, “Analysis of Parameterization Approaches for Aging Modeling of Lithium-Ion Batteries," Semester Thesis, Technical University of Munich, 2020.

[45] D. Schmitt, “Entwicklung eines Alterungsmodells zur Vorhersage des Widerstands für Lithium-Ionen Batterien," Master’s Thesis, Technical University of Munich, 2021.

[46] M. Wanisch, “Lebensdauerprädiktion von Li-Ionen Batterien mittels künstlicher Intelligenz," Master’s Thesis, Technical University of Munich, 2019.

[47] C. Kirst, “Data-Based Aging Modeling of Li-Ion Batteries," Semester Thesis, Technical University of Munich, 2019.

[48] F. Näher, “Datenbasierte Alterungsmodellierung von Lithium-Ionen-Batterien mittels künstlicher neuronaler Netze," Master’s Thesis, Technical University of Munich, 2020.

[49] P. Bilfinger, “Implementation of Transfer Machine Learning Methods for the Aging Prediction of Li-Ion Batteries," Master’s Thesis, Technical University of Munich, 2020.

[50] R. Droop, “Architekturen Künstlicher Neuronaler Netze zur Alterungsmodellierung von Architectures of artificial neural networks for modeling," Semester Thesis, Technical University of Munich, 2020.

[51] D. Weinzierl, “Integration of external knowledge in deep learning methods for the life time prediction of Li-Ion batteries," Master’s Thesis, Technical University of Munich, 2020.

[52] F. Diller, “Entwicklung eines stressfaktorbasierten Alterungsmodells von Lithium-Ionen Batterien mittels maschinellen Lernens," Semester Thesis, Technical University of Munich, 2021.

[53] D. Aygül, “Development of a Hybrid Semi-Empirical and Data-Based Aging Model for Li-Ion Batteries," Master’s Thesis, Technical University of Munich, 2021.

[54] J. Niedermayer, “Analyse und Simulation von Betriebsstrategien für Brennstoffzellenfahrzeuge," Semester Thesis, Technical University of Munich, 2019.

[55] J. Buberger, “Modellierung, Parametrierung und Validierung der Brennstoffzelle in der Längsdynamiksimulation eines Brennstoffzellenfahrzeugs," Semester Thesis, Technical University of Munich, 2019.

[56] P. Rosner, “Experimentelle Analyse des Betriebsverhaltens eines Brennstoffzellen - Elektrofahrzeuges," Semester Thesis, Technical University of Munich, 2019.

[57] R. Büechl, “Modellierung, Parametrierung und Validierung der Längsdynamiksimulation eines Brennstoffzellenfahrzeugs anhand realer Fahrzyklen," Master’s Thesis, Technical University of Munich, 2019.